Friction Stir Extrusion: Control Processes and Unique Applications

By

Adam Jarrell

Thesis
Submitted to the Faculty of the
Graduate School of Vanderbilt University
in partial fulfillment of the requirements
for the degree of

DOCTORATE OF PHILOSOPHY
in
Mechanical Engineering

May 12th, 2023

Nashville, Tennessee

Approved:

Alvin M. Strauss, Ph. D.

Kenneth Frampton, Ph. D.

Kenneth Pence, Ph. D.

Kevin Galloway, Ph. D.

Thomas Withrow, Ph. D.

ACKNOWLEDGMENTS

This dissertation is the summation of multiple years of work spanning multiple stages of my life. First, I would like to thank Dr. Alvin Strauss for his guidance and patience. I would also like to thank my committee members: Dr. Kevin Galloway, Dr. Ken Frampton, Dr. Ken Pence, and Dr. Thomas Withrow for their guidance and flexibility. Through the years, I had a large number of safety buddies, machine shop partners, and Peer reviewers, including but not limited to Todd Evans, Jay Reynolds, Jake Matthews, Kelsay Neely, Darren Tinker, Conor Strawn, Ben Snyder, Lucas Wilkins, and Brayden Terry. I would also like to thank Phil Davis for his advice and expertise in all things welding and machining.

I would also like to thank my family, My brother, Clay Jarrell, who did everything he could to assist me, my father, Gary Jarrell, who was always available to talk through papers or find slipped negatives, my mother, Direnda Jarrell, who made this all possible, my two children and wife, Baylee Jarrell who always make the hard days better.

Financial support was provided through the NASA Space Grant Consortium and Vanderbilt University.

TABLE OF CONTENTS

LIST OF TABLES

LIST OF FIGURES

TERMS AND DEFINITIONS

FSW - Friction Stir welding

TWI - The Welding Institute

FSW - Friction Stir Welding

FSE - Friction Stir Extrusion

SEM - Scanning Electron Microscopy

EDS - Energy Dispersive X-Ray Spectroscopy

HRA - Hardness Rockwell A

HRF - Hardness Rockwell F

CDRX - Continuous Dynamic Recrystallization

TWB - Tailor Welded Blanks

HAZ - Heat Affected Zone

TMAZ - Thermo-Mechanically Effected Zone

TEM - Transmission Electron Microscopy

EBSD - Electron Backscatter Diffraction

GP Zone - Guinier-Preston zones

NDT - Non-Destructive Testing

CHAPTER 1

Introduction

The joining of multiple individual components into larger assemblies is essential in modern manufacturing. Selection of joining methodology for a given application requires consideration to the joint topology, materials to be joined, required strength, speed of production, and cost of the process, among other factors [1]. The scale of production also factors into selection. Mechanical fasteners might be economical on small scales. However, mass production will often make welding the preferred method [2]. Process maturity and regulations can affect the selection of a joining methodology. For example, riveting has been the aerospace industry's joining method of choice for decades. Riveting offers greater consistency than other conventional joining processes and does not introduce heat into the joined materials. So, the temper of the materials to be joined is not disturbed. The heat from fusion welding significantly changes the properties of the age-hardenable aluminum alloys used to construct modern aircraft. Therefore, fusion welding is not used [1].

The transportation industry is often cited as the motivation for innovation in the field of joining. Economic and regulatory pressures lead to higher performance, safer, and more efficient vehicles. These goals can be achieved through multi-material construction. Enabling the joining of dissimilar materials enables the optimal material for each application, leading to weight reduction and greater efficiency. [2]. Different materials are optimal depending on the specific application and manufacturing method. Corrosion resistance, formability, modulus, and strength are all factors in material selection. A typical automobile has many components that have different requirements and experience different stresses in use. So, there is no single optimal material to build a car. For example, automobile chassis are constructed to be stiff around the passengers to provide a safety cage in the case of a crash. This region is often constructed from steel. Other areas of the chassis are designed to crumple in a crash and provide adequate support for drive train components. These areas can be constructed out of aluminum alloys [1].

Solid-state welding technologies are often the best method for joining dissimilar materials. The higher temperatures in conventional fusion welding processes allow chemical reactions between dissimilar pairs. The result is a variety of intermetallic compounds that are detrimental to the joint [1]. Additionally, differences in thermal expansion coefficients and the higher temperatures of fusion welding cause issues.

Friction stir welding is a solid-state welding process developed at TWI in the 1990's [3] that, along with its derivative technologies, has been demonstrated an aptitude for joining dissimilar materials. The process utilizes a rotating non-consumable tool. The tool plunges into the surface and transverses along the length of the weld seam. Material is heated and plasticized along the tools path, forming the two materials into a single piece, Figure 2.1. FSW has several advantages over conventional welding techniques. FSW does not use other consumables such as filler metal or shielding gas. FSW operates below the solidus temperature of the material, not the melt temperature. So, FSW introduces less heat into the material than conventional welding methods, enabling the production of very high joint strengths over a wide range of materials. It has been shown to be applicable to a wide range of materials: Steel [4, 5, 6, 7], aluminum [8], plastic [9], dissimilar materials [10], Titanium [11], Inconel [12, 13], metal matrix composites [14], magnesium [15], and copper [16] have been show to be weldable via the process. FSW creates a low distortion joint with excellent mechanical properties, without fumes, porosity, or spatter present in other welding technologies [17]. A wide variety in material thicknesses, <1mm to >50mm, can be joined in a single pass [18].

The process is prevalent in many industries: transport, aerospace, and maritime, to name a few. A majority of FSW-related patents are filled by the transportation industry, with the automotive industry accounting for a majority of patents filed [19]. A majority of research papers of both similar/dissimilar combinations focus on tensile strength and microstructural properties [19]. An increasing number of FSW Variants have been developed aiming to enhance the process or extend its capabilities [19].

Friction Stir Welding has been suggested as a method for in-space manufacture even though the process has never been tested in space. Friction stir welding does not utilize an electric arc or beam to metal, which increases the safety of the process in vacuum and microgravity. FSW does not rely on convective flow for weld formation, unlike conventional welding processes. FSW is relatively easy to automate, further increasing its safety over conventional welding techniques. However, its relatively high force requirements make it unpractical for hand-held applications, requiring investment in rigid machinery and work holding [20].

Current uses of FSW in aerospace are limited but normally result in significant weight savings. The Eclipse 500 is the first, and to date, only plane to primarily use FSW for its construction [21, 22]. For FSW and derivative processes to break into aerospace manufacturing in a more significant way, regulations and standards need to apply to FSW, allowing for the certification of designs that contain FSW joints [23]. Currently processes are being developed using site-specific hardware this can make it difficult to predict the results when welds are reproduced using new tools. New Zealand/Australia adopted one of the first standards covering FSW leading to more straightforward industrial adoption [24]. The MMPDS, the materials and joining reference that the Military, FAA, and NASA reference, has begun to reference FSW [25].

While FSW in the aerospace industry is limited, one common use for FSW is for fabricating lightweight fuel and oxidizer tanks. NASA began to evaluate FSW for use in joining large cylindrical barrel sections for use in the STS external fuel tank early in the history of the process [26]. FSW was used to fabricate the Super Lightweight Tank variant of the External Tank for the Space Shuttle from STS-130 [27]. United Launch Alliance has utilized FSW to produce lightweight aluminum tanks for their Delta, Atlas, and upcoming Vulcan rockets. SpaceX utilized FSW to fabricate propellant tanks from Aluminum Lithium alloy for the Falcon 9 [28]. Beyond fuel tanks, the Orion Space Capsule utilized 7 Self-reacting Friction Stir welded reducing the vehicle weight by 700 lbs [29].

The automotive industry explored utilizing FSW for the assembly of Tailor Welded Blanks (TWB). TWBs are welded sheets of dissimilar thickness material intended for additional forming operations. The thickness of the sheet can be tailored to the requirements of the formed components, leading to reduced weight. First Generation Ford GT center tunnel was friction stir welded to increase rigidity and create a vapor-tight fuel tank. The rear doors and hood of the Mazda RX-8 utilized friction stir spot welding to reduce spatter, and energy consumption during production [30]. Mazda utilized Friction Stir Spot welding to join aluminum to steel in the trunk lid, and bolt retainer of the MX-5 [31].

Friction Stir Welding has also become a popular choice for joining aluminum extrusions. The maritime industry uses the process to weld together extrusions to form decking panels, bulkheads, and hulls. The construction of large panels has increased productivity, and reduced cost at shipyards by using large prefabricated panels [32]. Fontaine Trailers have integrated StirLITE Aluminum floors into their flatbed trailers, reducing tire wear by 30% and increasing fuel economy by 3% due to the increased rigidity [33]

This work aims to advance the Friction Stir Extrusion (FSE) process towards a production capable joining technology. FSE is a derivative process of FSW developed at VUWAL to enable the joining of dissimilar materials through an in-process formed mechanical interlock [34]. Except in the case of preformed geometry, FSE has the unique advantage that it requires no additional tooling over a standard FSW process. The intention is to integrate the formation of the geometry in the manufacturing of the components to be formed.

Joining thin sheet stock, .063in. to .03 in., demonstrated FSE in a unique regime, where similar work has focused on thick plates >.25 in. The process featured a formed groove rather than one formed subtractively. Further work demonstrated a heat treatment process for FSE joints. The treatment process used a novel approach of a low-temperature soak to precipitate any solutionized alloying elements into strengthening precipitates. Further work will demonstrate control of the process, both in adapting to variations in groove geometry and direction.

CHAPTER 2

Literary Review

2.1 Friction Stir Welding Basics

Threadgill outlined basic terminology used in the field of FSW [35], including the basic features of the welding tool. The basic tool is cylindrical with a second cylindrical feature protruding from one of the flats, Figure 2.1. The 'probe' or 'pin' is the protruding portion of the tool. The probe remains fully submerged in the material during the weld. The tool 'shoulder' is the flat of the larger cylinder. The shoulder rides on top or slightly into the material surface. The probe can come with multiple features, such as threads, flats, and tapers, to enhance specific characteristics of the tool's performance. While it is typically shown as cylindrical, the probe can come in various prisms and more complex shapes. The shoulder can also come with multiple surface features (scrolls or smooth) and tapers (flat, convex, or concave). The application of these features can be used to enhance material flow, heat generation, defect production, and tool life [36].

A Friction Stir Weld is defined by three process parameters: Weld Speed, Tool Rotation Rate, and Lead Angle. The welding speed also called the transverse speed, is the speed at which the tool moves through the material. The tool rotation rate is the angular velocity of the FSW tool. The lead angle is the angle between the normal of the material and the tool's axis of rotation. Another parameter with great significance is the plunge depth. The plunge depth is defined as the distance the tool shoulder has penetrated the material or the total distance the tool has penetrated the material. These parameters are easy to understand. However, they do not accurately indicate the underlying physics of the weld.

Together, these parameters can be used to control the energy deposition rate and

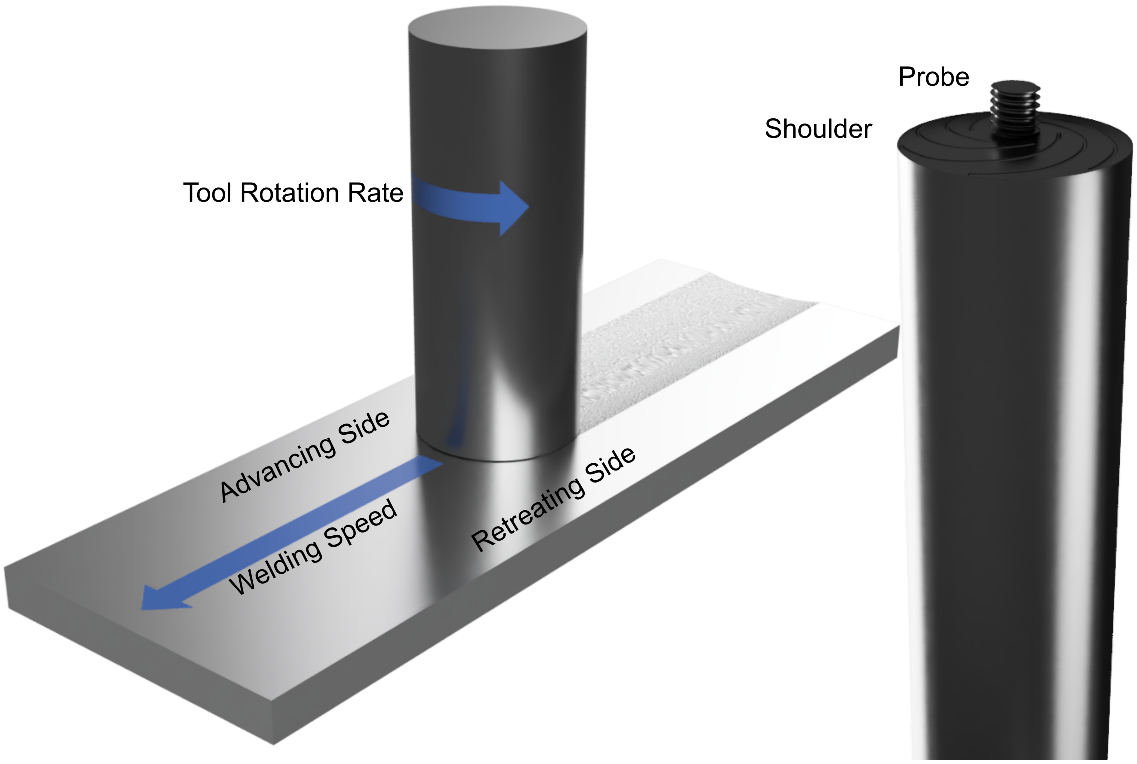

Figure 2.1: The Friction Stir Welding Process.

forging pressure. Colligan and Marshra developed a conceptual map that demonstrated the relationship between the welding setup and process parameters, what they called the independent process variables, with the dependent process outcomes [37].

When referencing the directions on the weld or movements of the welder, the directions will be defined with respect to the axis of the milling machine. The x-axis will be defined as along the long axis of the milling machine, also known as the transverse axis. The Y-axis will be defined as the short axis of the milling machine, also known as the lateral axis. The Z-axis will be along the vertical axis of the milling machine. Unless otherwise noted, the weld is aligned with the seam down the x-axis of the milling machine.

There are two different ’sides’ during a friction stir weld: the advancing and retreating side, Figure 2.1. On the advancing side, the tangential speed of the tool due to its rotation adds to the welding speed. So, the material under the tool experiences a higher tool speed in the x-direction than the welding speed. On the retreating side, the tangential speed of the tool is subtracted from the welding speed. So, the material on the retreating side experiences a lower tool speed than the welding speed. The two sides have different characteristics that will be detailed later.

Friction stir welding is a multiphysics process. Heat transfer, mechanical effects, and metallurgical evolution interact and play in important roll in the FSW process [38]. All three of these physical processes are determined by the processing parameters and other process inputs.

2.1.1 Heat Generation

The temperature distribution and maximum temperature reached during friction stir welding is critical to the process as well as the strength of the final outcome. The elevated temperature lowers the yield strength of the material and makes the material easier to plastically deform, and forged together to from a single piece.

There are two primary sources of heat generation. First, frictional heat is generated by the contact between the rotating tool and solid aluminum. The frictional heating is governed by the coefficient of friction between the aluminum and the tool, and the axial force through the tool. The second source of heating is mechanical dissipation from the plasticized material. The yield strength of the material governs the amount of heat created through mechanical dissipation.

Friction Stir Welding is though to be self-balancing in maximum temperature when performed in an open loop configuration. An increase in temperature causes a decrease in heat input, and results in a decrease in temperature. Likewise, a decrease in temperature causes an increase in heat input, and results in an increase in temperature. Frigaard stated that localized melting above the eutectic temperature or solidus temperature would cause a reduction in frictional heating [39]. Tang et.

al. found that increasing spindle speed had diminishing returns for increasing max weld temperature [40]. They stated that an increase in temperature resulted in a decrease in yield strength. reducing heat generation through mechanical dissipation. Both the coefficient of friction and yield strength depends on the temperature of the material. When the temperature increases around the tool, the heat generation decreases—causing a reduction in temperature, balancing out the process.

Schmidt introduced the sliding/slipping condition and developed an analytical model for heat generation to encompass variable contributions from each condition [41]. Slipping indicates the material does not rotate with the tool inducing frictional heating. The sticking condition indicates that the material sticks to the spinning tool, causing mechanical dissipation as the material is strained. from experimental fitting of the model, Schmidt concluded that the contact condition was predominately sticking or close to sticking. Schnider described a periodic deposition of embedded tracers within friction stir welds and concluded that there was a sporadic seizure of the contact condition, a periodic transition between sliding and sticking, at the edge of the weld shoulder [42].

The heat generation in Friction stir welding is asymmetic and periodic in nature. transitioning between slip and stick conditions through each rotation of the too.

The internal temperatures are difficult to measure directly. There are two methods for measuring the temperature in-situ. In the first method, thermocouples are embedded into the welded material through drilled holes [40, 43]. This method can be prone to error because of destruction or movement of the thermocouple due to the passage of the tool [44]. The second method is to measure tool/workpiece interface temperature through the tool. Thermocouples inserted into cross-drilled holes in the weld tool have been used to measure the weld temperature at the tool/material interface [45, 46, 47, 48]. Also, techniques like Tool/Workpiece Thermocouples (TWT) use the tool and workpiece like a thermocouple to mearsure temperature at the interface

[49, 47].

Tang embedded thermocouples in the welded aluminum and multiple locations accross a range of processing parameters [40]. He concluded that the FSW process was indeed a solid state process, measuring max temperatures lower that 80 percent of the melt temperature. Silva-Magalhaes measured peak temperature to be at the pin shoulder interface [47]. Fehrenbachrer completed a series of weld at various tool rotation rates and weld speeds. Temperatures were measured under the solidus temperature except at the highest rotation rates and lowest transverse speeds, where the temperature could slightly exceed the solidus temperature at the tool shoulder. The pin interface was cooler than at the shoulder [50].

When the temperature at the tool/weld interface is measured by thermocouples with a high enough sampling rate, an asymmetric temperature distribution can be measured [46, 50]. Higher temperatures are measured on the trailing edge and advancing side [44, 47, 50]. These measurements support the asymmetry of the welding process.

2.1.2 Material Flow

During FSW, the tool induces a plastic flow in the welded material. This flow is hard to observe directly due to the inability to see through the metals welded or the tool.

Researchers have gleaned information about the material flow present in FSW by embedding a secondary material into the bulk or welding to dissimilar alloys or materials. These tracing methods leave a trail of material that can be observed in the post-weld analysis, and the material flow can be inferred.

Early work on embedded tracers has led researchers to define the FSW process as an extrusion process, where the material is extruded around the retreating side of the tool. Colligan used embedded lines steel ball-bearing parallel to the weld to trace material flow at multiple locations across the weld. It was found that material outside of the influence of the shoulder was not ”stirred”; the material was extruded around the pin [51]. Reynolds used AA5454 inserts in AA2195 base material to trace material flow around the pin during FSW. The inserts were oriented with their long axis perpendicular to the direction of travel to provide a snapshot across the weld. He argued that the tool forms an extrusion chamber with the non-plasticized material, and no material is sent around the front of the tool [52]. Seidel and Reynolds used the same technique later to conclude that the stirring action is only present near the surface, where the shoulder interacts with the material. The pin extrudes material backward by no more than one pin diameter [53]. Krishnan pointed to the onion rings as evidence of the periodic nature of the process. Material is plasticized and extruded around the tool and deposited into the voids left by the pin each rotation [54]. Arbegast assumed five zones: Preheat, Deformation, Extrusion, Forging, and Cool Down, and used mass balance and flow stress to develop a predictive tool for process parameters [55]. Schneider et al. used CT imaging to trace the motion of a lead wire embedded in aluminum during the welding process. The lead wire was dispersed into arc-like structures behind the welding tool with gaps between arcs. The results suggest a periodic nature of radial flow within the weld, indicating a periodic contact condition between the material and tool called the slip-stick condition [42].

Reynolds summarized material to flow around the tool as three different regimes: (1) Shoulder-driven flow - Material from the retreating side of the tool is sent around the tool and deposited on the advancing side (2) Pin-driven flow - Material from in front of the tool is pulled around the retreating side in a ”shear layer” and deposited behind the tool. (3) Root-flow - Flow present at the bottom flat of the pin, similar to the shoulder-driven flow, with the influence of the backing plate to be a successful weld, the sum of all of these flows must follow a mass balance [56].

EBSD was used to analyze the microstructure of dissimilar FSW AL6181-T4 and

DP600 sheets. The aluminum was placed on the retreating side of the weld, and the pin was exclusively in the aluminum. The plastic flow advancing side contained vortex-like features that form behind the tool. Material on the retreating side deforms upward and escapes the pin tangentially [57].

Corroborating evidence for the periodic nature of FSW can be found in the period and direction of Planar processing forces. Researchers have developed ”force footprints” by plotting the planer processing forces on a polar plot. Hattingh et. al. observed a bi-lobe plot for multiple combinations of spindle speed and welding speed and speculated that the shape of the plot might be related to plastic flow [58]. Balasubramanian theorized that material being extruded around the retreating side forced the tool to the advancing side, creating a force footprint predominately on the advancing side. It was additionally shown how the force footprint rotates back to the trailing edge of the tool when there are voids in the nugget [59]. Balasubramanian also examines force foot prints for Friction Stir Channeling and demonstrated how z-force cyclically increases as the extruded material is forged together each rotation [60].

From the above work, it can be concluded that the Friction Stir Extrusion Process is periodic in nature and repeats each rotation of the tool. Each rotation of the tool, material on the leading edge of the tool is plasticized and extruded around the retreating side of the pin. The plastizied material is deposited behind the tool and forged by the shoulder. This process was modeled by Pei and used to predict the causes of defect formation [61].

2.1.3 Microstructural Effects of Friction Stir Welding

Friction stir welding is a solid-state welding process and operates at a temperature below the melting point of the material to form joints. However, elevated temperatures and plastic deformation still cause microstructural changes in the aluminum.

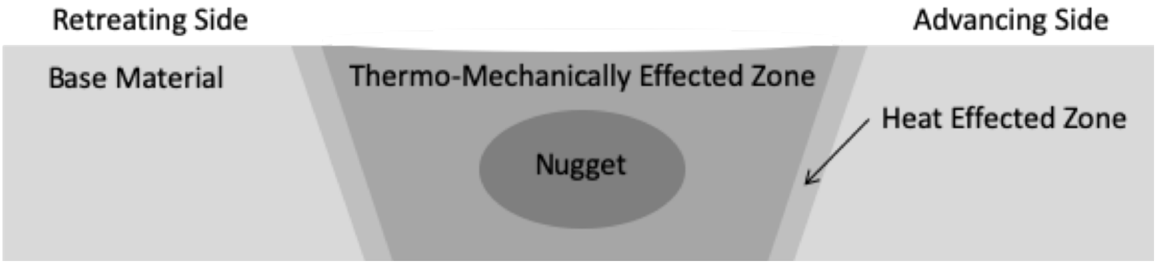

Figure 2.2: Conceptual model of the Macrostructure of a Friction Stir Weld.

FSW achieves temperatures approaching the solidus temperatures around the tool [50] and decreases with distances from the weld center-line. The grain size and shape can be changed due to the elevated temperature and mechanical strain, and the precipitate structure can be changed due to over-aging or dissolving of alloying elements. Both of these effects can change the strength of the aluminum through grain growth described by the Hall-Petch relationship and Zener Pinning. Additionally, the weld tool plastically deforms the crystalline structure, causing dynamic recrystallization in some aluminum alloys. The conditions change based upon location and distance from the tool. As a result, A Friction stir weld has a layered internal structure with three distinct regions, Heat Affected Zone (HAZ), Themo-Mechanically Affected Zone (TMAZ), and the Nugget, determined by the conditions the material experiences during the weld, Figure 2.2. The microstructural features can be segregated according to the region.

The Heat Affected Zone is the outermost layer and is present in most welding technologies. This region experiences a significant rise in temperature from heat conducted away from the weld, resulting in granular growth and overaging in heat treatable aluminum alloys. In Friction Stir Welding, the welding process significantly heats the zone, but it is not mechanically mixed by the tool. The HAZ is characterized by larger-than-parent granular size and lower-than-parent hardness. The HAZ tends to be the weakest part of the weld, and most failures occur in the HAZ. The HAZ is prominent in heat-treatable aluminum alloys and contains the Low Hardness Zone

(LHC). A region were overaging produces the lowest hardness measurements [62].

Mahoney et. al. identified a low strength region of the HAZ that failed at 45 degrees shear fractures from FSW AA7075 Tensile Specimans [43]. A post-weld heat treatment did not improve the strength of the welded samples due to coarsened strengthening percipitates in the heat treated sample.

Liu and Ma demonstrated that the Low Hardness Zone (LHZ) in the HAZ determines the weld's fracture location and ultimate tensile strength. They divided the HAZ of FSW AL6061-T6 into three regions: HAZ I, HAZ II, and HAZ III. HAZ I was closest to the base material, and HAZ III was closest to the stirred zone. HAZ I experienced the lowest thermal cycle. As a result, there was little change in the precipitates present in HAZ I. HAZ II reached peak temperatures of around 360 to 370 C. This thermal cycle resulted in significant overaging, producing the LHZ. HAZ III had the highest thermal cycle, mostly dissolving precipitates [63].

Lakshminarayanan mapped the LHZ for many combinations of welding speed and rotation rate for FSW AL2219. While the weld samples all failed in the LHZ on the advancing side, decreasing the rotation rate and increasing the weld speed changed the position, hardness, and angle of the zone.

The Thermo-Mechanically Affected Zone (TMAZ) is the region that has been mechanically affected and significantly heated. It extends from the HAZ on either side of the weld. The TMAZ is characterized by high aspect ratio grains.

Su et al. analyzed the microstructure of FSWed AA7050-T651 and divided the welding into four zones: HAZ, TMAZ I, TMAZ II, and the Nugget. The TMAZ I had a highly deformed structure, coarsened subgrains, and high dislocation density. A duplex hardening precipitate population observed implied that partial dissolution had occurred, leading to both coarse and fine precipitates. The TMAZ II contains recovered grains with a high density of sub-grains. The region had low dislocation density and fine precipitates distributed inhomogeneously. Precipitates were completely dissolved during the welding process [64].

In aluminum and other materials where it is hard to induce recrystallization, the recrystallization is concentrated in an additional region, the nugget [35]. This region experiences the highest temperatures and plastic deformation. The nugget typically follows the probe's path through the material, and the material extrudes around the probe. The nugget displayed a fine equiaxed grain structure separated by high-angle grain boundaries. Arora et al. constructed a Taguchi Matrix to analyze the effects of processing parameters and tool sizing on Friction Stir Welded Al2219-T87. Microstructural analysis revealed a fine recrystallized granular structure in the nugget, ten times smaller than the base material[65].

The fine granular structure found in the microstructure of the nugget points to some form of dynamic recrystallization. There are three possible processes for dynamic recrystallization in FSW. Continuous Dynamic Recrystallization forms new grains by rotating low-angle subgrains under strain. Eventually, the misorientation is sufficient to produce high angle grain boundaries with little movement of existing boundaries [66, 67]. Geometric dynamic recrystallization (GDRX) is where a new grain structure is formed due to a change in grain geometry during deformation [67]. Discontinuous Dynamic Recrystallization (DDRX) involved the nucleation of new grains smaller gains at existing grain boundaries.

The mechanisms for recrystallization during FSW very based on material, processing parameters, and region of the weld. Jata and Semiatin studied the weld nugget on FSW Al-Li-Cu alloy and determined that granular size followed the Zener-Hollomon parameter, similar to a hot working process. They concluded from Optical and TEM analysis that grains in the nugget were formed by CDRX [68]. Su et al. proposed that subgrains formed and rotated to form high-angle recrystallized grains by absorption dislocations introduced by plastic deformation [64]. CRDX is a variety of dynamic recrystallization. Etter et al. categorized the dynamic recrystallization process for Friction Stir Welded AA5251 O and H14 [69]. They observed CDRX in H14 sample and Geometric Dynamic Recrystallization in to O sample. The difference between the two was a result of the stored energy from cold rolling. Yu et al. developed a Monte Carlo simulation of recrystallization during Friction Stir Welding [70]. They concluded that different forms of Dynamic Recrystallization occurred at different quadrants around the tool. The leading edge was dominated by geometric and continuous dynamic recrystallization. The retreating side was characterized by continuous and discontinuous dynamic recrystallization. Geometric dynamic recrystallization occurredsa around the trailing edge of the tool.

Arora et al. found the precipitates had largely dissolved in the nugget with few coarsened precipitates. The dissolution of hardening precipitates was suggested to be the major factor in the decrease in the hardness of the nugget. [65]. Su also found the precipitates within the nugget had fully dissolved during welding. Overall nucleation of new precipitates was heavily dependent on dislocation density. In the nugget, precipitates nucleated heterogeneously. [64]

The thermal and mechanical history of the welded material primarily drives the precipitation behavior of heat-treatable aluminum alloys. At elevated temperatures, the hardening semi-coherent phases present in heat treatable aluminum alloys grow, some becoming incoherent phases, averaging the material. When the material reaches the dissolution temperature of the precipitate, the strengthening precipitate dissolves into the base aluminum. The precipitate behavior can broadly be split according to the traditional weld regions.

Digital image correlation (DIC) provides a possible avenue for determining macrostructural properties of a Friction Stir Weld. DIC utilizes a fiducial pattern added to the surface of a tensile specimen to calculate the strain field during a tensile test [71]. DIC has been utilized to determine the strain field during a tensile test of welded AA2024. The yield strength was then calculated for five distinct regions from the strain field and used to develop an FEA model of a loaded weld. Good agreement was demonstrated between measured and modeled strain. Sources of error could be from the Iso-strain assumptions [72].

2.1.4 Defects

Similar to all other forms of welding, defects can be formed during the FSW process. Defects form due to the use of sub-optimal processing parameters leading to issues of material flow and forging pressure for the specific materials being welded or the welding set up. There has been a significant amount of work to relating weld speed and rotation rate to the formation of welding defects through analytical models [61, 73], and through the development of processing window by physical observation [74, 75]. Some work has been done to examine at the effects of axial force [74, 76], and tooling setups.

Weld flash is a thin sheet of material ejected from the joint from the tool shoulder on one or both sides of the weld. It is usually attached to the base material at the edges of the weld. This type of defect can be formed by excessive heat input due to high rotation speed and low welding speed [74]. Flash formation can also lead to other defect formation. Material loss due to flash formation lead to insufficient material to completely bond on the advancing side leads to cavity formation on the advancing side[76, 77].

Wormholes, Root defects, cavities, and Lack of fill can all be considered volumetric defects. Wormholes, root defects, and cavities are tubular structures that form at the interface between the weld nugget and shoulder driven flow. Typically volumetric defects occur on the advancing side of the weld.

Kim identified two different causes for volumetric defects: Abnormal stiring and insufficient heat generation [74]. Both causes can be difficult to differentiate as they appear similar in shape and location. However, Abnormal stirring typically happens at higher rotation speeds. The weld nugget is malformed indicating discontinuous flow. Additionally, weld defects caused by insufficient heat input can be reduced by increasing axial force, but defects caused by abnormal stirring are not significantly effected.

Pei further reclassified insufficient heat input as insufficient plastic flow [61]. However, the cause is the same. Low rotation rates result in an temperature to low to sustain the plastic flow. The result can be lack of fill defects and other cold weld defects. Kumar found that increasing Axial force above 7.4kN for FSWed AL 7020 reduced defect formation but increased asymmetry between advancing and retreating sides [76]. It is likely that increasing axial force improve these defects because it increases frictional heating by the shoulder.

Abnormal Stiring is caused by insufficient shear band width formation in front of the pin [61]. The defects can be alleviated partially by increasing weld speed but primarily by reducing rotation rate.

A Kissing bond is an incomplete fusion of the welded material. Often located at the bottom of welds, kissing bonds occur when the mixing effect of the tool does not reach the bottom of the material.

A number of defects can be determined by post-weld testing. Destructive means such as taking longitudinal slices of the weld to obtain a cross-section is an effective way to reveal the micro and macrostructure of the weld. The cross section can be mechanically polished and etched with an etchent such as Keller's Reagent or AWS D1.2. The cross-section can be imaged the multiple means to reveal the inner structure of the weld. Defects are revealed in the cross section.

However, detecting defects during and after welding without destroying the weld, Non-Destructive Testing (NDT), is of great interest. Knowledge of the quality of mission-critical joints is critical in many industries, such as aerospace or space flight. Some of the defects can be easily identified by visual inspection of the surface of the weld. The internal structure of the weld can be imaged by sophisticated techniques such as x-ray, ultrasound, or neutron imaging.

In-process detection can be achieved by various data streams collected during the weld: acoustic emissions [78, 79], processing forces [80, 81, 82], or Vibration to name a few. Gibson et al. utilized neural networks to achieve a 95.2% classification rate of defined defects [82].

Control schemes have be developed to detect tool wear [83]

2.2 Controls

Often, Friction Stir Welding is performed by setting tool RPM, transverse rate, and plunge depth, the processing parameters, to constant values. The weld program will hold these values constant through the weld. This basic control system is often called open-loop control or positional control. This type of control system does not react to any disturbance or improve the weld quality.

The effects of modifying the processing parameters is an easy to understand, and has a directly visible effect on the welding machine. It is also simple to set and command the welder to perform to the processing parameters, However, they do not capture what is physically occurring in the weld. FSW is a complex thermo-mechanical process, and the processing parameters are linked to the physics of the weld process through complex non-linear relationships.

Heat generation/distribution, temperature, forging pressure, and tool contact among others are really the values that are modified when the processing parameters are changed. These values can not be set at the start of the weld, but they can be measured or inferred through the processing forces (or direct measurement in the case of temperature). A closed-loop control systems can bridge the gap between the processing parameters and the physical weld by sensing some aspect of the processing forces or temperature and modifying the processing parameters accordingly.

The processing forces, torque, z-force, x-force, and y-force, are the forces the tool experiences during the weld. These forces can be measured through piezoelectric systems or strain gauges. Torque can also be measured through current measurements. The processing forces can be measured by commercial solutions like low stir or Kistler dynamometers. Low-cost alternative solutions have been demonstrated [84]. Gibson utilized link deflection during the weld to measure the z-force on a large weld head [85]. The processing forces along with weld temperature most often provide the feedback mechanism to FSW control systems.

Some of the earliest examples of controllers for FSW were to compensation for complaint welding fixtures and robotic welder deflection. This can be done by detecting tool contact and adjusting the plunge depth to maintain sufficient contact. When joining large large AL2195 cylinders at the Vertical Welding Tool (VWT), NASA and Lockheed Martin had to implement a z-force based controller to compensate for the cylinders deflection [26, 86]. Boeing developed a Force Actuator to attach to a standard milling machine used for FSW [87]. The addition of the force actuator significantly increased weld quality.

Robotic arms are an often used manufacturing tool due to their flexibility. However, they can exhibit joint compliance and link deflection when used in high force applications. These issues can lead to a lack of forging pressure when the robot is used for FSW [17]. Force control was presented as a method for compensating for the compliance. These controllers change the plunge depth to control the z-force. Smith implemented a axial force controller by measuring robotic joint torque to compensate for a robots lack of stiffness [88]. Without the controller, the robot could not maintain adequate tool contact and forging pressure. The Robotic Friction Welding Application and Technology Centre (RIFTEC) pursued the implementation of a force controller using a load cell on the end effecter of a tricept robot [89]. The feedback from the controller was used to modify a pre-planned route to maintain constant axial force. Later work has gone towards the use vision based systems to compensate for other directions of robotic compliance.

Later controllers focused on improving weld quality through temperature regulation and power control. These controllers were developed to respond to disturbances, and detect characteristics of the weld in process.

As described above, elevated temperature can lead to grain growth and overaging. So, heat input during the weld has been tied to weld quality and strength. There has been an interest in developing a control system to control the heat/power input to improve weld quality and reject disturbances.

The temperature of the weld zone can be problematic during friction stir welding. The temperature under the tool is difficult to measure, and the tool completely obscures the temperature of the aluminum underneath from optical measurements. The temperature under the tool and in the material can be measured through thermocouples embedded in the tool or the material.

Temperature could be controlled directly by measuring weld temperature in process. Fehrenbacher et al. embedded thermocouples in the weld tool and data acquisition capabilities for an angular resolution of 10°. It was determined that there was some critical temperature for the shoulder and pin interface below which weld quality significantly degraded, and above the solidus temperature, weld quality also decreased. An effective temperature control system was implemented [90].

Temperature could also be controlled by controlling the input power into the weld.

Weld Torque is closely related to power input. Torque, τ, can be related to power, P, through the relationship $P = \tau\omega$, where ω is the tool rotation rate. The torque value can be modulated by plunge depth, weld speed, or tool RPM. The power output of the spindle motor can also be used to estimate weld power through the relationship $P = IV$, where I is the current and V is the voltage. However, the power measurement contains parasitic losses through the spindle and has to be corrected.

Axial Force is not as closely linked to Weld power through temperature. Longhurst stated that changes in axial force during the weld are due to thermal softening of the material [91]. Frictional heating is also a function of Contact pressure. So, modulating the axial force does effect the amount of heat through friction generated. But, axial force is better at measuring forging pressure.

Controllers were developed to maintain a constant input power and, as a result, maintain a constant weld temperature. Longhurst controlled axial force by modulating plunge depth, weld speed, and rotation rate [92, 91]. Weld speed modulation resulted in the most constant z-force and energy deposition. However, only plunge depth modulation was able to compensate for height variations and link deflection. He argued that by maintaining a constant axial force, contact pressure and heat generation also remained constant. So, changing the weld speed, also changed the energy deposition into the weld. Longhurst also demonstrated controlling the torque input energy by varying the transverse speed, and plunge depth. torque was used as the feedback mechanism. Ultimately, Longhurst suggested that torque is a good alternative to z-force for controlling plunge depth due to better coupling between tool surface area engaged and the change in torque [93]. Buffa et al. varied rotation rates to maintain constant heat input of variable thickness butt welds. The samples had a 0.1 mm variation in thickness, either a hump or dip, perpendicular to the weld direction. It was found that a 300 rpm decrease for the hump condition and 500 rpm increase for the dip condition significantly increased the joint efficiency over the uncontrolled welds [94].

While input power could be controlled, neither axial force or torque is sufficient to determine the weld temperature. The proportion of frictional vs mechanical dissipation of energy into the workpiece, and the volumetric distribution of the heat would have to be known. Additionally, disturbances like material thickness variation, regions of preheated material, or edges of the material could drive instability in the weld temperature

While open loop FSW might be a thermally self balancing process, the effect that Mayfield and Sorensen demonstrated that torque leads temperature during friction stir welding, and controlling input power outside of its open loop value could cause power based controllers to become unstable due to thermal softening of the material. They proposed a two stage control scheme. An inner loop that kept torque constant by controlling spindle speed, and an outer loop that maintains a constant weld temperature by setting torque [95]. Ross found that to decrease weld temperature torque must initially increase, but be offset by a decrease in spindle speed [96]. The opposite is true for an desired increase in weld temperature. Cederqvist implemented a cascaded power controller and successfully welded Copper Fuel canisters[97]. Bachmann attempted to mitigate the instability from controlling torque by developing an semi-analytical model for use in the L1 Adaptive control scheme [98].

Some controllers have been developed to control for both energy input as well as axial force. Fehrenbacher et al, developed a Multi-Input Multi-Output control system to control both axial force and temperature for a complaint FSW robot [45]. The control system was effective at disturbance rejection due to a number of different process variations including changes in material thickness and heat loss to the backing plate.

Controllers can also be developed to detect physical misalignment between the expected and actual weld seam locations. In traditional welding, visual or optical techniques are commonly used to track weld seams. This technique can also be used in Friction Stir Welding. DeBacker demonstrated the use of vision and laser based control systems for compensating for lateral robotic link deflection during FSW [99]. However, FSW has multiples joint topographies where the seam can be effectively obscured by the top sheet. The weld tool penetrates fully through the first sheet to complete the weld. In these cases, through-the-tool sensing techniques can be used. This is done by determining if an measured attribute that is effected by joint misalignment is outside of an expected range or by driving the attribute to a local max or min.

One way of detecting the minimums and maximums is through weave tracking. In this technique the weld tool follows a path with a symmetric repeating pattern. Three examples of the pattern are square wave, sinusoid wave, or trapizoidal wave. The measured processing forces are used to determine on which side of the line of symmetry the maximum or minimum resides. The line of symmetry can then be moved to center over the found location.

Fleming et al. was able to detect and predict tool misalignment from the center of a t-joint welds by measuring axial force. The welding fixture was structured such that a void was underneath the skin to either side of the stringer. So, any misalignment would cause a higher fraction of the tool to be in 'open air' [100]. Fleming was then able to develop the first weaving algorithm using the prior collected data, and use it to track the seam on a t-joint. The weaving controller was then demonstrated centering welding tools down the center of the overlapped portion of lap welds [101]. Gibson et al. used axial force and the weave tracking technique to track the weld path between two beads of sealant on a lapped weld [102]. The weave tracking system was first demonstrated for FSE by Jay Reynolds [103]. A Misalignment was able to be corrected between the initial weld path and groove path using a sinusoidal weld path.

2.3 Dissimilar Material Joining

The joining of dissimilar materials is of great interest in the industry to enable the creation of multi-material engineered structures that drive greater efficiency and performance. Welding competes against other non-welding joining methods in joining dissimilar materials. Each method will have advantages and disadvantages. No single joining method is best for all applications. joining methods are selected based upon application details.

Mechanical fasteners such as bolts are rivets can be used to join dissimilar materials. Mechanical fasteners require overlap between the materials to be joined. They also require additional physical components that add cost and weight to the joint. The joint efficiencies are under 100% [1]. Mechanical fasteners can create a disassembleable joint.

Adhesives can also be used to join dissimilar materials. Generally, adhesives have lower yield strengths than the base material in shear and even worse in the peel. A sound joint depends on adequate surface preparation and considerable overlaps between sheets for application area [1]. Adhesives can be used to join a wide variety of materials both metallic and non-metallic.

Welding can be used to join some dissimilar material combinations. There are a few considerations that must be made when welding dissimilar materials. Differences in the thermal expansion can lead to stress cracking during cooling. The lower melting temperature material melts first in fusion welding and can result in the evaporation of some alloy in elements, causing inferior welds. In solid-state processes, differences in the decrease of yield strength with increased temperature cause problems [104]. Chemical incompatibility can lead to the diffusion of alloying elements across the joint. The elevated temperatures present in welding can lead to the formation of intermetallic compounds that, when sufficiently thick, can compromise the joint.

Newer welding technologies with highly focused heat input are of great interest. Laser welding [105], Electron beam welding [106], and plasma arc welding [107] all have higher heat flux than conventional welding techniques that result in more localized heating and smaller heat affected zones. The high heat flux of processes like electron beam welding can alleviate some complications with dissimilar material joining such as dissimilar melting temperatures and residual stress. But, issues with metallugical compatibility still exist [108]. Interface layers can be used to prevent metallurgical incompatibility and intermetallic growth. Wu examined the use of a CU interlayer when using plasma arc welding to join steel to aluminum [109].

Solid-state welding processes processes operate at a lower temperature than fusion welding processes. So, they avoid some of the issues of welding dissimilar materials such as dissimilar thermal expansion coefficients and melting points.

Friction stir welding has been utilized to weld dissimilar materials in multiple topologies and both directly and using derivative technologies.

FSW can be used to directly join two dissimilar alloys or materials. Since the process operates below the melting temperature, differences in melting temperature can be minimized. However, differences in yield strength and thermal softening can be problematic. However, the elevated temperature does lead to some intermetallic compound formation at the weld joint. These compounds are brittle, and thick layers are detrimental to the weld strength. For each joint configuration, parameters should be optimized to produce defect-free welds with thin IMC layers [1].

When FSW dissimilar materials, several different arrangements can be examined. The two materials can either be abutted for a butt weld or lapped for a lap weld. When performing a butt weld, the harder the two dissimilar materials can be placed on either the advancing or retreating side, and the tool can be offset to either side of the seam. When performing a lap weld, the harder material can be placed on the top or bottom of the stack, and the tool can fully penetrate the two materials or remain in the top material.

When performing a butt weld between dissimilar materials, the harder of the two materials is often placed on the advancing side, and the tool primarily transverses through the softer material. Little interaction between the tool and harder material prevents excessive tool wear, and heating [1].

Liu et al. successfully jointed TRIP 780 to AL6061-T6 via FSW of butted sheets. The tools were offset to the aluminum side with steel on the advancing side of the weld. Four distinct failure modes were observed dependent upon processing parameters: Fracture of the base aluminum, along with a continuous steel protrusion, along steel fragments embedded in the aluminum, and at the aluminum/steel interface [110].

Lap welding of AZ31B and Steel with pin penetrating through the steel resulted in a hooking structure that formed a mechanical joint. The hooking structures could be enhanced through modifications to the process parameters [111].

FSW has a large community of derivative technologies and associated processes. Each of the processes has been developed to enhance a characteristic or mitigate a shortfall of direct friction stir welding.

Friction Stir Riveting encompasses a wide range of derivative processes that join two materials by first rapidly spinning a consumable fastener, and plunging a consumable fastener into two lapped sheets. Friction Stir Riveting combines the advantages of Friction Stir Welding and riveting, eliminating the need for predrilling and rivet insertion [112]. Two examples of processes that could be considered Friction Stir Riveting are Friction Stir Self Piercing Riveting and Friction Stir Blind Riveting.

Friction Stir Self Piercing Riveting utilizes a fasten shaped like a hollow cylinder. The top of the fastener caps off the cylinder and includes some driving mechanism that can be disengaged by either shearing off the top of the rivet or a one-way meshing mechanism. During the process, an anvil is placed behind two lapped sheets. The anvil is shaped such that when the rivet is plunged into the lapped sheets, the leading edge of the cylinder is flared out, interlocking the two sheets [113].

Most FSW processes require access to both sides on a joint. Friction Stir Blind Riveting (FSBR) attempts to reduce the requirement by utilizing an ordinary blind pop rivet. Like the Friction stir riveting process, the rivet is spun rapidly and plunged into lapped materials. After the rivet is plunged through the two sheets of material, the center pin is pulled, flaring the tubular portion of the rivet, locking the two materials together. FSBR has been shown as a method for joining AL6061 to Aural-2 cast aluminum [114].

Friction Melt bonding does the reverse of some of the prior joining techniques. Typically dissimilar lap welds are performed with the softer of the two materials on top and the harder material on the bottom. The shoulder interacts with the softer material, and the harder material primarily interacts with the pin. Friction Melt Bonding places the harder material on top and utilizes a pinless tool to create a localized heated zone. The heated zone melts the aluminum underneath it forming thin intermetallic layers to join the material [115].

Friction Stir Spot Welding is of great interest for industrial applications. The process is fast and can be performed with a C-clamp-style actuator at the end of a robotic manipulator. The process is similar to FSW. However, the tool is retracted from the material after the dwell phase is complete. It has been demonstrated for joining Aluminum alloy to steel [116, 117]

Two-Sided Friction Stir riveting by extrusion is a novel process that utilizes a double-sided counter-rotating to plasticize aluminum plate sandwiching steel sheet. The plasticized material flows into holes punched in the steel sheet, locking together the sandwich of materials [118].

Utilizing the plastic flow present in Friction Stir Welding to form raised features or interlocking joints has been a direction for research since the early days of friction stir welding. In 1998, TWI demonstrated using the plastic flow present in FSW to transfer embossed lettering from the anvil to the welded material [119]. Then, in 2003, Nishihara pioneered the development of Friction Stir Forming by demonstrating the transfer of surface roughness of an open die to the welded material and cladding steel with aluminum by extruding into circular-cut geometries, [120]. TWI developed the Stir-lock™process, forming a dissimilar material transitioning joint by welding over perforated materials [121].

Work has continued on processes that join by extrusion, such as friction stir forming. All of the processes take advantage of the ’extrusion zone,’ formed around the tool into an interlocking geometry that can be formed through various means. There are advantages to this process. Typically, the joint can be formed without the tool contacting both materials. There are a few processes that do not prevent contact: Friction Stir Scribing [122, 123, 124, 125, 126] and Friction Stir Dovetailing [127, 128, 129, 130]. This is done to enhance the process over non-contact processes in some way. However, Not requiring that the FSW tool contacts both materials convey several advantages. The tool can exclusively contact the ’softer’ of the two materials. This can be the less abrasive material, requires less energy input to weld, or has greater formability. Tool wear can be significantly reduced. Smaller energy input into the joint and lower temperatures can reduce IMC formation, voids, and porosity formed from different thermal expansion coefficients.

Two preformed geometries have been studied thus far, lines of holes through the material and milled grooves. Typically, the through-holes are used on thinner sheet material, and grooves are used for thicker plates. Ohashi et al. demonstrated the creation of pseudo linear dissimilar material joint via Friction Stir Forming by extruding into a grid of pre-punched holes. They also observed an offset to the advancing side between the weld centerline and the center of the extrusions. They cited the asymmetry between advancing and retreating sides as the cause of the offset [131]. Evans demonstrated joining of 1/4” steel and aluminum sheets through a dovetail and slit saw groove milled into the aluminum sheet in a process dubbed friction stir extrusion [34].

Friction Stir Dovetailing developed at PNNL joins two dissimilar materials, such as Aluminum with RHA(Rolled Homogeneous Armor), by plastically deforming and forging one material into milled dovetails in the second, using a modified FSW tool to promote metallurgical bonding at the bottom of the dovetail. The modified friction stir welding tool has a carbide insert affixed to the bottom of the pin. During the weld, The pin extends through the first material and to the bottom of the dovetail . The addition contact between the carbide insert and the bottom of the dovetail generates localized heating and exposes fresh steel that drives the formation of metallurgical bonding [129].

Friction Stir Dovetailing seeks to enhance the strength of an extruded dovetail by creating a beneficial metallic bond in addition to a mechanical interlock [130]. Temperature control has been demonstrated to control and reduce the thickness of IMC layers and promote joint strength [129]. IMC layer served to more evenly spread the load across the dovetail, moving the failure location from a stress concentration at the edge of the dovetail to the HAZ/TMAZ zone of the AL Weld [128].

A multi-step process was developed to joint AA7099 to RHA by creating an AA6061 interface layer [127].

friction stir scribing utilizes a special tool with an offset cutter on the bottom of the pin to join to lapped dissimilar materials. The cutter forms a beneficial geometry in the bottom of the lapped materials, and the top material is extruded into the geometry forming a joint [122]. Friction stir scribing was found to form a mechanical and a chemical joint when joining AL6061 to RHA. The mechanical joint is formed from a hooking structure formed in the bottom of the lapped sheets. The chemical is a diffusion layer at the material interface resulting in IMC formation [132]. Friction Stir Scribing was also shown as an effective way to joint aluminum to polymers, creating a mechanical hooking structure [123].

CHAPTER 3

Friction Stir Extrusion of Thin Sheet Stock

3.1 Abstract

A novel approach for applying Friction Stir Extrusion to thin sheet is tested to join AA6061 and steel. A dovetail geometry is formed in the steel through press dies, and aluminum is extruded to form an interlocking joint. Two transverse rates are tested, 50.8 mm/min and 76.2 mm/min, as well as two steel alloys, A36 and 4130. Sectioned into 6.35 mm samples, the welds failed through deformation between 280 N to 748 N. However, the 50.8 mm/min, A36 samples expressed an additional metal-to-metal bonding mechanism, increasing the strength to 1485 N. This research suggests unique geometries could improve the process.

3.2 Introduction

The joining of two lapped thin sheets is a common task in the manufacture of car bodies and aerospace fuselages. Mechanical fasteners or conventional welding techniques are typically used. When the two sheets are dissimilar materials, conventional welding techniques often do not form an effective joint [133]. Mechanical fasteners are expensive, time consuming, and leave openings for crevice corrosion to take place. Forming a continuous mechanical joint through friction stir welding processes could form an effective alternative to current technologies.

Friction Stir welding (FSW) is a solid-state welding technology developed at The Welding Institute (TWI) in Cambridge [3]. It offers multiple advantages over conventional techniques, making it attractive to manufactures [134, 18]. FSW can be used to join lapped dissimilar materials by plunging the pin through the first material into the second [135]. However, the interaction between the pin and the second material can lead to defect and void formation [124]. When welding aluminum to steel, preventing tool and steel contact reduces tool wear, enabling the use of ordinary steel tools, but bonds the materials through intermetallics [116].

Friction Stir Extrusion (FSE) is a new technique to join dissimilar materials. Instead of mixing the two lapped materials, FSE operates by extruding one material into a preformed geometry present in the second harder or more abrasive material, forming and interlocking feature. The tool does not come into contact with the second material during the process. So, cheap steel tools can be used, and intermetallics at the material interface is minimized and not detrimental to the joint. [136, 34].

Prior work on joining through extrusion has focused on using subtractive methods to create the required geometry. Extrusion through punched or drilled holes in steel sheets has been used to join thin sheets [118, 137]. However, a continuous joint was not formed. Also, penetrations of the material, like those used in riveting, create a leakage path that can cause corrosion around the joint, requiring special consideration and sealants during construction [138]. FSE forms a strong continuous mechanical interlocking joint without surface penetration. Traditionally applied to thick sheet applications, prior work on FSE focused on milling an interlocking geometry in thick sheet [34]. Milling a groove of sufficient size is not possible in thin sheet. Instead, a novel solution of using press dies to form a dovetail geometry along the length of the steel was developed. This solution simplifies corrosion concerns through surface penetrations, and can be sealed through an in-process application of sealant [139].

3.3 Material and Methods

For this study, 0.762 mm A36 and 4130 steel were selected for the harder material, and 1.6 mm AA6061-T6 sheet was selected for the softer material. The steel alloys were selected because they are readily available and adequate analogs to the alloys used in the automotive and aerospace industries.

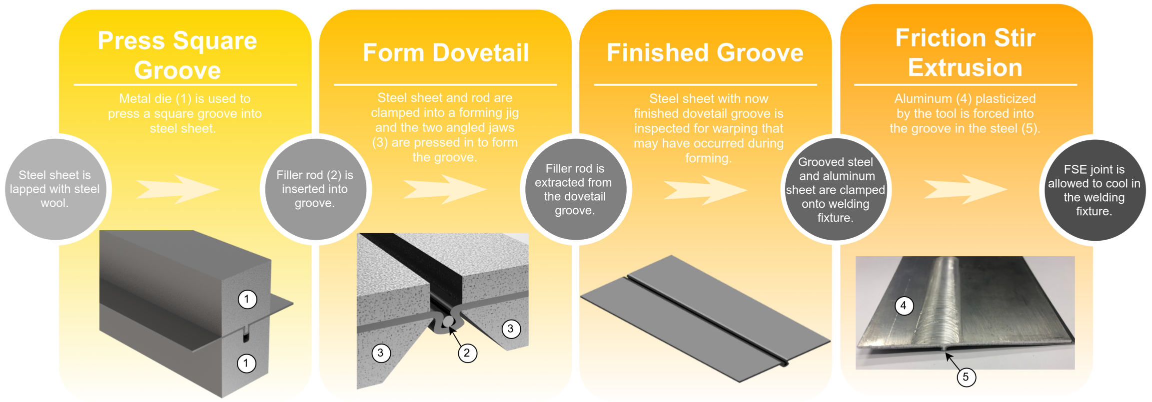
Steel sheet is lapped with steel wool.

Press Square Groove

Metal die (1) is used to press a square groove into steel sheet.

Filler rod (2) is inserted into groove.

Form Dovetail

Steel sheet and rod are clamped into a forming jig and the two angled jaws (3) are pressed in to form the groove.

Filler rod is extracted from the dovetail groove.

Finished Groove

Steel sheet with now finished dovetail groove is inspected for warping that may have occurred during forming.

Grooved steel and aluminum sheet are clamped onto welding fixture.

Friction Stir Extrusion

Aluminum (4) plasticized by the tool is forced into the groove in the steel (5).

FSE joint is allowed to cool in the welding fixture.

Figure 3.1: Process for forming dovetail groove in sheet steel and performing a thin sheet Friction Stir Extrusion.

The press dies formed the dovetail in two steps. First, a square-shaped groove was formed by pressing the steel sheet between two dies. One die block possessed a raised rectangular feature, and the second die block had a matching slot. Second, the top corners of the square groove was clenched with a jig, composed of two wedges, to create a dovetail shape. A 1.14 mm diameter rod was placed in the square groove before clenching to maintain a uniform cavity. The result was a dovetail with approximately a 0.635 mm opening and 1.14 mm diameter cavity at the base. The process is described in Figure 3.1.

Prior to welding, the aluminum sheet and the grooved steel sheet were abraded with Grade #00 steel wool to remove any oxides present on the joining surface, and acetone was used to remove any residue. Both sheets were mounted in a welding fixture in a lap configuration. Then, they were welded using a modified Milwaukee Model K milling machine.

Two transverse rates were compared, 50.8 mm/min and 76.2 mm/min, called transverse rate 1 and 2 respectively. The spindle speed was held consistent at 1500 rpm. The tool used for both sets was a 25.4 mm diameter convex scrolled shoulder, pinless tool that was plunged to a depth of 0.762 mm. The tool had a 1.5° lead angle and was offset to the advancing side of the groove as described in prior work [136].

3.4 Results

Samples from each combination of materials and parameters were sectioned into approximately 6.35 mm strips, and subjected to a shear tensile test. A summary of the results are shown in Figure 3.2. The mild steel samples welded at transverse rate 1 had an average UTS of 1554 N, and the samples welded at transverse rate 2 has an average UTS of 281 N, much lower than those welded at transverse rate 1.

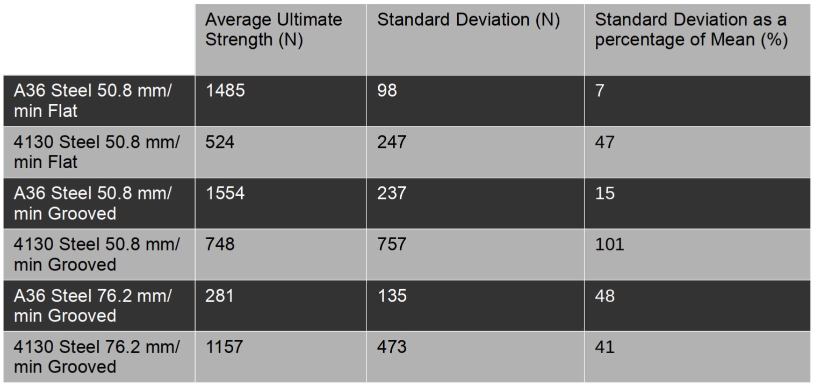

	Average Ultimate Strength (N)	Standard Deviation (N)	Standard Deviation as a percentage of Mean (%)
A36 Steel 50.8 mm/min Flat	1485	98	7
4130 Steel 50.8 mm/min Flat	524	247	47
A36 Steel 50.8 mm/min Grooved	1554	237	15
4130 Steel 50.8 mm/min Grooved	748	757	101
A36 Steel 76.2 mm/min Grooved	281	135	48
4130 Steel 76.2 mm/min Grooved	1157	473	41

Figure 3.2: Summary of mean ultimate strength and standard deviation is provided in a chart.

During the shear tensile tests, it became apparent that the two transverse rates tested expressed different failure modes. The samples welded at transverse rate 1 always failed through deformation of the steel sheet at the dovetail. When the dovetail was sufficiently deformed, the aluminum extrusion slipped out, resulting in a relatively weak joint. The samples welded at transverse rate 2 appeared to have some form of metal to metal bonding occurring around the top of the dovetail. The failure of the joint was observed as a two-step process in a majority of the samples. In the first step, the joint would rotate due to the offset grip of the machine on the two sheets, separating the two sheets. The aluminum and steel resisted separation around the opening of the dovetail. The joint bore the highest load before fracturing from one the side of the dovetail. In the second step, the joint continued to rotate, until the steel straightened out, and the other side of the dovetail bore the load. The joint failed when the last bond at the opening of the dovetail failed. In a few cases, the steel sheet failed before the joint. A visual representation of the two step failure process is described in Fig. 3.3 along with the load displacement diagram comparing the three variation observed.

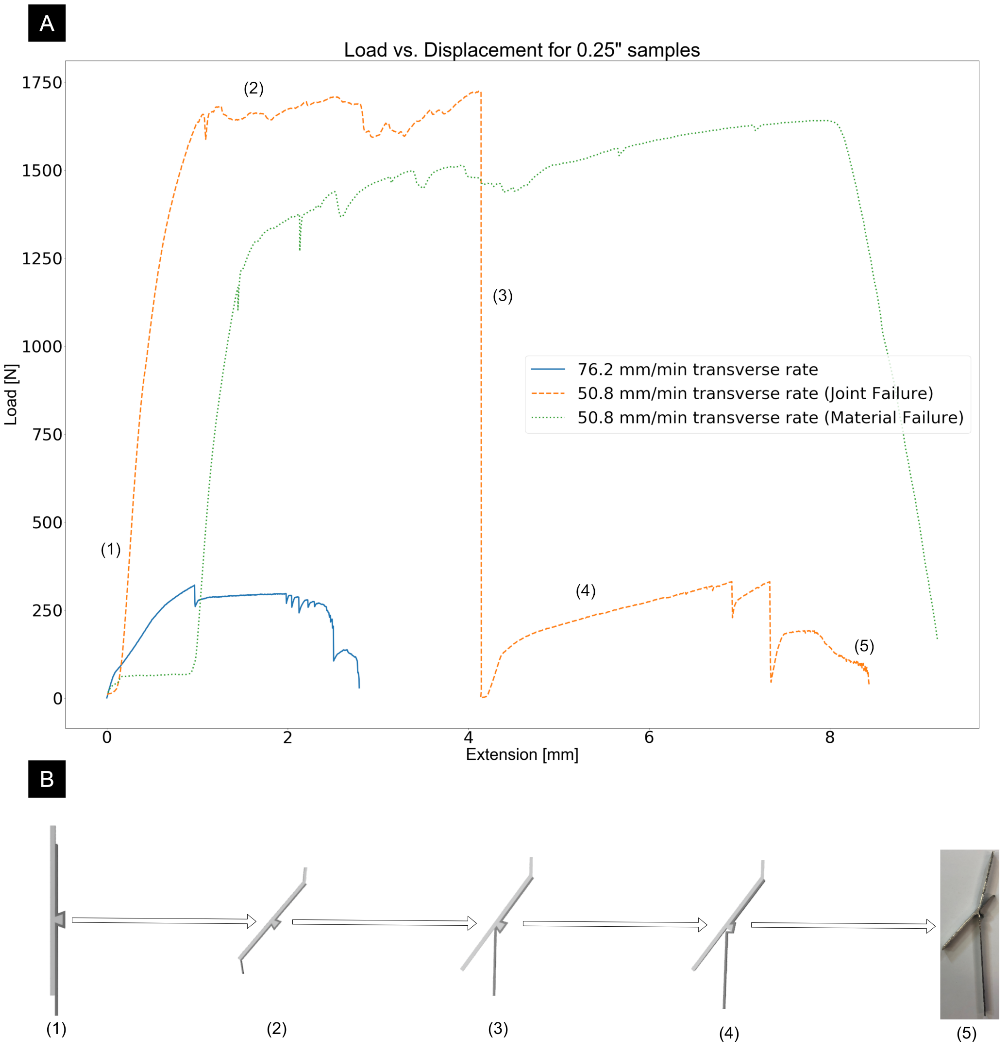

Figure 3.3: (A) Load vs displacement for both 50.8 mm/min and 76.2 mm/min samples. The differences between material failure of the steel and failure of the joint are displayed. (B) When the 50.8 mm/min samples failed at the joint, the sample expressed a multi-step failure. All of the steps are displayed as well as their relationship to the load vs displacement diagram.

The grooved 4130 steel displayed an opposite behavior. The samples welded at transverse rate 1 had an average ultimate strength of 748 N, and the average ultimate strength of the samples welded at transverse rate 2 was 1157 N. All samples failed through deformation of the steel sheet as described above and no bonding between the two metals were observed.

A second set of welds were performed at transverse rate 1 by lapping the aluminum over the steel without the dovetail groove to further quantify the bonding present. The resultant joints had widely different joint strengths. The A36 and 4130 steel samples lap joint exhibited a ultimate strength of 1485 N and 524 N respectively. These results imply that a majority of the joint strength gained from reducing transverse rate in the A36 samples came from the metal to metal bonding mechanism.

3.5 Discussion

The samples welded at transverse rate 1 had an extremely large standard deviation, Figure 3.2. The samples tested were cut from three different welds. It is theorized that difficulty forming the groove in the 4130 steel lead to large variations of joint efficacy. Samples from one weld in particular vary widely. When that sample is removed, the mean is reduced to 523 N with a standard deviation of 63 N.

Similar work with no contact between the steel sheet and tool noted intermetallic formation around the joint [116]. A36 samples from transverse rate 1 were embedded in epoxy, and a Zeiss Merlin SEM in analytical mode was used to image the samples and perform Energy-Dispersive X-ray Spectroscopy (EDS) to investigate the nature of the bond, and determine the presents of intermetallics. The analysis was focused around the edge of the dovetail, the areas that exhibited the bonding. The sample was imaged with an accelerating voltage of 20 KeV, Everhart-Thornley Detector, and 8.5mm working distance. EDS analysis did not provide strong evidence for intermetallic formation, Figure 3.4. The map scans showed clear segregation between aluminum and steel regions, and the overlap in line scan can be explained by the interaction volume of the electron beam.

It is theorized that the aluminum extruded into small surface features of the steel. The steel exhibited visible surface roughness that was completely filled by aluminum, some of which could form an interlocking geometry, effecting a bond through “micro-extrusion”. This effect could be similar to the ”hooking” seen in some other lap welding techniques [124, 133].

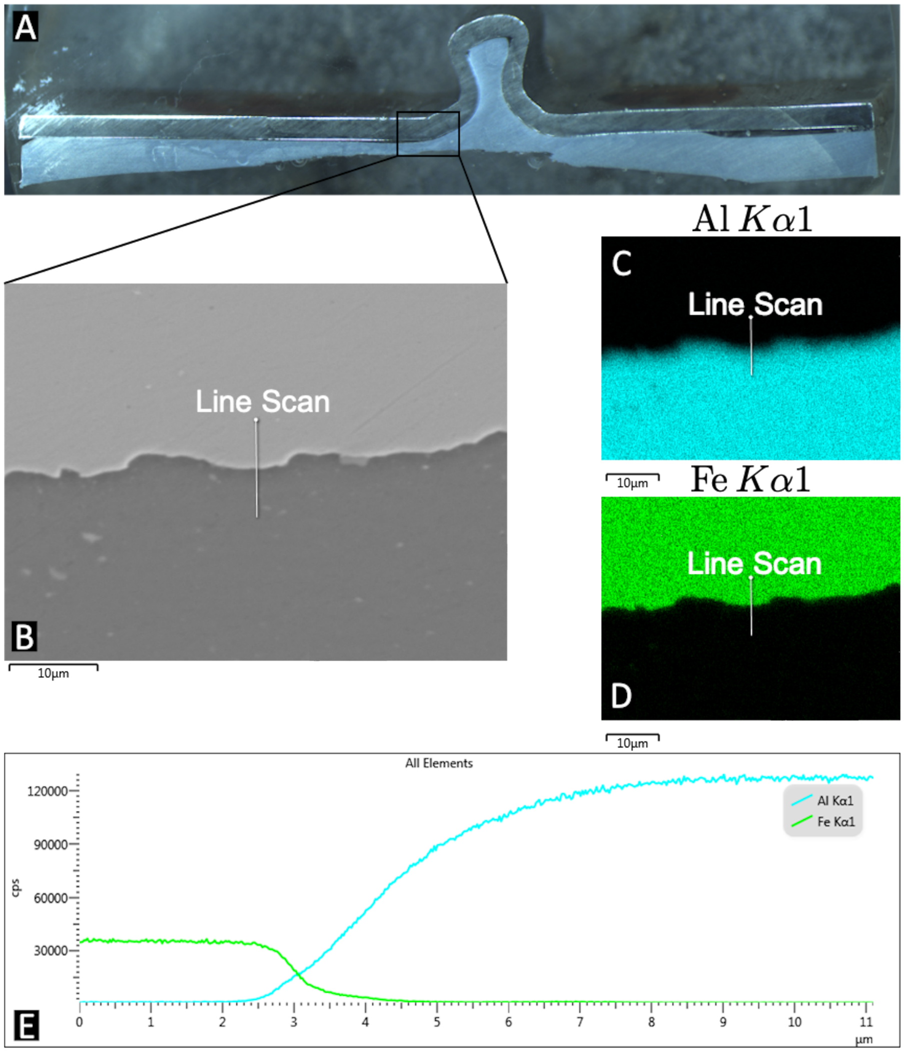

Figure 3.4: Microscopy and EDS Spectroscopy for the 50.8 mm/min sample. (A) Image of the welded sample mounted in an epoxy resin. (B) Micrograph at 2Kx Magnification just outside the edge of the dovetail. Aluminum (dark) fills all of the surface features in the steel (light). The location of the EDS line scan is noted. (C) The location of the aluminum in the micrograph. (D) The location of the iron in the micrograph. (E)EDS line scan data across the aluminum/steel interface.

3.6 Conclusion

The novel approach of forming preformed geometries for FSE was shown to be an promising method for joining thin sheet materials. An interlocking groove was formed without the use of subtractive techniques milling. Iterations on the forming steps and basic dovetail design could achieve better results for both materials. Additionally, the FSE joint can be formed without any surface penetration, reducing the need for extra sealing process.

Slower transverse rates resulted in stronger joints when using the A36 steel sheet. No such increase was seen when using the 4130 steel. The increase in strength is theorized to be due to ”micro-extrusion” into the surface roughness of the steel. However, the exact nature of bonding mechanism could be better quantified with further research.

3.7 Funding Sources

This work was funded by the Tennessee Space Grant Consortium.

CHAPTER 4

Development of an Aging Process for Friction Stir Extruded Joints

4.1 Abstract

Friction Stir Extrusion is a derivative process of Friction Stir Welding for joining dissimilar materials. The process forms a mechanical joint through extrusion to form interlocking features between two metals. When joining AA6061-T6 to mild steel through extrusion of a dovetail, much of the T6 heat treatment of the aluminum in and around the weld is lost during the process. This paper details the examination of a post processing aging process to return AA6061 to the T6 condition. Through a 10 hour precipitation hardening process at 170 C. The welds experienced a 23.9% increase in tensile strength from 2193 N as-welded to 2718 N after 10 hours. Hardness measurements showed a return close to T6 conditions in both the weld nugget and extruded material, 67.5 to 83.5 HRF and 54.7 to 81.8 HRF, respectively during the heat treatment period. The steel showed no substantial changes in hardness during the heat treatment. SEM analysis revealed significant changes in the sizes of two species of inclusions within the aluminum during both the welding and post processing.

4.2 Introduction

The joining of dissimilar materials has become of special interest in recent years due to pressure to reduce the weight and increase the efficiency of transportation vehicles. Friction stir welding (FSW), a solid state welding process developed in the 1990s at TWI [3]. has demonstrated the ability to join dissimilar materials [140]. The process utilizes a rotating tool to join multiple pieces of metal together. FSW is becoming a popular choice of the manufacturing industry due to its advantages over other welding processes [17, 18]. The welds formed between dissimilar metals depend upon mechanical locks, diffusion layers, and atomic bonding to joining the dissimilar metals. However, thick intermetallic compound (IMC) layers decrease joint strength [1]. A large number of derivative processes have been developed to decrease the effects of thick IMC layers by relying on mechanical locks. Friction Stir Riveting (FSR) attemps to combine the benifits of both Friction Stir Welding with mechanical fastening [112]. Friction Stir Self-Piercing Rivets Plunges a rotating rivet based upon a hollow cylinder into two overlapping plates. A die on the back side Flairs both the rivet and the metals, locking the plates together [141, 142]. Plunging a rotating blind rivet in dissimilar aluminum alloys allowed the joining of the alloys from a single side and eliminating the need to pre-drill holes [114]. Friction Stir Scribing utilizes a carbide cutter in the pin of the welding tool to enhance mechanically interlocking features [126]. The addition of resistance heating to Friction Stir Spot Welding of AL6061 to TRIP 780 Steel resulted in more uniform hooking structures but thinker intermetallic layers [143].

The Friction Stir Extrusion (FSE) process is a derivative technology of Friction Stir Welding (FSW) that utilizes the plastic flow present in the weld to form an in situ interlocking geometry, joining the two materials [34]. Of the two dissimilar materials used, a preformed geometry is generally created in the material that is considered more difficult for traditional FSW due to factors such as high hardness or abrasiveness. The softer of the two materials is lapped on the other, allowing extrusion into the milled geometry. When the tool transverses through the softer material and over the preformed geometry, material is displaced downwards, filling the geometry, Fig. 4.1. The joint formed is purely mechanical, depending on the interlocking geometry to join the dissimilar materials. Since the tool never comes in contact with the harder material, low cost steel tools can be used. In this work, mild steel was used for the harder material and AA6061-T6 for the softer material. The high temperatures present during FSW, and by extension FSE, will cause a loss of the

T6 temper conditions of most aluminum alloys. There is a lack of literature on the effects of post weld heat treatment for FSE joints. This paper aims to demonstrate the heat treatment process and examine the effects on the extruded joint.

Heat-treatable aluminum alloys are hardened through precipitation hardening, where secondary phases are precipitated through the granular structure. The heat treating process is typically a three step process in production: solutionizing treatment, quenching, and aging. Solutionizing treatment raises the temperature above the solvus temperature but below the melting temperature, approximately 450 to 550 Celsius. The alloying elements are fully soluble in the aluminum within this temperature range. The metal is then quenched, forming a super saturated solution. Generally, Guinier-Preston (GP) zones form after the quench at room temperature. The GP Zones are distorted regions within the lattice of the bulk material where the solute atoms are incorporated into the lattice. They are not discrete particles or have their own lattice. During artificial aging, the temperature of the aluminum is raised such that the solutes can diffuse through the crystal matrix to form precipitates, 150 - 210 C for up to 18 hours. First, coherent particles are formed. The precipitates grow into semi-coherent and then incoherent precipitates [144, 145].

AA6061 is a structural alloy with magnesium and silicon as the major alloying elements. The precipitation reaction in AA6061 can be summarized as $\alpha_{ss} \rightarrow (Mg) + (Si) + (Mg, Si) \rightarrow$ GP Zones $\rightarrow \beta$" $\rightarrow \beta' \rightarrow \beta$. From a super saturated solution, α_{ss}, clustering regions of Mg and Si form. β" is a coherent precipitate of Mg_2Si. β' is the semi-coherent precipitate that is responsible for the hardening of AA6061. Overaging is the formation of large amounts of the incoherent, β, phase precipitate [145].

Early work on tracing flow present in FSW found the process to have extrusion like characteristics. Colligan classified FSW as an extrusion process after he observed material flow during tracer experiments with AA6061 and AA7075 [51]. Reynolds used Al 5454 tracers to study flow in butt welds. He described an "extrusion chamber"

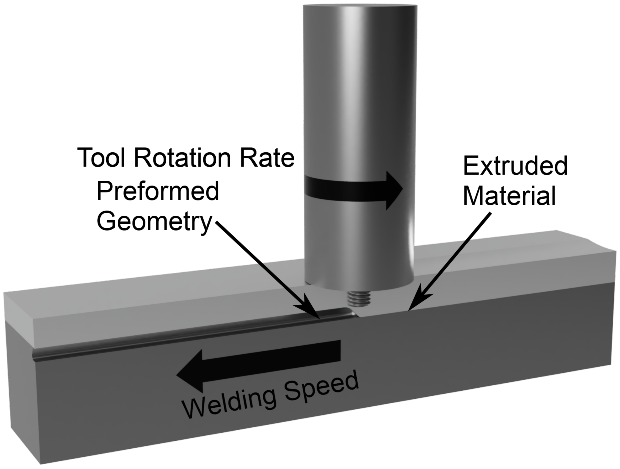

Figure 4.1: Diagram of the extrusion process.

formed via the tool shoulder, backing plate, and cold metal around the tool [52]. Modeling also defined the material flow around the pin of the tool as extrusion. Arbergast developed a model for material flow in FSW characterized by three zones: deformation, extrusion, and forging [55]. Krishnan stated that for each rotation of the tool, a cylindrical section of material is extruded around the probe [54]. Nunes described a rotating plug model in which a plug of plasticized material is extruded around the pin of the tool each rotation [146]. Pei modeled a periodic localized shear model in which the shear banding around the tool is formed reach rotation [61].

There is a large body of work characterizing the microstructural state of welded aluminum. Most welding processes, fusion and solid state, are accompanied by heating of the base material. The heat influx inherent in welding causes overaging, dissolution, and precipitation. The heat effected zone (HAZ) is overaged, showing a large proportion of incoherent precipitates. When considering Tungsten Inert Gas (TIG) welding, the precipitate structure is characterized by overaging and partial dissolution in the HAZ, and eutectic Al-Si structures in the melt zone because of dilution of Mg by the Al-Si filler metal [147]. Cabello Munoz found that FSW of Al-4.5Mg-0.26Sc alloy caused less dissolution of precipitates than TIG welding. However, the dissolution process made TIG welds more receptive to post processing heat treatment [148]. With ultrasonic welding of AA6111-T4 sheet, peak temperatures of 500 C were observed and served to resolutionize the precipitates. Post weld natural aging led to the weld being harder than the base material. It was theorized that vacancy generation in the weld led to an accelerated aging process [149]. Partial dissolution/coarsening of the precipitates was observed in the weld nugget of friction stir welded AA2219-T87 due to thermal cycling [65]. The weld nugget in FSW AA2024-T351 was found to contain fine scale S and large Ω phase precipitates due to precipitation from a solutionized state. Similarly, the Thermo-Mechanically Affected Zone (TMAZ) contained regions of overaging and dissolution depending on distance from the weld center [150]. 7050-T651 was friction stir welded and its precipitate distribution analyzed. Precipitates in the HAZ were found to have coarsened. The TMAZ was split into two regions. The outer layer was characterized by coarsened precipitates and partial dissolution. The inner layer precipitates were dissolved and re-precipitated as fine precipitates. The nugget contained uniformly dispersed fine precipitates. All populations largely contained equilibrium precipitates, and GP zones were found in the inner layer of the TMAZ and nugget [64]. Liu divided the HAZ of FSW AA6061-T6 into three regions depending on temperature history during welding. The outermost region experiences a low peak temperature, leaving the precipitates largely unchanged. The second region experienced a peak around 360 C to 370 C, resulting in overaging. The innermost region experienced the highest temperatures, resulting in dissolution of most of the precipitates [63].

Based on the literature, the precipitate distribution is a function of the thermo-mechanical history of the region of the weld. The thermal peak declines with increasing distance from the weld. The outer most layer, the HAZ, is typically overaged with large equilibrium phase precipitates. In the TMAZ, coarsening and partial dissolution has been observed. In the weld nugget, full dissolution is common with large fractions of fine equilibrium phase precipitates. Dissolution of precipitates coincides with a decrease in hardness of heat treated aluminum. However, an artificial hardness process could lead to the precipitation of additional hardening phases.

When considering the TMAZ and nugget of FSE, it is safe to assume that the extruded material originates from these regions. The precipitates involved were either partially or fully dissolved with the remainder coarsened. The ASM handbook Volume 4 states that some alloys (6063, 6463, and 7005) are insensitive to cooling rate, and they can be can be air cooled or water quenched from a final hot working step. It is common practice to move directly to an precipitation heat treatment with extrusions of these alloys, and the extrusions can obtain similar strengths without a separate solutionizing treatment [144].

This manuscript seeks to explore the validity of post processing FSE joints by moving directly to an artificial aging step after welding, similar to the process used for aluminum extrusions. There is little published work regarding the post processing of FSW joints, especially when beginning with heat treated stock. Using T6 aluminum stock and moving directly to aging would have several advantages over starting with annealed stock.

Skipping a solutionizing treatment offers several advantages over a traditional heat treatment regime. The lower temperatures required for aging make it more practical for large weldments. Preheating and stress relief is common for large weldments, especially in cast structures and could be easily adapted to artificial aging of FSE joints. Solutionizing treatment can cause distortions in large weldements [151]. Additionally, FSE is a process for joining dissimilar materials. A solutionizing treatment might damage the temper of the second material, but a low temperature aging would reduce that risk. Additionally, the temper designation of the base material could be preserved. Process could be particularly beneficial to applications where weight reduction is key such as the aerospace industry, or applications where the temper of the harder material is important.

4.3 Methods

FSE was used to join 6.35mm mild steel with 6.35mm AA6061-T6. The steel had a single dovetail milled on one face, and the aluminum was extruded into the dovetail. The welds were performed according to the setup and processing parameters outlined in Evans [34], an tool rotation speed of 1500 RPM and weld speed of 76.2 mm/m. These parameters are not optimized for weld strength but produce consistent extrusion. In the end, six 200 mm long plates were produced: one plate for each microstructural and hardness testing, four for tensile testing. The plates were sectioned into ten to twelve 6.35 mm samples, while taking care not to significantly heat the samples. No samples were taken from the region within 25.6 mm of the start or end of the weld.

Samples from each weld were placed in a 170 C oven. One sample from each weld was removed at 9 different time skews: 10 min, 20 min, 40 min, 1 hour, 2 hours, 4 hours, 6 hours, 8 hours, and 10 hours. One or two samples from each plate was left in the as-welded condition for analysis. Two of the samples had enough material for 11 hour samples. The data is included in the manuscript and considered in the analysis. The temperature and time were selected using the guidance of the ASM Handbook Volume 4 [144]. 170 C was selected to produce significant results within a single day of heat treatment and prevent microstructural change within the steel or the base aluminum. At 170 C, the welded material should reach a maximum strength at approximately 10 hours, and the base material is expected to not see a significant decrease in strength until 24 hours.

Samples were subjected to Rockwell hardness tests, SEM imaging, and tensile shear tests. One sample from each time skew was prepared for hardness testing. After the first test, the samples were resurfaced and retested. Base Material, as-welded,

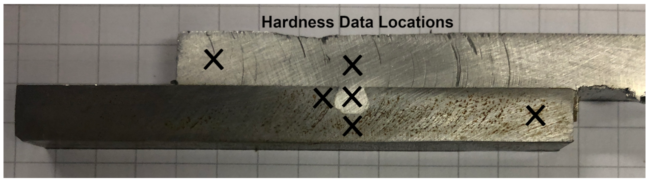

Figure 4.2: Three Locations in each the aluminum and steel were chosen to represent different heated regions during the weld. In the aluminum, the base material, extruded material, and weld nugget were tested. In the steel, bottom of the dovetail, side of the dovetail, and base material were tested.

10 min, and 10 hour samples were polished for imaging. All remaining samples were used for tensile shear tests.

The specimens were tested to failure using a load frame with a strain rate of 2 mm/min. The hardness of both the aluminum and steel was tested using the HRF and HRA scales, respectively. They were tested in three locations, each shown in Fig. 4.2. The aluminum was tested within the extruded material, base material, and the weld nugget above the extruded material. These locations were thought to be most indicative of joint strength. The steel was tested in the base material, beneath the dovetail, and to the side of the dovetail under the pin of the tool. These locations were determined to be most affected by the thermal cycling of the weld and heat treatment. The quantity and size of Mg_2Si precipitates and iron inclusions were analyzed using SEM imaging and EDS for the base material, as-welded material, 10 minute samples, and 10 hour samples. The samples were imaged using Vanderbilt University's Ziess Merlin SEM with an accelerating voltage of 20 KeV and a working distance of 8.5 mm. The images were taken using the back scatter detector. The samples were imaged just above the base of the dovetail within the aluminum.

4.4 Results

The welded regions were initially substantially softer than the base material. Throughout the heat treatment process, the welded material rapidly narrowed the gap between the as-welded hardness and the base material hardness, Fig. 4.3. During the 10 hour heat treatment process, the weld nugget increased in hardness from 67.5 HRF to 83.5 HRF, a 24% increase. The dovetail had a hardness of 54.7 HRF in the as-welded condition and 81.8 HRF at 10 hours heat treatment, a 54% increase. The base material's hardness stayed relatively constant from 87 HRF to 90 HRF during the heat treatment process. As-welded, the base material was 29% harder than the weld nugget and 59% harder than the dovetail. After the 10 hour heat treating process, the difference had closed to 8% for the weld nugget and 10% for the dovetail.

The aluminum samples regained a majority of the hardness of the T6 condition in the nugget, while the base material remained around the T6 hardness. Both the dovetail and nugget material in the as-welded condition were below that of a T4 condition. The dovetail material was approximately 10 HRF lower than the nugget. During the heat treatment process, both materials rose above the T4 condition and approached that of a T6 condition.

The steel maintained approximately the same hardness throughout the heat treatment process, Fig. 4.4. The steel beside the dovetail had a hardness of 57.8 HRA as-welded and 57.7 HRA after 10 hours of heat treatment. Beneath the dovetail, the steel had a hardness of 59.5 HRA as-welded and 59.3 HRA after 10 hours of heat treatment. The base steel had a hardness of 61.6 HRA as-welded and 61.3 after 10 hours of heat treatment.

While the steel has a relatively homogeneous hardness, the base material is generally the hardest, followed by under the dovetail, then the side of the dovetail. This indicated that the welding process had some effect on the hardness of the steel. Typically, the highest temperatures during welding are concentrated around the probe, coinciding with the softest material directly below the probe, the side of the dovetail. Beneath the dovetail, the steel was heated by the extruded material and is not very close to the tool. The base material was minimally heated, so retained hardness.

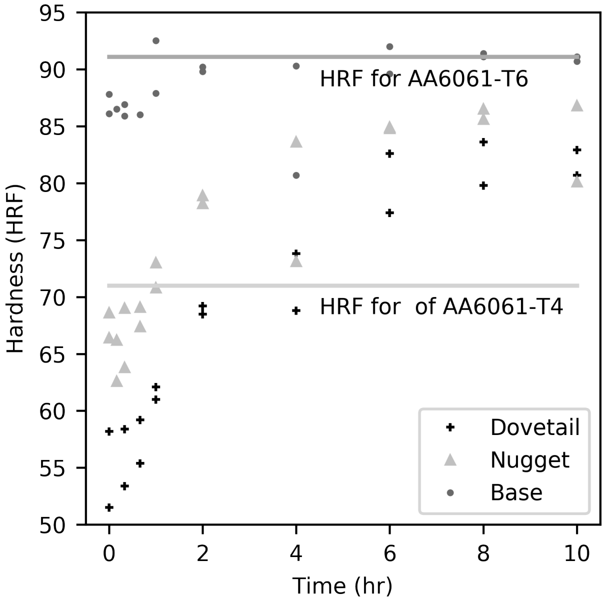

Figure 4.3: Hardness of the aluminum samples, measured in the Rockwell F scale, at three different locations plotted versus aging time.

Two varieties of constituents, an iron and a magnesium-silicon compound, were found in the SEM images by comparing the micrograph and EDS images, Fig. 4.5. These inclusions appeared as black or white particles within the bulk. The iron inclusions are an extremely common impurity found in aluminum alloys and does not contribute to precipitation hardening. The magnesium-silicon compound is the intermetallic hardening phase, Mg_2Si found in 6XXX series aluminum [145].

The base material displays consistent, larger iron inclusions with few Mg_2Si precipitates. After welding, Many smaller inclusions of both variety are seen. The breaking up of larger inclusions is consistent with the mechanical mixing process in friction stir welding. Within 10 minutes of heat treatment, the Mg_2Si precipitates appear to be much larger, but the distribution of Mg_2Si precipitates appeared relatively equal after 10 hours. Iron inclusions continued grow until the 10 hour mark.

An image processing script was written to facilitate in the unbiased analysis of particle size. The micrographs were converted into binary images by thresholding.

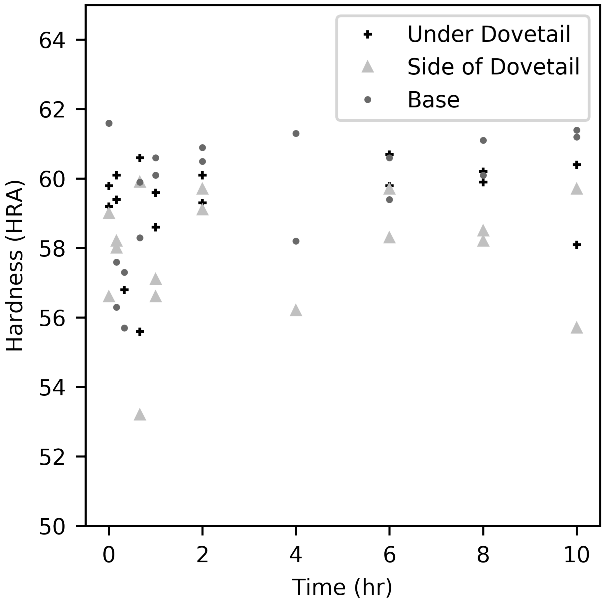

Figure 4.4: Hardness of the steel samples, measured in the Rockwell A scale, at three different locations plotted versus aging time.

Two thresholds were determined, one to identify the white precipitates, and one to identify the black precipitates. Any precipitates under 10 pixels in size was removed from analysis. They could not be identified as a precipitate by eye. After filtration steps, the visible area of each particle was calculated. The size distribution was determined by plotting the calculated sizes in a histogram, Fig. 4.6, 4.7.

It is evident from the histograms that the inclusion sizes do not fit a Gaussian distribution. So, the median was determined to be the best measure of central tendency. The median size for the Mg_2Si precipitates in the base, as-welded, 10 min, and 10 hour samples is 0.69 μm^2, 0.16 μm^2, 0.4 μm^2, and 0.33 μm^2 respectively. The median area for the iron-magnesium inclusions in the base, as-welded, 10 min, and 10 hour is 0.49 μm^2, 0.32 μm^2, 0.37 μm^2, and 0.4 μm^2 respectively. The distributions agree with what can be visibly seen in the SEM micrographs. The base material has few but larger inclusions. The welding process has produced a distribution of much smaller inclusions. During the heat treatment process, the number of smaller inclusions decreased, while the number of larger inclusions increase. The iron-magnesium distribution followed the trend through 10 hours. However, the median silicon-magnesium inclusion area decreased after the first 10 min. One possible explanation is that significant gains in inclusion size continue to occur after 10 minutes, and variations in image locations bias the inclusions size. Significantly more iron inclusions were imaged than Mg_2Si precipitates, Making a statistically representative average harder to obtain.

The tensile shear test showed the ultimate tensile strength increased from 2193 N to 2718 N, a 23.9% increase from as-welded to 10 hours. There was a steep initial rise in strength until around 4 hours of heat treatment. Beyond that point, the data begins to scatter. Generally the UTS increases beyond four hours as shown by the average, but a possible peak is reached sometime between 6 and 8 hours, Fig. 4.8. Gains in UTS largely dropped off by the 8 hour mark.

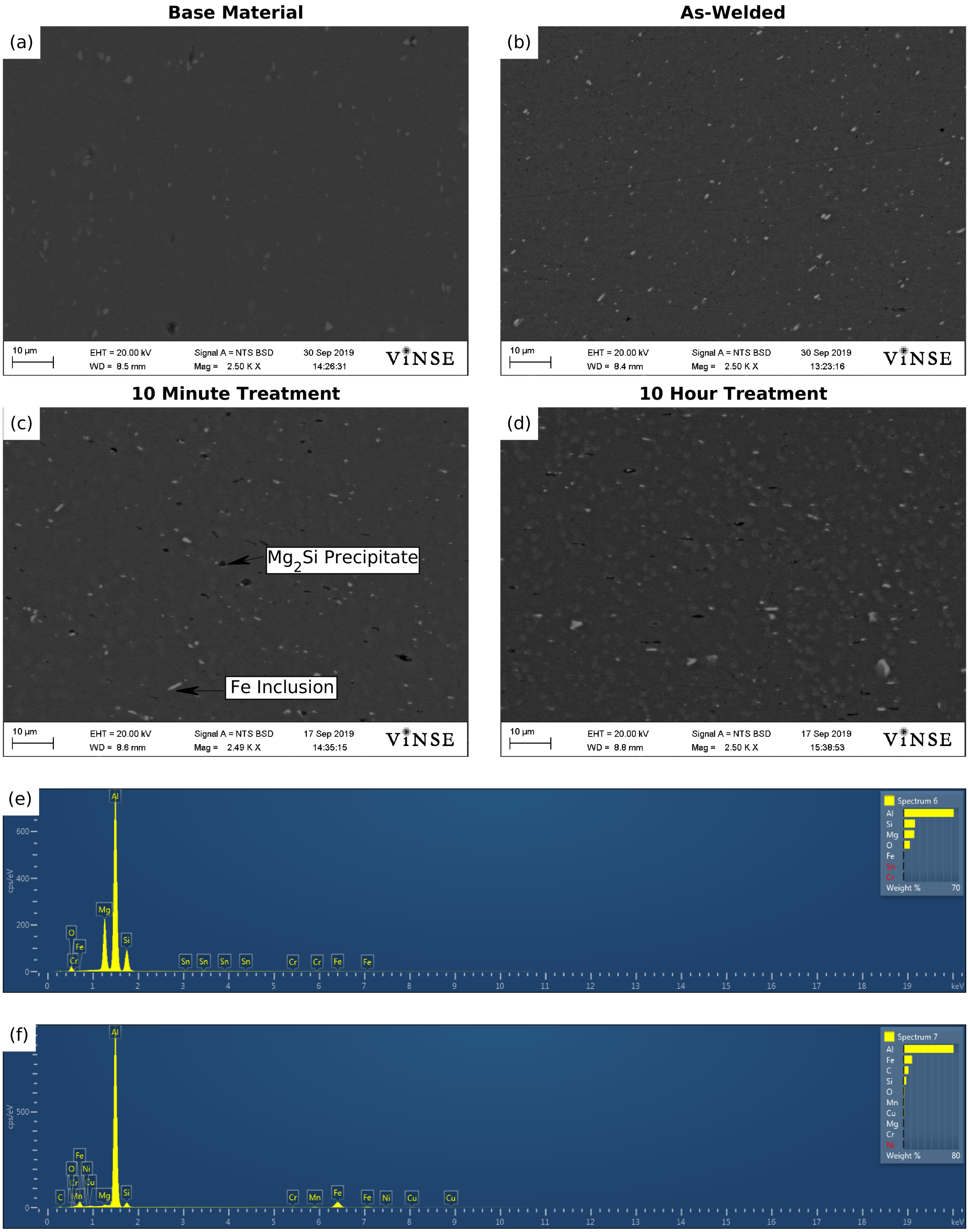

Figure 4.5: SEM micrographs of (a) base AA6061-T6, (b) As-Welded AA6061, (c) AA6061 after 10 minutes of heat treatment, (d) AA6061 after 10 hours of heat treatment. All FSE samples were imaged at the base of the dovetail. All Micrographs were taken at 20 KeV, 2.5 K magnification,and 8.5 mm working distance with the Microscope in analytical mode and Back Scatter Detector. EDS spectra for the (e) Mg_2Si precipitates and (f) iron inclusions.

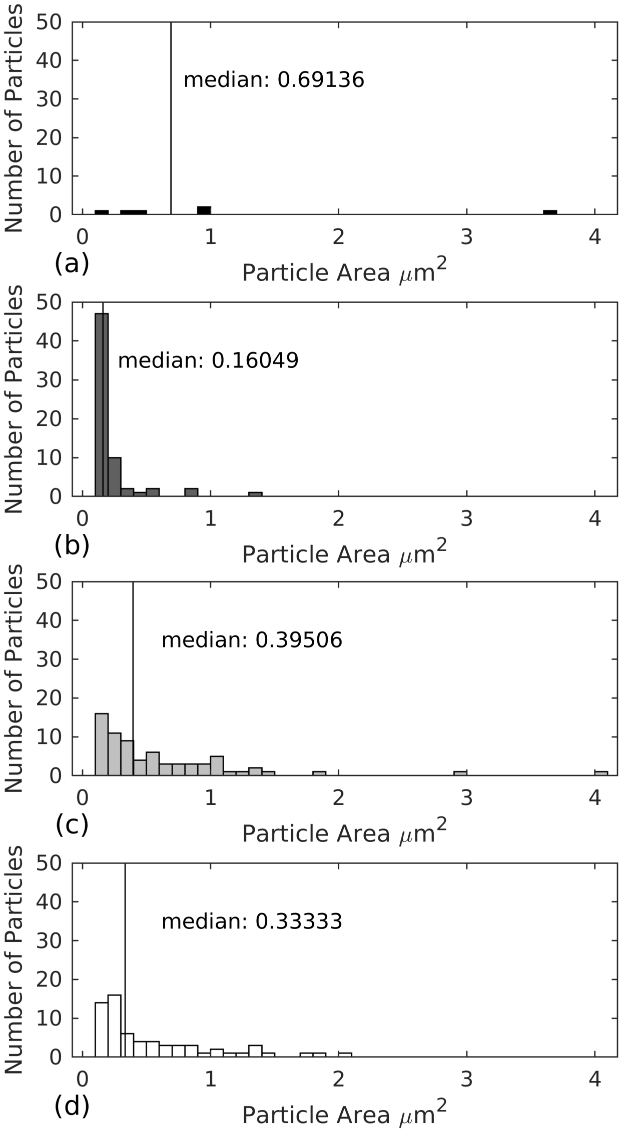

Figure 4.6: Histogram of Mg_2Si precipitate area for (a) base material, (b) as-welded, (c) 10 minutes, and (d) 10 hours of heat treatment. The median precipitate size is reported along with its relationship to the distribution.

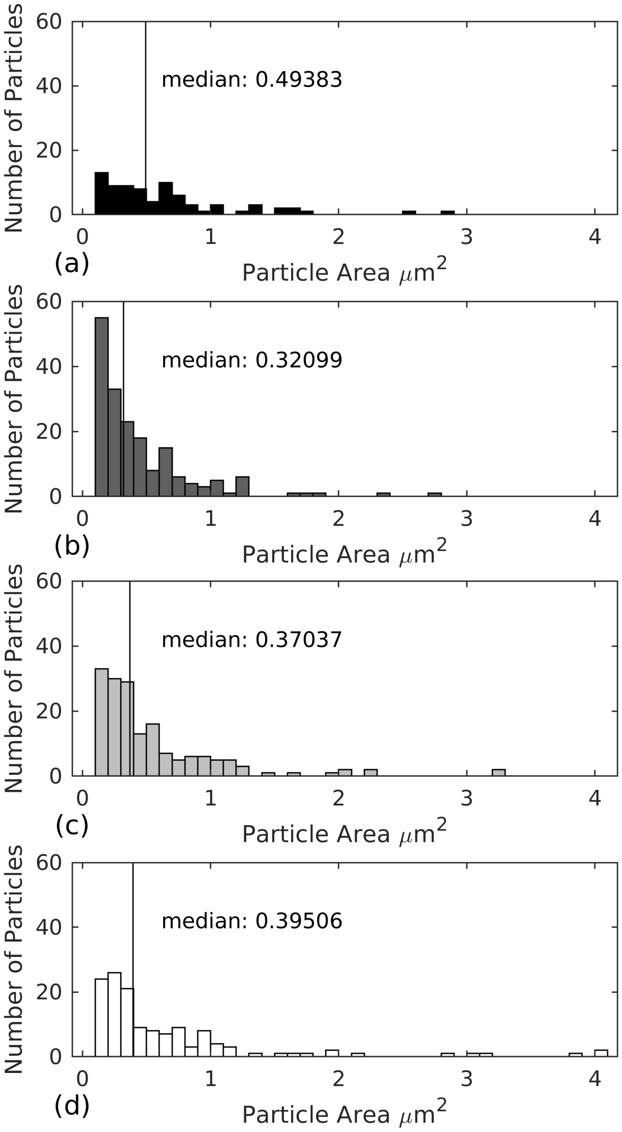

Figure 4.7: Histogram of iron inclusion area for (a) base material, (b) as-welded, (c) 10 minutes, and (d) 10 hours of heat treatment. The median particle size is reported along with its relationship to the distribution.

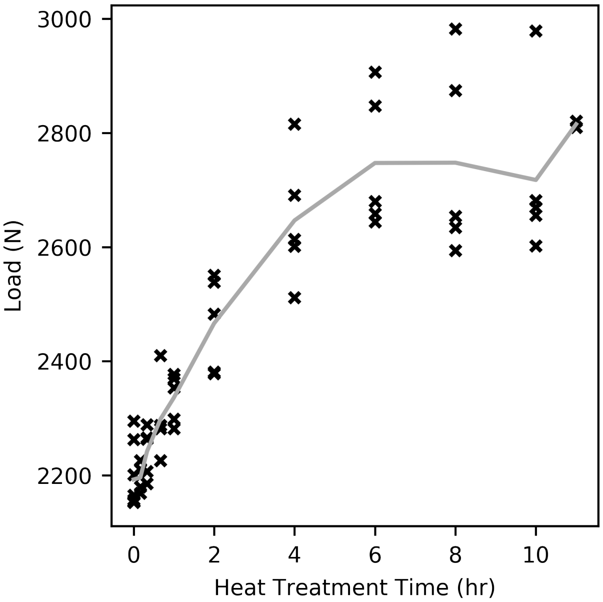

Figure 4.8: Ultimate tensile strength for each time skew from as-welded to 10 hour. The gray line represents the average value at each heat treatment time.

4.5 Discussion

During the aging process, the hardness of the nugget and dovetail significantly increased. The dovetail began around a 65 HRF, slightly lower than a T4 condition, and approached the T6 condition with a hardness of 82 HRF. Between the measured hardness and literature, it can be inferred that the nugget region experienced partial to full dissolution of the hardening precipitates, and that hardening β' precipitates reformed during the aging period [65, 150, 64].

The extruded material in the dovetail generally has a lower hardness at each heat treatment time. This implies that the material that filled the dovetail when through a different mechanical and thermal history than the nugget. The SEM analysis suggests that only partial dissolution occurred during extrusion, as large precipitate can be seen in the bulk. SEM and EDS analyses are insufficient to image β' and β" phases. Typically TEM imaging is used to analyze the crystal structure. Therefore, the precipitates observed in Fig. 5 are most likely β phase and does not contribute greatly to the strength of the material. However, it does provide some evidence for a thermal history similar to the TMAZ I region in Su et al. [64]. With partial dissolution, less of the β' hardening phase was able to form in the dovetail material. Güven İpekoğlu and Gürel Çam applied a post weld heat treatment process to friction stir welded dissimilar alloys AL6061 and AL7075 in both the T6 and O condition. They applied both solutionizing and precipitation hardening treatments, and observed a similar increase in hardness across the weld. The authors stated the increase hardness is due to the increase of hardening particles in the post heat treated samples [152].

The iron inclusions are impurities from the refining process and do not contribute to the strength of the aluminum. However, they do appear to have gone through a similar coarsening process.

Analyzing the failure mechanism in shear tensile tests, all samples failed by shearing at the neck of the dovetail. The shear surface was estimated by the width of the neck and length of the samples, Fig. 4.9. Using this calculated area, the ultimate tensile strength of the joint was transformed into an ultimate shear stress of the aluminum extrusion. The results of the analysis are displayed in Fig. 4.10. In the figure, textbook shear strengths for O, T4, and T6 are noted [153]. All of the samples can be fit between the O and T4 condition.

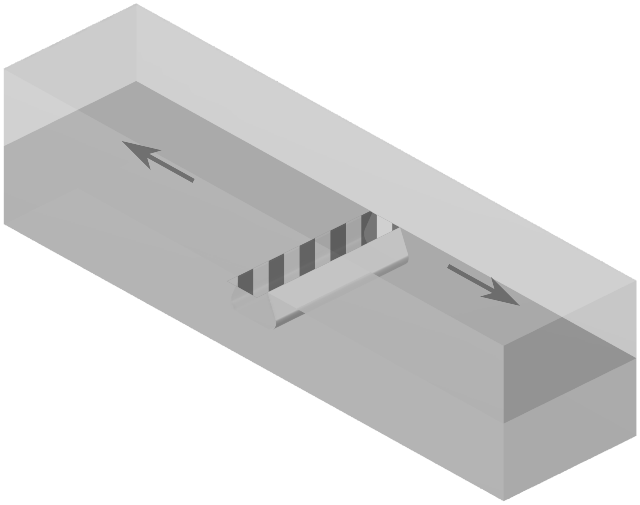

Figure 4.9: The sheared surface of the extrusion samples.

The measured hardness values are comparable to the T6 condition for AA6061. However, the estimated ultimate shear strength is lower than the T4 condition. The discrepancy can be explained by inaccuracies caused by the shear tensile test and geometry of the samples. The offset nature of the lap weld cause a moment about the weld, resulting in stress concentrations and crack formation at the corner of the dovetail. Additionally, the ends of the dovetail take the approximate form of a blade, assisting in shearing the material during the test. A more accurate estimation would require a simulation accounting for plastic deformation and contact between the two pieces.

Some initial work was done on standard butt welds with similar processing and aging parameters and tested for tensile strength. Since they were cut into standard ASTM E8 dogbones, their ultimate tensile strength can be reported with more cer-

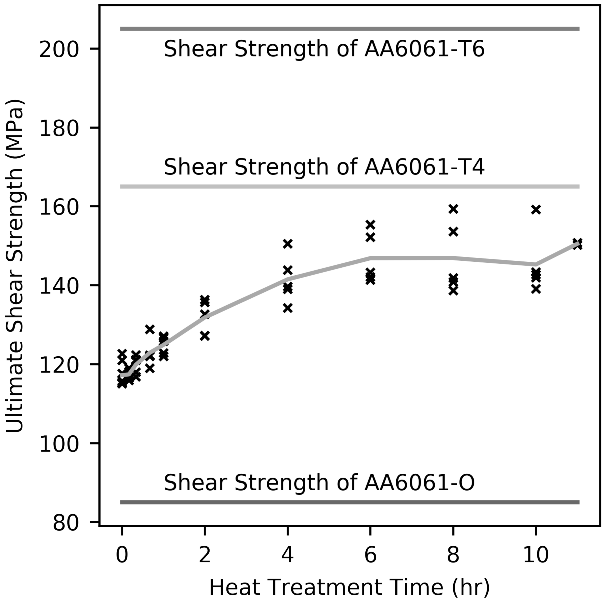

Figure 4.10: Estimated Ultimate Shear Strength of the extruded samples versus time spent at 170 C. The gray line represents the average value at each heat treatment time.

tainty. Similar to the FSE samples, the ultimate tensile strength tends to gather between the O and T4 conditions, Fig. 4.11. However, it might not be a complete fair comparison. The butt weld specimens all failed within the heat effected zone, a notoriously weak zone. The heat effected zone contains the Low Hardness Zone (LHZ). A region that experiences a peak temperature around 360 C during welding, leading to overaging and a minimum in material properties [63]. In contrast, The FSE joints experiences a thermal history similar to that of the TMAZ with partial dissolution of precipitates.

The butt welded specimens do show that precipitation hardening post weld does substantially increase the strength of FSW joints. During the heat treatment process the ultimate tensile strength of the butt welds rose from 187 MPa to 215 MPa, a 15% increase in tensile strength. Further characterization would be useful in explaining the nature of the strengthening mechanism.

The study shows that during FSE, the extruded material experiences significant

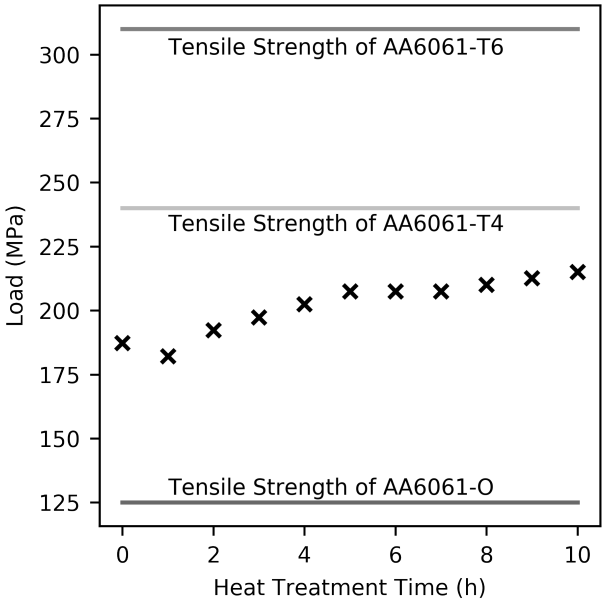

Figure 4.11: Ultimate Tensile Strength of dogbone samples versus time spent at 170 C.

changes to its micro structure and a loss in strength and hardness. The results from hardness and tensile tests indicate that significant changes in the joint occur within the first 4 hours of the precipitation hardening process. After the 6 hour mark, both hardness and tensile strength gains are minimal or non-existent. The peak appears to be before the expected 10 hour mark [144]. Possible explanations could be the joint geometry favoring a material with greater elongation, differences in alloy vendors, or condition of the as-welded material.

4.6 Conclusion

Skipping the solutionizing treatment and moving straight to an artificial hardening process has been shown to be an effective way of recovering some material strength of butt welded as well as FSE joints. The tensile strength of the FSE joint increased from 2193 N to 2718 N, a 23.9% increase. The hardness of the weld increased for both the nugget and dovetail. The hardness increased from 54.7 HRF to 81.8 HRF in the dovetail, and from 67.5 HRF to 83.5 HRF in the weld nugget. The base aluminum and steel remained largely undisturbed within the 10 hour heat treatment. The inclusions within the extruded aluminum experienced a large decrease in size and growth during the treatment process. This process could allow for post process of FSE joints without over-aging the aluminum base or annealing the steel substrate.

Further work should be done to expand the relevance of the study. Samples should be heat treated beyond the 10 hour mark to determine a critical aging time that base material begins to be over-aged. The extruded material could continue to see gains in material strength after 10 hours. The mild steel used was not in a hardened state, but was most-likely closer to an annealed state. Subsequently, the steel did not react to the aging process. The study should be repeated with a hardened steel specimen to observe the effects on material not in an annealed state.

4.7 Acknowledgment

Thanks go to Dr. Anthony Hmelo for assistance on SEM Imaging.

All funding for the project was provided through the NASA Tennessee Space Grant.

CHAPTER 5

Applying Torque Based Control to Friction Stir Extrusion

5.1 abstract

A series of Friction Stir Extrusion welds with varying groove geometries were performed to determine the effect on processing forces. A clear correlation with groove geometry was observed for z-force, torque, and y-force. The data was used to design a torque-based plunge depth controller. All the welds from the prior series of welds were repeated with the controller applied. When comparing the controlled welds to the uncontrolled welds, the use of the controller eliminated surface defects at larger groove cross-sectional areas, and the controlled welds maintained ±10% of the reference torque. The controller demonstrated good transient performance for both a step and continuous linear increasing groove widths.

5.2 Introduction

Friction Stir Extrusion (FSW) is a derivative process of Friction Stir Welding (FSW) that has been presented as a dissimilar material joining method [34]. The process joins two lapped plates by utilizing the plastic flow present during FSW to extrude material from the top plate into a preformed geometry in the bottom plate. The groove is structured such that the extrusion forms a mechanical interlocking joint. There are other derivative processes that form joints through similar mechanisms [118, 154, 131, 155, 130, 125]. In FSE, the welding tool only directly contacts one of the two materials to form a sound joint. Only contacting one of the two materials gives several advantages to the FSE process over other dissimilar joining techniques. For example, the need for expensive or exotic tooling can be reduced, and detrimental formation of intermetallics can be avoided. In many cases, a cheap and ordinary tool made of tool steel is sufficient for the process. The FSE process applies to a wide variety of materials. Therefore, it is beneficial to generalize the naming of the two materials to be joined. The two different materials are dubbed the softer and harder materials. The softer material is designated as the material that is more advantageous to contact the FSW tool. It is placed at the top of the lap joint, and the tool processes the material. Some considerations to select the softer material are the yield strength, abrasiveness, thermal softening, solidus temperature, etc. The harder material could be difficult or impossible to FSW but formable through other means. It is at the bottom of the lap joint, and the preformed geometry is formed in it.

The process has been used to join aluminum to steel [34, 136] and aluminum to titanium [156] in both a lap-joint [34] and T-joint [136] configurations. Applicability to the thin sheet regime has been demonstrated [157]. The process has also been extended to other previously impossible or problematic weld combinations such as aluminum and graphite [158].

The current state of the art is prone to produce surface defects. The surface defects forms typically on the advancing side of the pin. Similar in location to where many cold processing voids are formed with conventional FSW [77]. Current works suggest that a loss of tool contact on the trailing side of the tool is responsible for defect formation [156, 136].

During testing, the surface defects were rectified by increasing the lead angle from 0° to 1.5° or reducing the cross-sectional area of the geometry. The plasticized material used to fill the preformed geometry originates from the plastic region around the tool. As a result, the region under the tool must experience a thinning proportional to the volume extruded. When the thinning is not accounted for by reducing the volume extruded or modifying the lead angle, defects will form.

Figure 5.1 illustrates how an increase in lead angle can help to increase tool contact and eliminate defect formation. The material loss is shown as the thinner material

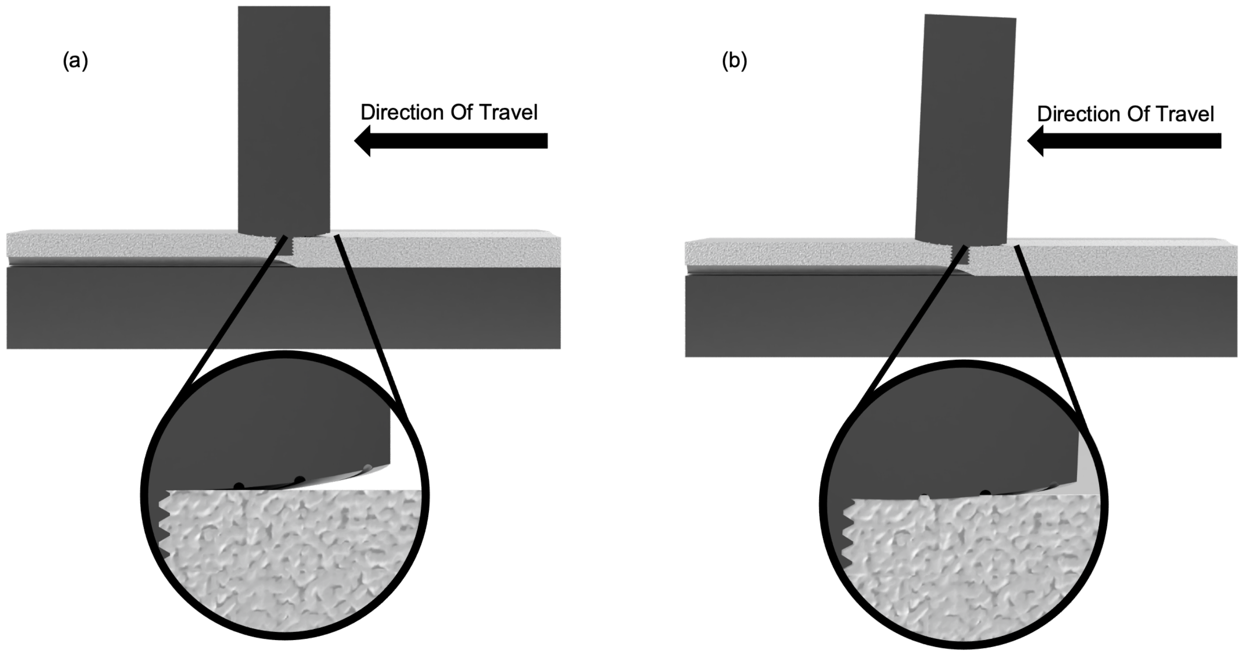

Figure 5.1: Comparison between 0° (a) and 1.5° (b) tool lead angle and the loss of forging pressure that could lead to surface defects.

behind the tool. The tool almost completely loses contact with the surface of the material with the 0° lead angle. The lead angle pushes the rear edge of the tool deeper into the material without increasing the plunge depth. This change helped to ensure that the tool stayed in contact across the whole surface area of the tool.

Manufacturing defects or variations in groove geometry to optimize design could lead to grooves with variable cross-sectional areas. Changing cross-sectional area requires extruding varying amounts of material during a single weld. Without compensation, defects could form and propagate through an FSE weld. A single set of processing parameters could lead to defect formation in one area of the welds and excessive flash formation in another area. Past studies have avoided this issue by using a consistent groove design and optimizing the processing parameters for the groove design.

Controlling tool engagement would adapt to variations in groove geometry while maintaining consistent surface quality. Referencing the geometry present in Fig.

5.1, two modifications to processing parameters can be made to increase the tool engagement: increasing lead angle again or increasing plunge depth. For this study, increasing plunge depth was examined. In-situ control of the lead angle would require more degrees of freedom than was available.

Extensive work has been done on controlling and monitoring the FSW process through acoustic emissions and processing forces to detect defect formation and improve consistency [159]. FSW, a complex thermo-mechanical process, depends on achieving sufficient heating, plasticization, and consolidation of the material to form an effective weld. However, these quantities are not easily set or measured. Instead, there are three controllable parameters, process parameters, readily apparent: spindle RPM, welding speed, and tool plunge depth [160]. These process parameters are linked to the welding physics through complex non-linear relationships that are not yet well defined. Very few predictive models have been constructed to relate processing parameters to successful welds [61]. As a result, controlling the welding process involves sensing processing forces and temperature in-situ and controlling the process parameters.

Processing forces are defined as the x, y, and z-forces applied by the welding tool, where the z-direction is into the anvil, and the x-direction is aligned with the direction of the weld seam, as well as the torque for this paper. The x and y forces can be grouped as the planar forces. Measurement of the processing forces and weld temperature is one of the few methods of in-situ process monitoring. Cook et al. showed a relationship between RPM, transverse rate, plunge depth, and z-force [134]. Therefore, they can be used as parameters to control the processing parameters and have been used extensively in sensing and control applications.

Implementing force control has long been a method for machines lacking sufficient stiffness for FSW applications. Axial force control has also been used to increase weld consistency and react to disturbances caused by material or manufacturing variations.

Lockheed Martin Michoud Space Systems developed an axial force controller to compensate for tooling deflection when welding AL2195 barrel sections for the space shuttle's external fuel tank [86]. Smith used joint torques to implement an axial force control to a serial arm robot to counteract deflection of the arm [88]. Longhurst et al. examined controlling z-force through three process parameters: welding speed, rotation rate, and plunge depth. While welding speed was the most accurate at maintaining a constant z-force and energy deposition, controlling plunge depth was the only method to control for deflection and height variations [91].

Torque can be tied to both input energy and tool engagement and has been used as a control parameter. Longhurst et al. demonstrated controlling the input energy by varying the transverse speed and tool engagement via torque and suggested that torque is a good alternative to z-force for controlling plunge depth due to better coupling between tool surface area engaged and the change in torque [93]. Gibson et al. used torque measurements to predict tool wear [83].

In-process monitoring of the processing forces has been proposed as a method for defect detection. Yang et al. used the Power Spectral Density of the axial force to develop a gap detection algorithm for FSW butt welds [80]. A neural network was able to identify welds containing defects from good welds with 95% accuracy using the Fourier Transform of the processing forces [81]. Additionally, Fleming et al. used z-force and planar force to detect misalignment of a frame member when welding in a T-joint configuration. Z and planar force were used because they provide a much better signal-to-noise ratio [100]. Gibson et al. used z-force as an indicator of misalignment when welding lapped sheets with a sealant [102].

There is little to no published work on controlling the extrusion process. This paper aims to demonstrate that the loss of contact can be sensed through multiple indicators and propose a basic control scheme to eliminate defect formation.

5.3 Methods

A series of positional control welds were performed with differing groove widths to determine the relationship between the processing forces and different extrusion conditions. The welding fixture was set up with multiple different groove widths. At 0 mm width, the groove widened to 3.81 mm with 0.64 mm increments. Three welds were performed at each groove width. Additionally, three welds were performed with both a step and a continuously increasing groove width area. In total, 27 welds were performed with positional control. Then, all 27 welds were repeated using a torque controller. All welds were performed with standard FSE parameters: 1500 RPM and 7.62 cm/min with 2.54 mm offset to the advancing side [34]. The offset was measured center-line of the groove to the center of the tool. A constant plunge depth of 5.59 mm was maintained during the positional control welds.

All welds were completed using an extrusion fixture that took the place of the normal bottom plate, Figure 5.2A. The fixture consisted of a base and sliding plate that created a groove with a rectangular cross-section with width adjustable from 0 to 6.25 mm, Figure 5.2B. The rectangular grooves simulate the conditions in an FSE weld without an interlocking groove design, allowing the welded plate to separate from the fixture while the fixture was still in place. The use of the fixture had multiple advantages. Many more tests could be completed with fewer consumables used. The extrusions could be examined across the length of the weld without destruction of the joint. All the welds could be performed without moving the fixture, so the groove position was more reliably known, increasing repeatability. An additional plate was created to simulate a step increase in groove width. A notch was milled into the edge to provide a .5 mm transition in the rectangular groove, Figure 5.2D. The notched plate was installed and adjusted for the step response to provide a 1.65 mm to 2.41 mm transition in grove width. The continuously expanding groove width was achieved by mounting the straight plate at an angle, Figure 5.2C. So, the square

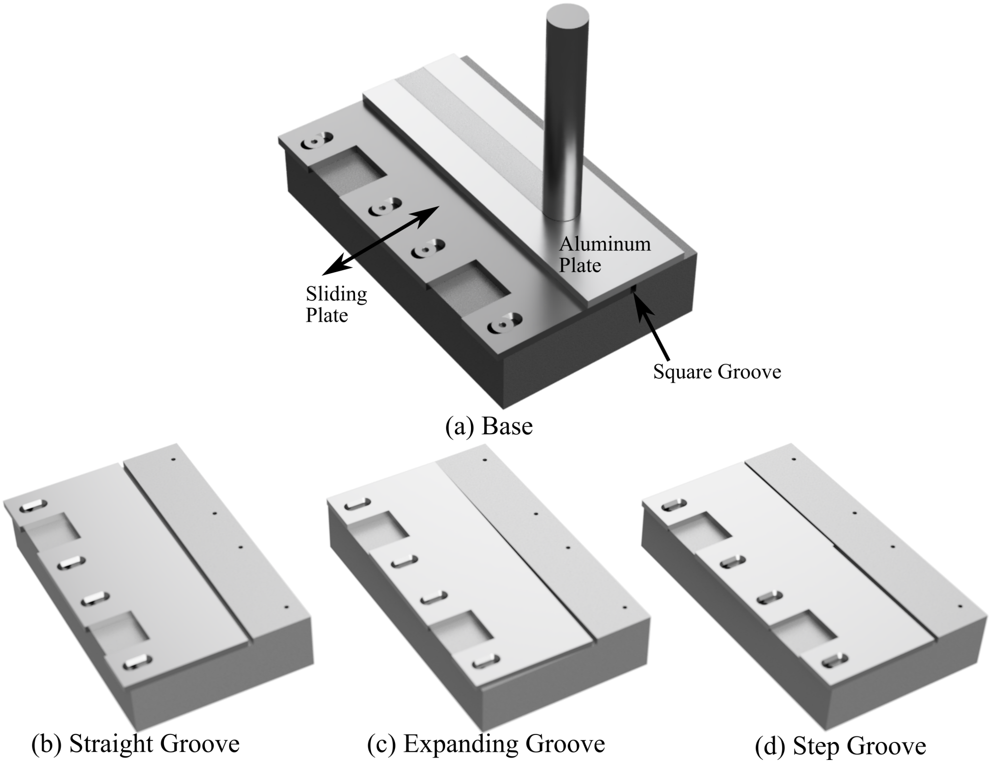

Figure 5.2: (a) The extrusion fixture was used as the bottom plate of an FSE weld. The fixture was configured in three different ways to provide different groove profiles: straight groove (b), expanding groove (c), and (step groove)

groove transitioned from 0 mm opening to 3.18 mm over the 25.4 cm length. The fixture was mounted onto the welder's table using strap clamps, and the lapped aluminum plate was similarly mounted.

A PID feedback loop was used to implement a torque controller, Figure 5.3A. The controller sets the vertical axis motor speed to maintain a constant torque. The state flow of the Welding process is presented in Figure 5.3B. Welds were initially position controlled. Then, the torque controller engaged when the plunge and ramp to full welding speed were completed. The control system was tuned by performing a series of bead-on-plate welds and using the Zieger-Nichols tuning method. Additional welds were performed, and the gains were then adjusted to achieve good stability and performance.

The quality of the weld was determined by visual inspection. The processing forces (torque, x-force, y-force, z-force) were sampled at 100 Hz by Kistler cutting force dynamometer. X and y-forces were determined using an absolute encoder tied to the spindle. The coordinate axis system was arranged such that the positive x direction is along the length of the weld, and the positive y direction is toward the advancing side of the weld. The tool rotates clockwise.

When presented as a graph vs. time, a low pass filter with a cut-off frequency of approximately 23 Hz was applied to the data (This reduces periodic effects due to the spindle rotation of 1500 rpm). The filter was also used to filter the measured torque during the welds. When presented as an average, the data was left unfiltered and was truncated only to contain the steady-state portions of the weld. This portion is from 25 mm after the welding speed ramp is complete to the end of the weld for the position-controlled welds. For the controlled welds, steady-state is from the controller engagement to the end of the weld, Figure 5.3C. The data was left unfiltered for averaging to prevent any need distortion. The truncation removed transient effects from the weld start-up procedure, either the procedure itself or passing over ridges of material from the plunge.

The machine used to perform the welds in this study is a 1944 Milwaukee Model K manual mill. The mill has been heavily modified to instrument and automate its operation. A Kistler 9124B rotating cutting force dynamometer measured the applied torque, z-forces, and planar forces. A current clamp was located on the power line of the spindle motor to collect current data. The machine was controlled by custom data acquisition and control software written in Matlab/Simulink and C#. Complete control over software and hardware enables the Vanderbilt University Welding Automation Lab (VUWAL) friction stir welder as an effective controls testbed.

The tool used was a scrolled convex tool with a threaded pin. The overall diameter of the tool was 25.4 mm. the pin was 4.83 mm long and 5.08 mm in diameter. The tool design allows for a greater range of stable plunge depths without excessive flash

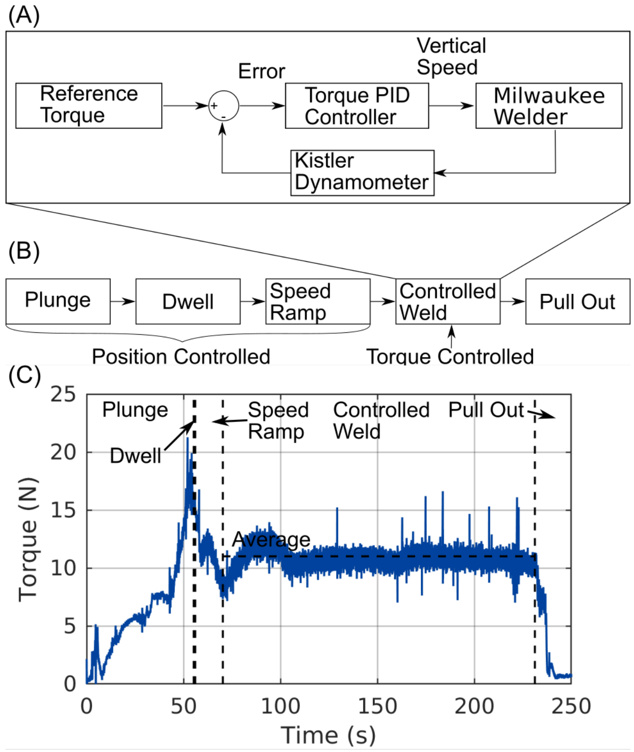

Figure 5.3: (A) Block Diagram of the Torque controller used in this study. (B) State diagram of the welding system: The weld's initial plunge and start-up states were position controlled. The torque controller engaged after the welder ramped to full transverse speed. (C) States of the controller marked on the torque plot of a standard torque-controlled FSE weld.

formation [161].

AA6061-T6 was used as the extruded material for these tests. Its superior extrusion characteristics and large process parameter window make it ideal for FSE studies.

5.4 Results

5.4.1 Expanding Groove Width

All of the welds performed with open-loop control were visually examined to look for defects and indicators of tool engagement, Figure 5.4. Flash or extra material expelled from the weld would indicate excessive plunge depth and tool engagement. Surface defects form from a lack of forging pressure caused by a lack of tool engagement. A slightly raised border can be seen on either side of the 0 mm groove welds and a rough but well-defined surface banding. As the groove width increases, the border shrinks, and the surface banding smooths out until the border disappears around 1.91 mm groove width. At 2.54 mm groove width, the surface banding has a seam from around the center of the weld. As the groove width expands further, the seam migrates to the advancing side. Between 3.18 mm and 3.81 mm groove widths, the seam transitions into a surface defect formed following the advancing side of the pin. The surface banding is formed due to a periodic extrusion process [54] . Discontinuities formed in the surface banding is likely due to changes in the extrusion process. Even though they all have the same plunge depth, the material lost to filling the groove seems to have changed the tool engagement. Through the observations, it was determined that the plunge depth for welds with grooves under 1.91 mm was too deep, resulting in the material beginning to be ejected from the weld. Additionally, the plunge depth with welds with grooves wider than 1.91 mm was too shallow, resulting in too little tool engagement. The seam that developed into a void was indicative of a loss of contact with the aluminum around the backside of the tool, and the rough onion ring pattern and extra material around the weld indicated the tool digging deeply into the material and expelling material to either side of the tool. It was concluded that the 1.91 mm groove width and plunge depth combination represented a well-matched set of parameters. Therefore, the average torque during those welds was used as the reference value for the torque controller. The reference torque was rounded up to 11 Nm.

The open-loop transient groove width welds expressed the same variations in surface banding and surface void formation through the length of each weld. Initially, the step groove welds had a good surface finish and no surface voids. After the step transition, a surface void following the advancing side of the pin developed in 2 out of 3 welds, and the last step weld developed surface irregularities after the step. Similarly, the continuously expanding groove welds formed surface voids or began to transition towards void formation at the widest portion towards the end of the weld.

The processing forces were averaged for the steady-state portions of the welds by the process described above. The averages of all the processing forces were plotted in Figure 5.5. The torque and spindle current strongly correlate with extrusion width and have tight groupings with few outliers, Figure 5.5A. The average z-force also expresses a proportional correlation with groove width, Figure 5.5B. X-force has a positive correlation to groove width, while the Y-force appears to stay constant, Figure 5.5A.

The torque vs. time and plots for all welds are presented in Figure 5.6. The torque response was consistent between welds at the same groove width, indicating good repeatability between trials. Few outliers or variations between welds exist. The plunge is represented by an initial rise in torque as the pin contacts the material, continuing to a sharp peak as the shoulder comes into contact with the surface. The peak is followed by a sharp decline in torque as the material heats up. After

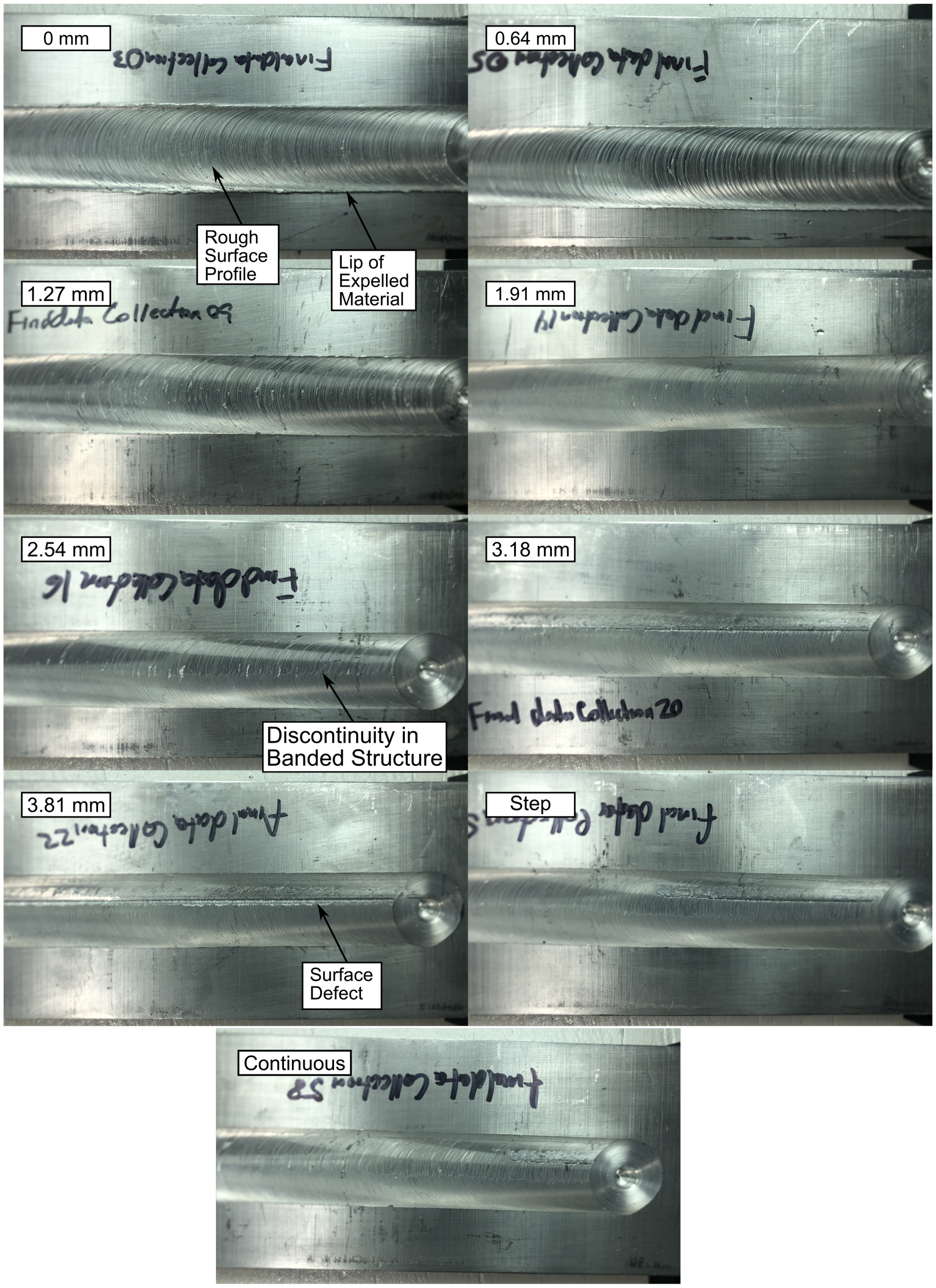

Figure 5.4: Photos of selected welds from the positional-controlled trail.

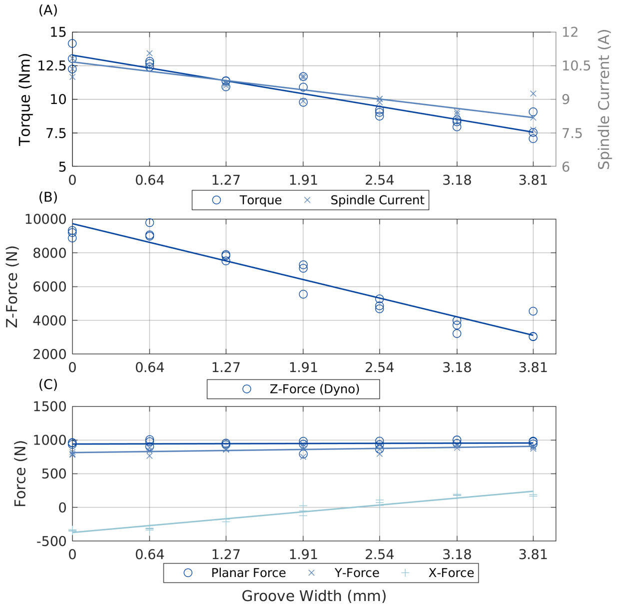

Figure 5.5: (A) Average torque, spindle current, (B) Z-force, and (C) XY-forces measured during each trial of the open-loop groove width trials. After the plunge, the average was evaluated from when the transverse rate reached a steady-state, to the end of the weld.

the plunge, each weld settles into a visually constant torque that is similar between welds, Figure 5.6. The step groove has a decrease in torque as the tool transitions over the step. The continuously increasing groove welds had a steadily decreasing torque through the weld duration. It was observed that larger groove widths correspond to larger signal-to-noise ratios.

The z-force vs. time plots for each weld is displayed in Figure 5.7. The plunge caused a similar response in the z-force, as was seen in the torque at the start of the weld—the z-force decreases with increasing groove width, except for a decrease in z-force after the initial contact of the pin. The z-force did increase towards the end of the weld for all constant groove widths. This is likely due to the thermal expansion of the material, especially as the weld reaches the edges of the plate. The step welds display a clear transition in the z-force around 120s from the narrow groove width to the thicker groove width. The continuously increasing groove width has a continuously

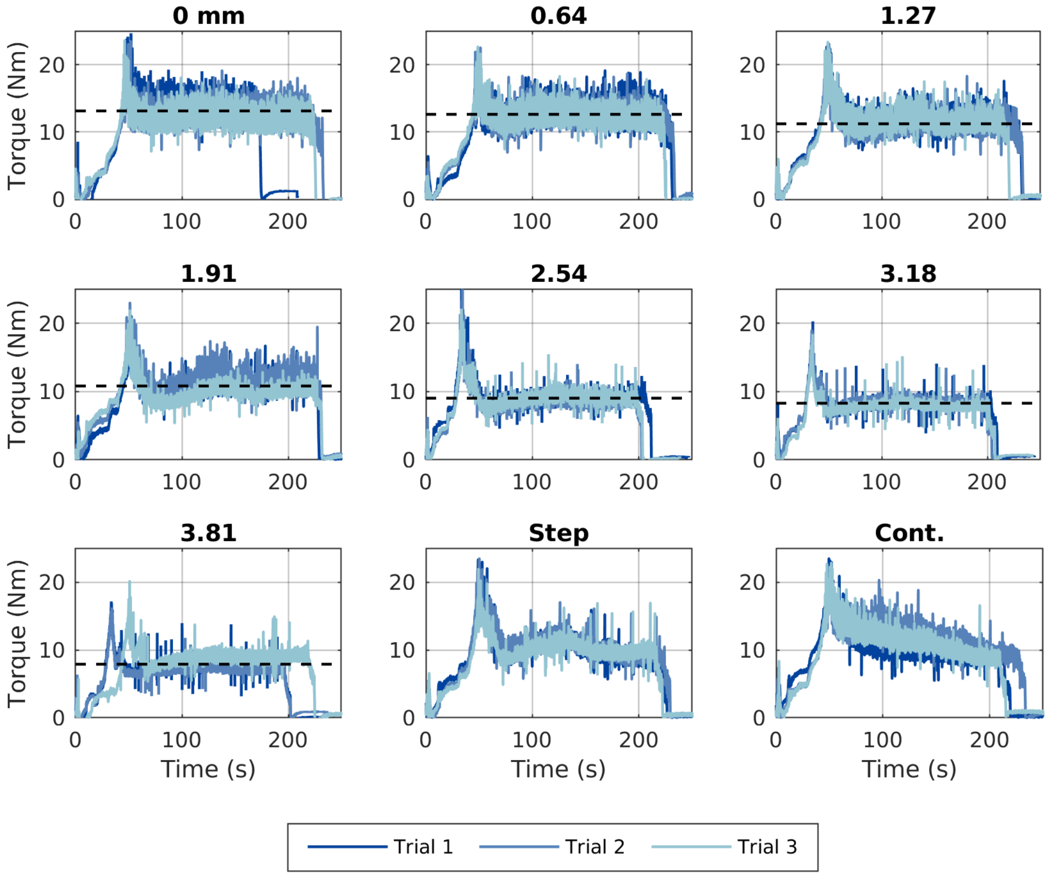

Figure 5.6: Comparison of the measured torque for each groove width during the open loop variable groove width trials. The average torque for each groove width indicated by a dashed line across the each plot.

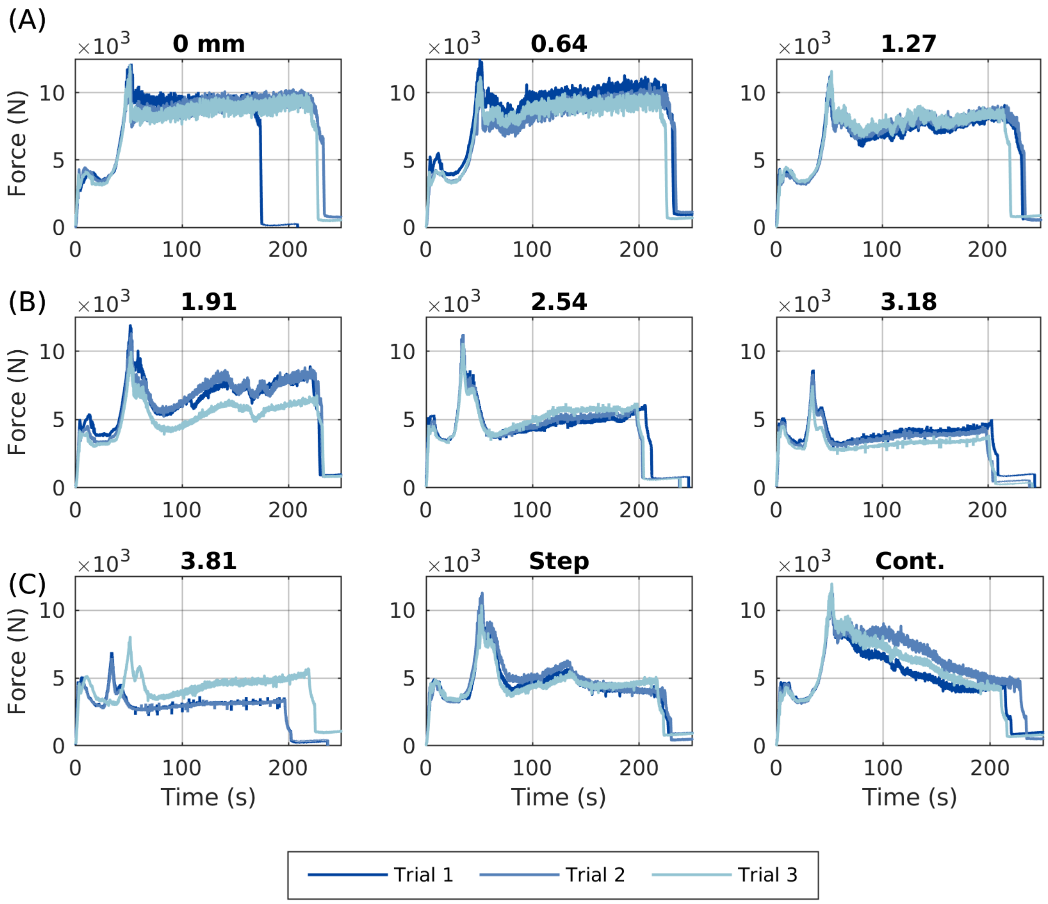

Figure 5.7: Comparison of the measured z-force for each groove width during the open loop variable groove width trials.

decreasing z-force as well. The signal-to-noise ratio for z-force was generally greater than for torque, and the same increase in signal-to-noise ratio for wider grooves can be observed.

5.4.2 Torque Controller

While both z-force and torque showed a strong correlation with groove width, it was decided to develop a torque-based controller. Torque-based controllers can be advantageous for a variety of reasons. The torque output of a spindle could be derived easily and cost-effectively from the input current of the tool spindle. Additionally, redundancy could be easily implemented by utilizing the spindle current measurements in addition to a dynamometer. Longhurst showed that the torque appeared to be less sensitive to temperature than z-force and that it can be easier to measure in the absence of commercial systems [93].

After the visual inspection of all of the positional control welds, the welds with 1.91 mm groove width were thought to have the best surface quality. The average torque during the welds was 11 Nm when rounded to the nearest whole number. Therefore, the reference torque for all welds was set at 11 Nm. It was thought that 11 Nm of torque would provide adequate tool contact across all groove widths.

The surface quality of all 27 torque-controlled welds is presented in Figure 5.8. The torque-controlled welds had better surface quality and lacked the surface voids present in the positional control welds across all of the constant groove width welds. Wider grooves still developed the seam in the surface banding similar to the positional control welds. However, it did not progress to the level of surface void formation. There was an initial formation of defects in both the 3.18 mm and 3.81 mm cases before the torque controller was engaged. After the controller was engaged, the surface defects were eliminated. Trial 2 with a groove width of 3.81 mm, did have excessive flashing and rougher surface banding. This is likely a symptom of over-plunging the tool. Variations of weld width appeared in welds with narrower groove width than 1.91 mm. The width variations indicate oscillations in plunge depth. The surface quality of the welds was best, around 1.91 mm groove width. There were no variations in weld width due to oscillation or seam in the surface banding. All of the step groove welds had good surface quality and lacked visible defects. One of the three continuously increasing groove welds developed a surface void near the end of the weld. However, by the end of the weld, the surface void appears to be dissipating. The other two welds were defect-free and had good surface quality.

The steady-state averages of the data collected from all of the welds are reported

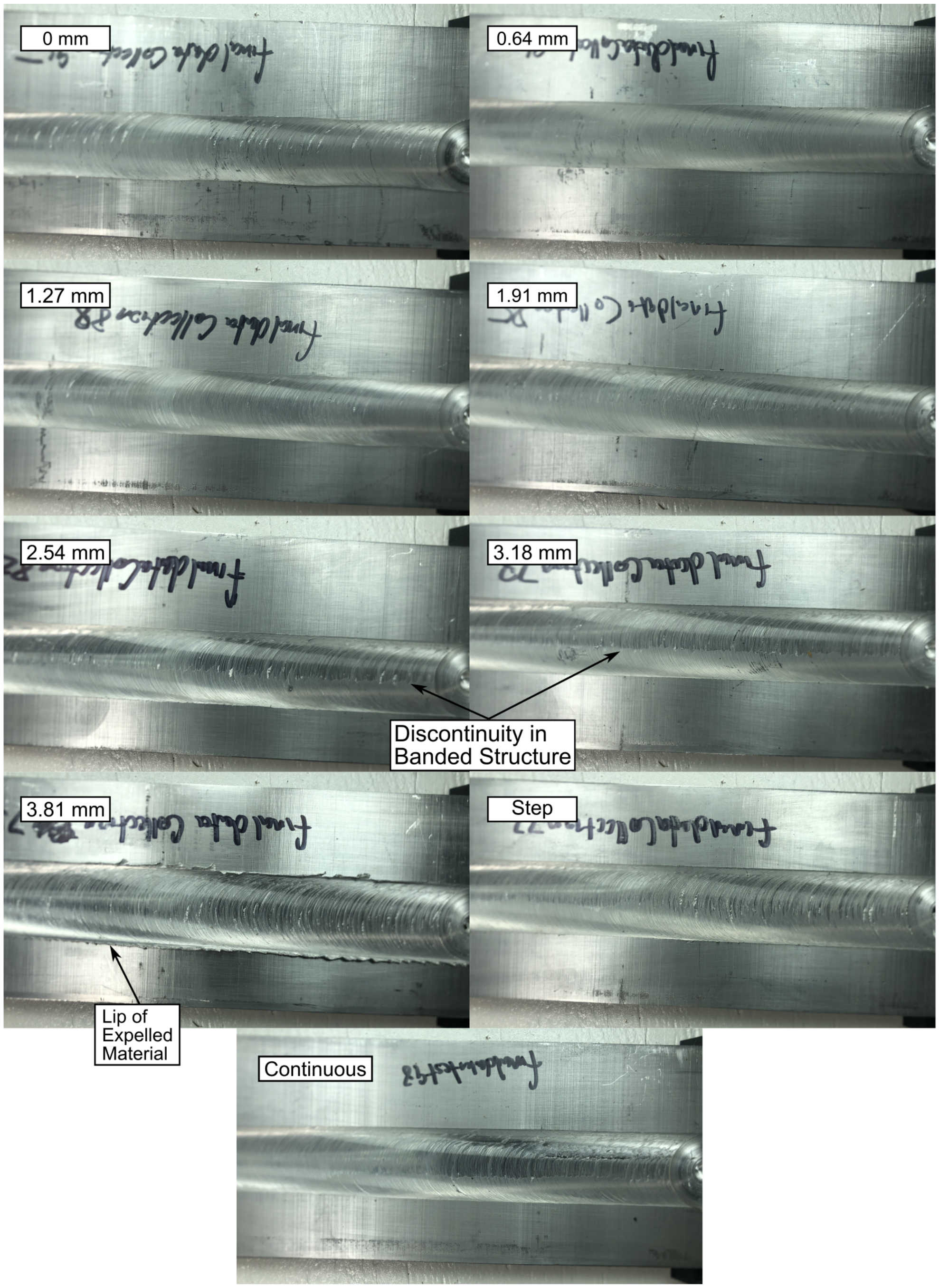

Figure 5.8: Photos of selected welds from the torque-controlled trail.

in Figure 5.9. The average value of both torque and spindle current was consistent for all controlled welds. The average torque value was within ±.1 Nm of reference. The average torque was closest to the reference value at a groove width of 3.18 mm, followed by 1.91 mm. The accuracy with a 3.18 mm groove width was likely a coincidence, but the accuracy at 1.91 mm groove width was largely expected since the torque corresponding with 1.91 mm groove width was selected as the reference. So, the controller should have had to make minor adjustments to minimize error. Generally, groove widths under 1.91 mm resulted in a lower than reference average torque, and groove widths wider than 1.91 mm resulted in a higher than reference average torque, resulting in an average torque that increased with groove width, Figure 5.9A. This result is consistent with what would be expected of steady-state error and inverted initial conditions.

The average z-force still decreased with increasing groove width. Groove widths less than 1.91 mm resulted in z-forces greater than 6 kN, and groove widths greater than 1.91 mm resulted in z-forces less than 6 kN, Figure 5.9B.

There is still a gap in explaining why z-force decreases with increasing groove width. Longhurst examined the differences between torque and z-force for a torque-controlled weld. He concluded that the vertical surfaces of the pin contribute to the weld torque but do not contribute to the z-force according to Nunes' rotating plug model [93, 162]. This effect can be most clearly seen during the plunge, Figure 5.6, 5.7, 5.10, and 5.11. The torque smoothly increases until the shoulder contacts the material surface, while the z-force initially rises when the pin contacts the material surface and gradually decreases as the material softens until the shoulder contacts the workpiece. This missing factor could contribute to the difference. However, it is expected that the effect would be the opposite of the observed. The increase in z-force would follow the increase in plunge depth.

It is more that there is a thermal effect involved. Torque control can also be used to modulate weld input power. Torque can be related to power by $P = \tau\omega$, where P is power, τ is torque, and ω is spindle speed. The result is that welds with lower than positional controlled torques will be cooler, and welds with higher than positional controlled torques will be hotter, thus reducing the material's axial force and shear strength. The material will require less load to flow into the groove with lower shear strengths.

The process of plasticizing, extruding, and forging material each rotation pushes the tool to the advancing and trailing edge in conventional FSW, [163]. For both controlled and uncontrolled welds, the y-force is positive towards the advancing side. However, the x-force transitions from trailing to the leading edge as the groove width widens, Figures 5.5C and 5.9C. The increasing x-force would imply that forging pressures behind the tool dominated the forward welding force with conventional FSW [163]. This explanation does not agree with the decreasing z-force over the same set of parameters, Figures 5.5B and 5.9B. Instead, it is proposed that material thinning around the advancing side of the tool caused differential shoulder contact and caused a net x-force toward the leading edge. The differential contact patches can be seen as a discontinuity in the banded structures in the weld path, Figures 5.4 and 5.8.

The torque vs. time plots for all groove widths and trials is presented in Figure 5.10. The controller was engaged after the plunge and initial ramp to full welding speed, indicated by the vertical dashed line. When the controller was engaged, groove widths narrower than 1.91 mm were above the reference torque and initially overshot the reference value. Then, the torque consistently oscillated through the remainder of the weld, largely staying within 11 Nm ±10%. For 1.91 mm grooves, the controller engaged when the torque appeared to have naturally settled within 11 Nm ±10%. However, An oscillation was induced that dampened out by the end of the weld. The controller was engaged when the torque had settled below the reference torque for groove widths wider than 1.91 mm. While the torque initially overshot the reference

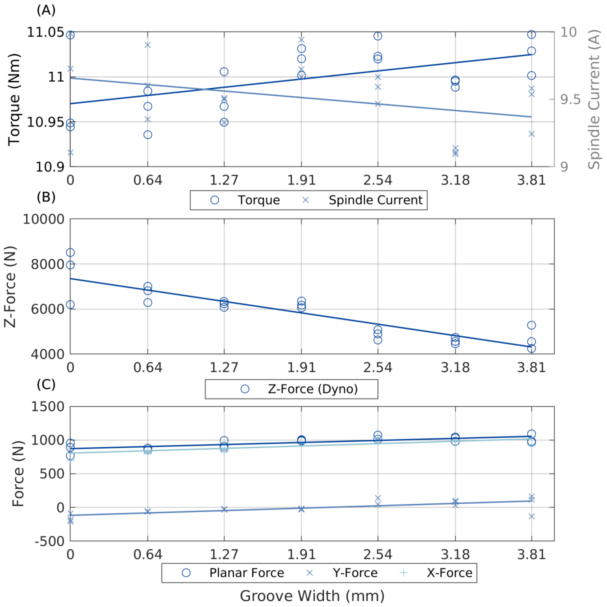

Figure 5.9: (A) Average torque, spindle current, (B) z-force, and (C) xy-forces measured during each trial of the closed-loop groove offset trials. The averages were taken from when the transverse rate reached a steady-state, to the end of the weld.

value, oscillations dampened out quickly, and the torque remained within 11 Nm ±10%.

The step welds demonstrate the capabilities of the torque controller. Initially, the torque oscillated similar to a weld performed with a groove narrower than 1.91 mm. The step can be seen as a quick drop in torque, and after the step, the oscillations dampened out. After 100s, the controller maintained a consistent 11 Nm torque similar groove widths greater than 1.91 mm.

The continuously expanding groove also had excellent consistency maintaining 11 Nm torque through the duration of the weld. All three trails initially overshot the reference torque but remained within ±10% of the reference torque for most of the weld.

The z-force followed the same trends that were identified in the torque signal, Figure 5.11. The oscillations that form after the controller engages can be more clearly seen in groove widths narrower than 1.91 mm. Unlike the torque centered

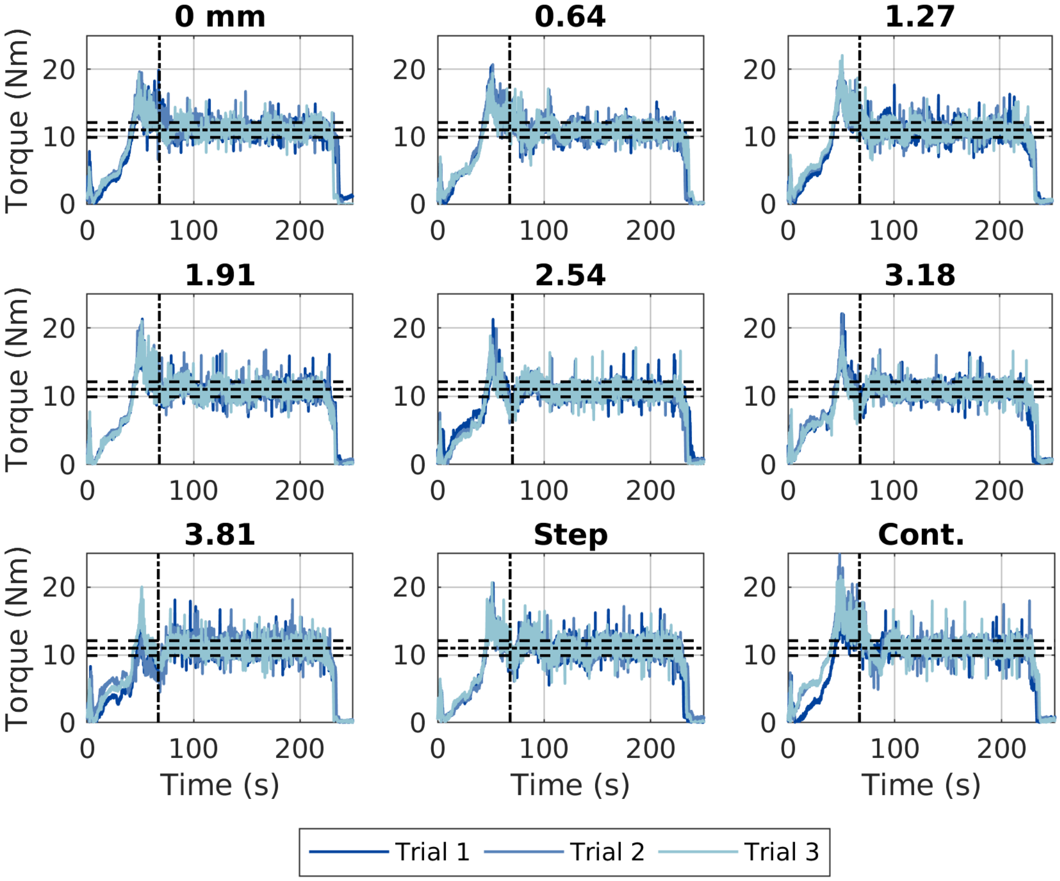

Figure 5.10: Comparison of the measured torque for each groove width during the closed-loop variable groove width trials. The reference torque and ±10% are represented on each plot by the horizontal dotted lines. The time of controller engagement is signified by a vertical dashed line.

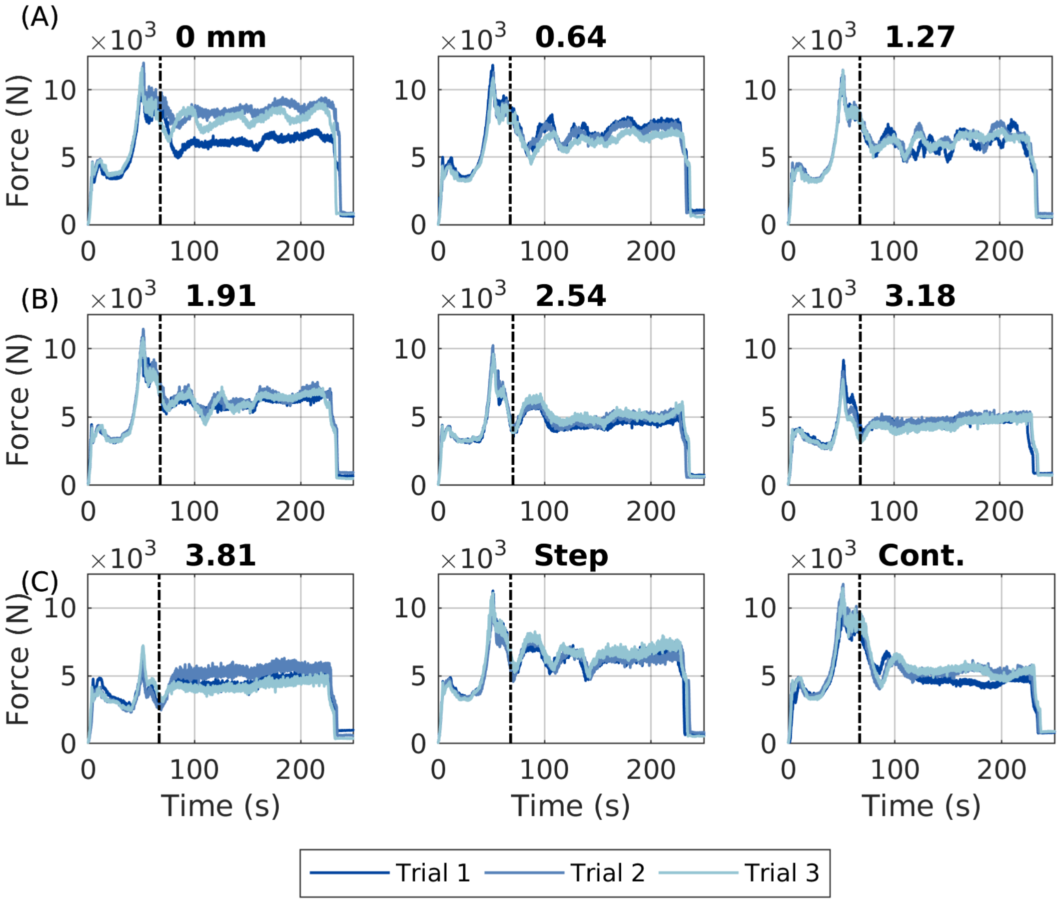

Figure 5.11: Comparison of the measured z force for each groove width during the closed loop variable groove width trials. The time of controller engagement is signified by a vertical dashed line.

around the reference, the z-force decreases as the groove width expands. The z-force is above 5000 N for groove widths 1.91 mm and under, and for groove widths greater than 1.91 mm, the z-force was under 5000 N. The oscillations until the step are mirrored in the z-force for the step weld. The continuously increasing groove width welds remained around 5000 N after an initial overshoot similar to what was observed in the torque.

The change over initial plunge depth was examined to look for trends between the different trials, Figure 5.12. Negative plunge depth represents the tool pulling out of the material, reducing the initial plunge depth. Positive plunge depths represent the

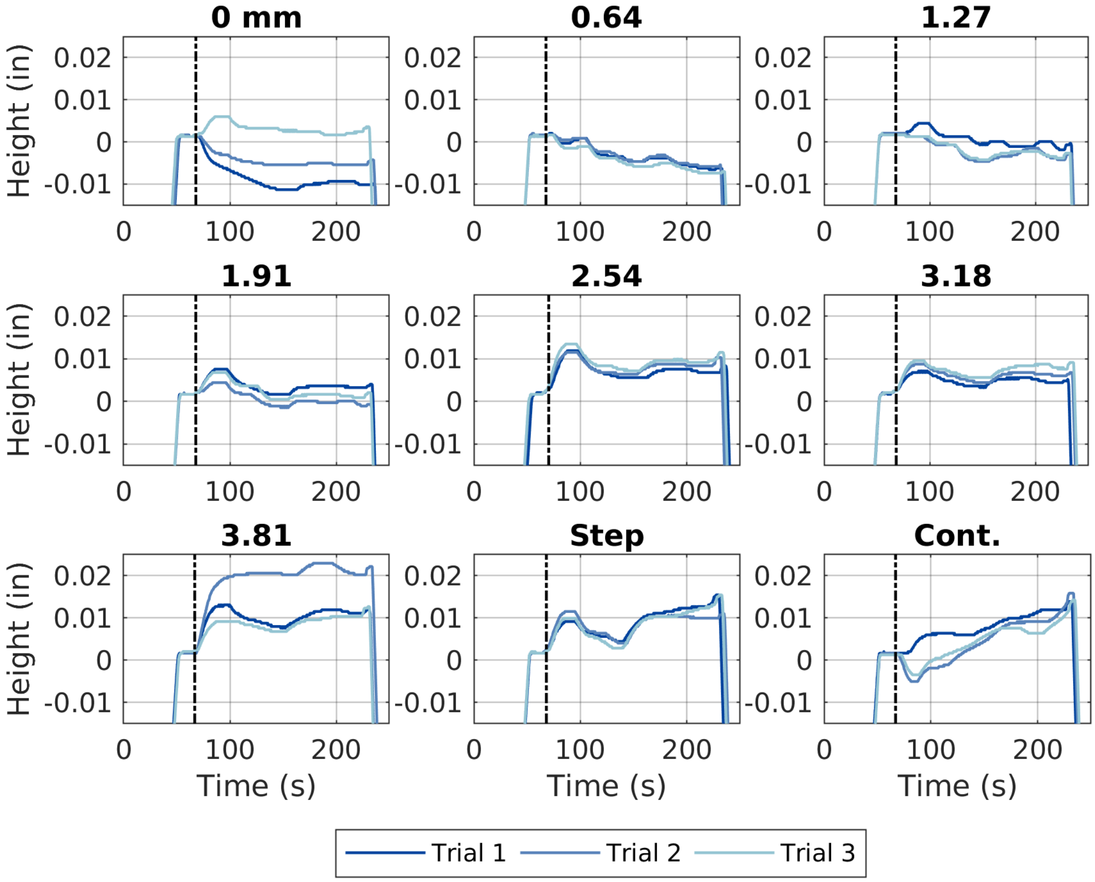

Figure 5.12: Comparison of the measured plunge depth for each groove width during the closed-loop variable groove width trials. The time of controller engagement is signified by a vertical dashed line.

opposite, plunging the tool deeper into the material and increasing the initial plunge depth. Groove widths narrower than 1.91 mm seemed to struggle to find a constant plunge depth before the end of the weld. 1.91 mm groove width required little to no modification to the plunge depth to maintain reference torque after an initial increase in plunge depth. In all welds after 1.91 mm groove width, there is an initial increase in plunge depth as soon as the controller is engaged, followed by a reduction in plunge depth before settling down to a more consistent depth approximately 0.25 mm deeper than the initial conditions. The initial peak in plunge depth is most likely the overshoot of the control system to meet the reference torque value.

Before the step increase in plunge depth, the step groove welds behaved similarly to the constant groove width welds around 1.91 mm in width. The plunge depth was slightly greater than the initial plunge conditions just before the step. After the step was passed, the controller increased plunge depth behaving similarly to a critically damped system. The increased plunge depth settled at a value similar to the 2.54 mm constant grooved welds.

Two out of the three continuously increasing grooves decreased the plunge depth rapidly as soon as the controller engaged. Then, continuously increased plunge depth tracking the increase in groove width. One trial initially increased plunge depth and continued to increase plunge depth through the weld. All three welds did tend to converge during the length of the weld.

5.5 Discussion

5.5.1 Controller performance

The average torques for both open loop and closed loop tests were collected and compared in Table 5.1. The uncontrolled welds decrease in torque sharply at 0.64 mm groove width and begin to taper off around 3.18 mm. The closed-loop welds maintain an average torque within 0.050 Nm of the reference value. The groove depths equal to and wider than 1.91 mm generally had torques above the reference value, and groove depths narrower than 1.91 mm had slightly lower torques than the reference value.

1.91 mm and 3.18 mm groove widths averaged torque was the closest to the reference value for both the torque-controlled and position-controlled welds. It was expected that 1.91 mm groove width would be close since the positional control weld was naturally closest to the reference torque. Therefore, the smallest change in plunge depth was required. The accuracy of the 3.18 mm groove width welds is likely due to a difference between sample and population averages.

Groove width (mm)	Position Controlled (Nm)	Torque Controlled (Nm)
0	13.1377	10.9799
0.64	12.6302	10.9624
1.27	11.2226	10.9742
1.91	10.7927	11.0177
2.54	9.0013	11.0294
3.18	8.2572	10.9934
3.81	7.9022	11.0258

Table 5.1: Average uncontrolled and controlled torque for each groove width

The transient performance of the torque controller can be broken up into three different categories. Under 1.91 mm groove widths, the response of the controller was characterized by steady oscillation in the torque around the reference torque. At 1.91 mm groove width, an oscillation in the torque value was induced when the controller was engaged. The oscillations were dampened out by the end of the weld. Groove widths wider than 1.91 mm initially overshot the reference torque, followed by a much smaller peak on the opposite side of the reference torque. After, the torque converges on the reference torque with little oscillation. These differences in controller performance is likely due to non-linear effects. The welds with groove widths wider than 1.91 mm are being performed with lower input power than the positional control welds, likely resulting in lower temperature welds. Likewise, the groove widths wider than 1.91 mm are being performed with a higher input power than the position-controlled welds. This is likely to introduce some non-linear effects due to changes in the shear strength of the aluminum.

5.5.2 Extrusion Depth

Examination of the extruded material after removing the weld sample from the fixture revealed a relationship between the extrusion height and the groove width. The extrusion height was defined as the maximum displacement of the material from the bottom of the plate. The height of the extruded material was measured at three locations along the length of each weld for both the position-controlled and torque-controlled welds, Fig. 5.13. The height was measured using a digital height gauge with the base on the bottom of the aluminum plate.

Minimal extrusion occurred at 0 mm groove width for the position-controlled and torque-controlled welds. Any extrusion that occurs is largely due to imperfect mating surfaces on the fixture. For the positional control welds, the height of the extruded material rapidly increases as the groove width widens, reaching a peak at 1.27 mm. After the peak, the extrusion height decreases and remains consistent after 1.91 mm. The torque-controlled welds increase in extrusion height to 0.64 mm. Then, remain relatively consistent for the remained of groove widths.

There was high variability in height for extrusion widths less than 1.91 mm for both position and torque-controlled welds. There are two possible sources for the variation in height observed. There was a cyclical torque response for the torque-controlled welds that could have driven variability in extrusion height. Schneider reported two fluctuations were observed in FSW with embedded lead wire. One of the two fluctuations was periodic and tied to the rotation rate of the tool. The second was much slower than the rotation rate of the tool and had irregular periodicity [164]. The variations in extrusion height were more widely spaced than the surface banding. Therefore, The second reported fluctuation might be responsible for the variations in extrusion depths seen at smaller groove widths. These fluctuations might also be responsible for the oscillations in torque and plunge depth observed in the closed-loop welds under 1.91 mm groove width welds.

5.5.3 Spectral Analysis

It was observed that with increasing groove width, the steady-state portion of the weld saw an increase in the signal to noise ratio in both the torque and z-force signals for the position-controlled welds, Figures 5.6 and 5.7. This effect was not observed

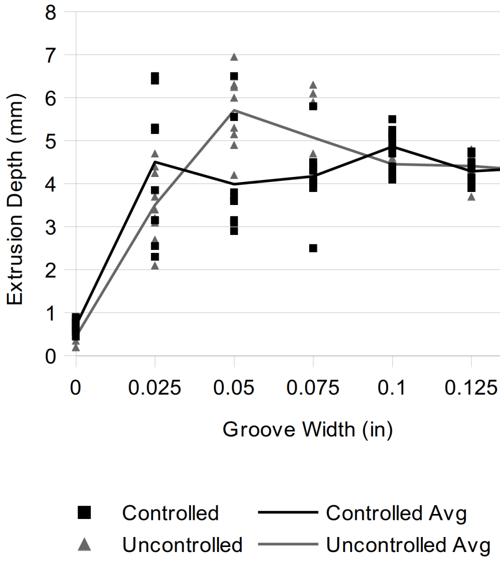

Figure 5.13: Height of the extrusion along three location (Start, Middle, End) of each weld.

in the closed-loop trials 5.10, and 5.11. This effect was further examined further by evaluating the power spectrum of the torque and z-force for each of the welds in the position-controlled welds, Figures 5.14 and 5.17, and the torque controlled trials, Figures 5.16 and 5.17.

The torque and z-force power spectrum were consistent between weld trials at each groove width. A strong peak at 25 Hz dominates both the torque and z-force spectrum for all trials. This peak corresponds to the rotation rate of the tool and is most likely the driving frequency of the weld phenomena. The torque and z-force spectra were largely identical after 25 Hz for all open-loop and closed-loop weld trails. There was a small peak around 33 Hz and 43 Hz and a harmonic of the 25 Hz peak at 50 Hz in the torque and z-force spectra. The region above 25 Hz likely contains little information about the extrusion phenomena, and the peaks in this region are believed to come from outside sources of inference.

The region below 25 Hz can be presumed to be a phenomenon excited by the tool. The power spectrum in this region decreases from a maximum at 0 Hz until

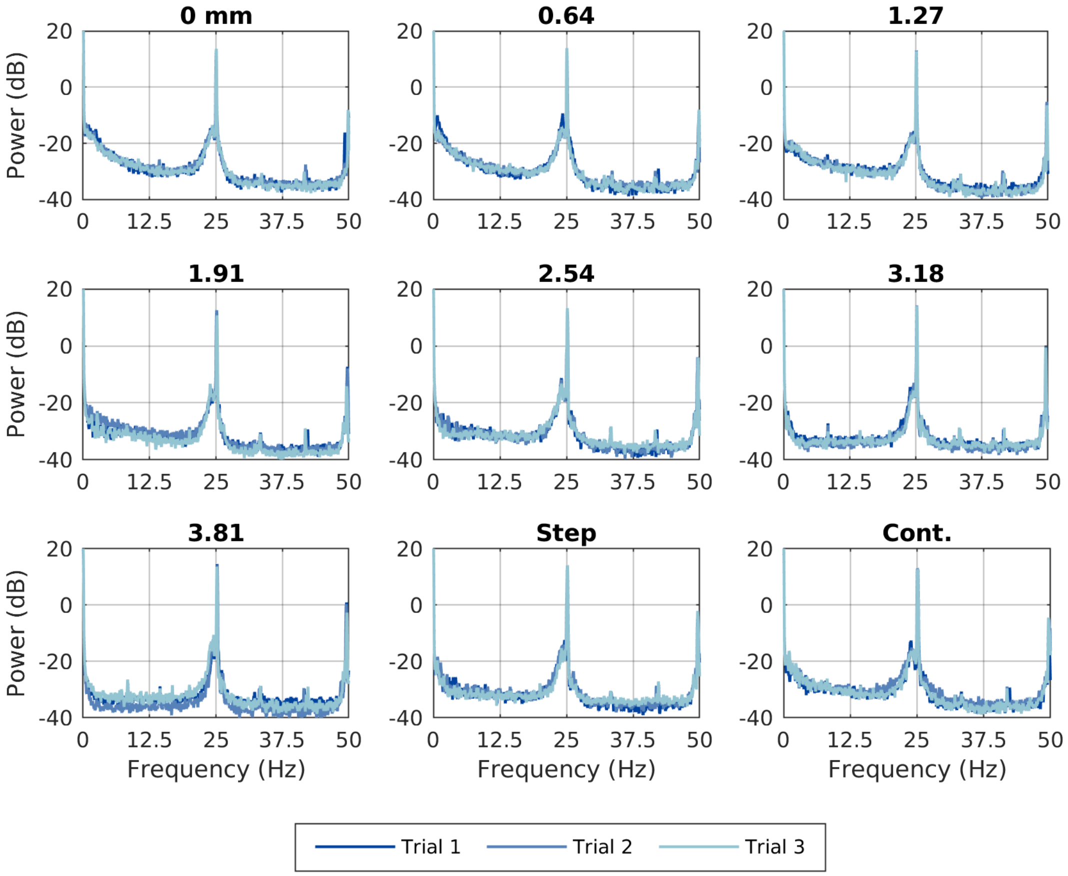

Figure 5.14: Power spectrum of the measured torque during the open loop variable groove width trials. The average power spectrum of each series of three trials has been included.

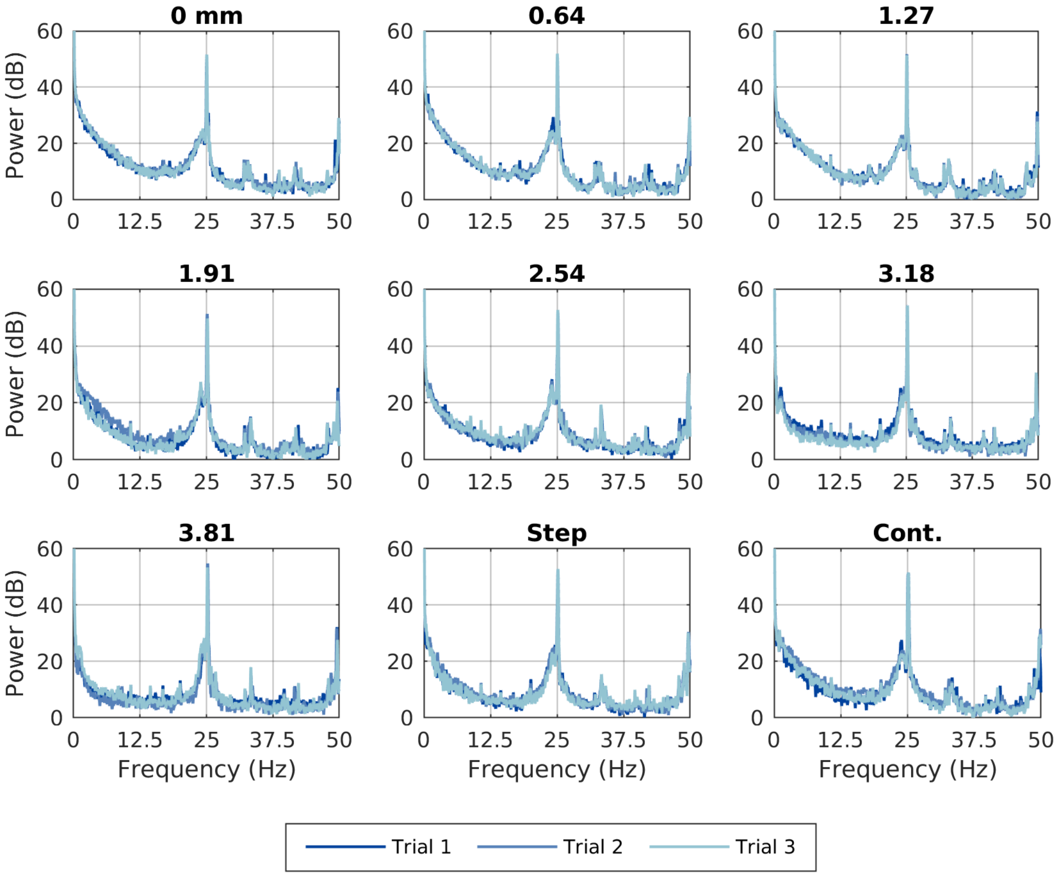

Figure 5.15: Power spectrum of the measured z-force during the open loop variable groove width trials. The average power spectrum of each series of three trials has been included.

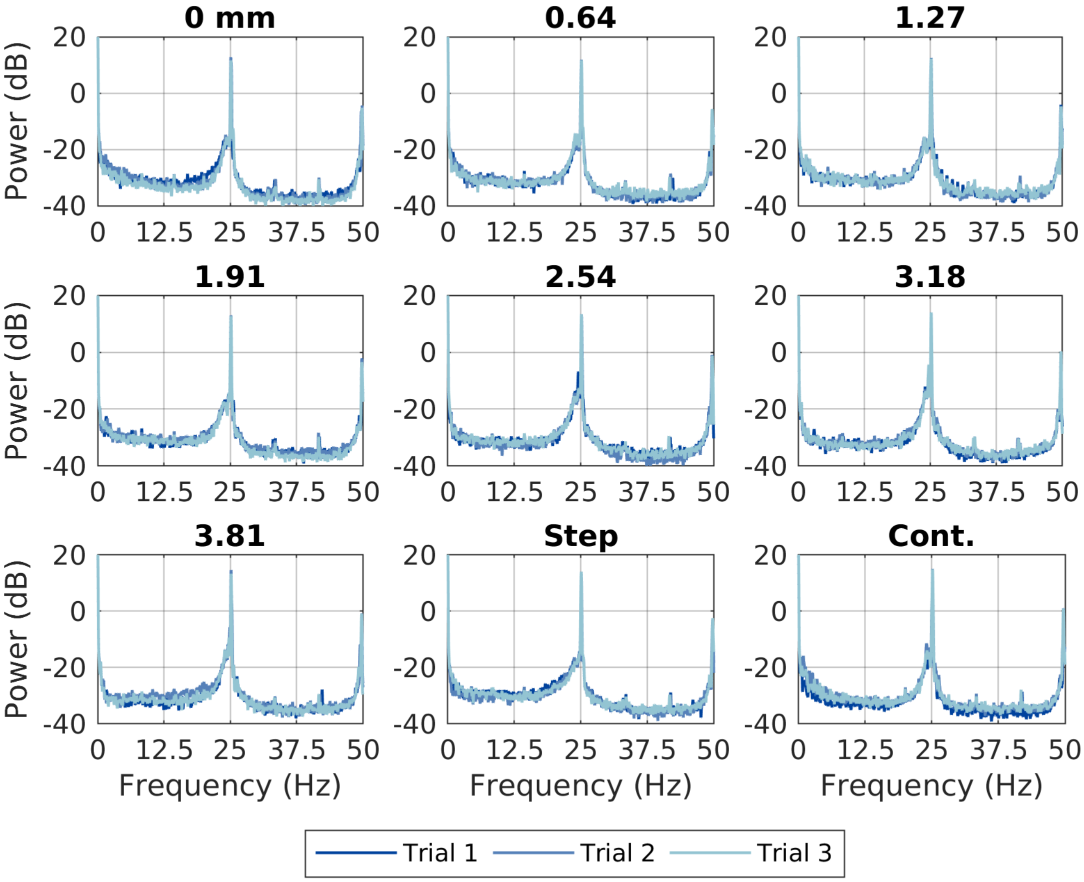

Figure 5.16: Power spectrum of the measured torque during the closed loop variable groove width trials. The average power spectrum of each series of three trials has been included.

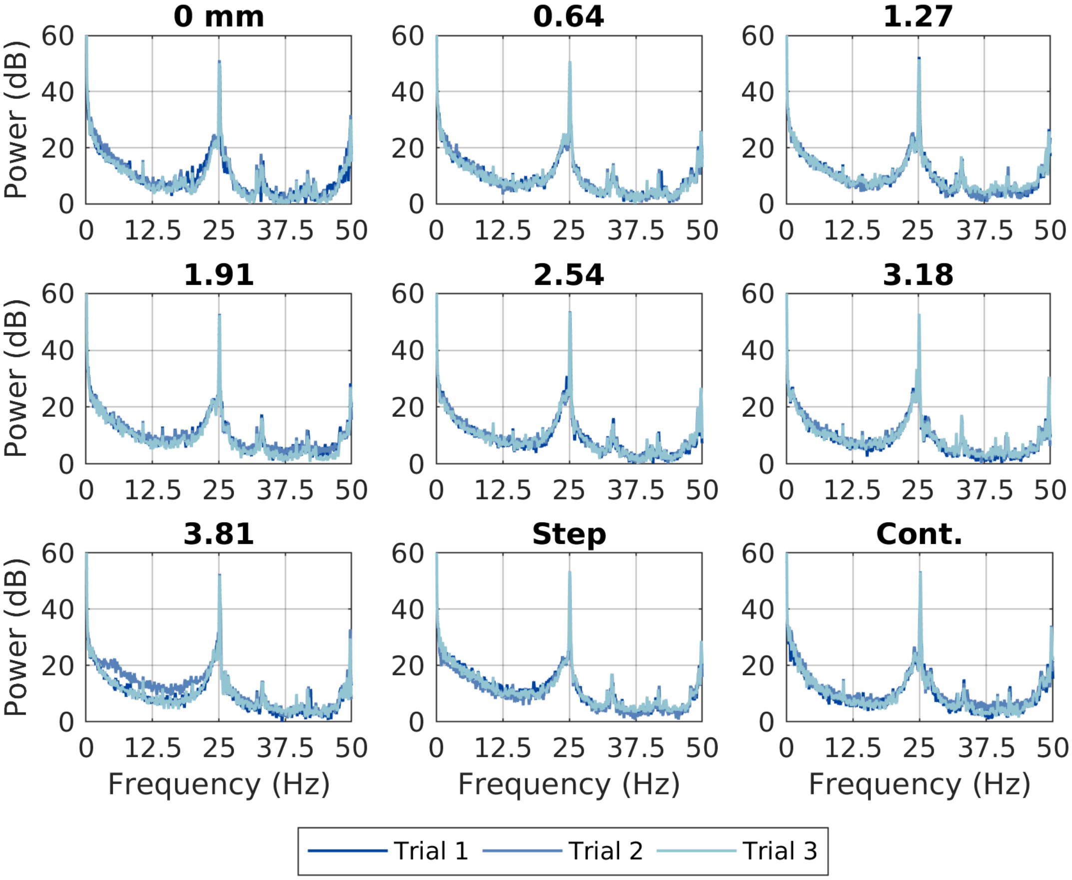

Figure 5.17: Power spectrum of the measured z-force during the closed loop variable groove width trials. The average power spectrum of each series of three trials has been included.

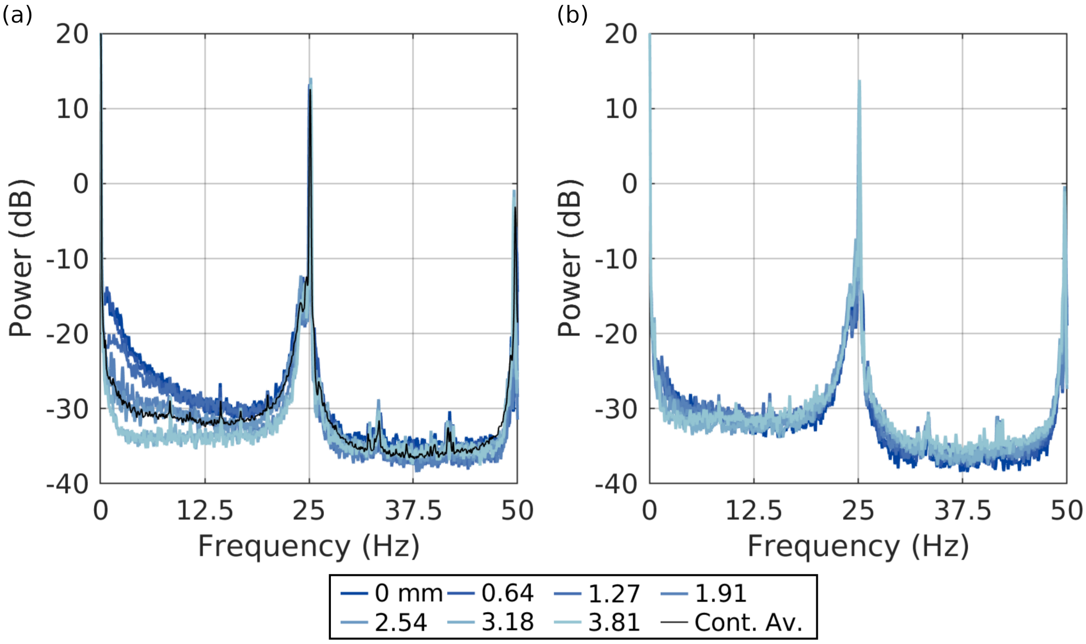

Figure 5.18: (a) Average power spectrum of torque for each groove width during the open loop data collection step. The averages were pulled from Figure 5.14. (b) Power spectrum of the measured torque during the closed loop variable groove width trials. The average power spectrum of each series of three trials has been included.

the 25 Hz peak . The rate of decay of the power spectrum between 0 Hz and 25 Hz increases as the groove width expands during the position-controlled welds. This effect is present in both the torque and the z-force. However, this effect is absent from the torque-controlled welds. The torque and z-force power spectra from all three trials per groove width were averaged to create one curve for each groove width to facilitate comparison between closed and open-loop tests, Figure 5.18 and 5.19. The averaging helped to remove random fluctuation and highlight trends.

The change of the spectrum between 0 and 25 Hz for each groove width with position control can be seen in Figure 5.18a and Figure 5.19a. With each increase in groove width, the power spectrum decays faster. However, the torque-controlled welds saw a much different effect. The power spectrum of the torque and z-force for all welds have converged to a single profile with no real trend between different groove widths, Figure 5.18b and Figure 5.19b. Interestingly, even though the z-force

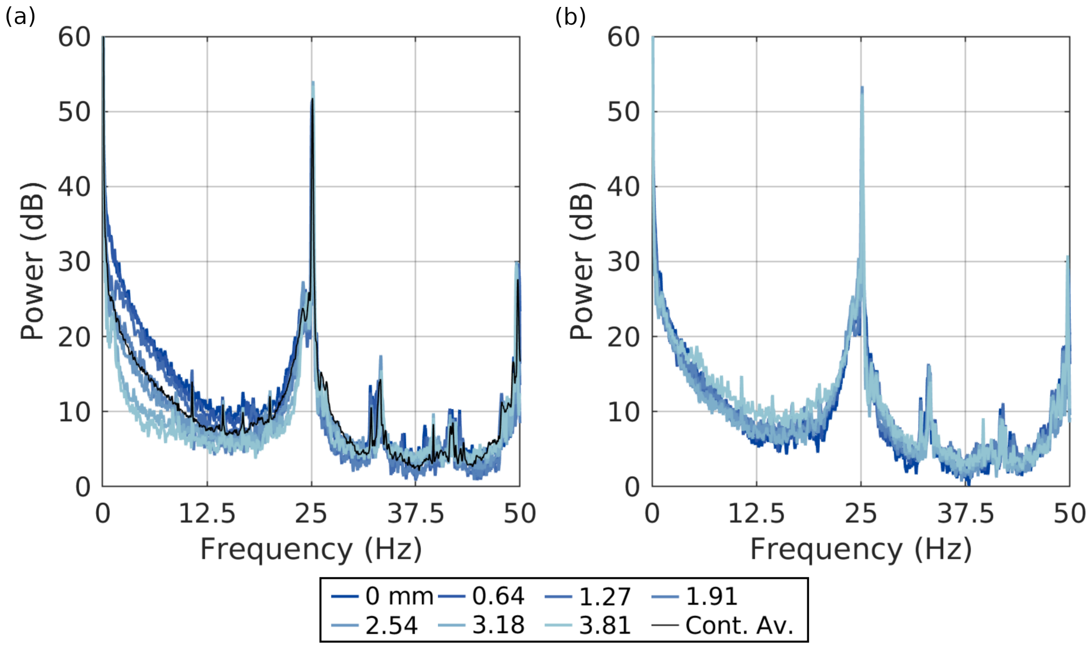

Figure 5.19: (a) Average power spectrum of z-force for each groove width during the open loop data collection step. The averages were pulled from Figure 5.15. (b) Average power spectrum of the z-force for each groove width during the torque controller data collection. The averages were pulled from Figure 5.17.

was not directly controlled and was still proportional to groove width after applying the torque controller, the power spectrum still converges to a single profile.

Since the torque and z-force power spectra for all the torque-controlled welds seemed to converge on a single profile, the spectra were averaged across all groove widths and plotted alongside the positional control spectra. The averaged torque-controlled spectra is represented by the blue line in Figures 5.18a and 5.19a. The torque and z-force averaged spectra are very similar to the 1.91 mm position-controlled frequency response. This agreement is sensible since the torque at 1.91 mm was used as the set point for the control system.

The fact that torque control of the plunge depth minimized differences in the power spectra across different groove widths supports the hypothesis that the material-tool interaction largely drove the differences in the frequency response. Likely, the variations in spectra were not driven by changes in the welding fixture. Therefore, the power spectrum of the torque and z-force could also be used as indicators of tool engagement and could be used for in-process monitoring and control of FSE welds.

Variation in the power spectrum during the step and continuously increasing groove width welds could not be displayed due to a lack of data at a single groove width. However, The effects of a changing signal-to-noise ratio can still be seen in the processing forces of the welds. The signal-to-noise ratio of the position-controlled step welds appears to be minimally affected by the increase in groove width. The position-controlled continuous welds did have some reduction in the signal to noise ratio of the torque during the weld, Figure 5.6. The torque-controlled welds of both scenarios appear to maintain a consistent signal to noise ratio, Figure 5.10. Future work will focus on longer welds with more gradual transitions between groove widths and increasing to faster sampling rates to further examine the effect of groove width on the power spectrum.

5.5.4 Outliers

The positional and torque-controlled welds were very consistent between trials at a groove width. However, some trials differed from the others in one or multiple measured processing forces. These outliers were examined to relate the measured forces to observed weld quality.

First, the outliers of the position-controlled welds were examined. Both Trial 3 at 1.91 mm and Trial 3 at 3.81 mm had significantly different z-force from the other two trials in the series. Trial 3 at 1.91 mm measured z-force was significantly lower than the other two, and Trial 3 at 3.81 mm measured z-force was significantly higher than the other two in the series. The differences in the surface quality of the three trials at 1.91 mm are minimal. However, Trial 1 and Trial 2 of the 3.81 mm welds resulted in void formation, and Trial 3 did not, Figure 5.4.

Second, the torque-controlled welds were examined for outliers. Trial 1 at 0 mm groove width decreased the plunge depth considerably, resulting in the lowest average z-force between the three trails. Trial 3 increased plunge depth resulting in the second-highest average z-force between the three trials. Interestingly, Trial 2 decreased the plunge depth less than in Trial 1, but Trial 2's average z-force was slightly higher than of Trial 3. This is contrary two what would be expected from the assumed relationship between plunge depth and z-force. Trial 1 had the best surface quality, and Trials 2 and 3 had an increased surface roughness.

Trial 2 at 3.81 mm groove width had a deeper plunge depth than the other two welds, and the weld appeared to be over plunged with some flashing and rough surface quality. The average z-force was significantly higher than for the other samples, and the region between 0 to 25 Hz in the power spectrum was higher than the other two trials.

While the toque was visually consistent between different weld trials, the z-force and plunge depth revealed several outliers from the other two trials. Trial 1 at 0 mm groove width had a significantly lower z-force than the other two welds, around 6 kN as compared to the 8 kN for the other two trials. Also, trail 3 increased plunge depth while 1 and 2 decreased plunge depth. Trial 1 has the best surface quality without any artifacts from over-plunging. Trial 2 at 3.81 mm groove width was another outlier. Trial 2 has an average z-force of approximately 5 kN, while the others averaged significantly less. Trial 2 at 3.81 mm groove width increased plunge depth to double that of the other two trials. In this case, the outlier appears to be over plunged and has a terrible surface quality.

The source for the outliers in both positional and torque-controlled welds is not known. Differences in initial conditions such as the temperature of the tooling or workpiece leading to differences in processing temperature might have caused the observed variation. The accuracy in the positioning system might have also caused the outliers. However, these outliers were identified by one or more of the collected processing forces and, in some cases, the power spectra of the processing forces. Future automation systems could flag wields for further inspection or control another processing parameter to eliminate the outliers.

5.6 Conclusion

It has been demonstrated that one set of processing parameters can produce a weld free of surface defects at one groove width but will produce surface voids and defects with an increased groove width. Material is lost from around the tool to fill the grove, resulting in corresponding decreases in torque and z-force and a change in the x-force.

A controller was developed and tuned that uses torque to control plunge depth. The controller successfully eliminated defects formed at wider groove widths with the same initial processing parameters. The controller maintained an average torque reading within ± 0.1 Nm of the reference torque. The torque controlled welds also reduced changes in z-force and x-force with increasing groove widths. The direction of the x-force can be tied to defect formation with positive x-force corresponding with the appearance of discontinuities in the surface banding of the weld.

Changes in the power spectrum for torque and z-force where the wider grooves resulted in less power between 0 and 25 Hz were found. The decrease is likely due to a change in the material flow around the weld tool.

5.7 Acknowledgment

All funding for the project was provided through the Tennessee Space Grant, NNX15AR73H.

CHAPTER 6

Through the Tool Following of Friction Stir Extrusion Lap Welded Joints

6.1 Abstract

Friction Stir extrusion requires positioning the weld tool over a preformed groove that is obscured under a second lapped sheet. The lapped sheet eliminates the possibility for optical sensing techniques. The current state of the art utilizes a minimum force tracker with pre-programmed path directions. First, this paper examines the differences in processing forces at multiple offset locations from the joint center. Then, A speed-controlled, multi-directional seam tracking control system is developed and demonstrated for both perpendicular offsets of 6.35mm (0.250") and angular misalignment of 10 degrees.

6.2 Introduction

Friction Stir Extrusion (FSE) is a relatively new derivative technology of Friction Stir Welding (FSW). It has been put forth as a technology to join dissimilar materials [34]. The process uses the severe plastic deformation present in FSW to extrude material into dies and preformed geometries. One side of an interlocking geometry is formed in the first material before welding to join two dissimilar materials. Then, the second material is lapped over the first, and the tool passes over the formed geometry. The second material is extruded into the geometry, forming the second half of the geometry and locking the two materials together. The first material is normally designated as the 'harder' material. This material is more problematic to weld due to abrasiveness, high yield strength, hardness, etc.; welding it directly might require more force or tools made from exotic material. The second material is called the 'softer' material. It is the material that can be extruded more readily and poses less issues to welding. A preformed geometry is milled into the 'harder' materials in common practice. However, It can be formed in other ways, such as bending [157].

This process has several benefits over conventional welding of dissimilar materials, since the tool can completely avoid contact with the hardest of the two materials. The formation of brittle intermetallics is effectively eliminated, and the tool wear can be greatly reduced. Therefore, tools can be made out of more conventional materials like tool steel when joining to and abrasive material reducing tooling cost and complexity.

Friction stir welding has been shown to be controllable by using processing forces and temperature as feedback signals [92, 165, 93, 91, 96]. Processing forces are defined as the forces and torque the welding tool exerts on the material during the weld.

Seam tracking for FSE is a currently researched topic, and the process poses a unique challenge to implementing seam tracking. In conventional FSW, the seam can be externally observed and tracked through vision-based techniques, like other welding techniques.

The process has been demonstrated with aluminum/mild steel joints [34], aluminum/graphite [158], and aluminum/titanium joints [156].

Seam tracking allows for flexibility in seam alignment/fixturing and for better quality joints adapting to manufacturing variations. This technology is becoming common in robotic welding systems. Seam tracking can be achieved through different sensing methodologies based upon the used welding technology. Conventional welding technologies most often use arc sensing or visual techniques to follow weld seams [166]. Vision and laser-based systems have also been demonstrated as a method to measure tool deflection of robotic arm for friction stir butt welds[99]. However, FSE is used to join two lapped materials, where the top of the two lapped materials completely obstructs the groove from line of sight. The alignment between the tool and pre-made groove geometry is critical for a sound joint.

Seam tracking techniques that utilize processing forces to infer the location of the groove have also been demonstrated for FSW and FSE. Fleming et al. demonstrated the ability to detect obscured features through axial force measurement. Lateral misalignment of a T-joint was predicted through measurement of the processing forces. This was accomplished by leaving voids in the fixturing set up on either side of the rib. When misaligned, material would be extruded into the voids reducing the processing forces [100]. The difference in processing forces due to extrusion opened the way for through-the-tool tracking systems that function by following a path of minimum or maximums of processing forces.

A series of controllers were developed that utilize the change in processing forces to make extrema trackers. The tool follows a cyclical path to ”scan” across the material’s surface to determine the location of extrema. The cyclical path is created out of the combination of two different paths. The base path is the center of the weld and the estimated groove center location. It defines the forward motion of the tool. The overlayed path is plotted on top of the base path to form the cyclical scanning away from the base path. Both sinusoids and trapezoids have both been used at the overlayed path. The scan over the material’s surface enables the controller to identify the extrema. Then, the controller modifies the base path to align the weld with the tracked extrema. Fleming et al. later used the developed fixture setup to demonstrate tracking of T-joints through comparing axial force at the extents of a trapezoidal path [167]. The same process was extended to lap joints [101]. Gibson et al. used a trapezoidal overlayed path with discrete lateral steps of the base path to track the void between two sealant beads in a lapped FSW. The controller attempted to track the minimum axial force by averaging the processing force at each flat of the trapezoid and comparing the average from the previous flat on the other side of the base path. The base path could then be stepped in the direction of lower average force [168]. Reynolds used a similar control system to track FSE joints and adapt to an initial offset between the weld path and preformed geometry. A sinusoidal overlayed path was used to eliminate discontinuities that could occur at the sharp corners of the trapezoids. Discrete steps of the base path were used to align the path with the preformed geometry [103].

Past Weave tracking systems had potential shortfalls that could have limited their application and accuracy. they did not control welding speed when following the combined base and overlayed path. Therefore, the total weld speed was variable throughout the weld, slower at the peaks of the cyclical path and faster near the zero crossings of the path. The varying speed could have added extra dynamic forces to the data.

One way to minimize the effect of the speed changes is to use a trapezoidal path where the tool dwells at the furthest lateral displacement from the base path, limiting data collection until the tool was moving parallel to the base path. Trapezoidal paths are used in some of the prior work. The collected processing forces could be compared from the dwell at either side of the base path and used to align with the groove. The time spent crossing from one offset location to the other is not used to determine the feature's location. The trapezoidal path results in the tool spending a large amount of time away from the base path. This could be disadvantageous with FSE, where the tool has to extrude material into a groove to form a sound joint.

The prior seam trackers modified the base path in discrete offsets perpendicular to the heading. The base path only moved along the transverse axis except for the discrete offsets. This limited the base path to moving in only one direction. The controller could not align the base path to angular misaligned groove or follow a continuous turn to move in a different direction.

The step size was also fixed. The fixed step size capped the reaction speed of the controller and limited the precision of the alignment between the base path and groove.

To solve these issues, this paper details the development and implementation of a novel weave tracking system that utilizes a new approach to motion and directional control. First, a methodical data collection approach is taken to better understand the relationship between distance offsets from the groove and processing forces. The gathered information was used to develop a sinusoidal, weaving tracking controller and evaluate it's affects on the measured processing forces. The new motion controller produces a smooth, continuous, and speed-controlled sinusoidal path that allows the steering through directional changes, not offsets.

Two different directional controllers are examined. The first controller functions by summing the forces experienced by the tool on either side of the base path. If the summations are unequal, then the system can modify the direction of the current path to turn toward the lesser of the two averages. The second control system projects where the groove will be by drawing straight lines through the minimum locations. Then, the base path can be steered towards converging with the projected path. Both the control systems allow for continuous directional changes where the magnitude of the directional change is correlated to the estimated distance from the minima.

6.3 Methods

A series of welds were performed to determine the relationship between processing forces and the offset from the groove centerline. Offsets were defined by the direction the tool was moved: advancing or retreating side and were measured from the centerline of the groove to the center of the tool. An offset to the retreating side was defined as the movement in the negative y-direction, and offsets to the retreating side will be measured as a negative number. When the tool is offset to the retreating advancing side, the groove relatively moves to the advancing side. The opposite is true when the tool moves to the advancing side. Three welds at 9 different offsets were preformed. Four different offset positions to both the advancing and retreating side, 0.635mm (0.025”), 1.27mm (0.050”), 3.18mm (0.125”), and 6.35mm (0.250”),

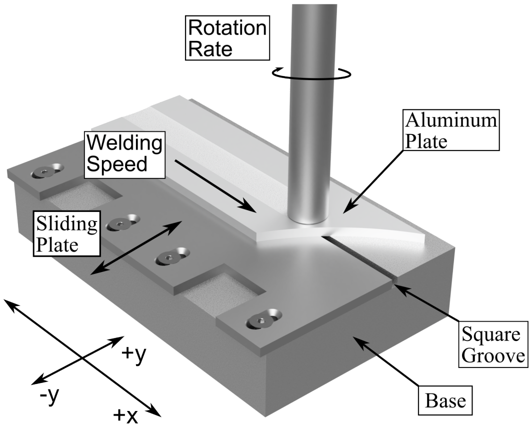

Figure 6.1: Square groove extrusion fixture utilized for this project. The fixture provides a 6.35mm (.250") deep groove that is adjustable between 0mm and 6.35mm (.250") in width.

and one directly over the groove were selected.

All the welds used a uniform groove width of 2.54mm (0.1"). The processing parameters were held constant through all welds, 5.6mm (0.220") plunge depth, 7.6cm/min (3 ipm) welding speed, and 1500 rpm rotation rate.

The welder used is a Milwaukee Model K milling machine. The machine has been modified to motorize all three axes and to instrument for positional and force feedback. The welder is run by a custom real-time control system run on Matlab Simulink.

A special welding fixture was used in place of the normal bottom plate to save consumables and improve repeatability, Figure 6.1. The fixture featured a square groove that could be adjusted from 0mm to 6.35mm (0.25") groove. The fixture could replicate the extrusion characteristics of FSE without forming an interlocking joint. Thus, the fixture could remain affixed to the machine table and each extruded sample removed. Therefore, the variable of positioning the grooved steel plate on the table for each weld could be removed. Special care was taken to ensure that the tool path was parallel to the groove by indicating in the fixture using dial indicators.

The welds were visually inspected to identify the depth of the extrusion and surface defects. The processing forces were measured at 100 Hz via a Kistler rotating force dynamometer. The spindle current was also recorded during the weld. The processing forces were averaged from 25.4mm (1”) beyond the plunge until the end of the weld. The delay was to remove any effects from the plunge and the transverse speed ramp up. The averages, as well as the time response of the processing forces, were analyzed. All processing forces were passed through a low pass filter with a cut-off frequency of 23 Hz. The filter assisted in eliminating any noise induced by external sources. The filtered processing forces are used when plotted against time, but the unfiltered processing force was used to calculate averages.

Within this paper, the x-direction is aligned with the transverse axis of the welding table, and the y-direction is aligned with the lateral direction, Figure 6.1. The direction of the base path is the propagation direction of the weld path. The direction of propagation does not have to be parallel with either the x or y-direction.

The weaving and directional changes during these welds make global definition of advancing and retreating sides ambiguous. The weaving causes the traditionally defined advancing and retreating side to be in-front occasionally and behind the weld heading. Therefore, the base path will divide the sinusiod into two sides. The positive side will be defined as the side where the traditional advancing side is on the outside of the sinusoid. Similarly, the negative side is where the traditional retreating side is outside the sinusoid.

The control system consisted of a motion controller and a directional controller.

6.3.1 Motion Controller

The motion controller contains a path generation algorithm that modifies the current location on the base path by iteratively adding heading time the elapsed time. Additionally, the generated sinusoidal overlayed path is not plotted on the coordinate axis system defined by the welding table. Instead, it is plotted on a coordinate axis system attached to the tip of the base path. Therefore, the oscillations remain orthogonal to the base path, even when the base path is steeply angled compared to the original heading. The whole path is speed controlled to prevent additional sources of uncertainty in force measurements.

The core of the motion control system is the path generation. The path generation consists of base path and sine wave overlay generation. The base path is iteratively solved by adding on a directional heading to the prior heading. The base path is then iteratively solved for a pseudo time variable:

$$\vec{r_b}(u) = \vec{v}(\theta)_b \delta u + \vec{r_b}(u-1) \tag{6.1}$$

where,

$$\vec{v}(\theta)_b = \begin{bmatrix} \cos\theta \\ \sin\theta \end{bmatrix}. \tag{6.2}$$

θ is the directional term and it is used by the directional controller to steer the path.

The path generation maintains the sinusoidal weaving perpendicular to the current direction by rotating and translating a coordinate axis system to the current position of the base path. The normal, tangent, and current positions of the base path are used to construct the rotation matrix to the new coordinate system. The following equation can then be used to evaluate the combined overlayed and base path:

$$\vec{r_o}(u) = R \begin{bmatrix} 0 \\ A\sin(\omega(u+\phi)) \end{bmatrix} \tag{6.3}$$

where,

$$R = \begin{bmatrix} \cos\theta & -\sin\theta & r_b(u)_x \\ \sin\theta & \cos\theta & r_b(u)_y \\ 0 & 0 & 0 \end{bmatrix}. \tag{6.4}$$

The Equation 6.3 allows for the amplitude, A, phase ϕ, and frequency, ω, of the wave to be controlled. At the start of the weld, the phase is adjusted so that the sinusoid starts at a zero-crossing, and the amplitude is gradually ramped from 0 to the final value. Both adjustments are necessary to smoothly start the controller and avoid damage to the machine during startup.

The constant speed was achieved by evaluating Equation 6.3 each iteration of the controller for a pseudo time, u, to maintain a constant path arc length. This is done in practice by adjusting the step size of the pseudo time to maintain a constant change in arc length per time step [169]. The governing equation,

$$\sigma = \left|\frac{d\vec{r}}{du}\right| \frac{du}{dt}, \tag{6.5}$$

is solved iteratively for $\frac{du}{dt}$. The path length, σ, is constant and determined by the target speed of the system. Thus, the next value of , u, for the time step can be determined.

The amplitude of the sine wave, the frequency of the sine wave, and the welding speed have control over the update rate of the controller and the forward propagation of the weld. Increasing the arc length of the path can slow down the forward propagation of the weld and slow down the update rate of the directional controller since the motion controller is speed controlled and an update the heading can only occur after one peak to peak sweep to identify the minima. The higher frequency or higher amplitude both increase the arc length of the path. An increased amplitude requires more movement perpendicular to the propagation direction and requires the tool to transverse greater distances between peaks. So, a wider area can be covered, looking for a minimum force at the cost of slower temporal updates to the directional controller and slower forward propagation. Similarly, increasing the frequency of the sine wave increases the density of the weaving, causing the tool to transverse greater distances for any forward movement. The increase in frequency increases the update rate to the directional controller but decreases the forward propagation. Finally, increasing the welding speed will increase both the forward propagation and update rate of the controller. Increasing the speed should have similar considerations as increasing the speed on conventional FSW, such as optimized processing windows for the material and machine load.

6.3.2 Directional Controller

The directional controller interprets the processing force data to infer the location of the minima resulting from the preformed geometry and change the path of the weld to center over the geometry—the controller interfaces with the path generating algorithm through the direction, θ. The directional controller can continuously adjust the direction of the path propagation. The greater directional control should result in better alignment with the preformed geometry, especially when the initial direction is angled with respect to the preformed geometry and the ability to follow curved groove profiles.

The controller used in the final welds had to meet multiple requirements. The controller had to have 2-dimensional directional control and not be limited to 1-dimensional offsets to align with the minima location. The controller had to produce paths that were achievable by the welding machine without causing permanent damage to welding equipment or compromising safety. Finally, the controller had to remain stable under disturbance and noise present during welding.

Prior work focused on an absolute magnitude of forces experienced [100, 168, 103].

In this paper, two control methods were tuned and evaluated using a simulation based on from the data collected from the offset weld set. The first controller was a PID loop controlling the heading based upon the difference between averaged forces. The second was a first-order minima path projection method. They were both simulated under a variety of circumstances, including initial offset step, angled, and circular paths. Ultimately the PID controller was chosen to perform physical welds due to its greater ability to reject noise.

The tested controller had several challenges to overcome for effective implementation. A conservative set of weaving parameters, amplitude, frequency, and welding speed, were chosen to maintain safety and produce a good raster pattern along the base path. Therefore, the update rate of the controller is relatively slow compared to the propagation speed and processing force sampling rate. A comparatively long distance will have been traveled, and many samples will be collected before one complete period of the sine wave is completed. The slow update speed creates multiple issues for effective implementation.

The first controller is a PID-based controller. The chosen processing force signal was summed when above and below the path center. During each period of oscillation, the sum of each zero-crossing was compared. The difference between the two averages served as the error signal to the PID controller. The resultant value was added to the heading from the prior iteration. Also, the PID controller had to update twice per period since the PID controller's sampling rate was tied to the period of the sinusoid. Otherwise, the system would wind up due to a lack of new data. An example of the controller's function is displayed in Figure 6.2.

The second controller works off a prediction of the future minima location. The controller is a first-order prediction, and the last two points of minimum processing force are saved and a line drawn between them is used to predict the future groove location. The minimum points were collected during each peak to peak sweep. A

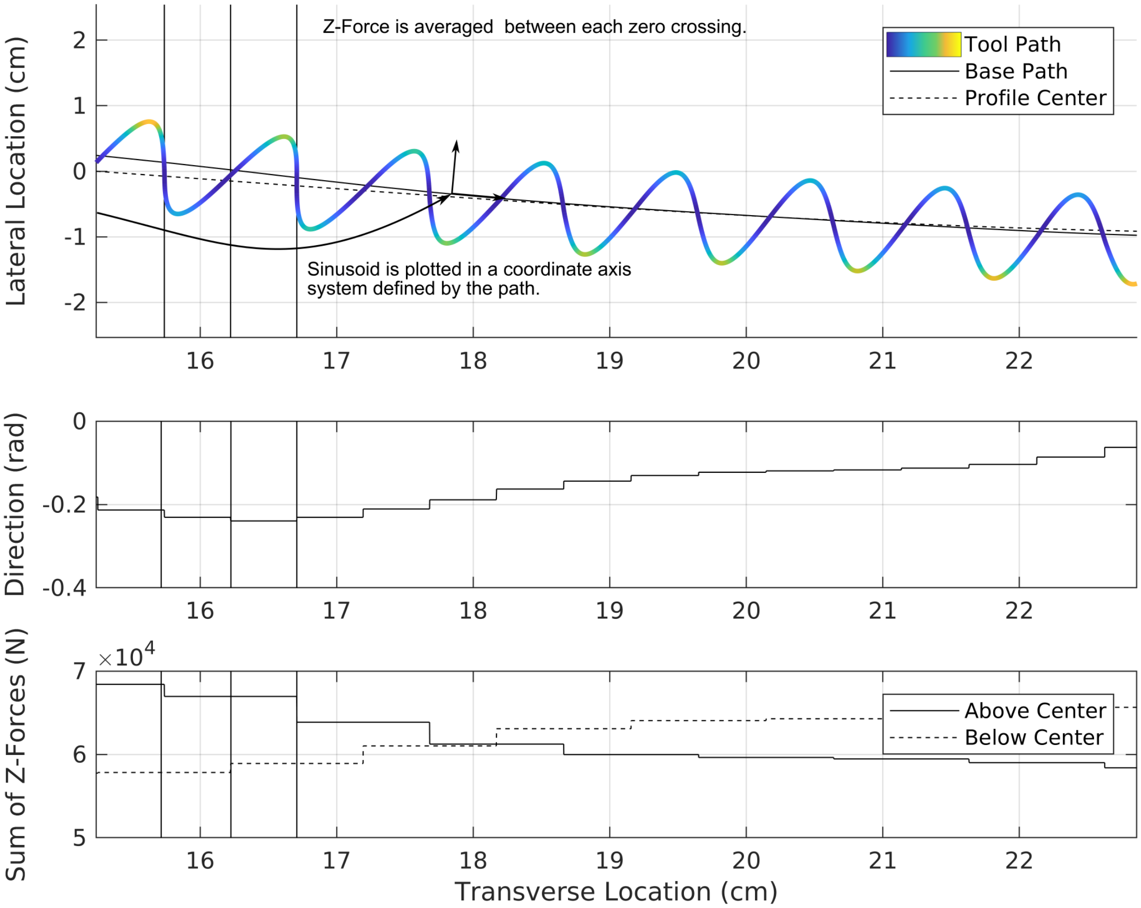

Figure 6.2: The PID-based controller operates by summing the measured processing force between each zero crossing, (A) defined as when the tool position crosses the path center. (B) The error signal is defined as the error signal as the difference between the summed forces and prior summed forces. (C) The direction of the base path is set after each zero crossing. The higher processing force is represented by the Tool Position transitioning between blue and yellow (Blue corresponds to lower force, yellow corresponds to a higher force.)

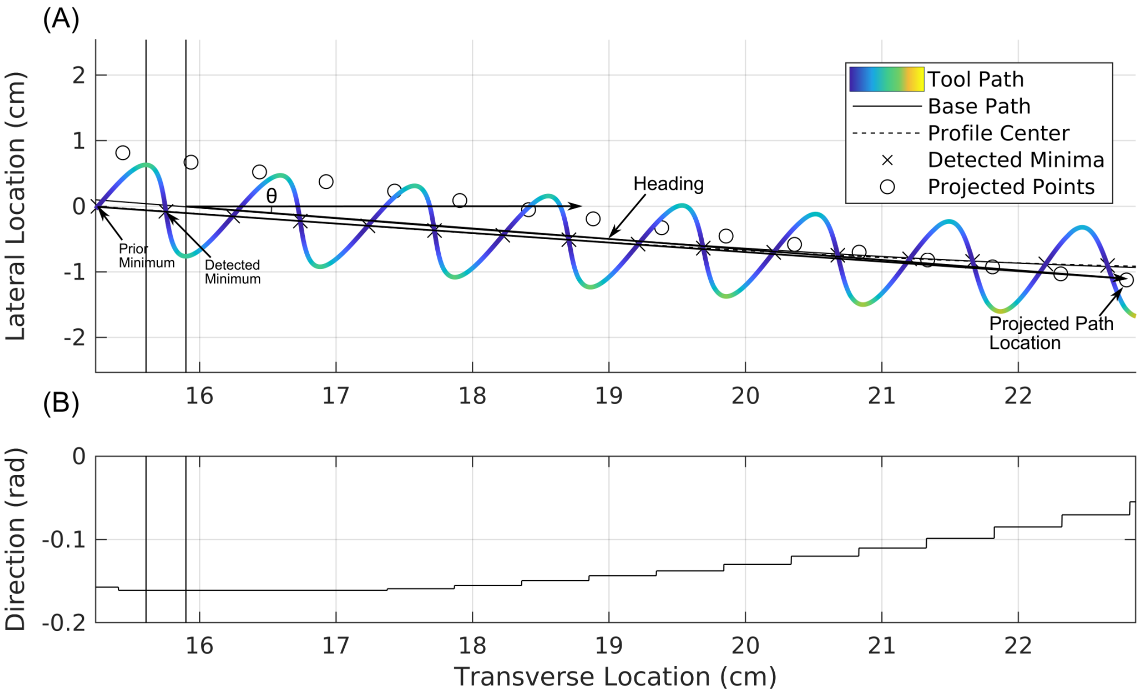

Figure 6.3: (A) The projection controller operates by identifying processing force minimums during peak to peak sweeps of the tool position. The controller assumes that the path is linear and projects a target point ahead of the current position. (B) The heading of the path generation is changed to converge with the target point. The detected minimums are the locations where the tool experiences the lowest processing force, where the tool position appears the bluest. The projected point and heading are updated at each peak.

point along the line ahead of the tool was selected as the future minimum location, and the direction is set to a weighted average between the current direction and the direct direction to the projected point. The directional change takes place at each peak of the sinusoid. An example of the projection controllers function is presented in Figure 6.3.

Two tuning constants is included in the control system. The first parameter, the projection distance, modified how far in front of the last detected minimum the projected point was placed. The point in the future was determined by multiplying the unit vector between the two prior minima locations and the projection distance and adding the result to the last minima location. The larger the projection distance, the slower the controller reacts to changes in the groove heading, and the linear assumption of the groove path becomes less accurate. If the projection distance is too small, then there is a danger of passing by the projected point before the controller updates. The second parameter, the averaging weight, determines the weighting between the prior heading and the calculated heading. This parameter is intended to lessen the effects of false minima detection caused by noise.

The control system was first simulated to perform software-in-the-loop testing. The primary purpose of the simulation was to allow for the testing of the control system safely before performing physical welds. The controller's inputs and outputs were set to be mathematical facsimiles of a physical weld. The input processing forces were constructed by fitting a polynomial to the collected data. A recreation of measurement noise was added into the processioning forces in some cases to test the noise rejection of the controllers.

Both control systems take some time to start up. After the plunge, the machine ramps to full welding speed in the x-direction. Then, the sine wave amplitude gradually increased until the final value is reached. The gradual ramp reduces wear on the machine due to dynamic loads. When the weaving amplitude reaches 90 percent of the final value, the tracking controller engages. Both controllers had to collect one complete period of data before beginning to make directional changes. The projection controller needed two points to project the groove path, and the PID controller needed two averaged peaks to produce an error signal.

Ultimately, the PID controller was implemented on the welder hardware and was tested using a 6.35mm (0.25”) offset to both the positive and negative side and a 10-degree inclined path.

The weaving welds were performed with the processing parameters: 1500 rpm, 76.2mm/min (3 ipm), and 5.6mm (0.220”) plunge depth. The sine wave had an amplitude of 6.35mm (0.25”).

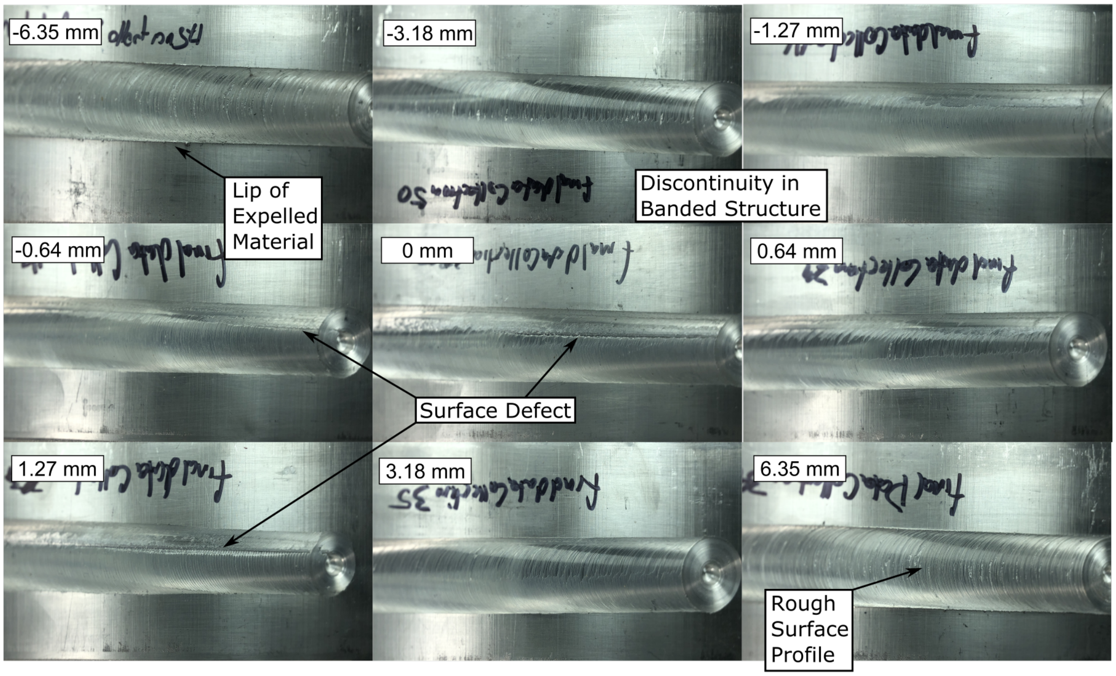

Figure 6.4: images of the top surface of select welds at each offset location.

6.4 Results

6.4.1 Groove Offset

The relationship between displacement from the groove and processing forces was examined by performing 27 welds, 3 each at 9 different offset distance. An example of the weld surface at each offset distance is pictured in Figure 6.4. The surface quality of the weld varies by offset from the groove. -1.27mm (-0.050”), -0.635mm (-0.025”), 0mm, 0.635mm (0.025”), and 1.27mm (0.050”) showed some signs of surface defect formation. The surface defect formation seems to be at a maximum around 1.27mm (0.050”). 3.18mm (0.125”) and 6.35mm (0.250”) did not show any surface defect formation on either side. 6.35mm (0.250”) and -6.35mm (-0.250”) had ridges on either side of the weld. The ridges were not present in 3.18mm (0.125”) and -3.18mm (-0.125”).

The averaged processing forces from the groove offset studies are plotted in Figure

6.5. Torque, z-force, and spindle current form a V-shaped relationship with distance from the groove center. The planar force and x-force did not correlate with groove offset. However, the y-force, perpendicular to the tool motion, strongly correlated to the groove offset. The differences in processing forces are likely caused by the volume of material extruded into the groove. When the tool is closer to the center of the groove, more material can be forced into the groove—leading to a loss of tool contact with the material and lower processing forces.

The torque profile was not symmetric about the center line, 0 mm. The torque and z-force increased more rapidly on the positive side to a higher ultimate value than on the retreating side. The torque increased from 8.4 Nm to 12.8 Nm, and the z-force increased from 3700 N to 8500 N over when increasing the offset to the positive side. The torque increased from 8.4 Nm to 11.2 Nm, and the z-force increased from 3700 N to 7500 N when increasing the offset to the retreating side. The absolute minimum for both torque, 8 Nm, and z-force, 3400 N, was observed at the 1.27mm (0.050”) offset. This offset position also corresponded to the largest void formation. The differences in flow characteristics from positive side to retreating side could help to explain the differences in processing forces. This could help to explain the minimum around 1.27mm (0.050”). This distance is close to one radius of the tool pin of the tool used to perform the welds offset to the positive side. Evans theorized that a pin can block the flow of material into the groove, and a slight offset can enhance the flow of material into the groove [34]. However, the same offset distance to the retreating side is roughly equivalent in z-force and greater in torque to the 0 mm position. This could be due to flow characteristics making material displacement on that side more difficult.

The torque and z-force between trials at each offset position was largely identical, Figure 6.6 6.7. Along with a visual inspection, it was determined that the welds were consistent between trails at each offset position. However, there were a few outliers.

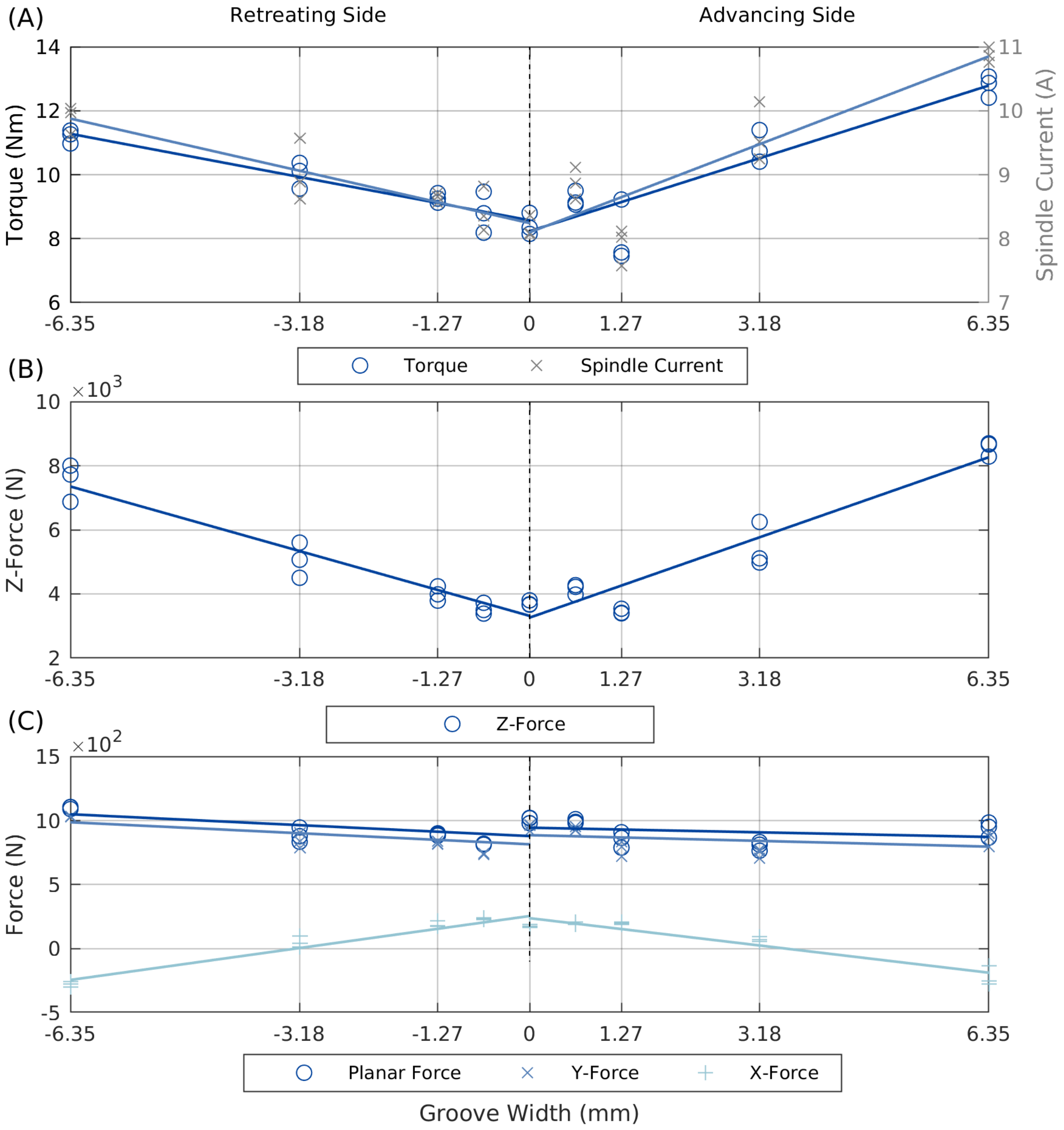

Figure 6.5: (A) Average torque, spindle current, and (B) z-force, (C) planar, and xy-forces measured during each trial of the open-loop groove offset trials. After the plunge, the average was taken from when the transverse rate reached a steady state to the end of the weld.

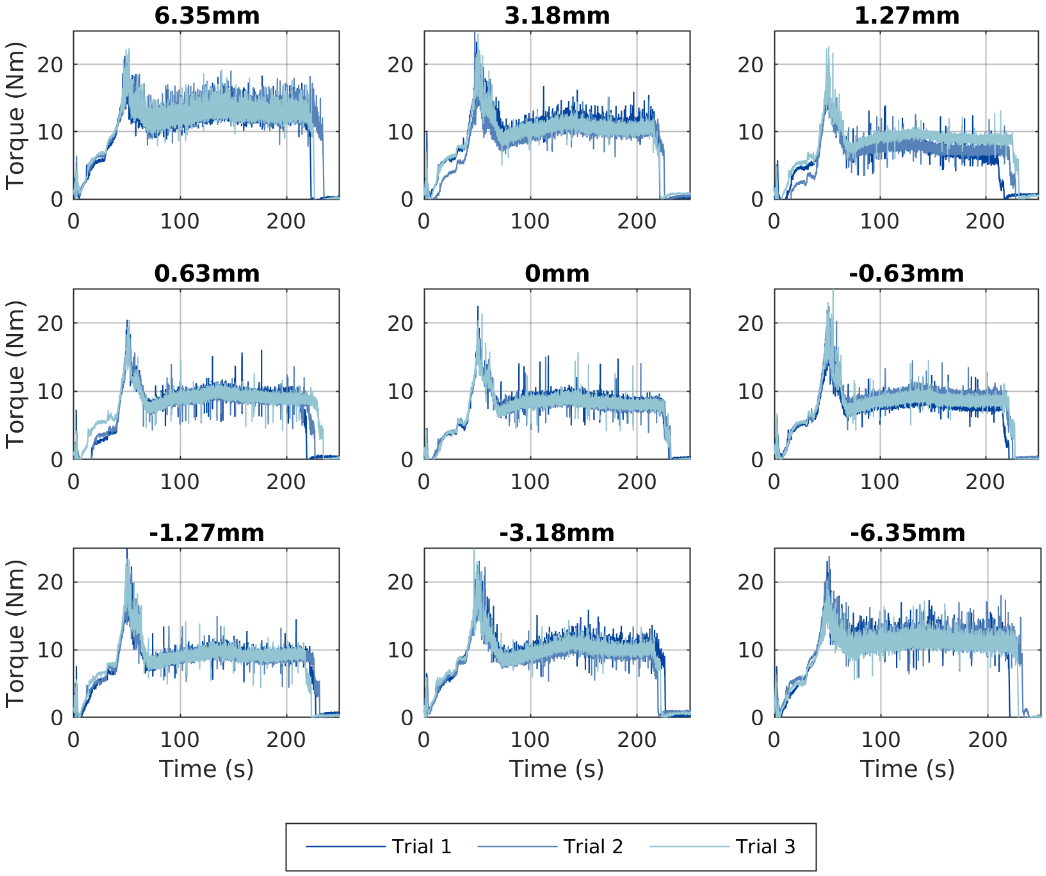

Figure 6.6: Comparison of the measured torque for each groove width during the open-loop variable groove offset trials. Generally, the torque decreased when the offset was reduced. Additionally, the magnitude of measured noise tends to decrease with decreasing offset. this can be seen as a reduction in the thickness of the steady-state torque.

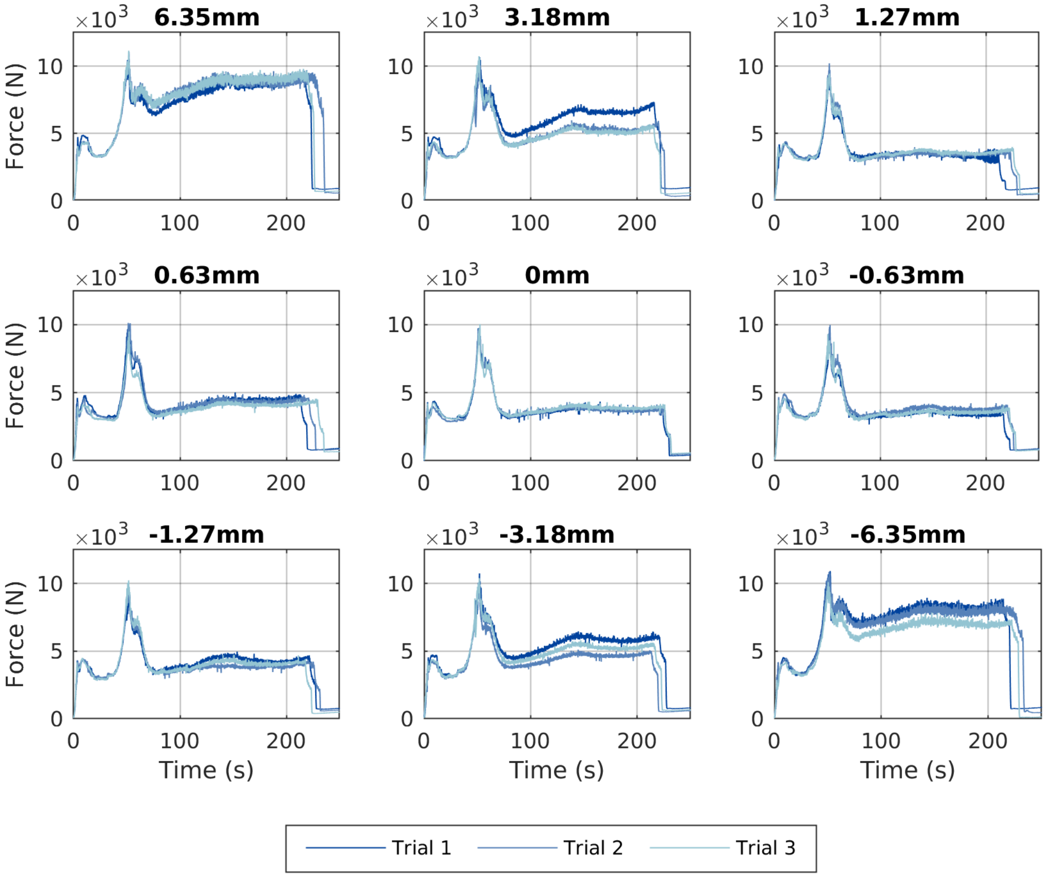

Figure 6.7: Comparison of the measured z force for each groove width during the open-loop offset groove weld trials.

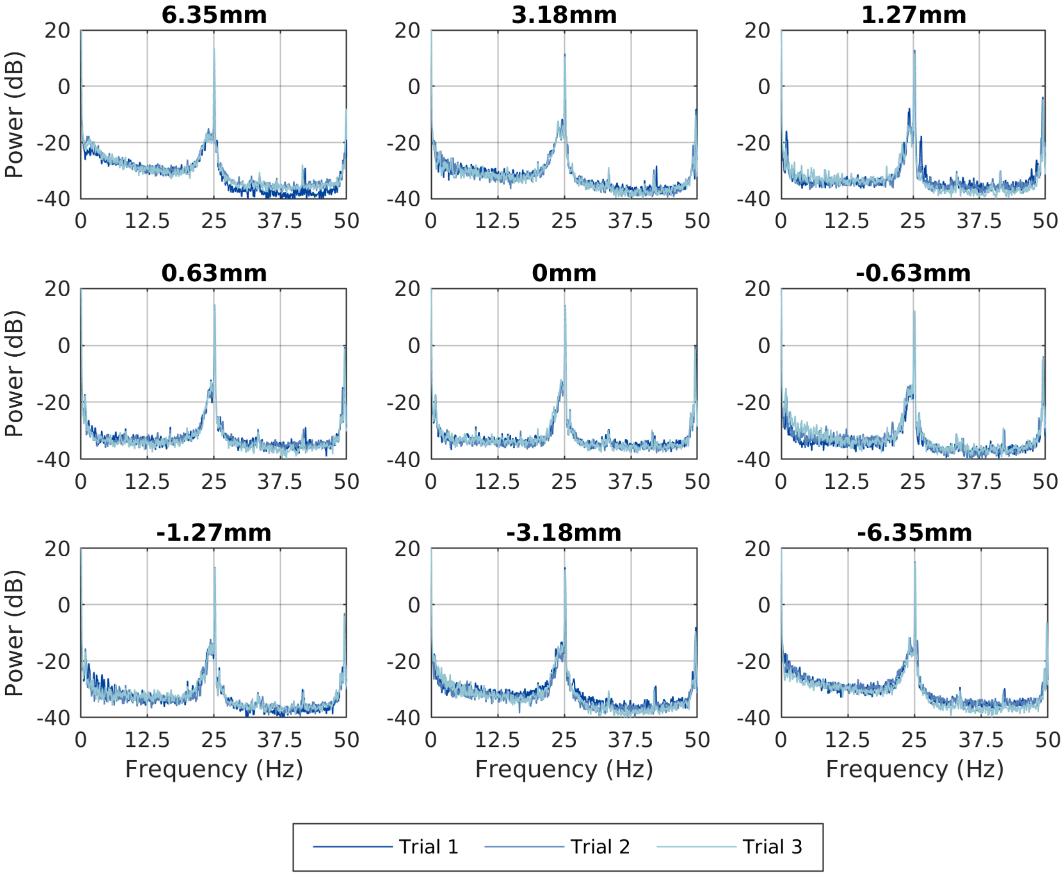

Figure 6.8: Power spectrum of the measured torque during the open loop variable groove offset trials. The average power spectrum of each series of three trials has been included.

3.18mm (0.125”) trail 1 has a higher z-force than the other two. All three trials are slightly spread out at -3.18mm (-0.125”) offset. It is interesting to note that the variability in the z-force is generally at the wider offset positions.

It was also noted that the noise present in both torque and z-force data was higher at the larger offset positions. To further examine the response the power spectrum of both torque and z-force was evaluated, Fig. 6.8, 6.9.

A large peak around 25 Hz dominates the spectra. This peak corresponds to the rotation rate of the spindle and divides the spectrum between background noise and weld phenomena. Between 0 and 25 Hz, the shape of the power spectrum showed a

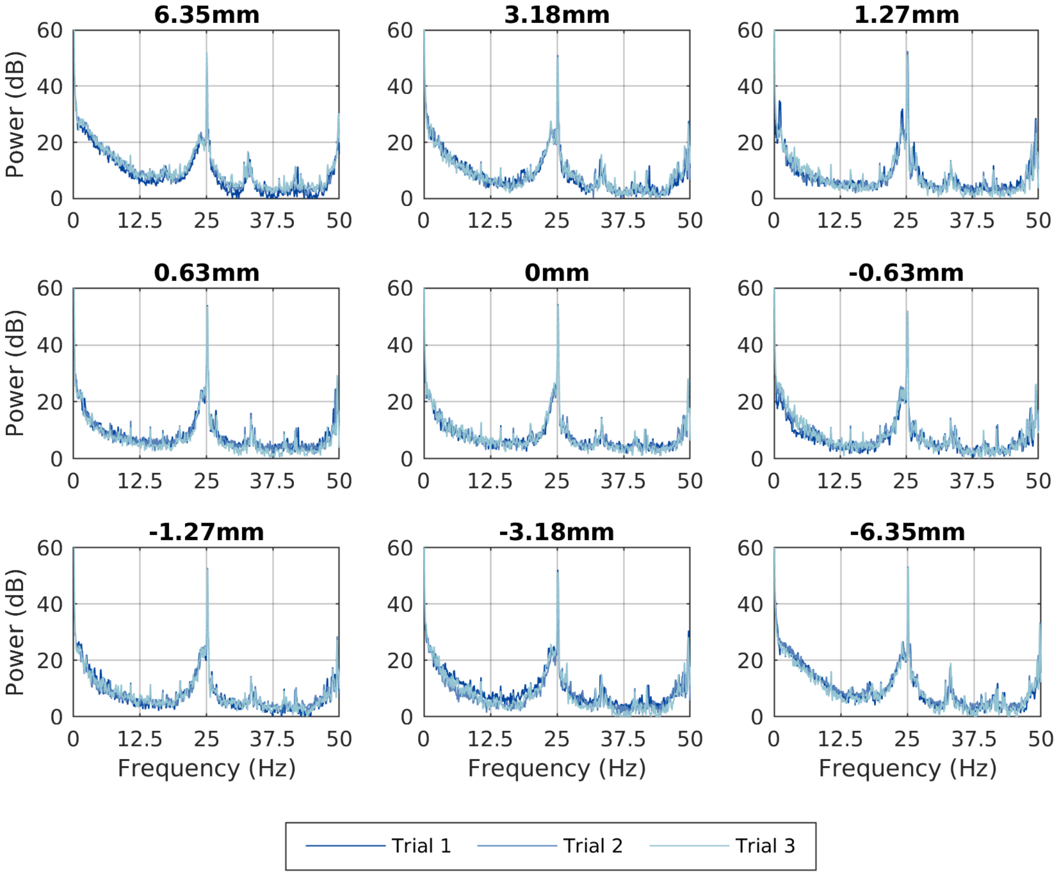

Figure 6.9: Power spectrum of the measured z force during the open-loop variable groove offset trials. The average power spectrum of each series of three trials has been included.

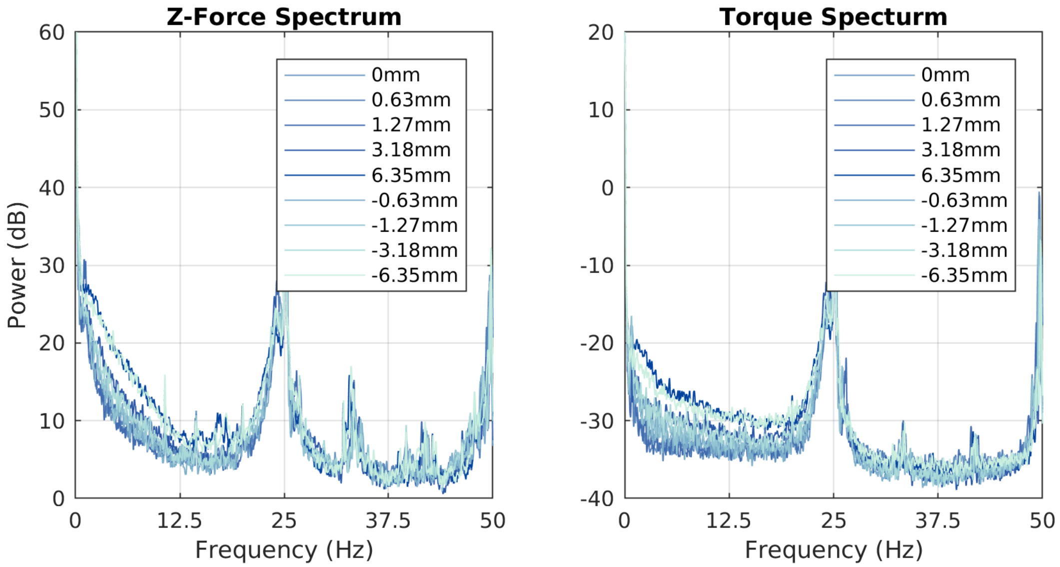

Figure 6.10: (A) The averaged torque power spectrum for the three welds at each offset distance. (B) The averaged z-force power spectrum for the three welds at each offset distance.

dependence on the groove offset. Higher offsets resulted in a larger spectrum between 0 and 25 Hz. From 25 to 50 Hz, the welds produced an identical response.

All three power spectra from one offset distance were averaged to compare between different offset distances. All offset locations were compared in Fig. 6.10 for torque and z-force. As noted prior, 25 Hz corresponds to the spindle speed, and the spectra are different in the region between 0 and 25 Hz. So, it is reasonable to assume that lower frequencies are excited by the spindle or emergent from the welding processes. Those above 25 Hz are likely from outside sources or measurement artifacts.

There was good agreement between the power spectrum on either side of the groove. The -6.35mm (-0.250”) and 6.35mm (0.250”) had the highest power. Both 3.18 mm (0.125) and -3.18 mm (-0.125) had slightly lower power and were largely identical. The three groove offsets with the lowest power were 0mm, 0.635mm (0.025”), and 1.27mm (0.050”) with -0.635mm (-0.025”) and -1.27mm (-0.050”) above them.

6.4.2 Simulated Response and Controller Tuning

It was decided to move forward with a z-force based controller due to the large variations in z-force and better signal-to-noise ratios.

The controllers were evaluated using three different simulated groove profiles: step, linear, and circular. The step impulse transitioned the simulated groove center from 0 to 6.35 mm in the lateral direction at 7.62cm (3") of transverse movement. The simulated linear profile was straight for the first 7.62cm (3") of transverse travel. Then, transitioned from a horizontal profile to one with a slope of 1 cm lateral change for 2 cm transverse change, a 26-degree incline. The simulated circular profile had a radius of 20.32cm (8"). The initial location of the weld was positioned such that the center would intersect the circular profile when the directional controller engaged.

Prior controllers have effectively handled the step groove profile. However, an linear or circular profile would have been difficult for prior controllers. Therefore, both groove profiles were simulated to validate the function of the controller. The linear profile represents an angled misalignment between the groove and initial weld direction during fixture and setup, and the circular profile represents a more complex profile where the groove following controller might be used.

A simulation of the tool position and forces were used to tune and evaluate the performance of each controller. The simulation also identified any potential issues, proving the controller could be implemented safely. Initially, the noise-free polynomial, fitted to the collected z-force data and projected along with a groove profile as a simulated processing force, was used for initial testing and tuning. Then, simulated measurement noise was added to the simulated processing force further to evaluate the noise rejection of each control system. The noise was added into the system by generating a similar power spectrum to those collected in the offset welds. This was achieved by filtering and scaling wide-band white noise with high pass filters until a similar spectrum to those displayed in Figure 6.9 was achieved. While the fitted

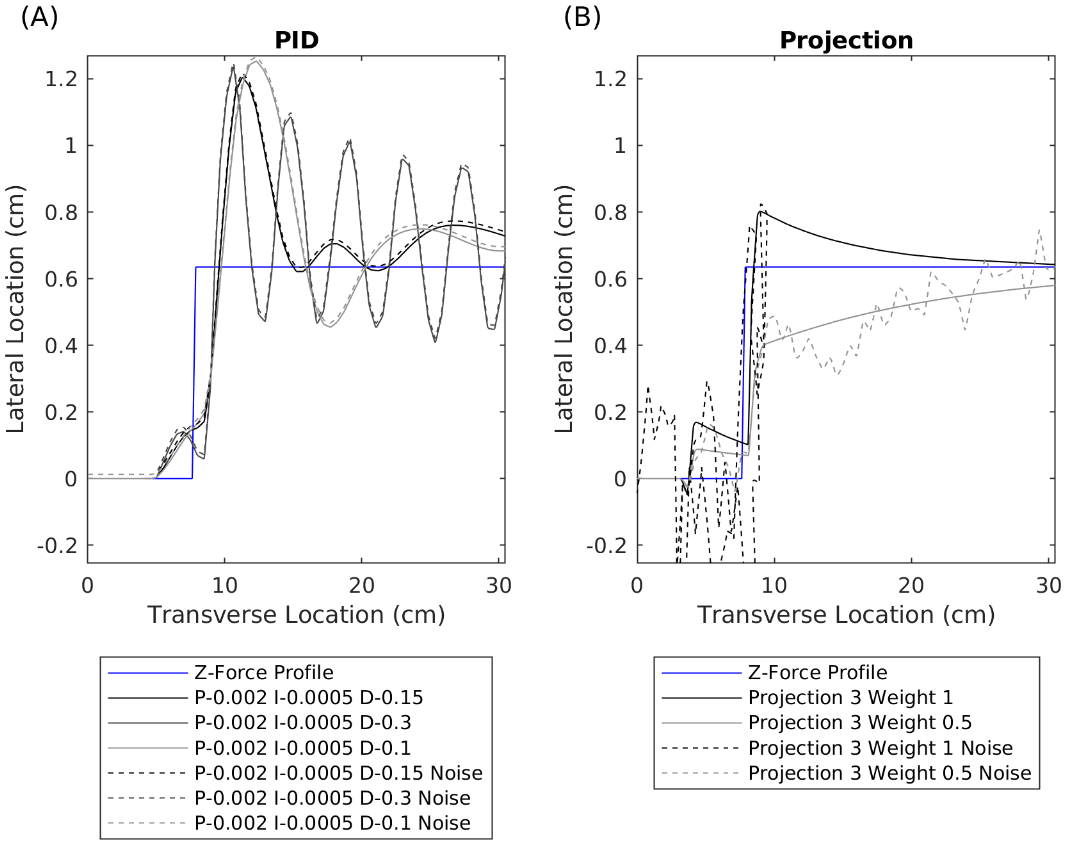

Figure 6.11: (A) Base path positions for multiple simulation trials, with and without noise, using different PID constants. (B) Base path positions for multiple simulation trials, with and without noise, using different projection constants.

polynomial is likely not the best model for the processing forces, it was able to provide a basis to test and evaluate the controller.

The step impulse was used to tune both the Projection and PID controllers. While many sets of parameters were tested, the simulated path center for a representative set of parameters for each controller can be seen in Fig. 6.11. Each set of parameters was simulated twice, with and without measurement noise. The controller's performance was evaluated by tracking how quickly the base path rose to meet and converged with the z-force profile.

The PID controller was very sensitive to both proportional and integral terms.

The two terms tended to cause instability, and slightly increasing the proportional or integral terms led to continuous oscillation. Since the direction was accumulated, the proportional and integral terms tended to ”wind up” the heading, and the derivative component functioned similarly to the proportional component in a conventional PID controller. Therefore, the controller performed best with the derivative term as the largest of the three. The parameters: $P = 0.002$, $I = 0.0005$, and $D = 0.15$ offered the best mix of fast rise times and controller stability. When the derivative term was increased to 0.3, sustained oscillations resulted, and when decreased to 0.1, the controller overshot the reference value farther.

The projection controller's response without measurement noise is characterized by an initial fast response followed by a long asymptotic approach to the groove path. Generally, a smaller projection distance resulted in a slightly faster approach to the groove path. Decreasing the averaging parameter decreased the initial response and slowed the approach to the groove path.

A smaller subset of the select control parameters were used to simulate both controllers' performance with the linear and circular profiles, Fig 6.12. The previously identified parameters where used for the PID controller. The PID controller adapted to the incline in the linear simulation with some oscillation before closely following the groove path with little steady-state error. The PID controller adapted the circular path similarly. There were a few oscillations before closely tracking the path with steady-state error to the outside of the circle. Two sets of parameters were simulated for the projection controller. The projection controller could react quickly to both the linear and circular simulations, following closely to the path center for both set parameters. But, a different trend was apparent with added measurement noise.

It was found that the PID loop was particularly resistant to noise. A relatively large number of signals are averaged between zero crossings to produce a single data point, and the noise was averaged out. Therefore, the difference in the response

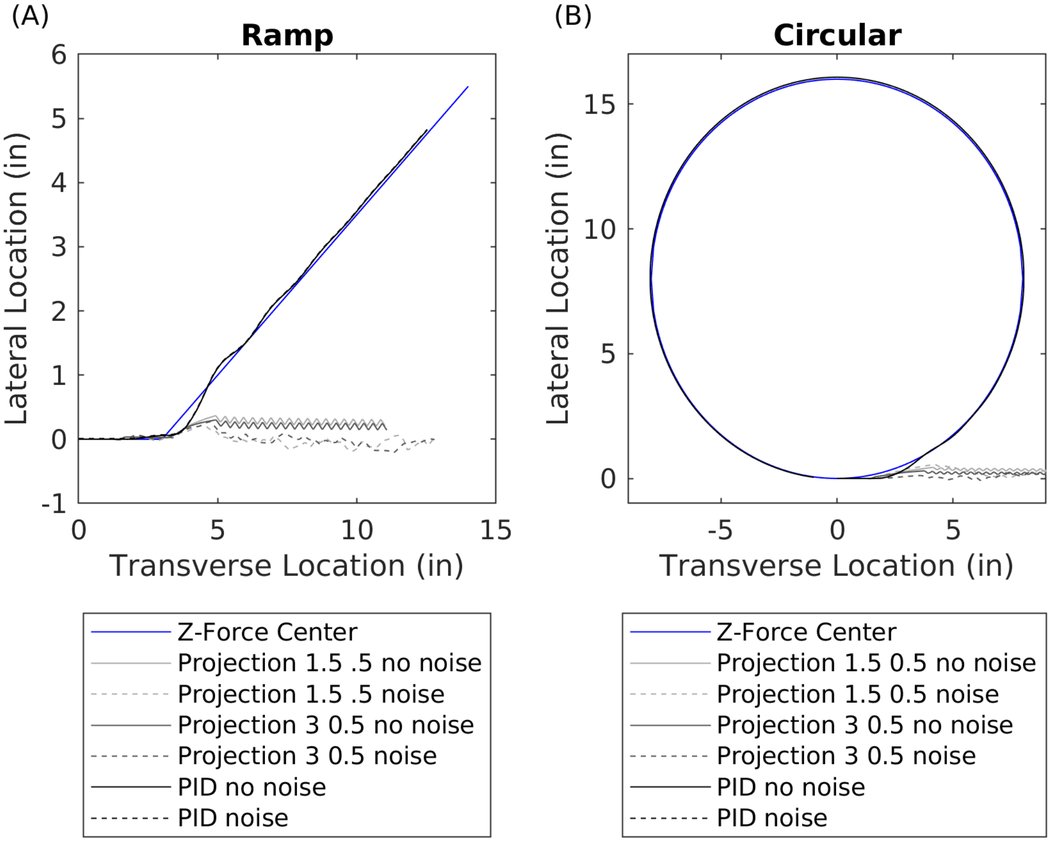

Figure 6.12: Center positions for multiple simulation trials with (A) ramp and (B) Circle profile, with and without noise, using both PID and Projection controllers. (

between the no noise and noise PID simulation was minimal.

The projection controller had poor performance in noisy situations. When the tuning parameters were increased enough to adapt to the linear and circular profiles, measurement noise caused the controller to be unstable.

Decreasing the averaging weight or increasing the projection distance had a dampening effect on the projection controller response. In noisy situations, large projection distances are preferred. Short projection distances cause rapid directional changes that, when following a false minima location, can rapidly cause the base path to diverge from the actual minima. The addition of measurement noise can create a false minima location, and the projected path location could be far from the true minima position. The controller will then attempt to intercept the projected point. However, decreasing the averaging weight and increasing the projection distance can stabilize the controller when noise is included at the cost of the rise time of the controller.

The projection controller does show great promise with a fast rise time and no continued oscillation. The controller resembles how a human would identify the groove location and direct the welder. However, The overall design of the controller made it vulnerable to noise, and the included noise caused the projection controller to be ineffective. The noise caused misidentification of the local minima location leading to the rapid directional changes that would drive the control system unstable and possibly risk damage to the machine. Better noise rejection and path planning methods would be needed to make the controller a viable option.

The PID controller was determined to be the best controller to use for physical welds. The best set of gains was $P = 0.002$, $I = 0.0005$, and $D = 0.15$, and these gains had the best response for both no noise and noise simulations.

The PID controller had to include additional logic to prevent a couple of issues found during the simulations. For example, the controller had to evaluate only after each zero crossing of the overlayed signal. Otherwise, the controller had no new data, and the controller could wind up.

In another case, If the summed forces are both rising, then the error signal will oscillate due to the comparison between the current summed forces to one considerably time-lagged. This situation causes the differential term to oscillate around zero, each zero crossing. The derivative term was modified to compare every other error update. The derivative term would only compare the error signal generated from the last two positive side peaks or negative side peaks. This feature was added to increase the stability of the controller.

6.4.3 Experimental collected data

Four welds were performed using the weave tracking controller. Similar to the prior welds,the square groove fixture was used as the bottom plate. Three welds were performed with the groove parallel to the initial heading of the weld. One weld where the tool was centered on the groove, Figure 6.13B, and two offset 6.35mm (0.25") to both the positive, Figure 6.13A, and negative, Figure 6.13C, sides. The last weld was performed with a 10 degree angle between the initial weld direction and the groove, Figure 6.13D. The initial location of the weld was positioned to pass over the groove after the controller is fully started. The angle was reduced from the simulated 26 degrees due to a slower response observed in the offset welds.

The weaving welds tended to produce a pronounced ridge of material on the negative side of the weld, Figure 6.13(E) , and surface defects can form at the directional change on the positive side, Figure 6.13(C).

The base and tool paths for the offset groove weaving welds are shown in figure 6.14. In the offset cases, the center of the groove was sufficiently distant that the initial oscillations just centered the tool path over the groove. As the welds progressed, the centers of the weld paths converged on the groove. However, there was a tendency to settle slightly to the negative side. All three tests ended with the groove center on

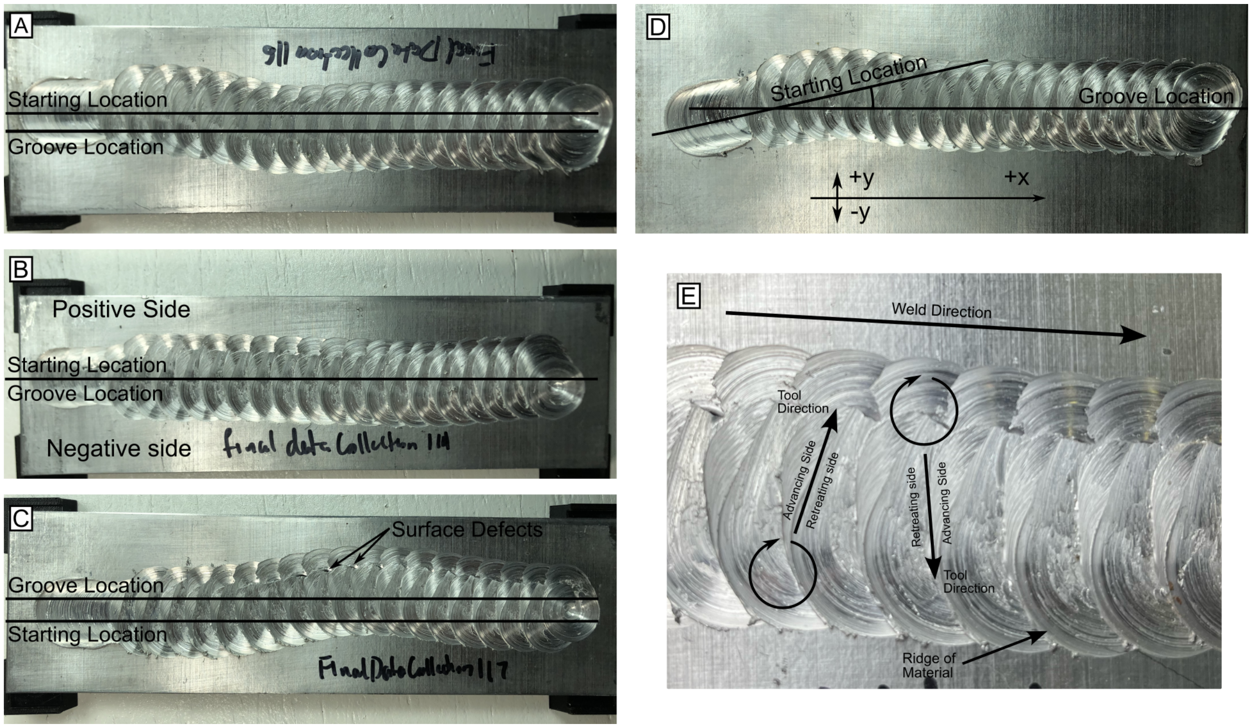

Figure 6.13: Images of (A) Positive offset, (B) centered, (C) negative offset, and (D) misaligned welds. (E) The path that the twld tool took through the Aluminum stock. The initial path and groove location is indicated for each weld. The tool rotation (E), and directional vectors (D) are also indicated.

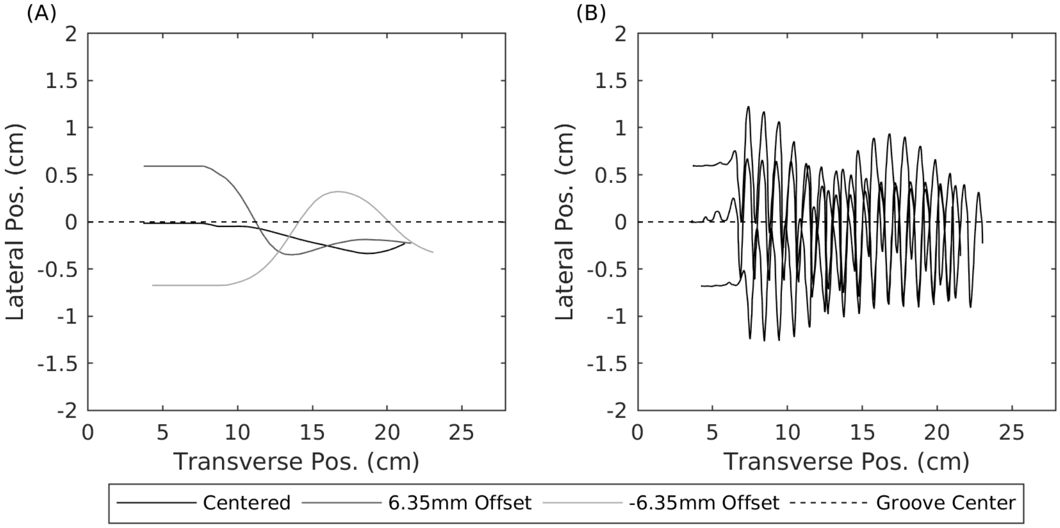

Figure 6.14: (A) Tool position from PID controlled weave tracking welds with 0 mm offset, 6.35mm (0.250") offset, and -6.35mm (-0.250") offset. The groove was centered at 0 mm, and the tool was centered at the offset position. (B) Path center from PID controlled weave tracking welds with 0 mm offsets, 6.35 mm offsets, and -6.35 mm offsets. The groove was centered at 0mm, and the tool was centered at the offset position.

the negative side of the groove. The preference can be clearly seen in the centered weld. It slowly shifted to a slight offset to the negative side. Also, The welds offset to the positive and negative sides were not mirrored images of each other. The -6.35mm (-0.250") offset weld performed worse than the 6.35mm (0.250") offset.

The differences in surface quality on positive and negative sides and path differences between positive and negative initial offset suggest some asymmetry in processing forces between positive and negative sides.

The estimated center and tool paths for the inclined groove weaving weld are shown in Figure 6.15. When the controller engages, the base path can be seen to bend towards the groove. After a slight overshoot, the profile center settled into a slight steady-state error with the groove path.

The groove location can be clearly seen as a trough in the profile formed by plotting the z-force against the transverse and lateral location of the tool, Figure

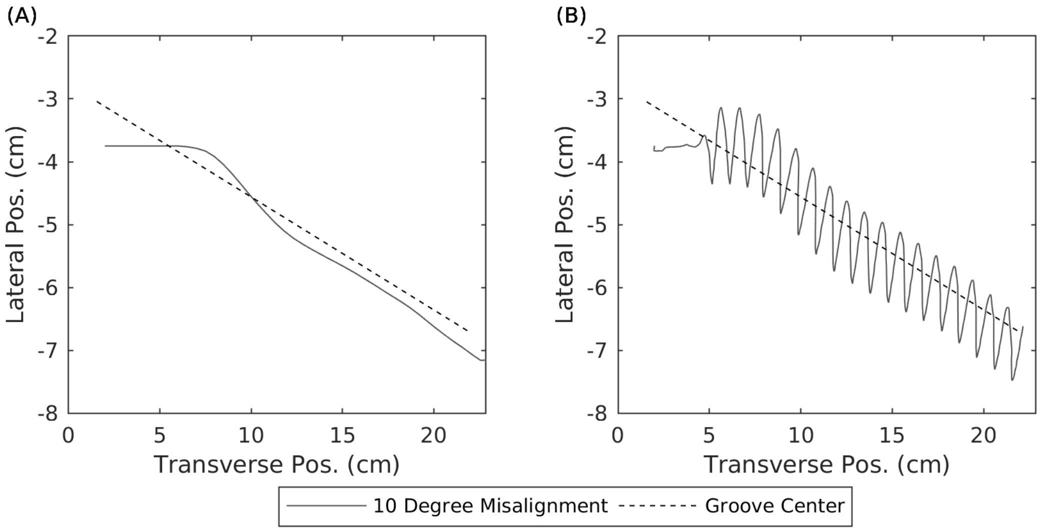

Figure 6.15: (A) Path center from a PID Controlled Weave tracking weld with 10 degree misalignment. (B) Tool Position from a PID controlled weave tracking weld with 10 degree misalignment.

6.16. Also, the z-force appears to follow a different profile depending if the tool is passing from positive to the negative side or vice versa. This loop can be seen as a second surface defined by the negative to positive path underneath the first.

The z-force progressively increased in three out of the four welds.

Similar to z-force, the torque signal was plotted along with the tool's transverse and lateral location during the weld, Figure 6.17. Unlike the z-force, the torque signal along the tool path does not obviously reveal the groove location.

Possible reasons for the obfuscation are the noise inherent in the signal as well as the reduction in the expected decrease due to the weaving process over ideal circumstances, I.E., the offset welding study.

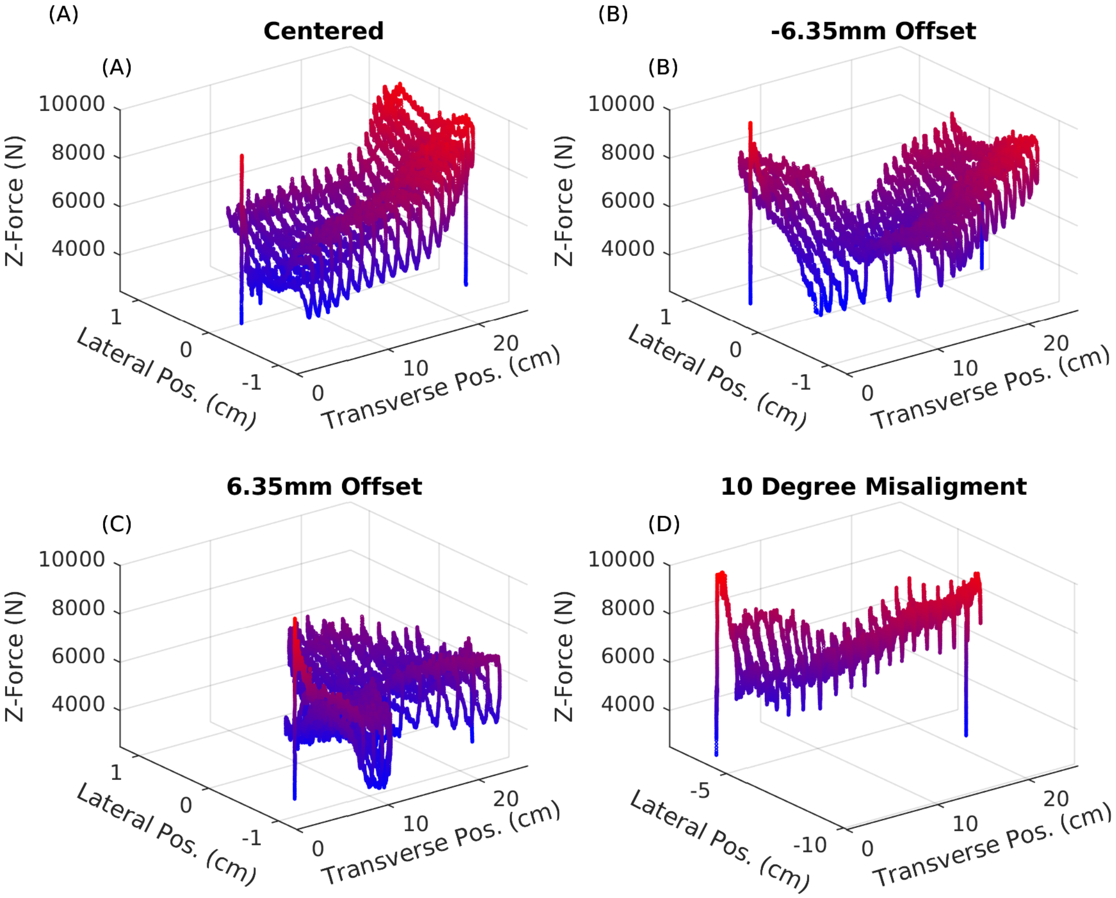

Figure 6.16: 3D profiles of the measured z-force (A) centered over groove (B) -6.35mm (-0.250”) offset (C) 6.35mm (0.250”) offset (D) 10° misalignment. The groove can be seen in as a valley in the profile.

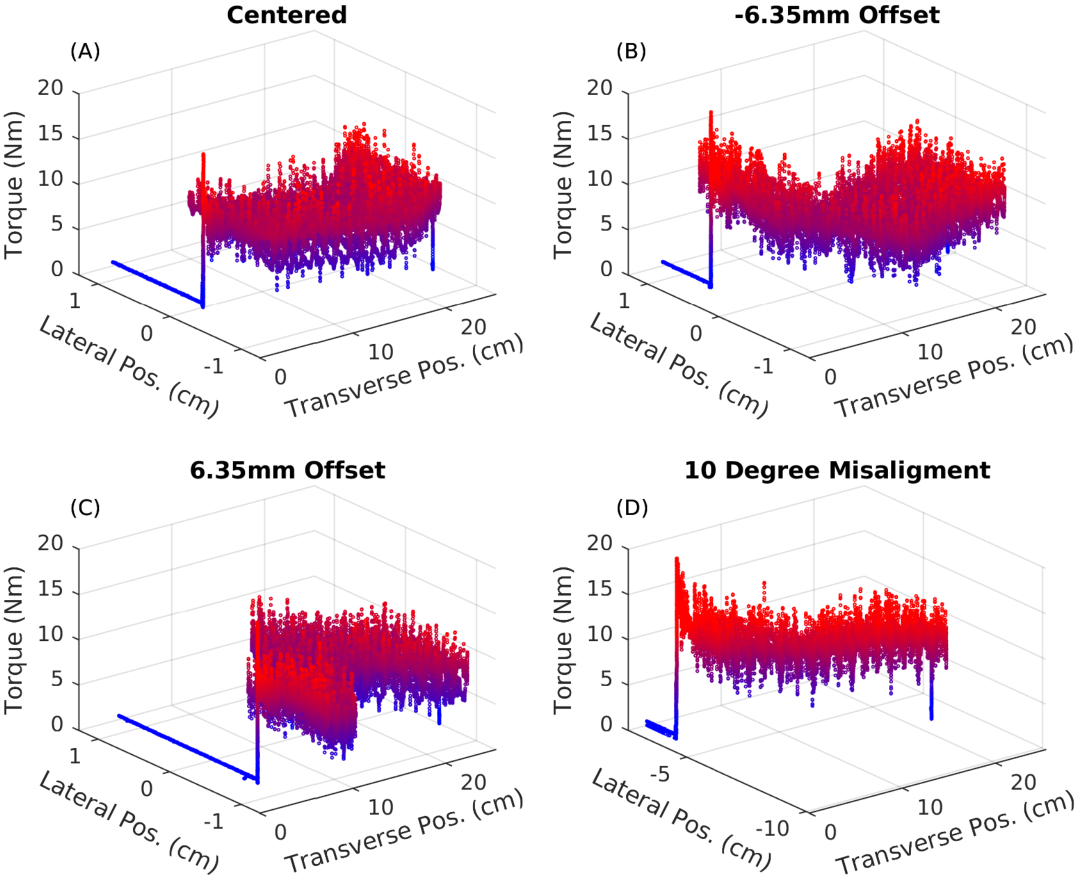

Figure 6.17: 3D profiles of the measured torque (A) centered over groove (B) -6.35mm (-0.250") offset (C) 6.35mm (0.250") offset (D) 10° misalignment.

6.5 Discussion

The weave control test welds were asymmetric between the positive and negative sides in both the physical appearance of the weld, and the response of the controller (preferential to the negative side), and the collected force signals. Asymmetries in the processing forces were examined further by plotting torque and z-force over complete periods of the sinusoidal path from multiple lengths along the weld path, Figure 6.18. Four locations along the weld path were examined: near the start, towards the start, towards the end, and near the end of the weld.

A directionally dependent loop of the processing forces was observed in each complete period of the weaving for both z-force and torque.

Starting at the groove center and moving towards the negative side, the z-force rises. When the tool begins to head back towards the positive side, the z-force drops rapidly a the local minimum at the inflection point. Continuing to the positive side, the z-force increases, then decreases toward the local minimum at the groove center. The z-force then gradually increases to the positive side peak, and closely follows the prior path back to the starting point at the groove center.

The torque closely resembles a triangular path with a sharp decrease in torque at the directional change on the negative side. The local minimum indicating the groove location, indicated by the dotted line at 0 mm, clearly visible in the z-force, is completely absent in the torque. The lack of the local minimum and the noise inherent in the signal demonstrates that the torque signal is likely a bad choice for weave tracking applications.

It was noted that the aluminum extrusion hight was variable and periodic, figure 6.19B. The distances between extrusion minimums was measured. It is expected that the minimum extrusion occurs when the tool is at the furthest distance from the groove, or at the peaks of the weaving. So, the peak to peak distance should be half that of one complete period the weaving. However, both the extrusion and weaving

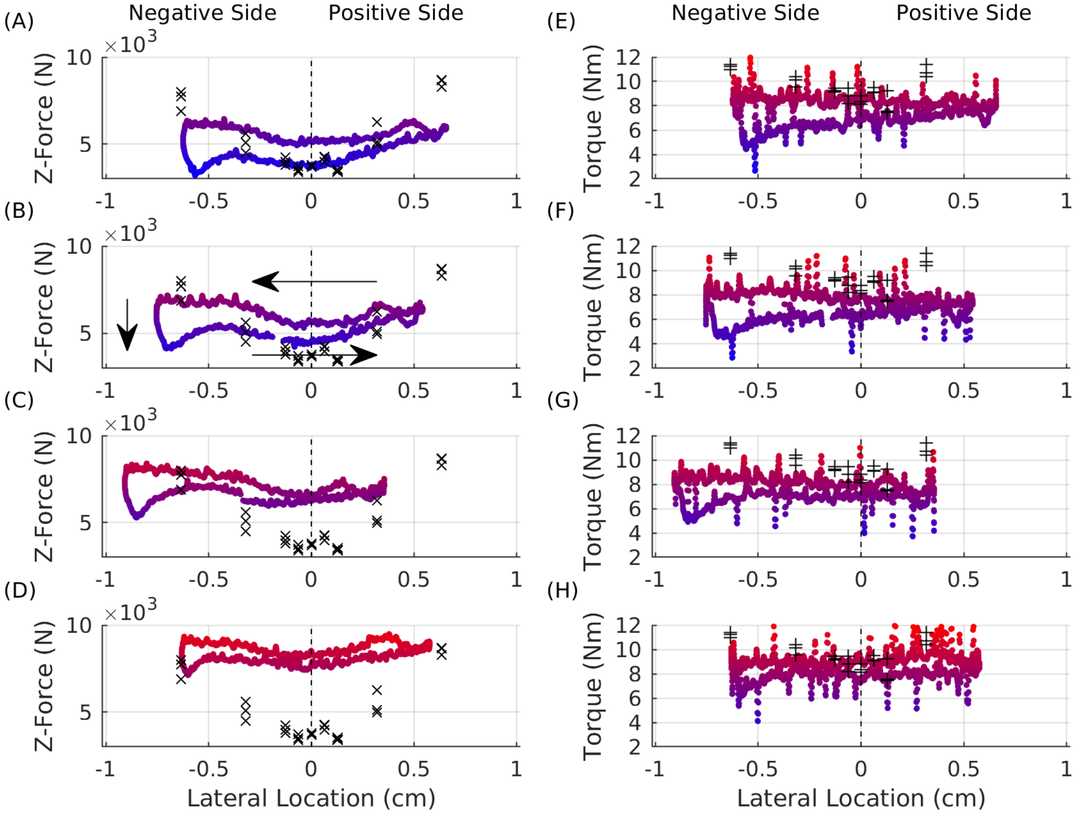

Figure 6.18: Z-force (A, B, C, and C) and torque (E, F, G, and H) data collected from one period of the weaving at the (A, E) start of the weld, (B, F) towards the middle of the weld, (C, G) towards the end of the weld, and (D, H) end of the weld. The direction of progression of the loop is indicated in (B). Average z-force and torque values collected from data collection step is shown on each graph.

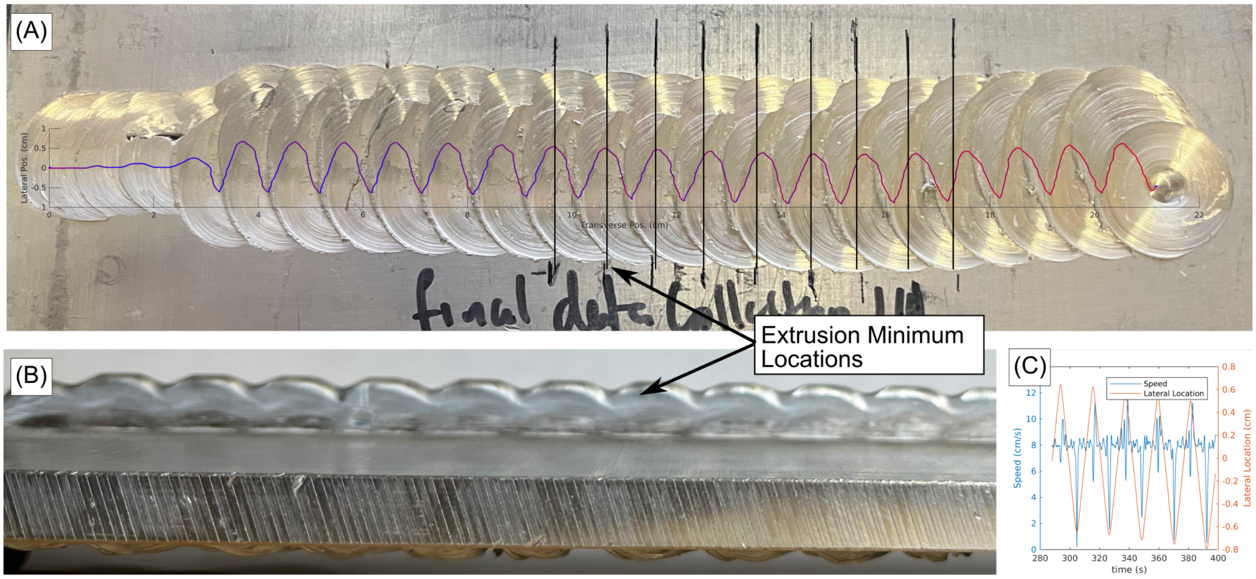

Figure 6.19: (A) Surface of the centered groove tracked weld. The tool path is overlayed. The weaving amplitude is not to scale. The locations of a group of the extrusion minimums are indicated by the vertical lines. (B) Side profile of the weld showing the cyclical extrusion. The minimum locations are indicated. The side profile is not to scale of the surface image.(C) Lateral location plotted in comparison to the weld speed.

have equal periods of 1 cm.

The minimum extrusion locations were transferred to the front of the plate by straight edge, and they were related to the tool location to further study the effect, Figure 6.19A. The minimums closely matched the positive side peaks.

The local minimum an possibly increased extrusion at the negative side peak could have been caused by the welder itself. Backlash present in the gearing between the y-axis motor and table lead screw might have caused a longer than normal pause at the peak, leaving more time to heat and extrude aluminum. This can be seen in the comparison between lateral location and weld speed, Figure 6.19C. It can be seen that the peak on the positive side maintained the controlled speed much more effectively than the peak on the negative side. Effectively dwelling the tool at the peak location.

The z-force and torque was higher when transitioning from positive to negative side than negative to positive side. This is likely caused by the asymmetry of FSW, the directional changes, and partially overlapping back over previous welds. The side of the tool contacting fresh un-welded material changes with each directional change, figure 6.13E. During FSW, material is plasticized in front of the pin, extruded around the negative side, and deposited behind the pin. There is little to none material flow around the positive side of the pin

When transversing from positive to negative side, the advancing side of the tool is contacting the non-welded material. It is likely that the thicker non-welded material was pulled into the plasticized material around the tool, increasing the welding forces. Observations in the surface of the weld support this conclusion. When moving from positive to negative side, a ridge of material is deposited on the negative side of the tool, figure 6.13E. There is also slight increase in z-forces when the tool just starts moving back to the negative side that corresponds with the start of the ridge of material, Figure 6.18.

Neither the z-force nor torque signals expressed a local minimum quite as prominent as those measured during the groove offset study. Several reasons could cause the observed difference. The dip in the processing force due to the groove could be dependent on the tool's angle with respect to the groove. During the groove offset study, the tool ran parallel to the groove, and the weaving system crossed the groove at an inclined angle. Another possible explanation is a time lag to observe a dip in processing forces. The tool passes over the groove rapidly, and aluminum is only given a limited time under the ideal conditions to extrude into the groove. The final possible explanation is that the groove area in front of the tool has already been partially filled by the prior crossing or the weld path approaching the groove. Leaving little additional room for the tool to extrude more aluminum and reducing the observed drop in processing forces.

Both the local minimum on the negative side and the shallower local minimum over the groove affected the controllers performance. The local minima on the negative side is likely responsible for the observed offset to the negative side by driving the sum of forces lower than expected. The shallower local minimum likely caused the controller did not respond as quickly as during the simulations. As a result, the degree of misalignment For the linear weld had to be reduced to 10 degrees down from the 26 degrees simulated

The directionally dependent loop is most pronounced at the weld's start and is nearly eliminated at the end. The local minima from the directional change become much smaller, and the separation between the two sides of the loop is reduced as the weld progresses—additionally, the z-force increases across the whole weave. This is likely due to a slight height difference in the welding fixture. The depth of the weld as well flash increase toward the end of the weld. Both are evidence of the plunge depth increasing over time. The most likely cause is a slight rise in the height of the fixture.

As stated earlier, the control system's sampling rate depends on the parameters within the overlayed signal generation and on the welding speed. Changing the parameters to increase the controller sampling rate could lead to better controller performance.

The sampling rate of the PID controller can be increased in multiple ways. Increasing the sinusoid's frequency, increasing the welding speed, or decreasing the sinusoid's amplitude would all increase the sampling rate of the controller. Increasing the welding speed would increase the update rate of the controller but also increase the forward propagation of the welding tool. The rotation rate of the tool might need to be modified to stay within the processing window of the material. Increasing the frequency of the sine wave would increase the number of periods per unit length of travel, increasing the density of the weave pattern and slowing down the forward propagation of the tool. This would increase the energy deposition of the weld and could cause higher temperature welds. Finally, decreasing the amplitude of the controller will reduce the distance the controller sweeps through each period of the sine wave. Both increase the forward propagation of the controller and reduce the number of samples taken on either side of the base path.

Conservative parameters for the overlayed signal generation were chosen for initial testing. The set of parameters chosen prevented the machine from performing rapid directional changes. However, changing the processing and path generation parameters should be further examined.

Future controller versions could adaptively change the path generation parameters like the amplitude and frequency-dependent upon the controller error. If the error is high, the amplitude could be increased, decreasing the frequency, forming a search path to help identify the groove location. If the error is low, the amplitude or frequency could be decreased-allowing for faster forward propagation speed.

The differences in strength between weave tracked extrusion welds, and conventional FSE Welds should be studied. The weaved FSE welds should have greater heat input over conventional FSE welds. However, the processed zone is greater in size, possibly increasing the size of the weld nugget.

6.6 Conclusion

A series of three welds at 9 different offset positions were performed using a FSE fixture. The data revealed that processing forces are related to the offset from the groove center. The data can be extracted from either torque or z-force via the magnitude or power spectrum.

A general-purpose constant speed weaving algorithm was developed utilizing well-known math to conserve arc length. The algorithm was structured to provide flexibility in the propagation direction, adaptability in process, and a platform for data collection. Unlike prior methods that relied on offsets in the y-direction while propagating in the x-direction, this system used a directional term to allows for a steerable path. The constant welding speed maintained a constant heat input into the weld. Later versions could implement temperature control routines by modifying welding speed without much effort.

On top of the algorithm, two different control systems for tracking local minima during the weld were developed and the two controllers were evaluated via simulation. The simulation was built off data collected by collecting processing forces at different offset locations. The PID-based controller displayed superior noise rejection and stability in simulation. Therefore, it was advanced to perform physical welds.

Four demonstration welds showed the controller's ability to detect and adapt to 6.35mm (0.250") offsets to either side of the groove and 10-degree misalignment. While the response was slower than the simulated scenarios, the controller was able to adapt to both the offset and misaligned tests. A flattening of the relationship between offset and z-force in the weaved tests could account for the slower response. A hysteresis loop was found within each period of the weaving and differences between the positive and negative sides of the weld were identified and determined to be a result of machine limitations or an effect of the asymmetry of FSW.

The research indicated several future directions to improve tracking ability. Refinements to the control routine could minimize the effects of the negative side minimum. Better controller tuning using actual weaving welds could increase responsiveness.Temperature and power input control could help to eliminate temperature increases during the weld. Additionally, adaptive Path generation parameters, sine wave amplitude, and frequency could be modified to improve controller performance and increase welding speed.

6.7 Acknowledgment

All funding for the project was provided through the Tennessee Space Grant, NNX15AR73H.

CHAPTER 7

Flow Characteristics of Friction Stir Extrusion by Welding of Dissimilar Alloy

7.1 Abstract

Friction Stir Extrusion joins dissimilar materials by extruding materials into a preformed geometry and is a unique scenario over prior material flow studies in Fiction Stir Welding. A series of Friction Stir Extrusion welds were completed with vertical layers of AA6061 and AA5052. The welds were etched to reveal the macrostructure of the weld. The positioning of the tool over the groove effected the thermo-mechanical history of the extruded material and the defect formation.

7.2 Introduction

During Friction Stir Welding (FSW), the material flow structure has been historically hard to observe. Past work focused on embedding a tracer material into the bulk that can be identified post weld[51, 52, 55, 42, 53]. The material flow is inferred from the tracers displaced location behind the tool. Other works focused on the macrostructure and microstructure characteristics of the weld to describe the plastic flow [170, 54].

State of the art describe FSW as an iterative process [61, 58, 42, 54] During each rotation of the tool, Material in front of the tool heats up until it plasticizes. Then, a slug of material extrudes around the retreating side of the tool, and it is deposited into a void formed behind the pin. The trailing edge of the tool forges the slug to the previously extruded material behind the tool. The plasticized slug of material can be observed in the forces experienced by the tool each rotation. When there is a mismatch between the void to be filled and the plasticized slug, defects form.

Friction Stir Extrusion (FSE) is a derivative technology of FSW that forms and interlocking mechanical joint in two lapped dissimilar dissimilar materials by extruding material in the top sheet into preformed geometries in the second [34]. The process has been demonstrated for multiple material combinations: Aluminum to steel [34, 136], Aluminum to Titanium [156], and Aluminum to Graphite [158].

Little research has been done on the material flow structure around FSE and how it differs from conventional FSW. Prior work has shown under certain conditions a surface defect can form behind the advancing side of the pin. In the past, FSE welds were performed with the tool offset to the advancing side. The offset was meant to reduce the effects of the tool ”blocking” the flow of material into the groove, when the tool was centered over the groove [34].

This work aims to fill the knowledge gap on the internal material flow of FSE welds by performing similar tracer experiments performed for FSW. Layered stacks of two dissimilar aluminum alloys were welded using FSE techniques, and post-weld displacement of the different alloys could be examined to shed light on material flow during the weld. Therefore, welds at three different offsets between pin to groove centers were performed and the resultant plates were analyzed to look at the differences in the weld structure.

7.3 Methods

Three welds were performed with the groove positioned to the advancing side (AS), retreating side (RS), and centered on the tool. All three welds used the same processing parameters: 1500 RPM, 76.2 mm/min (3 IPM), and 5.59 mm (.220”) plunge depth.

Friction stir extrusion requires two sheets. A top sheet that is extruded, and a bottom sheet that contains the preformed geometry. For these welds, the top sheet was formed from four stacked layers of AA6061 and AA5052 1.6mm (0.063”) thick sheets for a total thickness of 6.35mm (0.250”). An extrusion fixture that formed

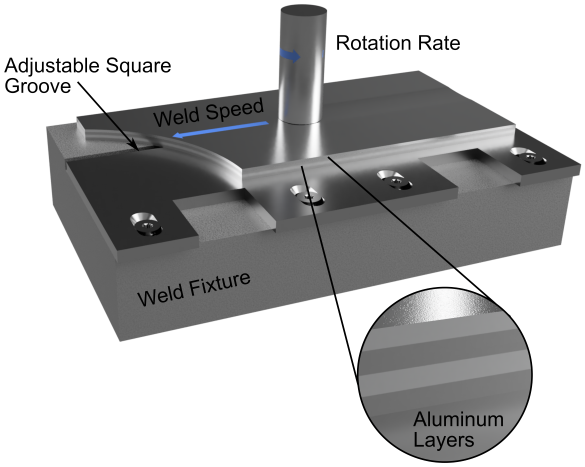

Figure 7.1: Multi-alloy layered sample welded using a fixture with a square groove.

a square groove 3.18 mm (0.125”) in width and 6.35 mm (0.250”) in depth from two pieces of steel replaced the bottom sheet, Figure 7.1. The fixture enhanced repeatability and enabled post-weld removal of the top sheet without damage to the extruded features.

The welded sheets were separated from the fixture and transversely sectioned. The sections were cut from the approximate center of the weld. The AS offset was also longitudinally sectioned. The sectioned pieces were polished to 2000 grit with sandpaper and etched with AWS D1.2 basic etchant to reveal the macrostructure. The etchant attacked the two alloys differently causing them to be differentiable under a microscope.

7.4 Result and Discussion

A composite image of each of the welds’ transverse sections is shown in Figure 7.2.

The welds are not symmetric across the weld center line. On the RS, the aluminum layers were deformed outside of the direct path of the tool. The bottom three layers lifted on the borders of the weld, and the RS offset resulted in the greatest lifting.

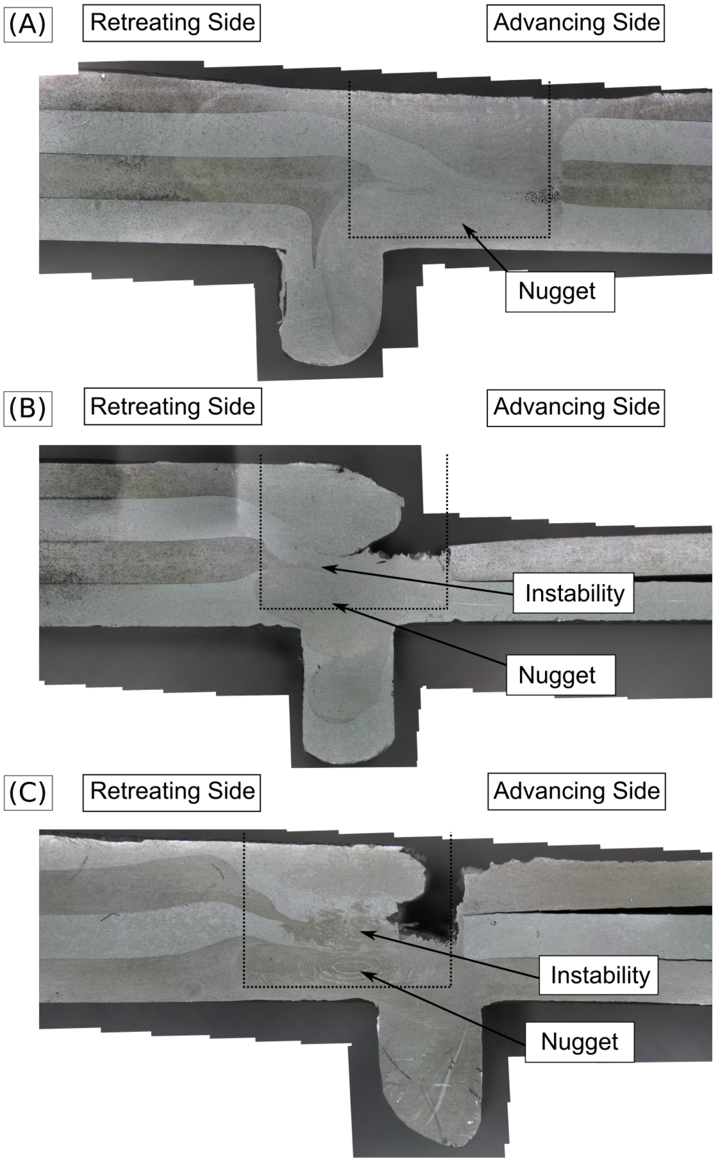

Figure 7.2: FSE weld with (A) tool offset to advancing side, (B) tool centered, and (C) Tool offset to retreating side. The darker etched alloy is the AA5052, and the lighter is the AA6061. The dotted lines show the estimated pin location.

Then, the middle layers are stretched downward as they reach the pin location. On the AS, the interface between the weld and the bulk material was immediate and distinct. There was no observable deformation or mixing of material layers outside of the direct path of the tool.

The nugget features a strongly banded structure similar to the banded structures that Krishnan first described [54]. Each one of the layers represents a shell of extruded material from one rotation of the tool. A second mixed layer at the surface of the weld is present for both AS offset and centered welds. It penetrated deeper as it traveled around the pin from RS to the AS. For the retreating offset and centered welds, the material flow above the nugget appears to be unstable. The second alloy layer appears to be broken up and discontinuous with variable layer thickness during the retreating side offset weld, Figure 7.2C. The second layer remains continuous but takes a winding path from retreating to advancing side in the centered weld, Figure 7.2B. Outside of the two regions discussed mixed through interaction with the tool, the aluminum alloy layers remained distinct and separate.

A highly mixed material originating from the weld nugget was included in the groove fill material for all three welds. For both the retreating offset and centered weld, the portion of the nugget extruded into the groove was in-cased in material from the bottom layer. The AS offset weld nugget occupied one half of the groove extrusion, split vertically, and extended to the bottom of the extrusion. Material from the bottom layer with small inclusions from the second from the bottom layer filled the remainder of the groove. The AS offset weld is the only weld to fill the groove with unmixed material from the second from the bottom layer.

All three samples had some defect form at the AS of the pin at the interface between material extruded around the tool and the base metal on the advancing side. For the AS offset, the defect was a small void above the nugget. Larger surface defects formed during both the centered and RS offset welds. These surface defects caused the top metal layers to disconnect from the weld cross-section.

The cross sectional area extruded was estimated using an image processing program. The AS offset was the lowest at 15.4 mm^2. The centered and RS offset welds were larger at 17.4 mm^2 for both samples.

The AS offset weld stands out as different from the other two because of the lack of a large defect. The extrusion had to have occurred around the trailing edge of the tool. The nugget is present at the bottom of the extrusion, indicating that the extrusion occured only after the nugget had formed behind the pin at the trailing edge of the tool. The other two locations began extruding into the groove before the nugget was formed, demonstrated by the non-mixed material at the bottom of the extrusion. This is supported by the total area of material extruded. The additional extrusion that occurred in front of the tool resulted in a total greater volume of material extruded.

All three welds displayed volumetric defects. A small void in the case of the advancing offset weld, and large surface defects for the retreating offset and centered welds. There are two different root causes for volumetric defects: Abnormal stirring and insufficient plastic flow [74]. The retreating offset and centered welds display some evidence of Abnormal stirring with the discontinuous or chaotic displacement of layers, Figure 7.2B,7.2C. Abnormal stiring can be attributed to insufficient shear band width in front of the pin [61]. This explanation provides further evidence that for retreating offset and centered welds, material began to fill the groove in front of the pin.

The smaller surface area of material extruded as well as the lack of material extruded before the pin contributed to the smaller defect present in the AS offset weld.

The longitudinally sectioned sample from the AS offset weld shows the banded structure of the weld nugget descending into the extruded material, Figure 7.3. The

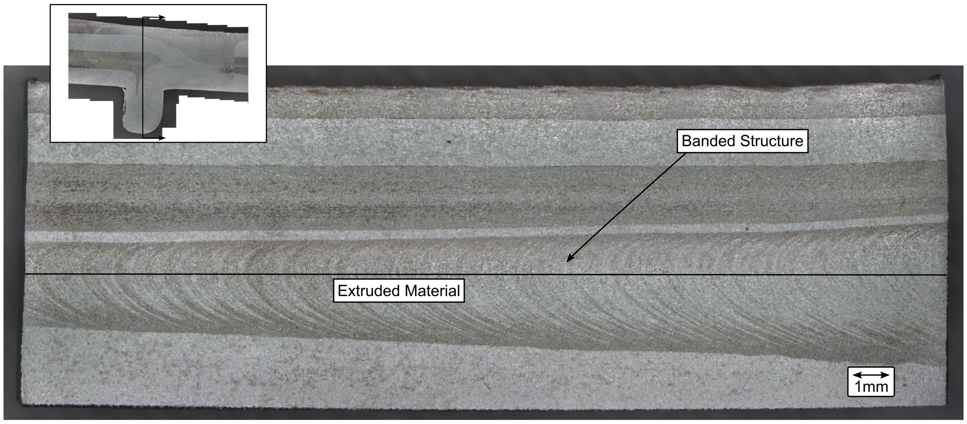

Figure 7.3: Advancing offset weld sample sectioned parallel to the weld direction polished and etched. The sample is polished such that the advancing side is into the weld.

banded structures are continuous and smooth as they are displaced down into the groove. This implies that each one of the perimeters represent a single extrusion shell. Combine with the band structure in the transverse cross section, the shape of the shell for the AS offset weld can be estimated as a deformed semicylinder built in multiple layers, Figure 7.4B, similar to the clay model displayed by Kishnan [54]. A reproduction of the model is presented in Figure 7.4A. The extrusion shells here are modeled as first forming normally then being extruded down into the groove at the trailing edge of the tool.

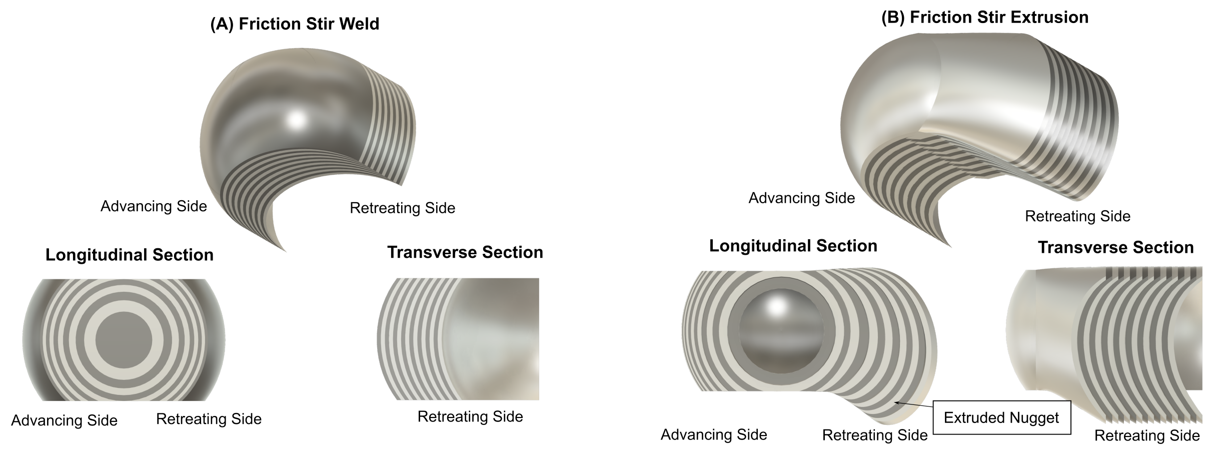

Figure 7.4: (A) Layered Extrusion layers during FSW. (B) Proposed layered Nugget structure during FSE for the advancing side offset welds.

7.5 Conclusion

FSE of layered aluminum alloys has been demonstrated to be an effective method to map the material movement around the weld and the material flow into the groove. Developing a good understanding of material flow within FSE joints can aid in the optimization of the process and lead to the development of accurate material flow models.

The etched welds revealed that highly mixed material, originally from the weld nugget, filled a large fraction of the extruded material regardless of the tool position. Outside of the direct path of the tool, the two aluminum alloys remained largely unmixed, with distinct boarders differentiating them. The present of the nugget at the bottom of the extrusion for the AS Offset weld provides evidence that the extrusion began later in the weld than the other two offset welds. The earlier start to extrusion in the other two welds likely resulted in abnormal stirring contributing to the large defects present in the welds, but contributed to a larger cross sectional area of extruded aluminum.

Offsetting the tool to the AS does not result in additional extruded material. However, it did result in a reduction in the size of defects formed using the same process parameters.

7.6 acknowledgment

Thanks to Jeff Cui for assistance with completing welds. All funding for the project was provided through the Tennessee Space Grant Consortium.

CHAPTER 8

CONCLUSIONS

FSE is a process that could be of great interest to industry. The process utilizes a standard FSW tool and can reduce tool wear. FSE can also join non-conventional material combinations. This work has demonstrated a method to bring FSE to a new material regime. A post weld heat treatment process was demonstrated that can increase ultimate tensile strength 24% and hardness by 49.5%. The ability to sense groove widths through multiple different processing forces, and the controllabilty process to maintain good weld quality was demonstrated though torque controlled plunge depth. Finally, a new minimum tracking technique was developed to better adapt to misalignment between the weld path and groove path. The tracking technique was demonstrated for .250" offset and 10 degree misalignment between weld and groove paths.

FSE has a unique set of benefits over other dissimilar material joining techniques, FSW based or not. The process can be applied to a wide range of material thicknesses, groove geometries, and base material. The process does not use any specialized equipment. Because a contact between the tool and a harder or more abrasive material can be eliminated, cheaper and more readily available tools can be used. The power and rigidity requirements for FSW machines increases with the yield strength of the material. Since, the tool remains in the lower yield strength material of the dissimilar pair, Machine power and rigidity requirements tracks the lower yield strength material. A machine capable of FSW aluminum is capable of preforming FSE with no additional specialized tooling. This can be a huge advantage when one of the limiting factors to design is the available machines and tooling.

The research presented in this dissertation significantly moves the FSE process to an industrially viable solution for dissimilar material joining.

A large amount of current derivative processes that form by extrusion focus on joining thick sheet materials. However, many consumer products a made from thin gauge material to save weight. This work demonstrated joining dissimilar thin gauge materials by a novel approach to form an interlocking geometry by metal bending instead of the more conventional welding techniques. Then, two thin sheet materials were joined together using the produced interlocking geometry. The strength of the joint proved to be sensitive to the processing parameters. The thin sheet FSE joints failed through deformation of the steel sheets and not through shearing of the extruded aluminum. The failure mode indicated that further optimization of the joining process can be preformed.

The process of using metal bending to form the interlocking geometries lends itself to the current way car bodies are formed. Sheets of metal are formed into complex geometries that are joined together to make a uni-body spaceframes. It is natural to include the forming of the interlocking geometries around the seems of the panel in the normal manufacturing processes.

The FSW processes often disrupts the temper of heat treatable aluminum alloys. The elevated temperature leads to the microstrutural changes that weaken heat treated aluminum alloys. Post processing techniques can ge used to recover some portion of the lost mechanical properties, and can be highly desirable for joints placed in demanding applications. There has been some research into applying post processing techniques to restore material properties post weld. However, little literature is available for the post processing of FSE joints. The dissimilar material joints require careful consideration to respect both material's chemistry. Otherwise, heat treating one material could lead to the loss of the seconds temper.

This work applies a post processing technique used for aluminum extrusions to aluminum to steel FSE joints. It was found that the treatment significantly increased the hardness of the extruded material while causing little to no change in the bulk material of either the aluminum or steel. The ultimate tensile strength of the welds was also significantly increased. The post processing technique would be ideal for high strength applications where the temper of the steel must be preserved, and the temperature requirements are low enough that larger weldments could be heat treated with thermal blankets and equipment commonly used for the preheating of cast materials.

It has be observed that during the formation of FSE joints large volumes of extruded material can cause the formation of voids and surface defects in the top sheet. It was theorized that the void formation is caused by a loss of tool contact behind the tool. Leading to a loss of forging pressure and consolidation of the material extruded around the pin. Therefore, the void foramtion would be detectable by a reduction in spindle torque or z-force.

A series of positional control welds were preformed to measure the changes in processing forces with different groove widths. Strong correlations were observed for both torque and z-force. Differences in the spectra between different groove widths where also observed.

A PID based torque controller was developed to minimize void formation from non-optima processing parameters and adapt to variations in groove profile. Prior literature pointed to torque as a strong indicator of tool engagement. Torque is also a cost effective processing force to monitor, because spindle current can be easily related to output torque.

The groove widths were selected such that the widest groove widths would form voids under positional control. The controller largely eliminated void formation at these groove widths. Additionally. the controller was able to adapt to a step and a continuous change in groove width during the weld.

Development of the torque controller is one step in the automation of the FSE process, and the collection of the processing forces enabled the in-process monitoring of both the positional and torque controlled welds.

Seam following algorithms for conventionally welding different joint topologies can easily utilize vision systems. FSE joints pose some unique challenges. Since the top plate completely covers the interlocking geometry, it is largely impossible to use a vision based tracking system. Therefore, some work has been done to develop through the tool extremum tracking techniques. It is assumed that when the tool is at the optimum position that the most material will be extruded into the preformed geometry. Therefore, the processing forces will be at a local minimum. The methods work by moving the tool in a second axis to find the local minimum.

Prior work focused on utilizing trapezoidal tool paths or only collected data at a single point due to a lack of speed control. Additionally, the direction of propagation of the weld path and offset axis were locked to the machine axis, effectively creating controllers that could only adapt to offsets in one direction. The uniqueness of this paper is the control algorithm that maintains a constant speed and allows for true direction of propagation changes.

In this work, a large body of welds were preformed with differing offsets from the center of the preformed geometry. The processing forces were collected during the weld, and a strong relationship between tool offset and processing forces was described for both torque and z-force. The collected data was used to develop a novel minima tracking system. The system was demonstrated reacting to both an offset and misalignment between the original weld direction and the preformed geometry. The data collected during the demonstration welds identified challenges to future control algorithms.

The novel welding algorithm demonstrated could be an enabling technology for the robotic welding of FSE, where joint deflection could lead to inaccuracies in positioning.

The advancements presented in this dissertation forward the development of the

FSE process with the development of new processes and control systems. The developments drive toward creating an capable and industrially viable process.

CHAPTER 9

Future Work

While the work presented in this dissertation pushed the development of FSE further, and reviled multiple additional avenues to drive the development of FSE. Those additional avenues of development are listed here as work to be done at a future date.

A unique method for forming FSE joints in thin sheet stock was demonstrated. The choice of groove geometries was constrained by the ease of production of the geometry. The dovetail shaped groove tended to fail by plastic deformation of the steel sheet. Different groove geometries that require slightly more skill or resources to produce might have preformed better. For example, a wider and shorter dovetail might have been much more rigid under tensile loads.

The efficacy of a heat treatment process commonly used on aluminum extrusions was tested for FSE. The heat treatment process involved skipping the solutionizing treatment and moving straight to an aging process post weld. However, this process depends upon the extrusion process, or weld behaving similar to a solutionizing treatment. However, the cooling rate post weld is currently uncontrolled and maybe suboptimal for the AA6061 used in the study. Some aluminum alloys are less sensitive to cooling rates after the high temperature solutionizing treatment. The AA6063 is one such alloy with very similar properties. Examining the effectiveness of the post-weld heat treatment on an alloy like AA6063 or by controlling the cooling rates with AA6061 might lead to better optimization of the post-weld heat treatment process for FSE.

Through the tool temperature measurement could be used to set torque reference values during through the tool torque control for FSE. The controller would be similar to that used in Sutton and Sorristine. However, the controller might require some modification since the controller is not designed to maintain a constant power input into the weld. The torque controller presented above was designed to maintain a constant tool contact to prevent lack of forging defects.

Temperature control of the anvil or temperature control within the weld would be beneficial to both power based control and post processing. The torque controller without temperature control could lead to hot welds, and continuously increases in plunge depth. Temperature control could help to prevent the thermal run away while maintaining good FSE performance. Additionally temperature control could be used to control both the solutionizing temperature and cooling rate for better post processing as mentioned above.

Torque was demonstrated as a method of sensing tool engagement during FSE welds. Litrature also points to z-force as an effective measure of tool contact or forging pressure. In the chapter above, the z-force was shown to be sensitive to the groove width along with torque. While it was thought that a torque controller might offer the best performance, A z-force based controller should be developed to contrast performance.

A grooving tracking controller was developed in an above chapter. The controller had many tuning parameters that can be tunned to provide better performance of the tracking controller. Both the amplitude and frequecy of the weaving are examples of parameters that can be tuned. Both of the paramters could increase welding speed or tracking accuracy. Infact, the weaving frequency or amplitude could be actively controlled allowing for the controller to increase its forward propegation or go into a wider sweep mode to find the groove center.

Collecting processing forces during weaving revealed that the forces under go a complex loop each period of the weaving. While part of the loop can be explained by momentary delays in travel while changing directions, a difference when transversing between sides of the sinusoid should be further studied. Trials should be run when transversing from advancing to retreating side and retreating to advancing side. The trials might shed some explanation on the source of the difference in processing forces observed in the full sinusoidal weave tracking, and result a better tracking algorithm.

The proposed future directions of study would further refine and optimize the work presented here. Each item would further the goal of making FSE into an industrial joining process.

BIBLIOGRAPHY

[1] W. Cai, G. Daehn, A. Vivek, J. Li, H. Khan, R. S. Mishra, and M. Komarasamy, "A state-of-the-art review on solid-state metal joining," Journal of Manufacturing Science and Engineering, Transactions of the ASME, vol. 141, mar 2019.

[2] M. Haghshenas and A. P. Gerlich, "Joining of automotive sheet materials by friction-based welding methods: A review," feb 2018.

[3] W. Thomas, E. Nicholas, J. C. Needham, M. G. Murch, P. Temple-Smith, and C. J. Dawes, "Friction Welding," nov 1992.

[4] W. M. Thomas, P. L. Threadgill, and E. D. Nicholas, "Feasibility of friction stir welding steel," Science and Technology of Welding and Joining, vol. 4, no. 6, pp. 365–372, 1999.

[5] W. M. Thomas, P. L. Threadgill, and E. D. Nicholas, "Friction Stir Welding of Ferrous Materials: A Feasibility Study," in 1st International Symposium on Friction Stir Welding, (Thousand Oaks, California, USA), 1999.

[6] T. J. Lienert and J. Gould, "Friction Stir Welding of Mild Steel," in Proceedings of the First International Symposium of Friction Stir Welding, (Thousand Oaks, California, USA), pp. 1–7, 1999.

[7] A. P. Reynolds, M. Posada, J. DeLoach, M. J. Skinner, J. Halpin, and T. J. Lienert, "FSW of Austenitic Stainless Steels," in 3nd International Symposium on Friction Stir Welding, (Kobe, Japan), pp. 1–60, 2002.

[8] N. R. Reddy and G. M. Reddy, "Friction stir welding of aluminium alloys - A review," International Journal of Mechanical Engineering and Technology, vol. 7, pp. 83–90, mar 2016.

[9] T. Nelson, C. Sorensen, C. Johns, S. Strand, and J. Christensen, "Joining of Thermoplastics with Friction Stir Welding," in 2nd International Symposium on Friction Stir Welding, (Gothenburg, Sweden), 2000.

[10] H. Larsson, L. Karlsson, S. Stoltz, and E.-L. Bergqvist, "Joining of Dissimilar Al-alloys by Friction Stir Welding," 2nd International Symposium on Friction Stir Welding, 2000.

[11] W. B. Lee, C. Y. Lee, W. S. Chang, Y. M. Yeon, and S. B. Jung, "Microstructural investigation of friction stir welded pure titanium," Materials Letters, vol. 59, pp. 3315–3318, nov 2005.

[12] F. Y. Ae, H. Fujii, A. E. Takuya, T. Ae, K. Nakata, F. Ye, A. H. Fujii, A. T. Tsumura, and A. K. Nakata, "Friction stir welding of Inconel alloy 600," J Mater Sci, vol. 41, pp. 5376–5379, 2006.

[13] M. M. Z. Ahmed, B. P. Wynne, and J. P. Martin, “Effect of friction stir welding speed on mechanical properties and microstructure of nickel based super alloy Inconel 718,” Science and Technology of Welding and Joining, vol. 18, no. 8, pp. 680–687, 2013.

[14] T. W. Nelson, H. Zhang, and T. Haynes, “Friction Stir Welding of Aluminum MMC 6061-Boron Carbide,” in 2nd International Symposium on Friction Stir Welding, (Gothenburg, Sweden), 2000.

[15] R. Johnson, “Friction Stir Welding of Magnesium Alloys Dr Richard Johnson TWI Ltd, Granta Park, Great Abington, Cambridge CB1 6AL, UK,” Magnesium, 2003.

[16] W. B. Lee and S. B. Jung, “The joint properties of copper by friction stir welding,” Materials Letters, vol. 58, no. 6, pp. 1041–1046, 2004.

[17] G. E. Cook, H. B. Smartt, J. E. Mitchell, A. M. Strauss, and R. Crawford, “Controlling robotic friction stir welding,” Welding Journal (Miami, Fla), vol. 82, pp. 28–34, jun 2003.

[18] R. Johnson and P. Threadgill, “Progress In Friction Stir Welding of Aluminium and Steel For,” in International Conference Hydrodynamics of High Speed Craft, pp. 11–16, 2003.

[19] V. M. Magalhães, C. Leitão, and D. M. Rodrigues, “Friction stir welding industrialisation and research status,” Science and Technology of Welding and Joining, vol. 23, pp. 400–409, jul 2018.

[20] T. Prater, “Welding in space: A comparative evaluation and candidate welding technologies and lessons learned from on-orbit experiments,” Proceedings of the International Astronautical Congress, IAC, vol. 11, pp. 8992–9011, 2013.

[21] B. Christner, J. McCoury, and S. Higgins, “Development and testing of friction stir welding (FSW) as a joining method for primary aircraft structure,” 4th International Symposium on Friction Stir Welding, 2003.

[22] B. Christner and E. A. Corporation, “Friction Stir Welding System Development for Thin-Gauge Aersopace Structures,” 4th International Symposium on Friction Stir Welding, 2003.

[23] D. Burford, P. G. Britos, E. Boldsaikhan, and J. Brown, “Evaluation of Friction Stir Weld Process and Properties for Aerospace Application,” tech. rep., National Institute for Aviation Research, Wichita, KS, oct 2010.

[24] S. W. Kallee, “Friction Stir Welding to Produce Aluminium Components/Panels - TWI,” New Zealand Engineering News, aug 2006.

[25] B. M. Institute, Metallic Materials Properties Development and Standardization (MMPDS-17). Battelle Memorial Institute, 2022.

[26] C. Jones and G. Adams, "Assembly of a full-scale external tank barrel section using friction stir welding," in 1st International Symposium on Friction Stir Welding, vol. 12, (Thousand Oaks, California, USA), pp. 1–10, 1999.

[27] K. Welzyn, J. C. Pilet, D. Diecidue-Conners, M. Worden, and M. Guillot, "External Tank-The Structural Backbone," in JANNAF 6th Liquid Propulsion Subcommittee Meeting, dec 2011.

[28] SpaceX, Falcon User's Guide. SpaceX, 2020.

[29] J. E. Martinez, "Opening Message: Friction stir welding used on the Orion Spacecraft - Fort Wayne Chapter," ASM Industry News, dec 2015.

[30] D. G. S. W M Thomas, S W Kallee and P. J. Oakley, "Friction Stir Welding : Automotive Processes and," in 2006 SAE World Congress, (Detroit, Michigan), pp. 1–15, apr 2006.

[31] Mazda Newsroom, "Mazda develops world's first steel and aluminium joining technology using friction heat," jun 2005.

[32] F. Delany, S. W. Kallee, and M. J. Russell, "Friction stir welding of aluminium plate," in International Forum on Welding Technologies in the Shipping Industry, jun 2007.

[33] Fontaine Trailer Company, "Fontaine Revolution ," 2020.

[34] W. T. Evans, B. T. Gibson, J. T. Reynolds, A. M. Strauss, and G. E. Cook, "Friction Stir Extrusion: A new process for joining dissimilar materials," Manufacturing Letters, vol. 5, pp. 25–28, aug 2015.

[35] P. L. Threadgill, "Terminology in friction stir welding," Science and Technology of Welding and Joining, vol. 12, pp. 357–360, may 2007.

[36] Y. N. Zhang, X. Cao, S. Larose, and P. Wanjara, "Review of tools for friction stir welding and processing," Canadian Metallurgical Quarterly, vol. 51, no. 3, pp. 250–261, 2012.

[37] K. J. Colligan and R. S. Mishra, "A conceptual model for the process variables related to heat generation in friction stir welding of aluminum," Scripta Materialia, vol. 58, no. 5, pp. 327–331, 2008.

[38] D. Jacquin and G. Guillemot, "A review of microstructural changes occurring during FSW in aluminium alloys and their modelling," feb 2021.

[39] O. Frigaard, O. Grong, B. Bjorneklett, and O. Midling, "Modelling of the thermal and microstructure fields during friction stir welding of aluminium alloys," 1st International Symposium on Friction Stir Welding, pp. 1–10, 1999.

[40] W. Tang, X. Guo, J. C. McClure, L. E. Murr, and A. Nunes, “Heat input and temperature distribution in friction stir welding,” Journal of Materials Processing and Manufacturing Science, vol. 7, no. 2, pp. 163–172, 1998.

[41] H. Schmidt, J. Hattel, and J. Wert, “An analytical model for the heat generation in friction stir welding,” Modelling and Simulation in Materials Science and Engineering, vol. 12, no. 1, pp. 143–157, 2004.

[42] J. Schneider, R. Beshears, and A. C. Nunes, “Interfacial sticking and slipping in the friction stir welding process,” Materials Science and Engineering A, vol. 435-436, pp. 297–304, nov 2006.

[43] M. W. Mahoney, C. G. Rhodes, J. G. Flintoff, R. A. Spurling, and W. H. Bingel, “Properties of friction-stir-welded 7075 T651 aluminum,” Metallurgical and Materials Transactions A: Physical Metallurgy and Materials Science, vol. 29, no. 7, pp. 1955–1964, 1998.

[44] A. C. Silva, J. De Backer, and G. Bolmsjö, “Temperature measurements during friction stir welding,” International Journal of Advanced Manufacturing Technology, vol. 88, no. 9-12, pp. 2899–2908, 2017.

[45] A. Fehrenbacher, C. B. Smith, N. A. Duffie, N. J. Ferrier, F. E. Pfefferkorn, and M. R. Zinn, “Combined temperature and force control for robotic friction stir welding,” Journal of Manufacturing Science and Engineering, vol. 136, no. 2, 2014.

[46] A. Fehrenbacher, N. A. Duffie, N. J. Ferrier, F. E. Pfefferkorn, and M. R. Zinn, “Effects of tool-workpiece interface temperature on weld quality and quality improvements through temperature control in friction stir welding,” International Journal of Advanced Manufacturing Technology, vol. 71, no. 1-4, pp. 165–179, 2014.

[47] A. Silva-Magalhães, J. De Backer, J. Martin, and G. Bolmsjö, “In-situ temperature measurement in friction stir welding of thick section aluminium alloys,” Journal of Manufacturing Processes, vol. 39, no. January, pp. 12–17, 2019.

[48] H. Su, C. S. Wu, A. Pittner, and M. Rethmeier, “Thermal energy generation and distribution in friction stir welding of aluminum alloys,” Energy, vol. 77, pp. 720–731, 2014.

[49] J. De Backer, G. Bolmsjö, and A. K. Christiansson, “Temperature control of robotic friction stir welding using the thermoelectric effect,” International Journal of Advanced Manufacturing Technology, vol. 70, no. 1-4, pp. 375–383, 2014.

[50] A. Fehrenbacher, J. R. Schmale, M. R. Zinn, and F. E. Pfefferkorn, “Measurement of tool-workpiece interface temperature distribution in friction stir welding,” Journal of Manufacturing Science and Engineering, vol. 136, no. 2, pp. 1–8, 2014.

[51] K. Colligan, “Material flow behavior during friction stir welding of Aluminum,” Welding Journal, vol. 78, pp. 229–237, 1999.

[52] A. P. Reynolds, “Visualisation of material flow in autogenous friction stir welds,” Science and Technology of Welding and Joining, vol. 5, no. 2, pp. 120–124, 2000.

[53] T. U. Seidel and A. P. Reynolds, “Visualization of the material flow in AA2195 friction-stir welds using a marker insert technique,” Metallurgical and Materials Transactions A: Physical Metallurgy and Materials Science, vol. 32, pp. 2879–2884, nov 2001.

[54] K. N. Krishnan, “On the formation of onion rings in friction stir welds,” Materials Science and Engineering A, vol. 327, pp. 246–251, apr 2002.

[55] W. J. Arbegast, “Modeling friction stir joining as a metal working process,” TMS Annual Meeting, pp. 313–327, 2003.

[56] A. P. Reynolds, “Flow visualization and simulation in FSW,” Scripta Materialia, vol. 58, pp. 338–342, mar 2008.

[57] R. S. Coelho, A. Kostka, J. F. Dos Santos, and A. R. Pyzalla, “EBSD technique visualization of material flow in aluminum to steel friction-stir dissimilar welding,” Advanced Engineering Materials, vol. 10, pp. 1127–1133, dec 2008.

[58] D. G. Hattingh, T. I. Van Niekerk, C. Blignault, G. Kruger, and M. N. James, “Analysis of the FSW Force Footprint and its Relationship with Process Parameters to Optimise Weld Performance and Tool Design,” Welding in the World, vol. 48, pp. 50–58, feb 2004.

[59] N. Balasubramanian, B. Gattu, and R. S. Mishra, “Process forces during friction stir welding of aluminium alloys,” Science and Technology of Welding and Joining, vol. 14, pp. 141–145, feb 2009.

[60] N. Balasubramanian, R. S. Mishra, and K. Krishnamurthy, “Process forces during friction stir channeling in an aluminum alloy,” Journal of Materials Processing Technology, vol. 211, pp. 305–311, feb 2011.

[61] X. Pei and P. Dong, “A selectively-coupled shear localization model for friction stir welding process window estimation,” International Journal of Machine Tools and Manufacture, vol. 123, pp. 89–104, dec 2017.

[62] S. R. Ren, Z. Y. Ma, and L. Q. Chen, “Effect of welding parameters on tensile properties and fracture behavior of friction stir welded Al-Mg-Si alloy,” Scripta Materialia, vol. 56, no. 1, pp. 69–72, 2007.

[63] F. C. Liu and Z. Y. Ma, “Influence of tool dimension and welding parameters on microstructure and mechanical properties of friction-stir-welded 6061-T651 aluminum alloy,” Metallurgical and Materials Transactions A: Physical Metallurgy and Materials Science, vol. 39, pp. 2378–2388, oct 2008.

[64] J. Q. Su, T. W. Nelson, R. Mishra, and M. Mahoney, “Microstructural investigation of friction stir welded 7050-T651 aluminium,” Acta Materialia, vol. 51, no. 3, pp. 713–729, 2003.

[65] K. S. Arora, S. Pandey, M. Schaper, and R. Kumar, “Effect of process parameters on friction stir welding of aluminum alloy 2219-T87,” International Journal of Advanced Manufacturing Technology, vol. 50, pp. 941–952, oct 2010.

[66] F. Humphreys and M. Hatherly, Recrystallization and Related Annealing Phenomena. Oxford, UK: Elsevier, 2nd ed., 2004.

[67] K. Huang and R. E. Logé, “A review of dynamic recrystallization phenomena in metallic materials,” dec 2016.

[68] K. V. Jata and S. L. Semiatin, “Continuous dynamic recrystallization during friction stir welding of high strength aluminum alloys,” Scripta Materialia, vol. 43, pp. 743–749, feb 2000.

[69] A. L. Etter, T. Baudin, N. Fredj, and R. Penelle, “Recrystallization mechanisms in 5251 H14 and 5251 O aluminum friction stir welds,” Materials Science and Engineering A, vol. 445-446, pp. 94–99, 2007.

[70] P. Yu, C. S. Wu, and L. Shi, “Analysis and characterization of dynamic recrystallization and grain structure evolution in friction stir welding of aluminum plates,” Acta Materialia, vol. 207, 2021.

[71] A. P. Reynolds and F. Duvall, “Digital image correlation for determination of weld and base metal constitutive behavior,” Welding Journal (Miami, Fla), vol. 78, no. 10, pp. 355–s, 1999.

[72] W. D. Lockwood, B. Tomaz, and A. P. Reynolds, “Mechanical response of friction stir welded AA2024: Experiment and modeling,” Materials Science and Engineering A, vol. 323, no. 1-2, pp. 348–353, 2002.

[73] N. Dialami, M. Cervera, and M. Chiumenti, “Defect formation and material flow in Friction Stir Welding,” European Journal of Mechanics, A/Solids, vol. 80, no. November 2019, p. 103912, 2020.

[74] Y. G. Kim, H. Fujii, T. Tsumura, T. Komazaki, and K. Nakata, “Three defect types in friction stir welding of aluminum die casting alloy,” Materials Science and Engineering A, vol. 415, pp. 250–254, jan 2006.

[75] A. K. Lakshminarayanan, S. Malarvizhi, and V. Balasubramanian, “Developing friction stir welding window for AA2219 aluminium alloy,” Transactions of Nonferrous Metals Society of China (English Edition), vol. 21, pp. 2339–2347, nov 2011.

[76] K. Kumar and S. V. Kailas, “The role of friction stir welding tool on material flow and weld formation,” Materials Science and Engineering A, vol. 485, no. 1-2, pp. 367–374, 2008.

[77] W. J. Arbegast, “A flow-partitioned deformation zone model for defect formation during friction stir welding,” Scripta Materialia, vol. 58, pp. 372–376, mar 2008.

[78] C. Chen, R. Kovacevic, and D. Jandgric, “Wavelet transform analysis of acoustic emission in monitoring friction stir welding of 6061 aluminum,” International Journal of Machine Tools and Manufacture, vol. 43, pp. 1383–1390, oct 2003.

[79] C. Chen, R. Kovacevic, and D. Jandgric, “Acoustic Emission in Monitoring Quality of Weld in Friction Stir Welding,” 4th International Symposium on Friction Stir Welding, no. May, pp. 1–14, 2003.

[80] Y. Yang, P. Kalya, R. G. Landers, and K. Krishnamurthy, “Automatic gap detection in friction stir butt welding operations,” International Journal of Machine Tools and Manufacture, vol. 48, pp. 1161–1169, aug 2008.

[81] E. Boldsaikhan, E. M. Corwin, A. M. Logar, and W. J. Arbegast, “The use of neural network and discrete Fourier transform for real-time evaluation of friction stir welding,” Applied Soft Computing Journal, vol. 11, pp. 4839–4846, dec 2011.

[82] B. T. Gibson, W. Tang, A. G. Peterson, Z. Feng, and G. J. Frederick, “Evaluating the Potential for Remote In-Process Monitoring of Tool Wear in Friction Stir Welding of Stainless Steel,” Journal of Manufacturing Science and Engineering, Transactions of the ASME, vol. 140, feb 2018.

[83] B. Gibson, G. Cook, T. Prater, W. Longhurst, A. M. Strauss, and C. D. Cox, “Adaptive torque control of friction stir welding for the purpose of estimating tool wear,” Proceedings of the Institution of Mechanical Engineers, Part B: Journal of Engineering Manufacture, vol. 225, no. 8, pp. 1293–1303, 2011.

[84] B. T. Gibson, Custom Low-Cost Force Measurement Methods in Friction Stir Welding. PhD thesis, Vanderbilt University, 2011.

[85] B. T. Gibson, C. D. Cox, W. R. Longhurst, A. M. Strauss, and G. E. Cook, “Exploiting robotic link deflection for low-cost force measurement in manufacturing,” Measurement: Journal of the International Measurement Confederation, vol. 45, pp. 140–143, jan 2012.

[86] Z. Loftus, R. Venable, and G. Adams, “Development and implementation of a load controlled friction stir welder loop,” 1st International Symposium on Friction Stir Welding, pp. 1–6, 1999.

[87] R. Talwar, D. Bolser, R. Lederich, and J. Baumann, "Friction Stir Welding of Airframe Structures," in 2nd International Symposium on Friction Stir Welding, (Gothenburg, Sweden), 2000.

[88] C. B. Smith, "Robotic Friction Stir Welding using a Standard Industrial Robot," in 2nd International Symposium on Friction Stir Welding, (Gothenburg, Sweden), 2000.

[89] A. von Strombeck, C. Schilling, and J. F. dos Santos, "Robotic Friction Stir Welding – Tool Technology and Applications," 2nd International Symposium on Friction Stir Welding, pp. 1–13, 2000.

[90] A. Fehrenbacher, J. R. Schmale, M. R. Zinn, and F. E. Pfefferkorn, "Tool-Workpiece Interface Temperature Measurement in Friction Stir Welding," in ASME 2012 International Manufacturing Science and Engineering Conference, (Huntsville, Alabama, USA), pp. 169–178, American Society of Mechanical Engineers, jun 2012.

[91] W. R. Longhurst, A. M. Strauss, G. E. Cook, C. D. Cox, C. E. Hendricks, B. T. Gibson, and Y. S. Dawant, "Investigation of force-controlled friction stir welding for manufacturing and automation," Proceedings of the Institution of Mechanical Engineers, Part B: Journal of Engineering Manufacture, vol. 224, no. 6, pp. 937–949, 2010.

[92] W. R. Longhurst, A. M. Strauss, and G. E. Cook, "Enabling automation of friction stir welding: The modulation of weld seam input energy by traverse speed force control," Journal of Dynamic Systems, Measurement and Control, Transactions of the ASME, vol. 132, no. 4, pp. 1–11, 2010.

[93] W. R. Longhurst, A. M. Strauss, G. E. Cook, and P. A. Fleming, "Torque control of friction stir welding for manufacturing and automation," International Journal of Advanced Manufacturing Technology, vol. 51, pp. 905–913, dec 2010.

[94] G. Buffa, D. Campanella, A. Forcellese, L. Fratini, M. Simoncini, and A. Barcellona, "Constant Heat Input Friction Stir Welding of Variable Thickness AZ31 Sheets through In-Process Tool Rotation Control," Journal of Manufacturing Science and Engineering, Transactions of the ASME, vol. 141, aug 2019.

[95] D. W. Mayfield and C. D. Sorensen, "An Improved Temperature Control Algorithm for Friction Stir Processing.pdf," in 8th International Symposium on Friction Stir Welding, pp. 918–933, 2010.

[96] K. Ross and C. Sorensen, "Paradigm shift in control of the spindle axis," in Friction Stir Welding and Processing VII, pp. 321–328, Springer International Publishing, jan 2016.

[97] L. Cederqvist, O. Garpinger, T. Hägglund, and A. Robertsson, "Cascade control of the friction stir welding process to seal canisters for spent nuclear fuel," Control Engineering Practice, vol. 20, pp. 35–48, jan 2012.

[98] A. Bachmann, J. Gamper, M. Krutzlinger, A. Zens, and M. F. Zaeh, “Adaptive model-based temperature control in friction stir welding,” International Journal of Advanced Manufacturing Technology, vol. 93, pp. 1157–1171, oct 2017.

[99] J. De Backer, A.-K. Christiansson, J. Oqueka, and G. Bolmsjo, “Investigation of Path Compensation Methods for Robotic Friction Stir Welding,” Industrial Robot: An International Journal, vol. 39, pp. 601–608, oct 2012.

[100] P. A. Fleming, D. H. Lammlein, D. M. Wilkes, G. E. Cook, A. M. Strauss, D. R. DeLapp, and D. A. Hartman, “Misalignment detection and enabling of seam tracking for friction stir welding,” Science and Technology of Welding and Joining, vol. 14, no. 1, pp. 93–96, 2009.

[101] P. A. Fleming, C. E. Hendricks, G. E. Cook, D. M. Wilkes, A. M. Strauss, and D. H. Lammlein, “Seam-tracking for friction stir welded lap joints,” Journal of Materials Engineering and Performance, vol. 19, pp. 1128–1132, nov 2010.

[102] B. T. Gibson, C. D. Cox, M. C. Ballun, G. E. Cook, and A. M. Strauss, “Automatic tracking of blind sealant paths in friction stir lap joining,” Journal of Aircraft, vol. 51, pp. 824–832, may 2014.

[103] B. Jay Thomas Reynolds, A. M. Strauss, and G. E. Cook, Improvements in Friction Stir Welding Control System and an Extremum Controller for Tracking Friction Stir Extrusion Process. PhD thesis, Vanderbilt University, dec 2017.

[104] R. S. Mishra, P. S. De, and N. Kumar, Friction stir welding and processing: Science and engineering, vol. 9783319070. Springer International Publishing, 2014.

[105] A. Sadeghian and N. Iqbal, “A review on dissimilar laser welding of steel-copper, steel-aluminum, aluminum-copper, and steel-nickel for electric vehicle battery manufacturing,” Optics and Laser Technology, vol. 146, no. May 2021, p. 107595, 2022.

[106] M. S. W glowski, S. Błacha, and A. Phillips, “Electron beam welding - Techniques and trends - Review,” Vacuum, vol. 130, pp. 72–92, 2016.

[107] A. Sahoo and S. Tripathy, “Development in plasma arc welding process: A review,” Materials Today: Proceedings, vol. 41, pp. 363–368, 2019.

[108] Z. Sun and R. Karppi, “The application of electron beam welding for the joining of dissimilar metals: An overview,” Journal of Materials Processing Technology, vol. 59, no. 3 SPEC. ISS., pp. 257–267, 1996.

[109] D. Wu, H. Li, Y. Yang, X. Cai, L. Wang, and D. Sun, “Plasma arc welding of dissimilar ultrahigh-strength steel and aluminum alloy assisted by copper transition layer,” Materials Letters, vol. 318, no. March, pp. 7–10, 2022.

[110] X. Liu, S. Zhao, K. Chen, and J. Ni, “Material flow visualization of dissimilar friction STIR welding process using nano-computed tomography,” Journal of Manufacturing Science and Engineering, Transactions of the ASME, vol. 140, nov 2018.

[111] S. Jana, Y. Hovanski, and G. J. Grant, “Friction stir lap welding of magnesium alloy to steel: A preliminary investigation,” Metallurgical and Materials Transactions A: Physical Metallurgy and Materials Science, vol. 41, pp. 3173–3182, dec 2010.

[112] H. A. Khan, J. Li, and C. Shao, “Analyses of Friction Stir Riveting Processes: A Review,” Journal of Manufacturing Science and Engineering, Transactions of the ASME, vol. 139, sep 2017.

[113] X. He, I. Pearson, and K. Young, “Self-pierce riveting for sheet materials: State of the art,” apr 2008.

[114] Y. W. Ma, Y. B. Li, B. E. Carlson, and Z. Q. Lin, “Effect of process parameters on joint formation and mechanical performance in friction stir blind riveting of aluminum alloys,” Journal of Manufacturing Science and Engineering, Transactions of the ASME, vol. 140, jun 2018.

[115] C. Van Der Rest, P. J. Jacques, and A. Simar, “On the joining of steel and aluminium by means of a new friction melt bonding process,” Scripta Materialia, vol. 77, pp. 25–28, apr 2014.

[116] C. Y. Lee, D. H. Choi, Y. M. Yeon, and S. B. Jung, “Dissimilar friction stir spot welding of low carbon steel and Al-Mg alloy by formation of IMCs,” Science and Technology of Welding and Joining, vol. 14, pp. 216–220, apr 2009.

[117] M. Watanabe, K. Feng, Y. Nakamura, and S. Kumai, “Growth manner of intermetallic compound layer produced at welding interface of friction stir spot welded aluminum/steel lap joint,” Materials Transactions, vol. 52, pp. 953–959, may 2011.

[118] W. T. Evans, C. Cox, B. T. Gibson, A. M. Strauss, and G. E. Cook, “Two-sided friction stir riveting by extrusion: A process for joining dissimilar materials,” Journal of Manufacturing Processes, vol. 23, pp. 115–121, aug 2016.

[119] W. Thomas, “Friction Stir Welding and Related Process Characteristics,” in INALCO ’98, 7 th International Conference on Joints in Aluminium, no. April, (Cambridge), 1998.

[120] T. Nishihara, “Development of friction stir forming,” Materials Science Forum, vol. 426-432, pp. 2971–2978, aug 2003.

[121] D. Staines, W. Thomas, S. W. Kallee, and P. Oakley, “Friction stir technology - recent developments in process variants and applications,” 2006.

[122] I. David, J. Rose, K. S. Us, and K. S. Us, "United States Patent Hovanski et al.," US Patent US8434661 B2, vol. 1, jun 2015.

[123] P. Upadhyay, Y. Hovanski, L. S. Fifield, and K. L. Simmons, "Friction stir lap welding of aluminum - polymer using scribe technology," in Friction Stir Welding and Processing VIII, pp. 153–161, Cham: Springer International Publishing, 2016.

[124] P. Upadhyay, Y. Hovanski, B. Carlson, E. Boettcher, R. Ruokolainen, and P. Busuttil, "Joining Dissimilar Material Using Friction Stir Scribe Technique," in Friction Stir Welding and Processing IX, pp. 147–155, Springer, Cham, 2017.

[125] T. Curtis, C. Widener, M. West, B. Jasthi, Y. Hovanski, B. Carlson, R. Szymanski, and W. Bane, "Friction stir scribe welding of dissimilar aluminum to steel lap joints," in Friction Stir Welding and Processing VIII, pp. 163–169, Cham: Springer International Publishing, 2016.

[126] P. Upadhyay, Y. Hovanski, S. Jana, and L. S. Fifield, "Joining dissimilar materials using friction stir scribe technique," Journal of Manufacturing Science and Engineering, Transactions of the ASME, vol. 139, mar 2017.

[127] M. Reza-E-Rabby, M. J. Olszta, N. R. Overman, M. McDonnell, and S. A. Whalen, "Friction stir dovetailing of AA7099 to steel with AA6061 interlayer for reduced Zn embrittlement at dissimilar interface," Journal of Manufacturing Processes, vol. 61, pp. 25–34, jan 2021.

[128] M. Reza-E-Rabby, K. Ross, M. McDonnell, and S. A. Whalen, "Numerical simulation and experimental validation of joint performance in aluminum-steel lap welds formed by friction stir dovetailing," Journal of Materials Processing Technology, vol. 277, p. 116459, mar 2020.

[129] M. Reza-E-Rabby, K. Ross, N. R. Overman, M. J. Olszta, M. McDonnell, and S. A. Whalen, "Joining thick section aluminum to steel with suppressed FeAl intermetallic formation via friction stir dovetailing," Scripta Materialia, vol. 148, pp. 63–67, apr 2018.

[130] M. Reza-E-Rabby, K. Ross, S. Whalen, Y. Hovanski, and M. McDonnell, "Solid-State Joining of Thick-Section Dissimilar Materials Using a New Friction Stir Dovetailing (FSD) Process," in Friction Stir Welding and Processing IX, pp. 67–77, Springer International Publishing, 2017.

[131] T. Ohashi, T. Ohno, H. M. Tabatabaei, and T. Nishihara, "Pseudo linear joining for dissimilar materials utilizing punching and friction stir forming," in Procedia Manufacturing, vol. 50, pp. 98–103, Elsevier B.V., jan 2020.

[132] E. E. Patterson, Y. Hovanski, and D. P. Field, "Microstructural Characterization of Friction Stir Welded Aluminum-Steel Joints," Metallurgical and Materials Transactions A: Physical Metallurgy and Materials Science, vol. 47, pp. 2815–2829, jun 2016.

[133] E. I. Barker, P. Upadhyay, Y. Hovanski, and X. Sun, “Predicting Lap Shear Strength for Friction Stir Scribe Joining of Dissimilar Materials,” Friction Stir Welding and Processing IX, pp. 261–267, 2017.

[134] G. E. Cook, R. Crawford, D. E. Clark, and A. M. Strauss, “Robotic friction stir welding,” Industrial Robot, vol. 31, pp. 55–63, feb 2004.

[135] S. Jana and Y. Hovanski, “Fatigue behaviour of magnesium to steel dissimilar friction stir lap joints,” Science and Technology of Welding and Joining, vol. 17, pp. 141–145, feb 2012.

[136] A. W. Jarrell, A. M. Strauss, and G. E. Cook, “Dissimilar Metal T-Joint of Aluminum and Steel Formed by Friction Stir Extrusion,” in Minerals, Metals and Materials Series, pp. 91–96, Springer, Cham, 2017.

[137] Y. Huang, T. Huang, L. Wan, X. Meng, and L. Zhou, “Material flow and mechanical properties of aluminum-to-steel self-riveting friction stir lap joints,” Journal of Materials Processing Technology, vol. 263, pp. 129–137, jan 2019.

[138] L. Calabrese, E. Proverbio, E. Pollicino, G. Galtieri, and C. Borsellino, “Effect of Galvanic corrosion on durability of aluminium/steel self-piercing rivet joints,” Corrosion Engineering Science and Technology, vol. 50, pp. 10–17, feb 2015.

[139] B. T. Gibson, D. M. Wilkes, G. E. Cook, and A. M. Strauss, “In-process detection of faying surface sealant application flaws in friction stir welding,” Journal of Aircraft, vol. 50, pp. 567–575, mar 2013.

[140] Z. L. Hu, H. Y. Yu, and Q. Pang, “Investigation of Interfacial Layer for Friction Stir Welded AA7075-T6 Aluminum to DP1180 Steel Joints,” Journal of Manufacturing Science and Engineering, Transactions of the ASME, vol. 142, sep 2020.

[141] Y. Li, Z. Wei, Z. Wang, and Y. Li, “Friction self-piercing riveting of aluminum alloy AA6061-T6 to magnesium alloy AZ31B,” Journal of Manufacturing Science and Engineering, vol. 135, dec 2013.

[142] Y. W. Ma, Y. B. Li, and Z. Q. Lin, “Joint formation and mechanical performance of friction self-piercing riveted aluminum alloy AA7075-T6 joints,” Journal of Manufacturing Science and Engineering, Transactions of the ASME, vol. 141, apr 2019.

[143] K. Chen, X. Liu, and J. Ni, “Friction Stir Resistance Spot Welding of Aluminum Alloy to Advanced High Strength Steel,” Journal of Manufacturing Science and Engineering, Transactions of the ASME, vol. 140, nov 2018.

[144] ASM Handbook Committee, ed., Heat Treating of Aluminum Alloys. ASM International, 1991.

[145] R. Shi, D. Wang, and Y. Wang, ASM Handbook Volume 4E: Heat Treating of Nonferrous Alloys. ASM International, 2016.

[146] A. C. Nunes Jr., "Metal flow in friction stir welding," Materials Science and Technology 2006/ASM International, pp. 15–19, jan 2006.

[147] M. Hakem, S. Lebaili, S. Mathieu, D. Miroud, A. Lebaili, and B. Cheniti, "Effect of microstructure and precipitation phenomena on the mechanical behavior of AA6061-T6 aluminum alloy weld," International Journal of Advanced Manufacturing Technology, vol. 102, no. 9-12, pp. 2907–2918, 2019.

[148] A. C. Muñoz, G. Rückert, B. Huneau, X. Sauvage, and S. Marya, "Comparison of TIG welded and friction stir welded Al-4.5Mg-0.26Sc alloy," Journal of Materials Processing Technology, vol. 197, pp. 337–343, feb 2008.

[149] Y. C. Chen, D. Bakavos, A. Gholinia, and P. B. Prangnell, "HAZ development and accelerated post-weld natural ageing in ultrasonic spot welding aluminium 6111-T4 automotive sheet," Acta Materialia, vol. 60, no. 6-7, pp. 2816–2828, 2012.

[150] M. J. Jones, P. Heurtier, C. Desrayaud, F. Montheillet, D. Allehaux, and J. H. Driver, "Correlation between microstructure and microhardness in a friction stir welded 2024 aluminium alloy," Scripta Materialia, vol. 52, pp. 693–697, apr 2005.

[151] F. Armao, "Aluminum Workshop: Achieving T6 designation for 6061 - The Fabricator," 2011.

[152] G. İpekoğlu and G. Çam, "Effects of initial temper condition and postweld heat treatment on the properties of dissimilar friction-stir-welded joints between AA7075 and AA6061 aluminum alloys," Metallurgical and Materials Transactions A: Physical Metallurgy and Materials Science, vol. 45, pp. 3074–3087, mar 2014.

[153] ASM, ASM handbook Volume 2 - Properties and selection: Nonferrous alloys and special-purpose materials, vol. 2. ASM International, 1993.

[154] F. Gagliardi, G. Ambrogio, R. Conte, and P. Russo, "Investigation of friction stir forming for mechanical interlocking high-performance polymers and aluminium sheets," Manufacturing Letters, vol. 27, pp. 31–38, jan 2021.

[155] T. Nishihara and A. Ito, "Measurement of die temperature during friction stir forming," Welding in the World, vol. 49, no. 3-4, pp. 22–26, 2005.

[156] W. T. Evans, G. E. Cook, and A. M. Strauss, "Joining Aerospace Aluminum 2024-T4 to Titanium by Friction Stir Extrusion," Friction Stir Welding and Processing IX, pp. 79–89, 2017.

[157] A. W. Jarrell, J. Cui, A. M. Strauss, and G. E. Cook, “Friction stir extrusion of thin sheet stock,” Manufacturing Letters, vol. 24, pp. 38–42, mar 2020.

[158] C. Strawn and A. M. Strauss, “Friction stir extrusion of aluminum AA6061 into isostatically molded graphite,” Journal of Manufacturing Processes, vol. 69, pp. 391–397, sep 2021.

[159] D. Mishra, R. B. Roy, S. Dutta, S. K. Pal, and D. Chakravarty, “A review on sensor based monitoring and control of friction stir welding process and a roadmap to Industry 4.0,” Journal of Manufacturing Processes, vol. 36, pp. 373–397, dec 2018.

[160] J. W. Pew, T. W. Nelson, and C. D. Sorensen, “Torque based weld power model for friction stir welding,” Science and Technology of Welding and Joining, vol. 12, no. 4, pp. 341–347, 2007.

[161] W. R. Longhurst, A. M. Strauss, and G. E. Cook, “The identification of the key enablers for force control of robotic friction stir welding,” Journal of Manufacturing Science and Engineering, Transactions of the ASME, vol. 133, pp. 1–11, jun 2011.

[162] A. C. Nunes, E. L. Bernstein, and J. C. McClure, “A rotating plug model for friction stir welding,” in 81st American Welding Society Annual Convention, (Las Vegas, NV), 2000.

[163] N. Balasubramanian, B. Gattu, and R. S. Mishra, “Process forces during friction stir welding of aluminium alloys Process forces during friction stir welding of aluminium alloys,” Science and Technology of Welding and Joining, vol. 14, no. 2, pp. 141–145, 2013.

[164] H. N. Schmidt, T. L. Dickerson, and J. H. Hattel, “Material flow in butt friction stir welds in AA2024-T3,” Acta Materialia, vol. 54, pp. 1199–1209, feb 2006.

[165] N. Mendes, P. Neto, A. Loureiro, and A. P. Moreira, “Machines and control systems for friction stir welding: A review,” Materials and Design, vol. 90, pp. 256–265, jan 2016.

[166] A. Rout, B. B. Deepak, and B. B. Biswal, “Advances in weld seam tracking techniques for robotic welding: A review,” Robotics and Computer-Integrated Manufacturing, vol. 56, pp. 12–37, apr 2019.

[167] P. A. Fleming, C. E. Hendricks, D. M. Wilkes, G. E. Cook, and A. M. Strauss, “Automatic seam-tracking of friction stir welded T-joints,” The International Journal of Advanced Manufacturing Technology 2009 45:5, vol. 45, pp. 490–495, mar 2009.

[168] B. T. Gibson, D. H. Lammlein, T. J. Prater, W. R. Longhurst, C. D. Cox, M. C. Ballun, K. J. Dharmaraj, G. E. Cook, and A. M. Strauss, “Friction stir welding:

Process, automation, and control," Journal of Manufacturing Processes, vol. 16, pp. 56–73, jan 2014.

[169] D. Eberly, "Moving Along a Curve with Specified Speed," apr 2019.

[170] J. A. Schneider and A. C. Nunes, "Characterization of plastic flow and resulting microtextures in a friction stir weld," Metallurgical and Materials Transactions B: Process Metallurgy and Materials Processing Science, vol. 35, no. 4, pp. 777–783, 2004.

Appendix A

Modifications to VUWAL's Friction Stir Welding Machine

The Friction Stir Welding machine used at VUWAL is a in-house developed machine. The lab has ”full stack” control over the hardware and software. Therefore, the machine tends to evolve with the changing needs of the lab. With each change, documentation is needed to insure that the machine remains operable to the next generation of students.

The research presented in this document has more demanding positional and speed control than previously done. So, a significant portion of the positional feedback system was redesigned to match the needs of the research. Additionally, modifications to improve data integrity across the machine as a whole has been undertaken. Many mechanical and electrical issues were also evaluated and mitigated. All changes to the hardware or software on the welder have been documented in these Appendices as well as any unique data analysis technique. The goal is for future generations of grad students to be able to replicate the work presented here as well as build off modifications preformed.

A.1 Hardware

A 1944 Kern and Trecker Model K milling machine provided the bases for VUWAL's friction stir welding machine. Prior generations of grad students motorized all three axis of the machine all three axis and built a data acquisition system to automate welds and record processing forces during welds. The mechanical system has largely remained unchanged for a long time. Some, maintenance needs to be done to replace or rebuild warn components, However, some mitigation strategies are listed here.

Numerous changes took place within the data acquisition and control portions of the welder. The block diagram before any of the changes detailed bellow follows that presented in Jay Reynolds thesis, Figure A.1 [103]. His work focused around the addition of a real-time control computer. The transition to a real-time target to manage motor control during welding increased the reliability and safety of the system.

After modifications were complete the block diagram of the system is presented in Figure A.2. The sensor box was completely replaced to a more expandable and robust system with off the shelf components and full schematics for any custom built electronics. The change of the sensor box necessitated several modifications to the connections. The four hall effect rotational sensors were removed and two sets of photointerupter encoders were put in their place.

A.1.1 Sensor Box

One of the major changes to the system was a complete redesign of the sensor box. A new signal conditioning/instrumentation case was constructed to improve data acquisition and simplify wiring. The case was plasma cut from 20 gauge steel and bent on a metal break. Mounting points for both BNC connectors and TE Connectivity's AMP Barrel connectors were cut into the back of the case, allowing for flexibility in the future use of the case, Figure A.3. A large cut out allowed for the installation of an ATX computer power supply. The case provided mount points for positional feedback circuitry and spindle oilier circuitry. The design of the electronics within will be detailed bellow. The computer ATX power supply provided power for the whole system. ATX power supplies provide a range of useful voltages (-12v, 3.3v, 5v, and 12v) with high current capacity. They are widely available and typically have good efficiency and regulation. Breakout board for the 24 pin power header are commercially available and proved access to all the voltages produced by the supply.

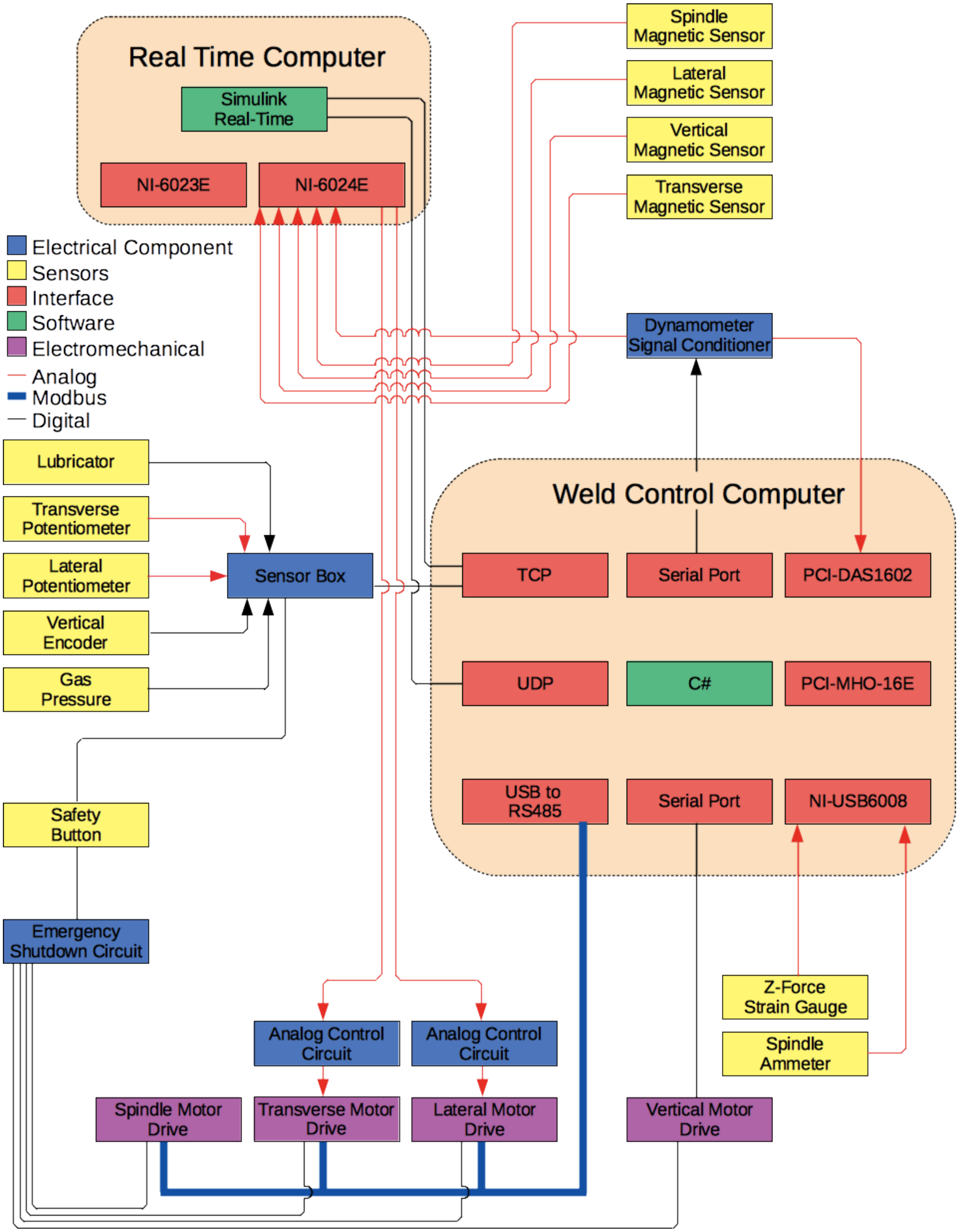

Figure A.1: Block diagram of the welder before the modifications detail in the appendix.

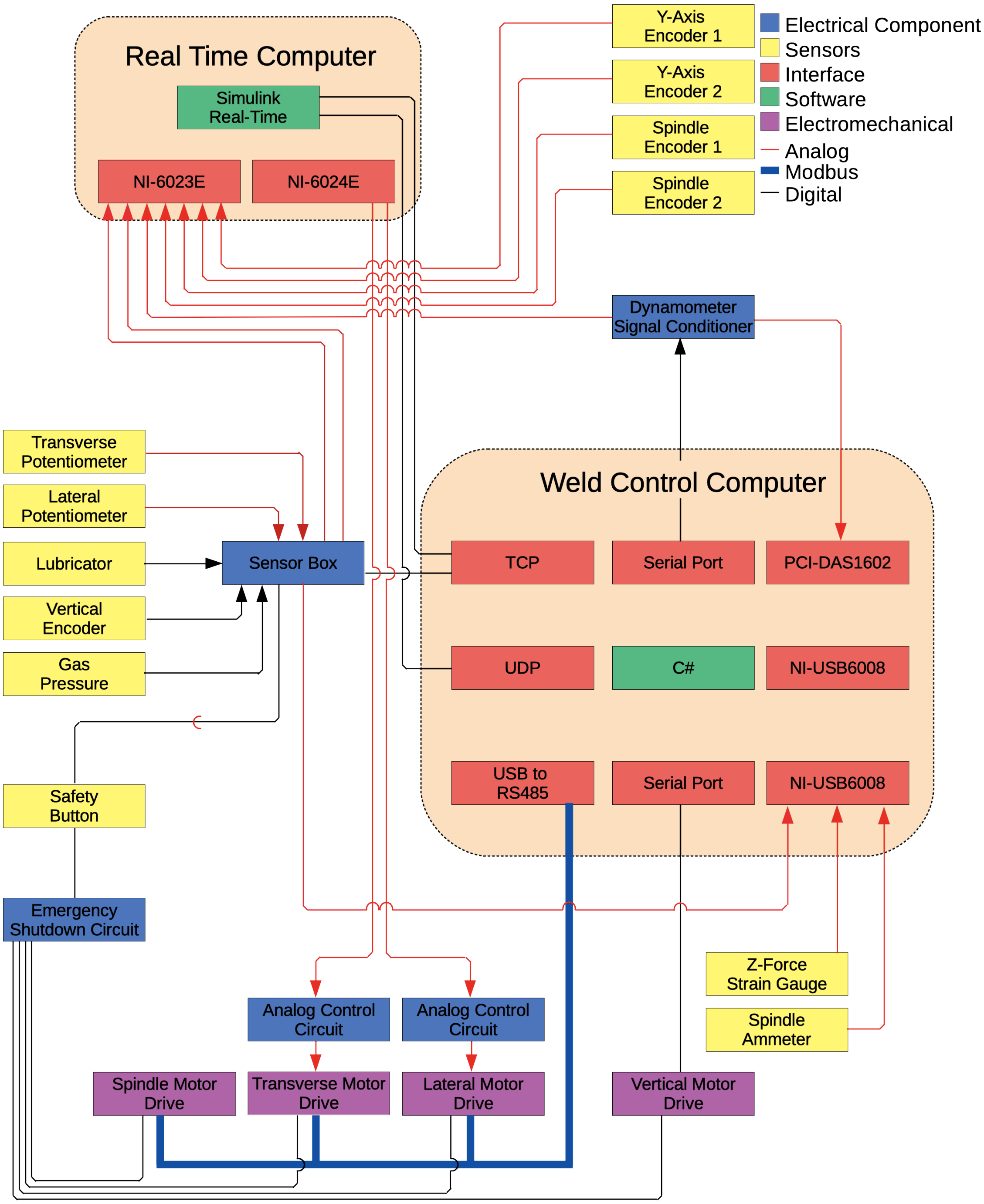

Figure A.2: Block diagram of the welder after modifications detailed in the appendix

Figure A.3: Render of the case constructed to hold the power supply and signal conditioning for the positional feedback system.

A.1.2 Reprogramming of the Transverse and Lateral VFDs

During a weld, the Transverse and Lateral VFD's output frequencies are controlled by a voltage output from the Control computer. This reduces latency that occur when commands come from the GUI computer and Modbus.

The transverse and lateral Axis VFD's Minimum outpout frequency was reduced to allow for more accurate path following. A side effect was that when either the transverse or lateral axis was set to a speed of 0 ipm, the axis would drift in one direction. The drift proved to be particularly problematic when implementing a path following algorithm.

It was determined that the analog control signal was the cause. The signal is generated from the NI-6024E DAQ in the control computer and sent via a CAT-5 cable to the motor control box. When measured at the DAQ 0 IPM resulted in a 0 volt signal. However at the cable end, .250 volts were measured. It was assumed that EMF from the other Motor Axis was causing the induced voltage. To eliminate the induced voltage, the CAT-5 cable was replaced with a shielded Coaxial cable, RG-58. The cable cut down on inducted noise in the long cable run.

The second step was to create a deadzone into the VFDs' output frequency to Volts relationship. The deadzone extended from $-.25$ V to .25 V volts. To determine the output frequency to input voltage relationship, the VFD output frequency to desired IMP needed to be defined. One point was already determined, 0 Hz or .25 V means 0 IMP. The desired maximum speed for each axis was 15 IMP.

Both transverse and lateral lead screws are 4 threads per inch, so one revolution equates to .250 inches of table travel. With gearing between the motor and lead screw, the transverse axis advances 0.0118" per revolution of the motor, and the lateral axis advances 0.0415" per revolution of the motor. Therefore, The transverse and lateral axis motors must turn at 1271 RPM and 361.5 RPM respectively to meet the 15 IPM target.

The relationship between input frequency frequency and RPM of an induction motor is given by

$$RPM = \frac{120\nu}{p}, \tag{A.1}$$

where ν is the frequency of the input voltage, and p is the number of poles of the motor. Solving for ν, transverse and lateral VFDs must have an output frequency of 42.4 Hz and 12 Hz. Due to limitations with the VFD interface, The output frequency had to be increased to 50 Hz.

With all of this factored in, We can calculate the top speed of the transverse axis to be 17.7 ipm and lateral axis to be 62.25 ipm. From Equation A.1, It can be determined that the max synchronous RPM of the 4 pole 3 phase induction motors is 1500 rpm.

The relationship between voltage and frequency can be developed using the maximum frequency. In addition to the first point of 0 Hz at .25 Volts, a second point of the max calculated frequency at 10 Volts can be added. These two points can be used to find m and b in the following Equation:

$$\nu = mv + b. \tag{A.2}$$

The VFDs' Voltage to output frequency relationship are dictated by six settings:

20.06 - Minimum Output Frequency - Range 0.1 to 20 Hz

20.07 - Maximum Output Frequency - Range 50 to 400 Hz

30.07 - Potentiometer Offset - Range 0 to 100 percent

30.08 - Bias Polarity - Range 0 or 1

30.09 - Potentiometer Slope - Range 0.1 to 300 percent

30.10 - Potentiometer Direction - Range 0 or 1

	Transverse	Lateral
20.07	50.0	50.0
30.07	2.6	0.4
30.08	1	1
30.09	102.6	21.3
30.10	0	0

Table A.1: Current settings for the Transverse and Lateral analog control.

The maximum output frequency and Potentiometer offset can be related by

$$30.07 = \frac{\text{offset in Hz}}{20.07} \tag{A.3}$$

Where the numerator is the desired frequency offset in Hz. These settings can be related to m and b by the following relationships:

$$m = 30.09(\frac{20.07}{10}) \tag{A.4}$$

and,

$$b = (20.07)(30.07)(-1)^{30.08}. \tag{A.5}$$

The target values of m and b had to be slightly modified to match the range and precision of the six VFD parameters. The final values of the VFD settings are contained in Table A.1. The resultant axial speed to output voltage relationships for both the transverse and lateral axis are displayed in Figure A.4.

The desired IPM is set by the state space block of the MatLab Simulink weld program. Then, the commanded IPM is routed to the output stage of the program. Using the gearing ratio and topology of motor, the associated input frequency is determined. Then, the above developed relationship between Frequency and Voltage is used to determine output voltage. The values of $1/m$ and $-b/m$ from equation A.2 solved for v was entered into the Simulink Control model to convert between desired

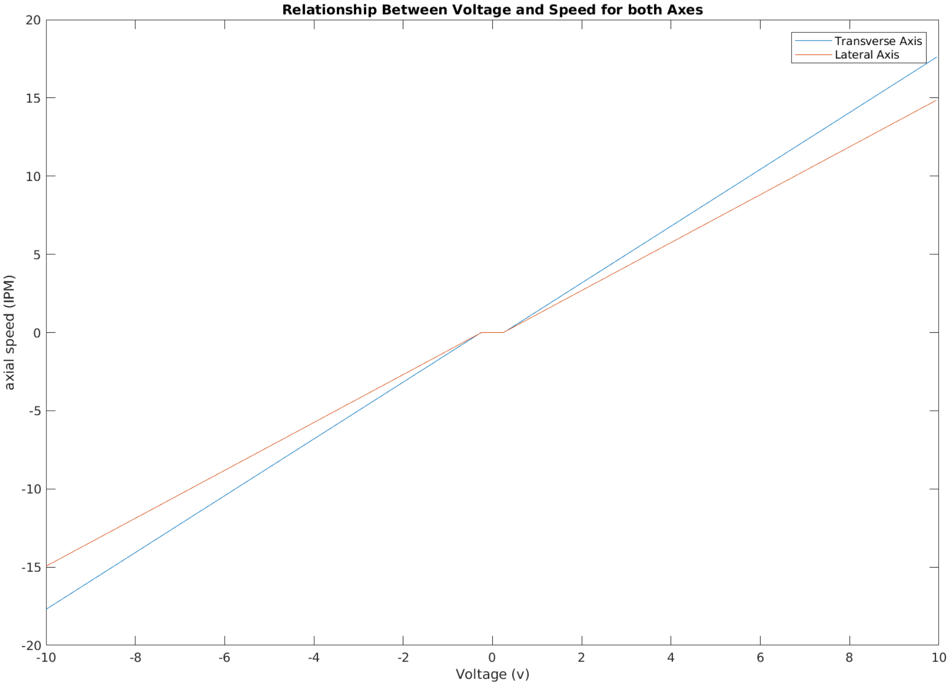

Figure A.4: Voltage to speed of the axis currently programmed into the transverse and lateral axis.

IPM and Output voltage. Finally, Output protection is used to saturate the signal outside of -10 to 10 volts to avoid damage to hardware. The output voltage is written to the DAQ's analog outputs.

A.1.3 Improvements in the XY potentiometer feedback

XY positional feedback is provided through a pair of string potentiometer. The transducers have a linear relationship between the extension of the string and the wiper voltage, when a constant voltage is supplied to the potentiometer. The potentiometers are fixed to one end of the axis and the end of the string to the other. Therefore, the voltage at the wiper is related to the absolute position of the axis.

The power supply and data acquisition system was not sufficient for the control schemes planned. The transducer was supplied through a 12 volt switch mode power supply. Therefore, the output range of the potentiometer was 0-12 volts. The voltage from both potentiometers were measured by a single board computer based on the Rabbit 3000 microprocessor. The system had a 11-bit A/D on a capable of up to 4100 Samples/s with a 0-20VDC range. The data was transmitted through TCP/IP to the GUI computer, then to the control computer via UDP, Figure A.1.

This arrangement did not use nearly half of the range of the A/D due to the mismatch in voltage range between the power supply and the A/D, and required two transmission steps before XY-positional information was available to the controller, introducing the possibility of long latency. The switch mode power supply used had significant artifacts in the output due to the switching frequency that might cause noise in the feedback signals.

A new positional feedback system was engineered to improve performance and packaging. The potentiometers were transitioned to be measured by the NI-6023E in the control computer and the NI-6008 on the GUI computer. The NI-6008 is used when positioning the weld table before welding. During the weld, the NI-6023E is

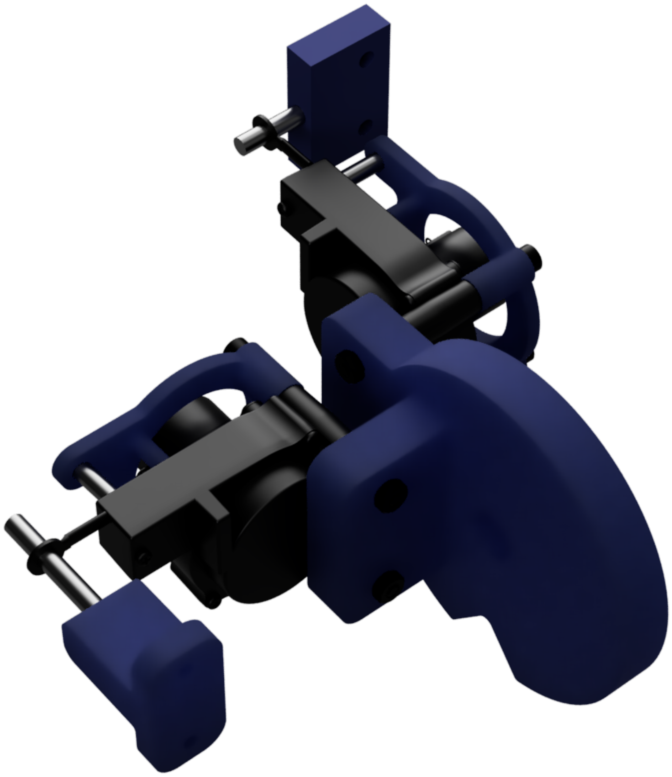

Figure A.5: Mount designed to gather the string potentiometers to one point of the machine, simplifying the wire runs and reducing noise.

primarily used to determine the location of the weld table. The NI-6023E has a 12-bit A/D capable of 200 KSamples/s with a Bipolar 10 Volt range. The NI-6008 was capable of mirroring the bipolar 10 Volt range.

Under the new system, the potentiometers are powered through a computer ATX power supply. The ATX power supply is still at its core a switch mode power supply and some additional stabilization was desired. A circuit was designed to provide a voltage reference to regulate ±12v to ±10v, perfectly matching the range of the NI-6023E.

It was found that new system was sensitive enough to pick up interference from the surrounding motors. This is because the potentiometers create a high impedance circuit path causing the cable runs to behave like an antenna, and should be avoided

PARTS LIST

ITEM	QTY	PART NUMBER	MATERIAL
1	1	STRING POT BRACKET	ABS PLASTIC
2	2	LX-PA-50	STEEL
3	1	SLIDEPIN	STEEL
4	2	LOOPRINGV2	ABS PLASTIC
5	2	LOOPRINGPIN	STEEL
6	1	POTENTOMETERSLIDER	ABS PLASTIC
7	1	COMPONENT7	STEEL
8	1	COMPONENT8	ABS PLASTIC
9	4	SOCKET HEAD SCREW M4 X 0.7 MM, 55 MM LONG	STEEL
10	4	HEX NUT M4 X 0.7 MM	STEEL
11	1	POTENTOMETER SLIDE	STEEL

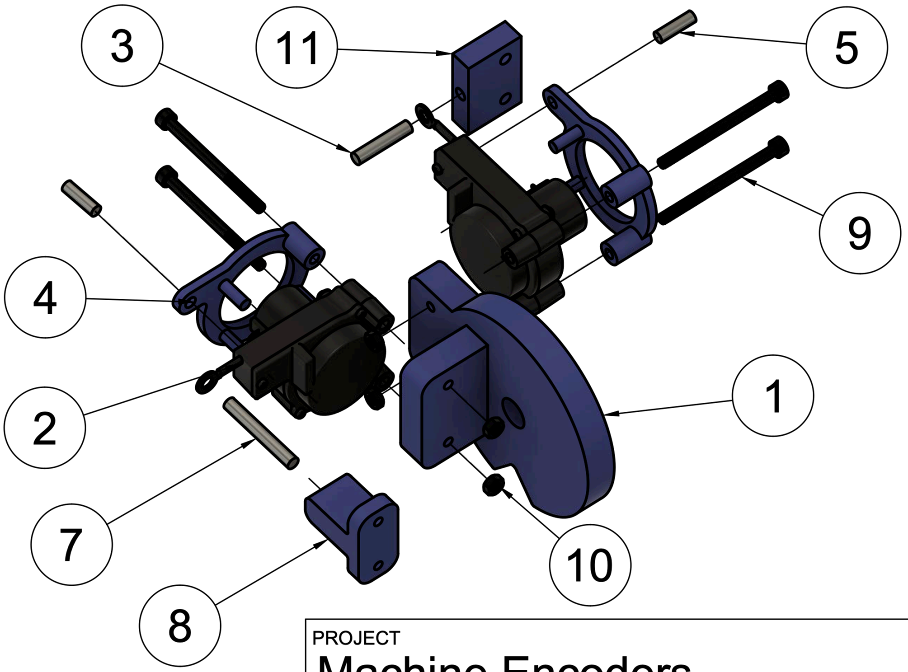

PROJECT
Machine Encoders

TITLE
XY Assembly

SCALE 1:2
DRAWN Adam Jarrell 11/4/20

Figure A.6: String Potentiometer mount assembly for X and Y axis.

for large wire runs. Isolation amplifiers provides a low impedance source for less interference, and allow for enough outputs to drive both NI-6008 and NI-6023E DAQs needed for use of the machine. Both potentiometers were been relocated to a single mounting point on the machine, Figure A.5,A.6. Then, the single conditioning and power supply circuitry could be moved close to the single mounting location, minimizing high impedance wire lengths. From there, the isolation amplifiers drive a low impedance twisted pair to the data acquisition boards. Additionally, braided copper shielding has been sleeved over the power and data lines running from the instrumentation case to the potentiometers. The sleeting has been grounded to chassis ground of the instrumentation case.

The relationship between the XY potentiometers and the output voltage was determined by measuring the displacement of the table and the output of the potentiometers at multiple locations. A standard measuring tape could be used for the X and Y axis. At each inch of table movement, the voltage output was measured. The linear relationship between output and table position could be determined from the collected data. The constant was modified to make the measured positions easily understood in relation to the current welding setup. The origin was placed at the common location to start welds.

A.1.4 Mounting of the dynamometer Telemetry Pick-up

The Kistler 9123C utilizes a telemetry system to wirelessly transmit data from the spindle. The fixed telemetry pick-up requires a 1-2 mm air gap between the spindle mounted dynamometer. The prior mounting system consisted of all-thread threaded into the acrylic safety shield on the spindle. The all-thread matched the mounting holes present on the telemetry pick-up. Nuts threaded on the all-thread could be placed both above and below the telemetry pick-up. This system allowed for great adjustability in the high of the telemetry pick up. However, it lacked significant rigidity, allowing the telemetry pick up to flex both towards and away from the dynamometer, and an air gap of approximately 20 mm was left between the acrylic plate and the telemetry pick up suspended on the all-thread with no adjustability to close the gap. So, it was impractical to maintain 1-2 mm spacing.

The first solution was to create thick steel stand-offs to fit around the all-thread and provide a more rigid mounting solutions. But, the lack of adjustablity in the distance from the dynamometer lead to this solution being discarded.

A better solution was designed to utilize the available mounting points is in the acrylic shield mounted around the spindle, Figure A.7. Not only does the telemetry pick-up had to be precisely placed in relation to the dynamometer, any mount must avoid a potential collision with the drive dogs on the spindle. A solid bracket was designed to mount the telemetry pick up securely, and a register around the top surface helped to accurately mount the pick-up. The bracket consists of a set two slotted 5/16” holes to allow for adjustment between the telemetry pickup and dynamometer.

A.1.5 Y-axis Encoder

During the weave tracking tests, it was determined that the y-axis positioning was limiting the accuracy of the weaving. The current y-axis feedback mechanism was not responsive enough to detect small changes in position. This limited the controllers ability to replicate the peaks of the sinusiodal wave or to account for the lag on directional change from backlash in the gear train.

A quadrature encoder was added to the Y-axis lead screw, Figure A.8. The location on the front of the milling machine knee was chosen because of mounting considerations and to avoid the excessive amount of backlash present through the Y-axis gear train between the motor and the lead screw.

The encoder utilized two Omron EE-SX672A NPN optical sensors and a single metal disk with 200 holes drilled in the parameter.

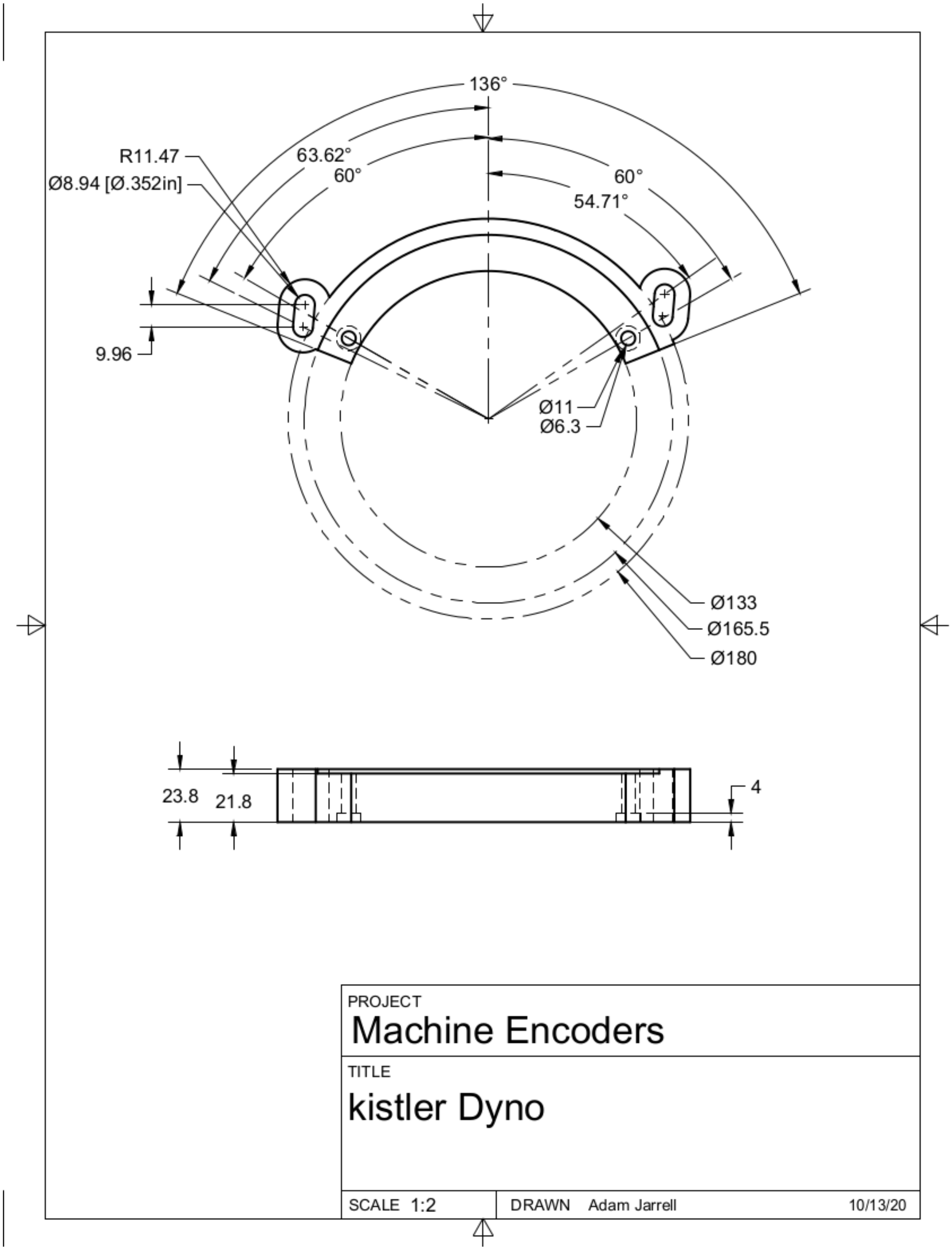

Figure A.7: Spacer for Kistler Dynamometer

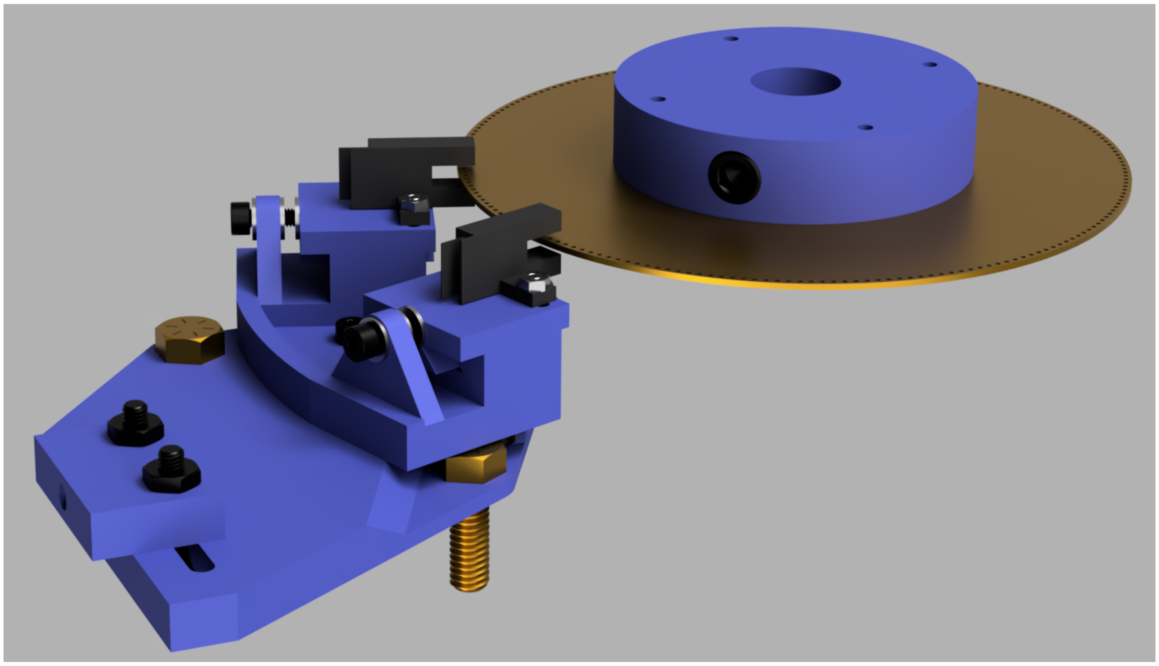

Figure A.8: The Y-axis encoder was designed to utilized the mounting points already available on the 1940s era milling machine.

The drawings for the y-axis encoder are available in Figures A.9, A.10, A.14, A.12.

PARTS LIST

ITEM	QTY	PART NAME	MATERIAL
1	1	DISK COUPLING	ABS PLASTIC
2	1	ENCODER DISK (200 HOLES)	STEEL
3	4	SOCKET HEAD SCREW 8-32, 5/8" LONG	STEEL
4	4	WASHER #8 3/8" OD	STEEL
5	1	FLAT-TIP SET SCREW 1/2"-13, 1/2" LONG	STEEL

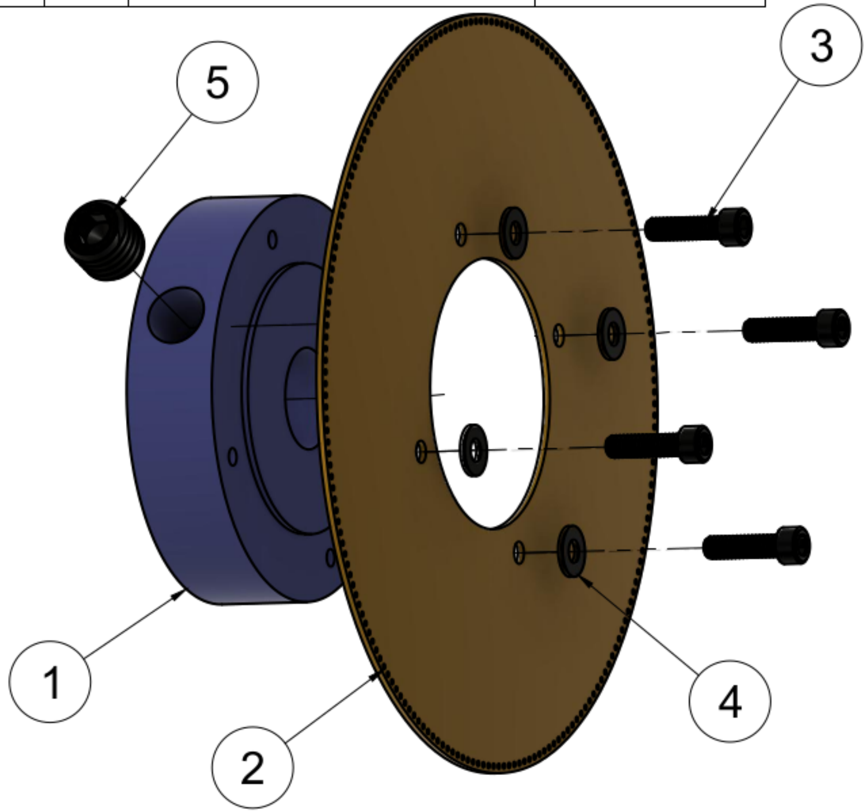

PROJECT
Machine Encoders

TITLE
Y-Axis Disk Assembly

SCALE 1:1
DRAWN Adam Jarrell 9/6/19

Figure A.9: Y axis encoder disk assembly

It was desirable to design a mount for the Omron NPN Photointerrupters that could be used in all current and future encoder designs. To this end, multiple design requirements were identified:

- Each mount would only contain one Photointerrupter, So that the number and location of interrupters could be changed without significant redesign.
- Built in adjustabiltiy along the long and short axis of the interrupter. This allowed for the adjustment of the interrupters position both radially and circumferentially with respect to the encoder disk.
- A consistent mounting method that would be accessible in most scenarios.

As a result, a dovetailed sliding mechanism was designed to mount each photointerrupter, Figure A.13. The slide has slotted and chamfered holes to allow for movement of the interrupter along its short axis. The dovetailed slide fits into matting block. The dovetail allows for large adjustment along the long axis. The dovetail is retained by a spring loaded bolt. The bolt goes through the slide housing and into the slide. This allows for easy adjustment without removal of the mount.

The drawings and deminsions for the mounts are available in Figures A.14, A.15.

PARTS LIST			
ITEM	QTY	PART NAME	MATERIAL
1	2	ENCODER MOUNT V27	
2	1	ENCODER BRACKET	ABS PLASTIC
3	1	ENCODERSLIDEMACHINEBRACKET V8	STEEL
4	1	Y-AXIS DISK ASSEMBLY V18	
5	3	HEX HEAD 5/16"-18, 1" LONG	STEEL
6	6	SOCKET HEAD SCREW M4 X 0.7 MM, 8 MM LONG	STEEL
7	1	POTENTOMETER SLIDE	STEEL
8	2	HEX FLAT HEAD 10-32, 1" LONG	STEEL
9	2	10-32 NUT	STEEL

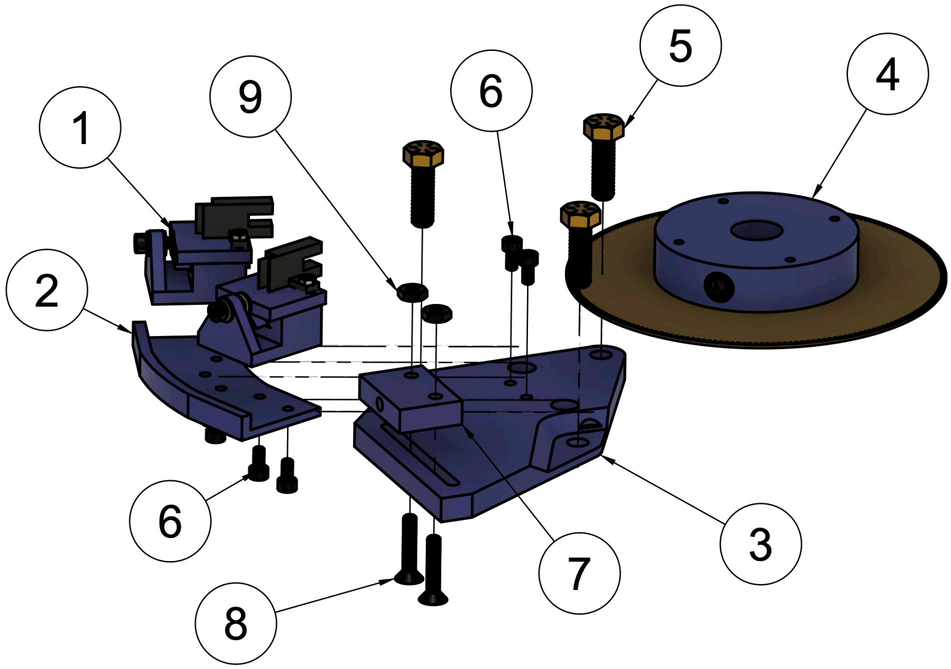

PROJECT
Machine Encoders

TITLE
Y-axis encoder

SCALE 1:2
DRAWN Adam Jarrell
9/6/19

Figure A.10: y-axis encoder assembly

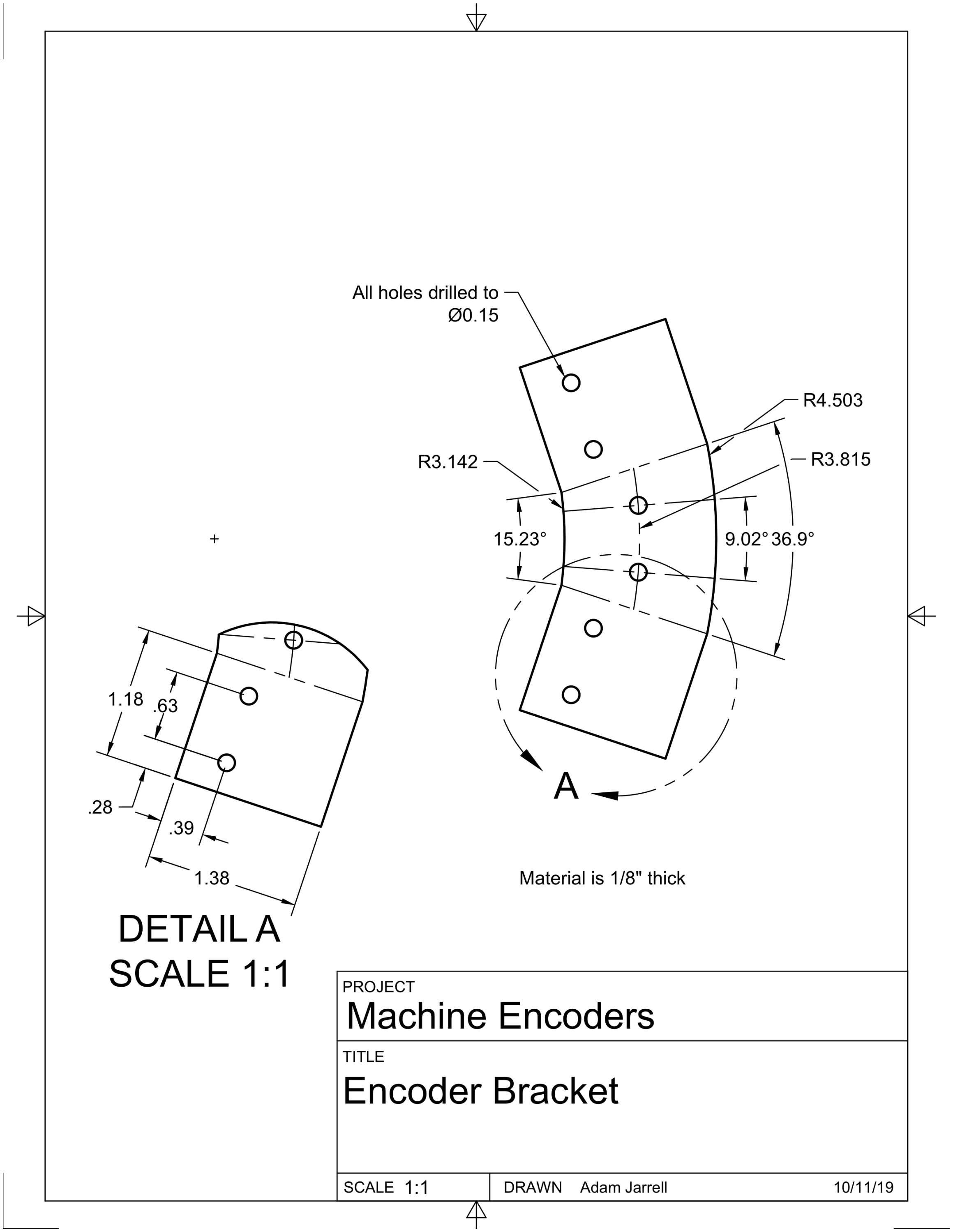

Figure A.11: Y-axis encoder bracket

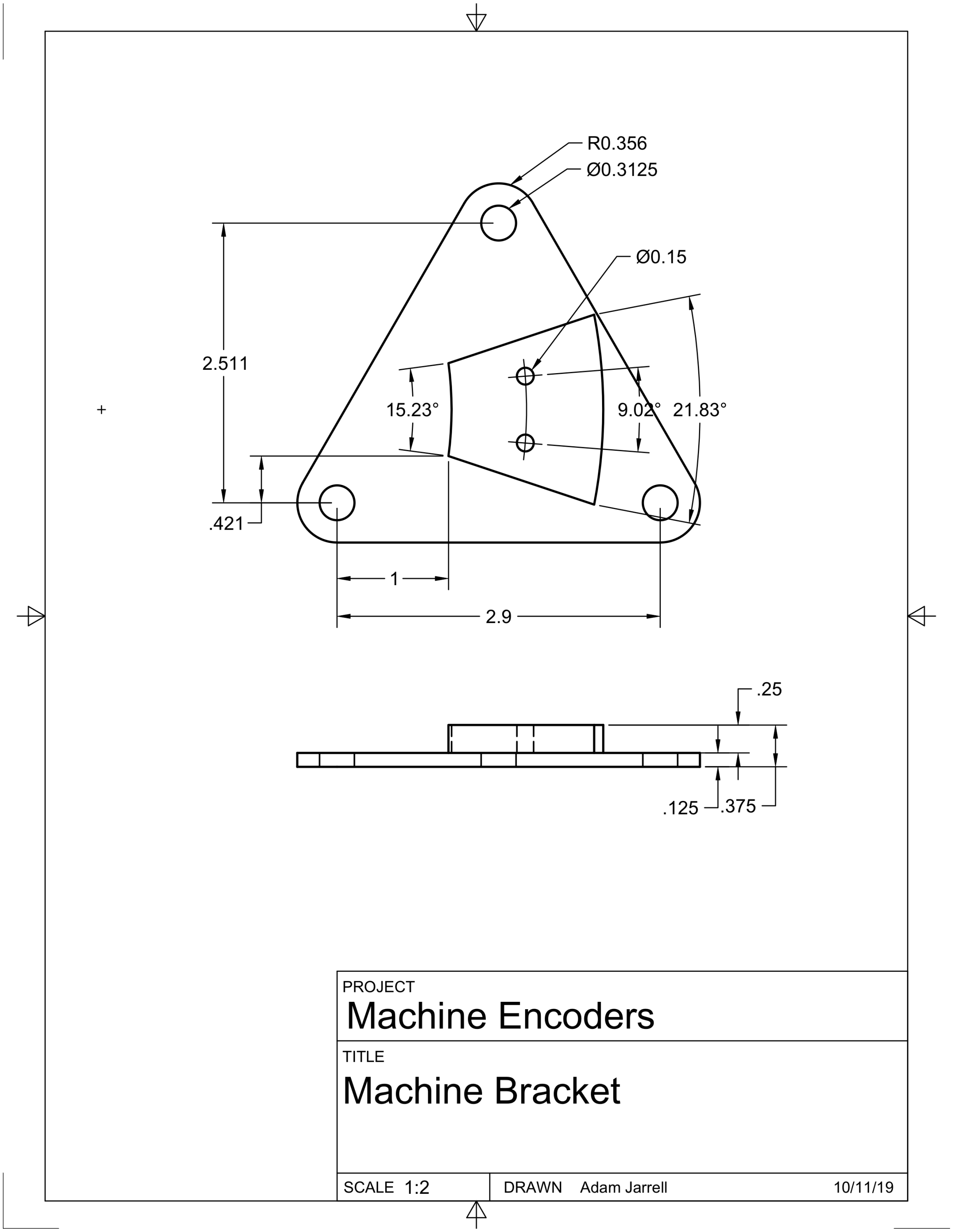

Figure A.12: Y-axis Encoder bracket mount

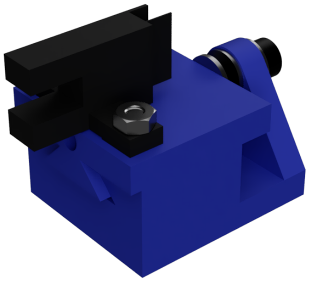

Figure A.13: The 3d-printed encoder mount allows for adjustment of the Omron photointeruper to insure reliable operation of the encoder.

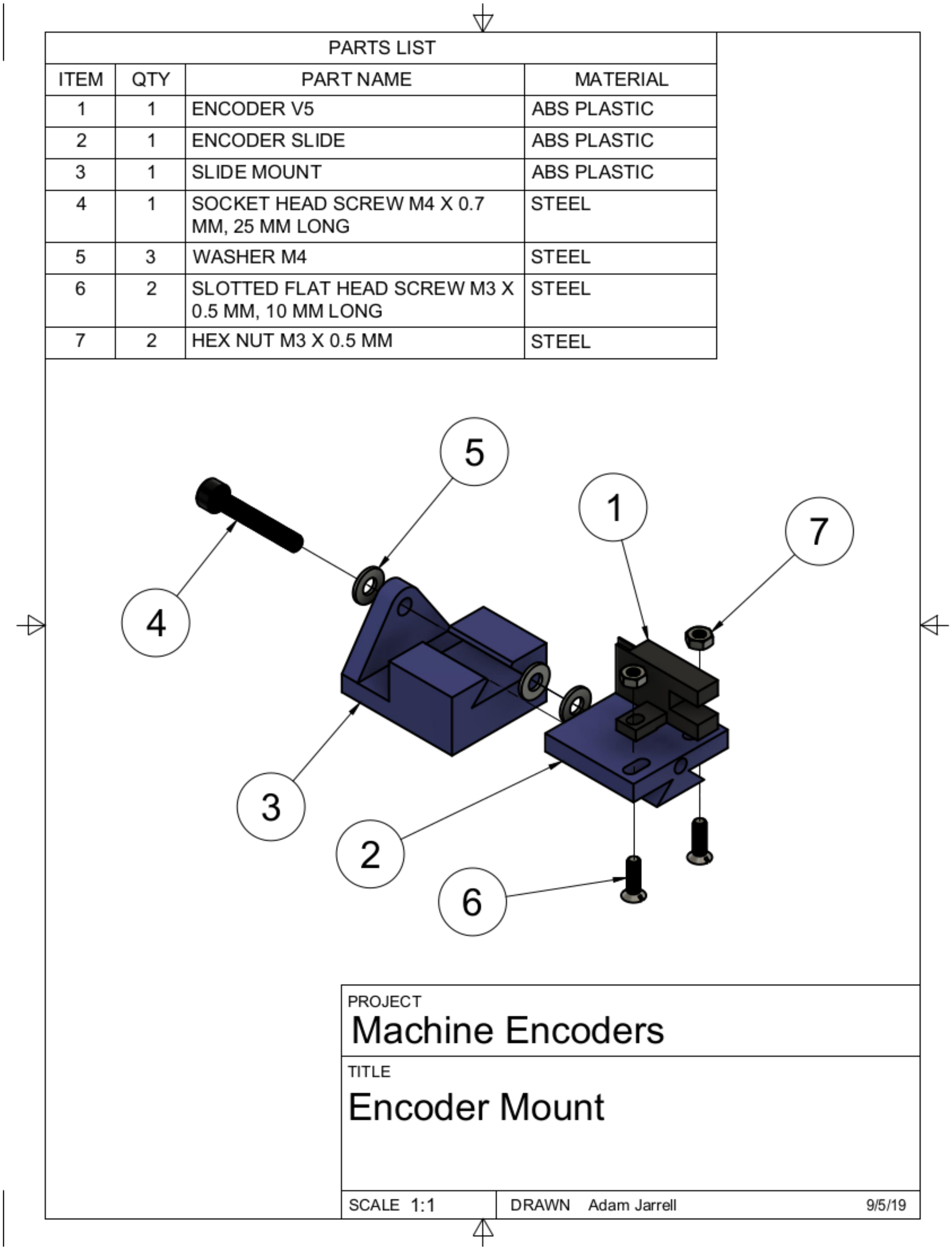

PARTS LIST			
ITEM	QTY	PART NAME	MATERIAL
1	1	ENCODER V5	ABS PLASTIC
2	1	ENCODER SLIDE	ABS PLASTIC
3	1	SLIDE MOUNT	ABS PLASTIC
4	1	SOCKET HEAD SCREW M4 X 0.7 MM, 25 MM LONG	STEEL
5	3	WASHER M4	STEEL
6	2	SLOTTED FLAT HEAD SCREW M3 X 0.5 MM, 10 MM LONG	STEEL
7	2	HEX NUT M3 X 0.5 MM	STEEL

PROJECT
Machine Encoders

TITLE
Encoder Mount

SCALE 1:1
DRAWN Adam Jarrell 9/5/19

Figure A.14: Spring loaded econder Mount

Pulse data from the encoder was transformed into a location through custom written Matlab software, Figure A.16.

The findState function takes the current state of both encoders and assigns a state based upon the four possible combinations of both signals.

```
% The findState function takes the raw digital signal from the DAQs and
% defines the current encoder state from the inputs.
function state = findState(signal1, signal2)
    if signal1 == 0
        if signal2 ==0
            state = 0;
        else
            state = 3;
        end
    else
        if signal2 == 0
            state = 1;
        else
            state = 2;
        end
    end
end
```

The findCount function takes the current state from the findState function and a reset signal. The reset signal allows for the encoder to be calibrated at the start of each weld. The backlash is handled via an accumulation parameter, Degree, in the conversion between the change of states and number of counts. If the accumulation parameter is not at its upper or lower limit, then the count value will remain unchanged. The calibration is handled at the start of each weld that uses the encoder system. When the state changes the degree variable is either increments or decrements depending upon the prior state. If degree is then above its upper or lower limit the count will be incremented or decremented respectively, and the degree will be reset to its respective limit.

```
% The findCount function takes in the current state and accounts for
% backlash in the system by adding a deadzone on directional chanegs.
function [Count, Degree] = findCount(state, reset)
persistent priorState count degree

%Setting the upper and lower limits of the backlash accumulator, degree
upperlim = 138;
lowerlim = 0;

%Initializing persistent variables
    if isempty(priorState)
        priorState = 0;
    end
    if isempty(count)
```

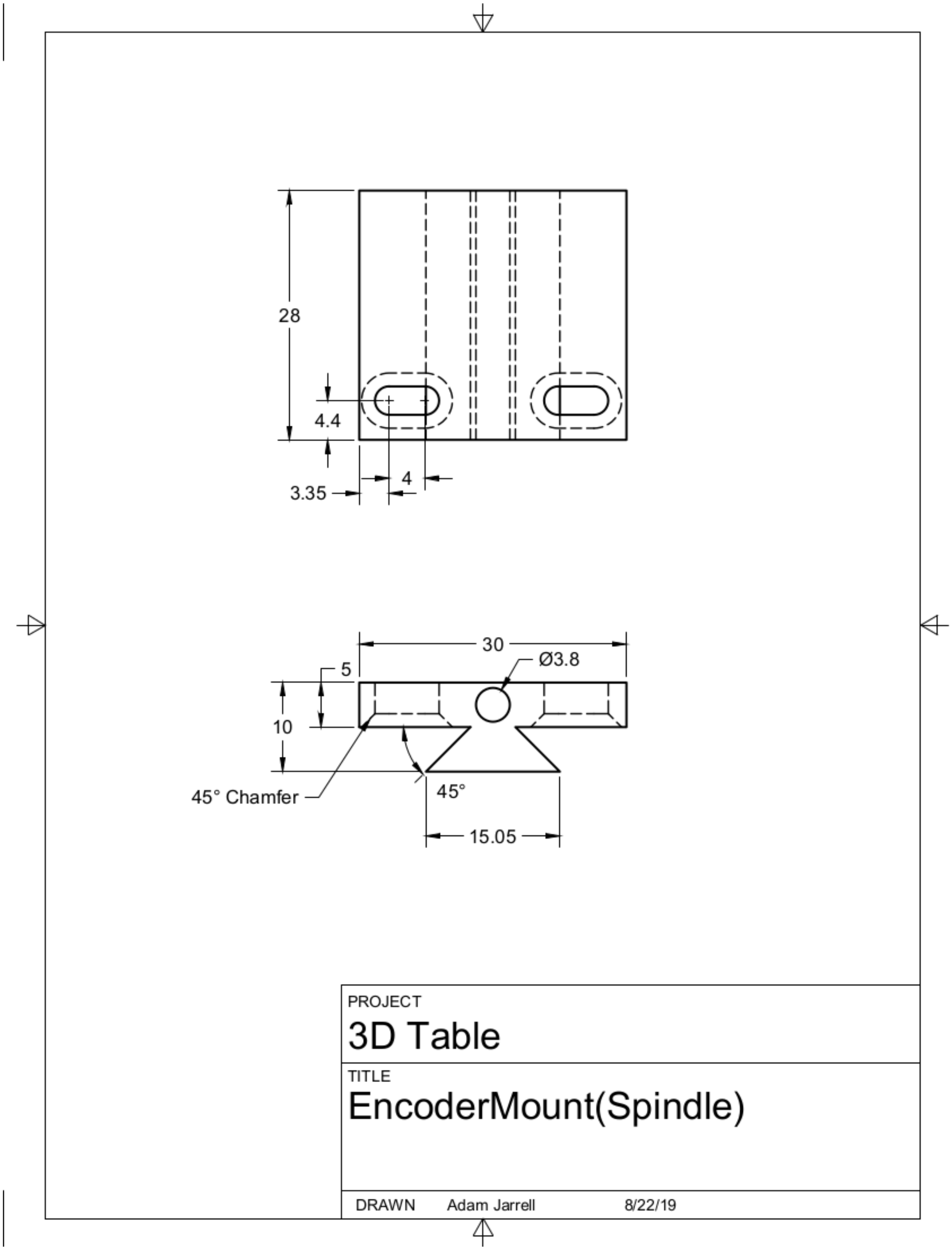

Figure A.15: Dovetailed encoder mount

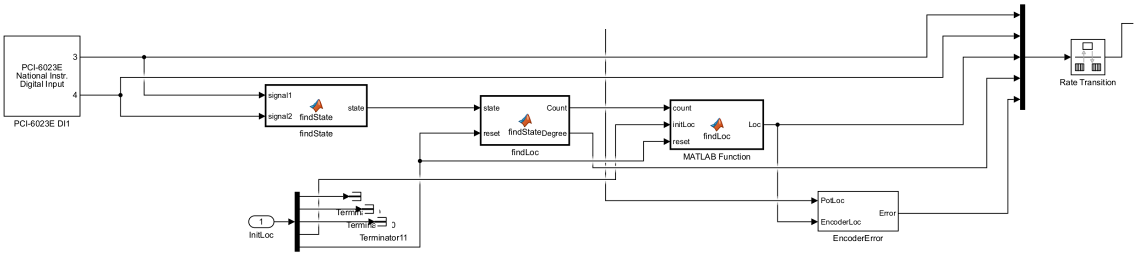

Figure A.16: The XY encoder was paired with a Simulink model to determine the XY forces on the spindle. The model was included in the input block of every weld program.

```
        count = 0;
    end
    if isempty(degree)
        degree = 0;
    end
    if reset
        degree = 0;
    end

    % if block increments or decrements the degree variable based upon the
    % state change
    if state == 3 && priorState == 0
        degree = degree - 1;
    elseif state > priorState
        degree = degree + 1;
    elseif state == 0 && priorState == 3
        degree = degree + 1;
    elseif state < priorState
        degree = degree - 1;
    end

    % if block increments the count when the degree variable gets to the
    % upper or lower limits.
    if degree > upperlim
        degree = upperlim;
        count = count + 1;
    elseif degree < lowerlim
        degree = lowerlim;
        count = count - 1;
    end


    priorState = state;
    Count = count;
    Degree = degree;
end
```

The findLoc function transforms the count into a machine usable location. The function captures the current count from the findCount function, the initial location, and a reset variable. Again, the reset variable allows the system to be calibrated on machine start up. The initial location, initLoc, Is captured from an absolute source like the string potentiometers at the start of each weld. The current location is found by subtracting the inital location by the product between the ratio of table movement to counts and the current count. The lead screw has 4 threads per inch and there are 400 state changes per one rotation of the lead screw. So, the ratio is ,25 in per 400 counts.

```
% The findLoc function takes in a count, inital location, and reset
% variable, and computes the current y-location of the weld table based
    on
% the topology of the encoder. The inital location can be reset by the
% reset variable, otherwise it is locked into its first recieved input.
function Loc = findLoc(count, initLoc, reset)
persistent initloc
    if isempty(initloc)
        initloc = initLoc;
    end
    if reset
        initloc = initLoc;
    end
   Loc = initloc - .25/400*count;
end
```

The backlash was measured by manually rotating the axis input and comparing against a dial indicator mounted against the Y-axis of the welder. A custom simulink model was written to assist in the tunning and evaluation of the encoders performance. The model contained the full code to run the encoder, a timer to send the reset variable, and a display to read out important variables. For calibration, the accumulator was disabled by setting the upper and lower limit to zero. The motor was de-energized so it could be rotated by hand. Then, the motor was spun in one direction until the dial indicator registered movement. This insured that all of the backlash of the gear train was taken up for this direction of rotation. The reset signal was then sent to the findState and findLoc functions to reset the counts. Then, the rotation of the motor was reversed while keeping track of the current count from the Simulink model. When displacement was registered on the dial indicator, the current count was the measured backlash of the system. The procedure was preformed again starting with rotating the motor in the opposite direction to insure the measured values were the same both directions. The measured backlash was 137 counts or about 62 degrees.

The encoder has to be calibrated at the start of every welds. This is because the encoder is not an absolute sensor, and the weld has to start in a know backlash state for the compensation to function correctly.

The method for setting the initial condition was inspired by manual machine tool techniques. When setting depth of cut on a lathe cross slide, it is best practice to not overshoot the desired measurement and then backup to the measurement. The backlash in the cross slide will lead to inaccuracies. The cross slide must be moved beyond the measurement to allow proper distance to take up the backlash of the system. Then brought back to the proper location. So the calibration process functions similarly. First, the machine remains in a constant location for 10 seconds, and data from the potentiometer is averaged. The averaging serves to eliminate the random noise present in the measurements, and provides an accurate initial location. Then, the machine offsets 1 inch from it measured position using the string potentiometer feedback, and averages the measured location for 10 seconds. At this point, the machine is at a known reference for position and backlash state, as all the slack in the gear train was taken up while traveling 1 inch. The reset can then be sent to the encoder module with the current measured location to calibrate the encoder. The welder can then return to its original position and begin welding. In some applications, it is beneficial to average positional data from the string potentiometer before beginning the weld to provide an accurate position for path planning applications.

The long term stability of the error between potentiometer feedback and encoder location was measured by setting the Y-axis motor a square wave output speed. The location and error between the two sensors was measured over many oscillations. The slow drift off was acceptable for the length and duration welds preformed in the lab.

A.1.6 Resolution of XY Forces

The Kistler cutting force dynamometer measures planer forces, X and Y forces, with respect to a coordinate frame attached to the dynamometer. To determine the force on the spindle in the coordinate axis frame of the table of the welder, the orientation of the dynamometer with respect to the table must be known. An absolute encoder was integrated on the spindle to enable the measurement of the spindles rotation with respect to the machine.

Prior encoder designs were integral to the tool holder or not rigidly mounted on the top of the drawbar. Both of these locations presented issues. The tool holder is semi-regularly changed, and removal of the tool would require calibration of the spindle encoder. Likewise, top of the drawbar is regularly accessed for manual rotation of the spindle. Both designs required frequent calibration due to frequent disturbance. A new design was implemented to attach to the spindle bellow the drive pulley and rigidly mount to the body of the spindle.

The encoder consisted of two stacked disks with a number of holes drilled around the parameter that in concert with Omron EE-SX672A NPN optical sensors could be used to derive the absolute position of the machine, Figure A.17. One disk had 50 holes drilled around the perimeter, and the other had one hole. The single hole disk provided an absolute reference location once per rotation. The top disk served to give the system a resolution of 7.2 degrees. Together, the system functioned as an absolute encoder with a resolution of 7.2 degrees.

The Omron optical sensors were mounted in the same sliding mount from the Y-axis encoder, Figure A.13. A bracket was designed to fit on to the spindle using

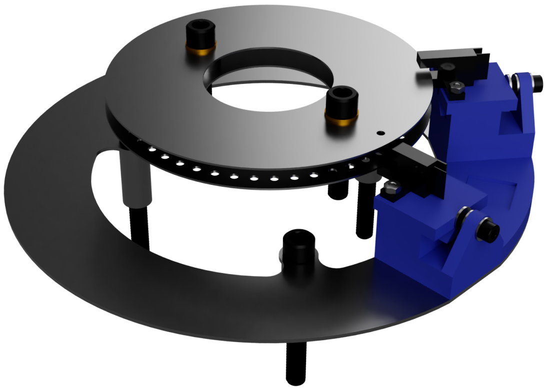

Figure A.17: The spindle encoder was designed to be adjustable and use existing mounting points on both the 1940s era milling maching and recent modifications for FSW use.

the top bearing mount holes. Spacers raised the height of the bracket to the encoder disks. The bracket rigidly mounted the optical sensors to the spindle.

The system was calibrated by placing a load on the tool in the x-direction and using the difference between the know direction and calculated direction to set the rotation offset.

All Assemblies and Drawings for Encoder Components are listed in Figures A.18A.19A.20A.21A.2

The encoder was paired with an associated Simulink model to calculate table reference frame X and Y forces, Figure A.24. The model counted the rising edges of the encoder signals, incrementing the 50 Hole encoder pulses, and resetting the count of the single hole pulse.

The following Force Footprints were calculated using the calculated X and Y forces. Since the Forces were only sampled at 100 Hz, the sample set were rearranged in order of rotation angle. This effectively increased the angular resolution but assumed that one rotation of the tool is identical any other rotation.

A.1.7 Minimizing Interference

This dissertation contains two sensing and control projects that had significant demands for a high signal to noise ratio. However, feedback signals generated by the transducers, such as the dynamometer and potentiometers, were excessively noisy. The it was suspected that the system had multiple issues related to grounding, shielding, and noise rejection. Electromagnetic emissions from the VFDs and motors require good grounding and shielding for both the motor and transducer to avoid interference. It was suspected that the building ground was insufficient to prevent EMF emission. So, multiple changes were made to prevent and reject interference.

Both VFDs and motors can create large amount of EMI. VFD's create different AC frequencies by rapidly switching on and off a DC signal. The rapid switching can cause large amounts of EMI. The many induced currents within a spinning motor can also cause interference. The best mitigation strategies is to tie each component to a good ground to remove any unwanted currents from the system. However, the welding machine still largely uses unshielded cabling between the VFD and Motor. The unshielded cable is a potential source for EMF emission. As a result, the milling machine produces large amounts of EMI when running.

DAQ inputs can be configured in three different ways depending upon the ground-

PARTS LIST			
ITEM	QTY	PART NAME	MATERIAL
1	2	ENCODER MOUNT V26	
2	1	ENCODER DISK STACK V12	STEEL
3	1	MOUNTING BRACKET	ABS PLASTIC
4	1	CIRCULAR MOUNT V10	STEEL
5	3	MOUNT SPACER V1	STEEL
6	3	SOCKET HEAD 5/16"-18, 2 1/2" LONG, ALL THREAD	STEEL
7	4	SOCKET HEAD M4 X 0.7 MM, 8MM LONG, ALL THREAD	STEEL

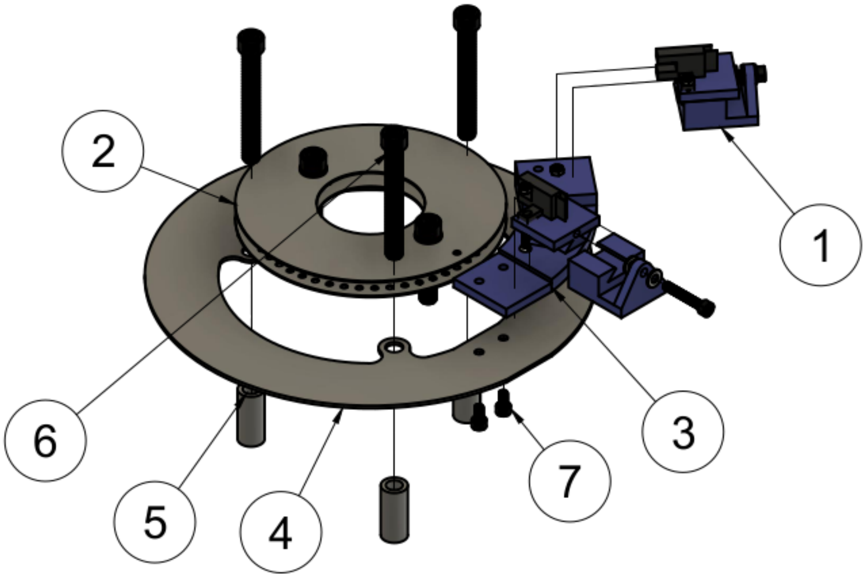

PROJECT
Machine Encoders

TITLE
Spindle Encoder Asssembly

SCALE 1:2
DRAWN Adam Jarrell 9/5/19

Figure A.18: Spindle encoder assembly

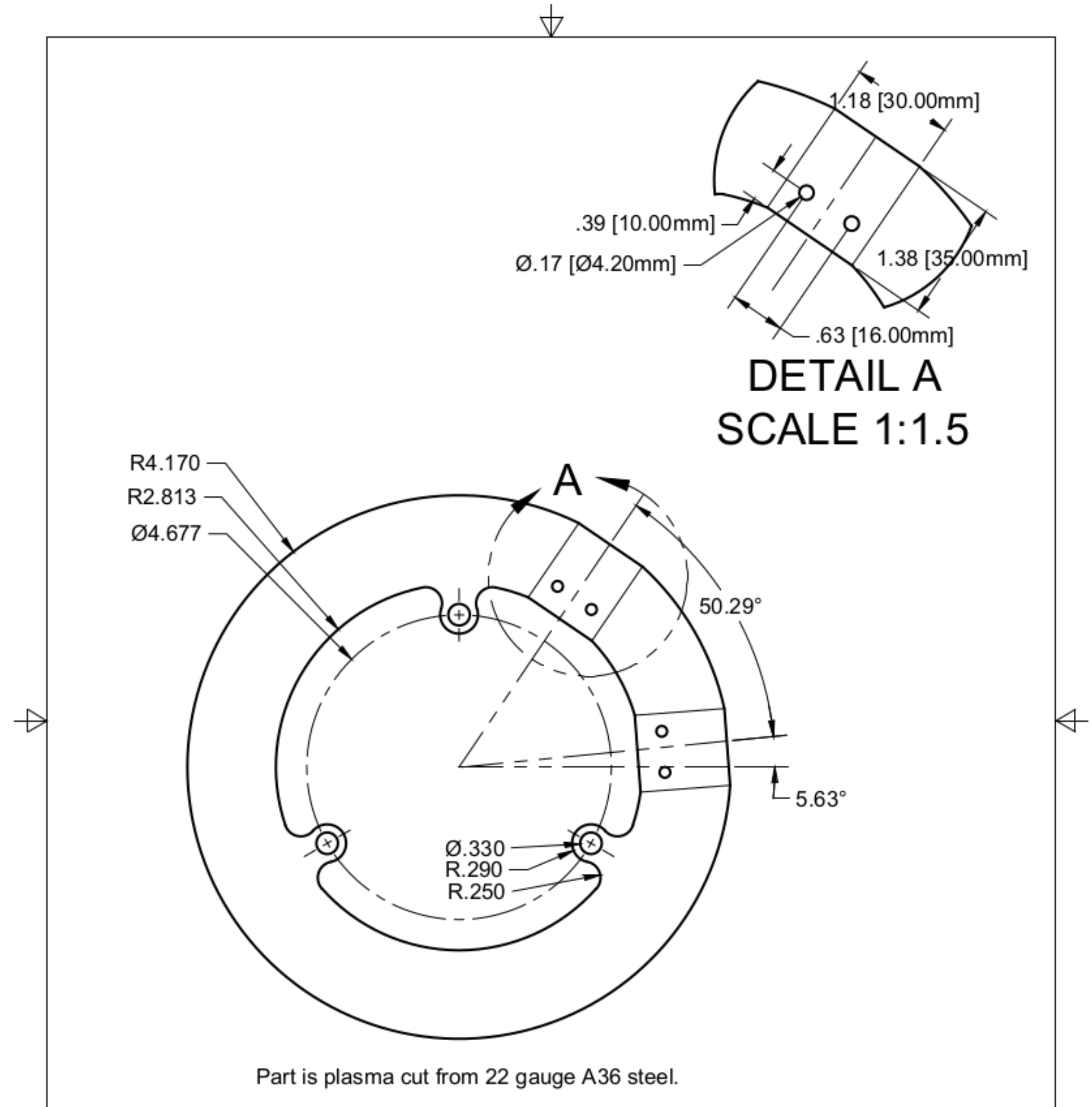

Part is plasma cut from 22 gauge A36 steel.

PROJECT
Machine Encoders

TITLE
Circular Mount

SCALE 1:2
DRAWN Adam Jarrell 9/6/19

Figure A.19: Circular encoder mount

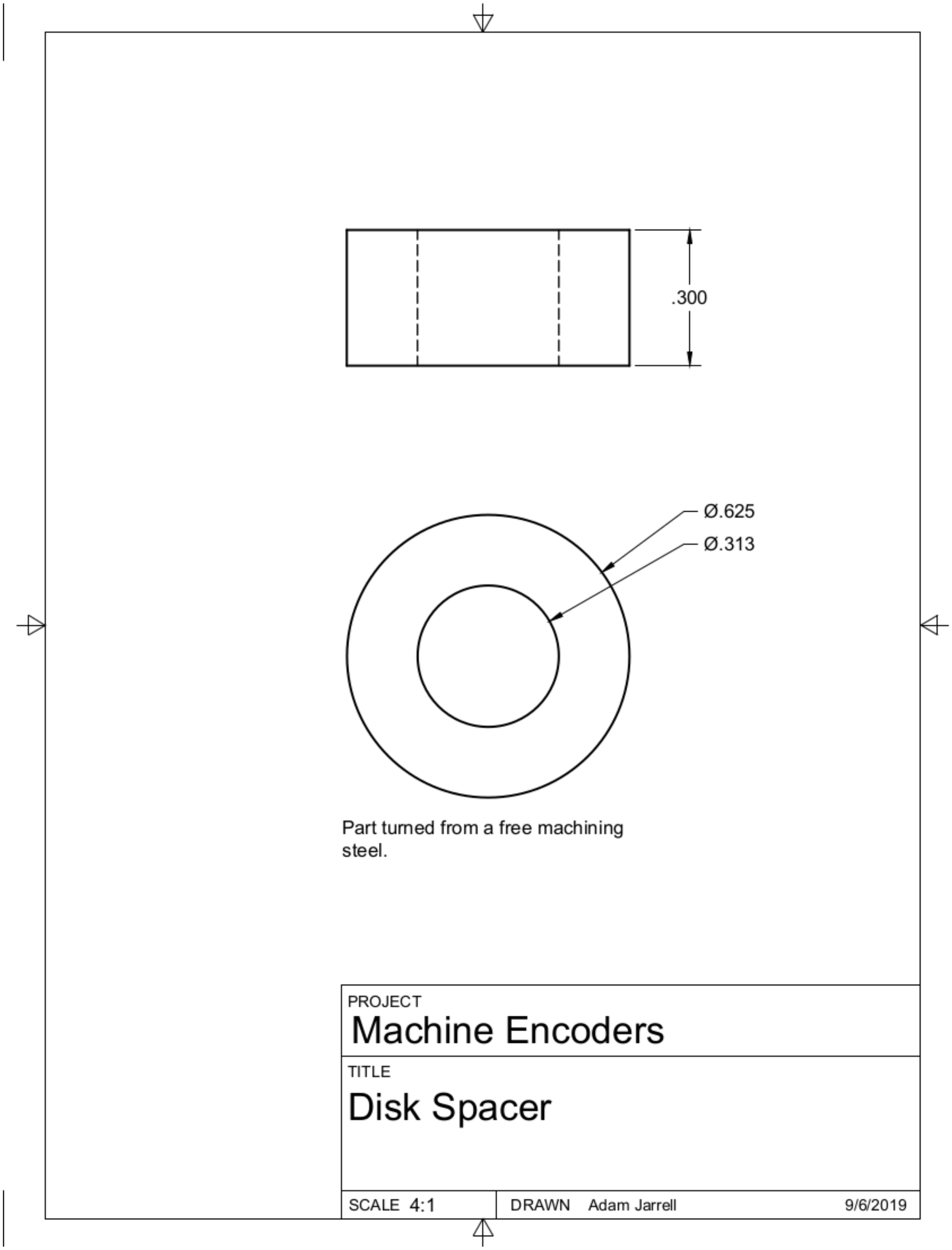

Part turned from a free machining steel.

PROJECT
Machine Encoders
TITLE
Disk Spacer
SCALE 4:1
DRAWN Adam Jarrell
9/6/2019

Figure A.20: encoder disk spacers

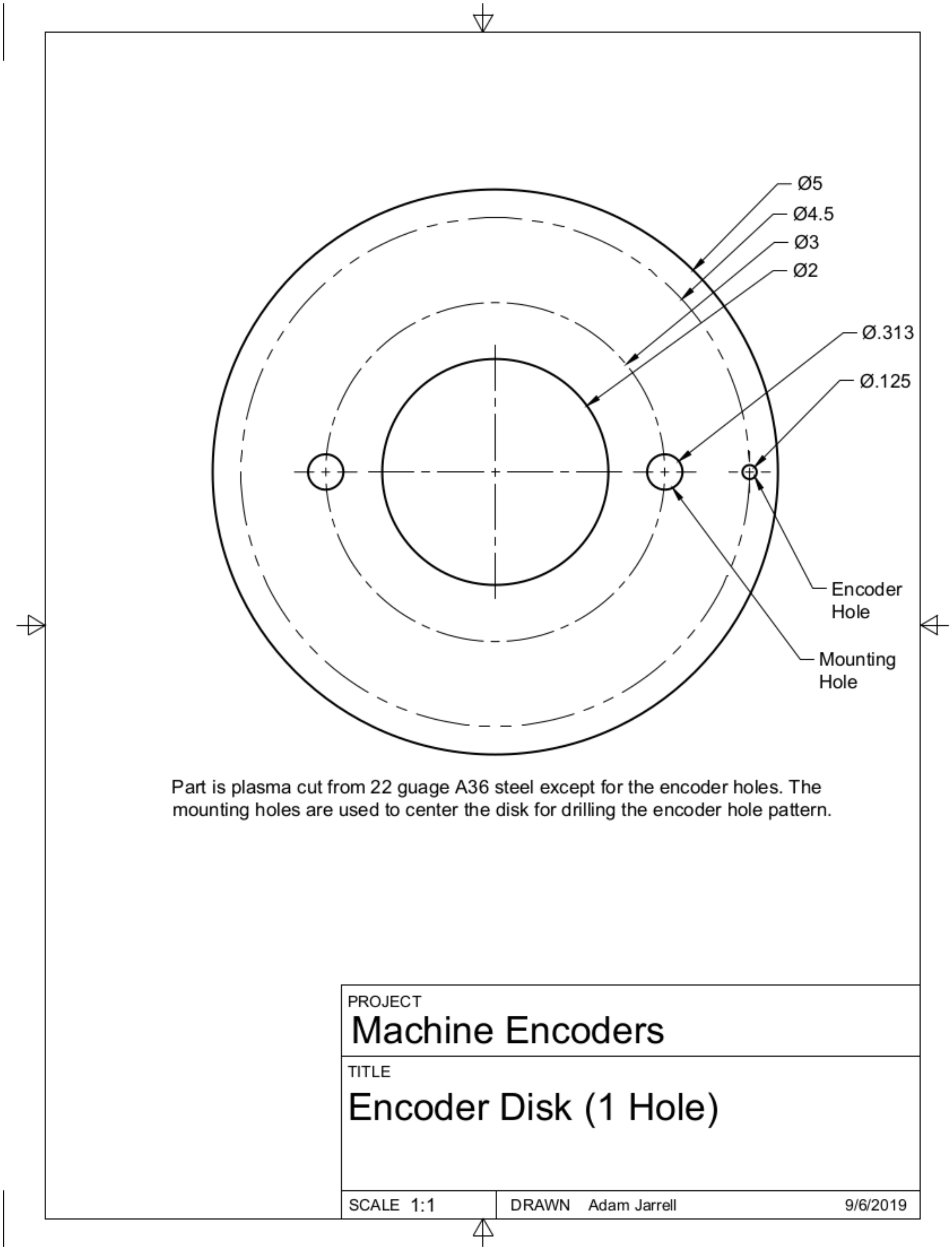

Part is plasma cut from 22 guage A36 steel except for the encoder holes. The mounting holes are used to center the disk for drilling the encoder hole pattern.

PROJECT
Machine Encoders
TITLE
Encoder Disk (1 Hole)
SCALE 1:1
DRAWN Adam Jarrell 9/6/2019

Figure A.21: Single hole encoder disk for spindle encoder

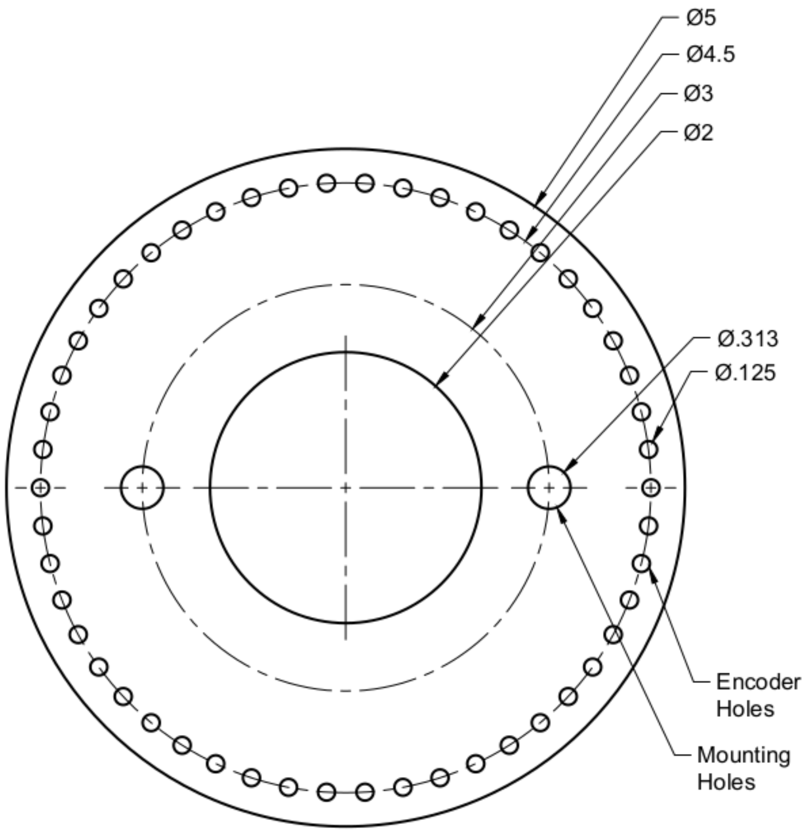

Part is plasma cut from 22 guage A36 steel except for the encoder holes.
The mounting holes are used to center the disk for encoder hole pattern.

PROJECT
Machine Encoders
TITLE
Encoder Disk (50 Hole)
SCALE 1:1
DRAWN Adam Jarrell 9/6/2019

Figure A.22: 50 hole encoder disk for spindle encoder

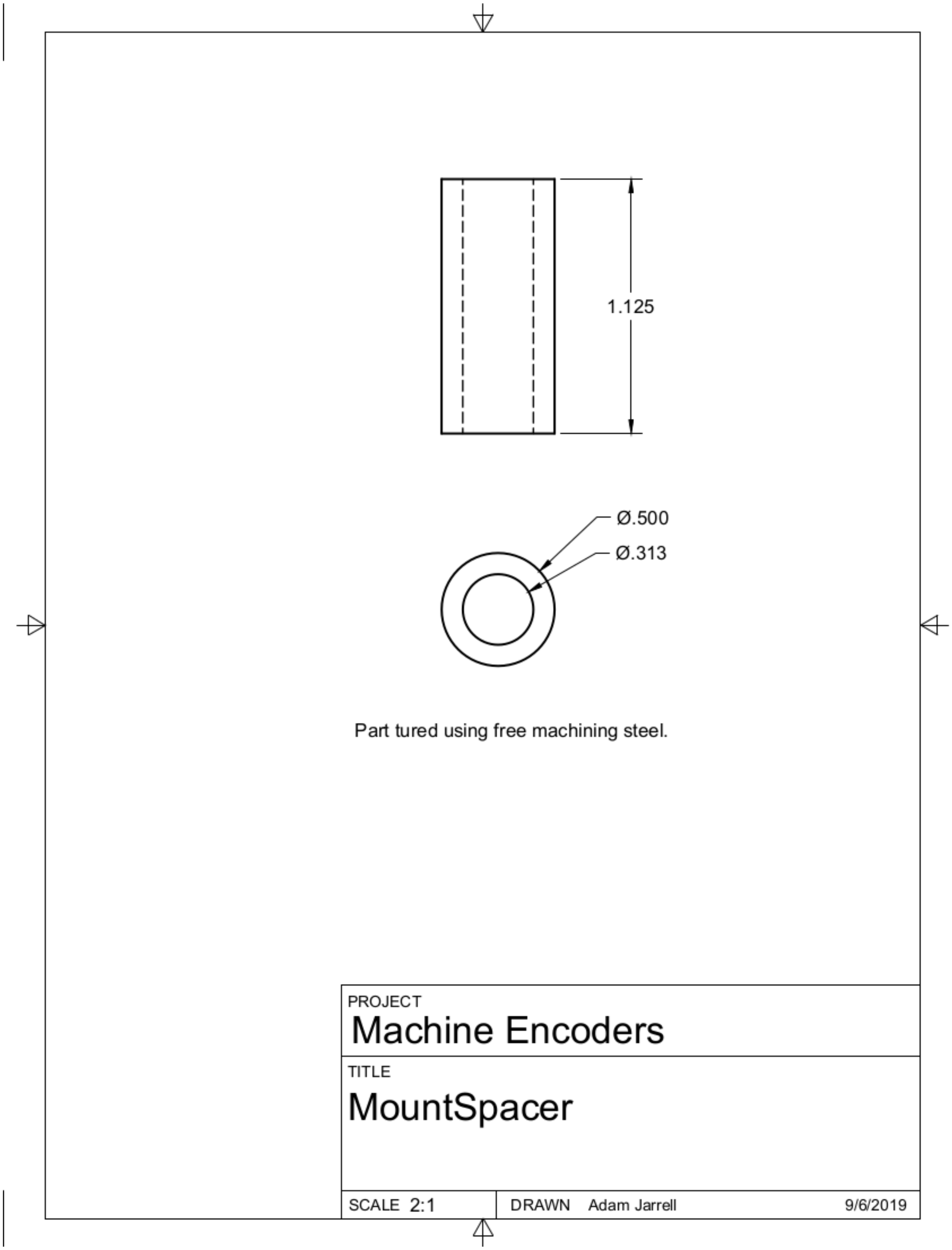

Part tured using free machining steel.

PROJECT
Machine Encoders
TITLE
MountSpacer
SCALE 2:1
DRAWN Adam Jarrell 9/6/2019

Figure A.23: Spindle bolt spacers

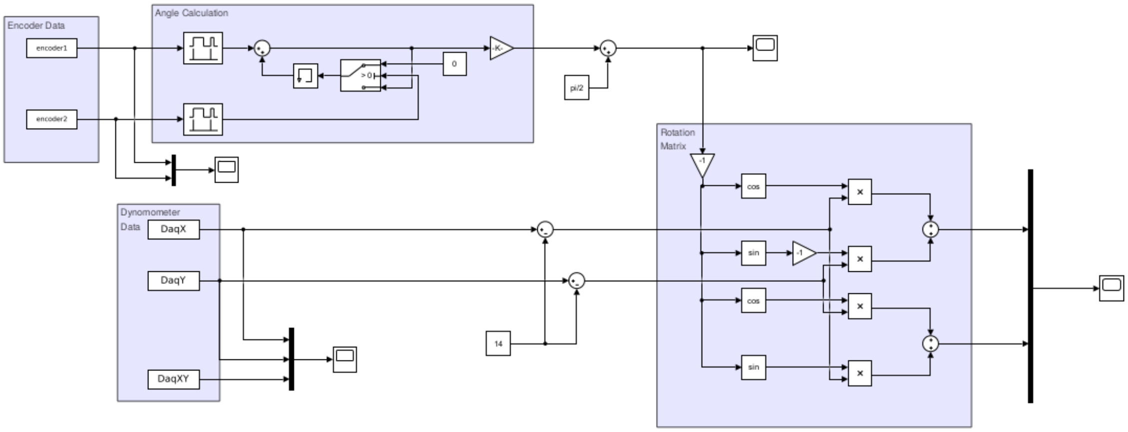

Figure A.24: Simulink model that manages the rotation of the spindle, and rotates the dynamometer date to the table reference frame.

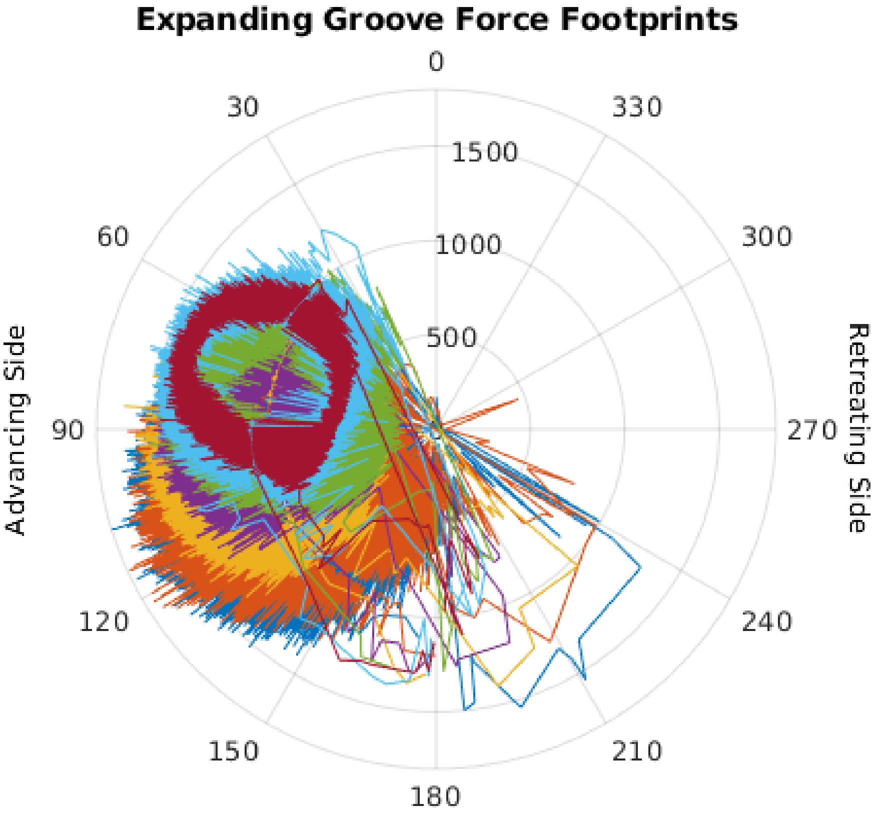

Figure A.25: Tool Force foot prints for uncontrolled welds with an expanding groove.

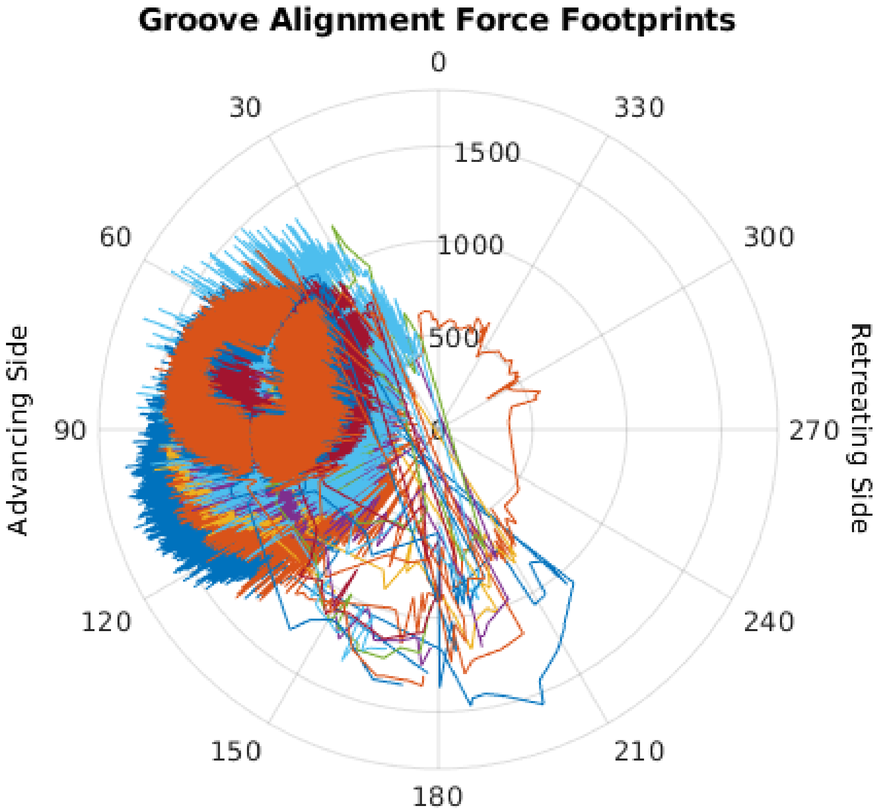

Figure A.26: Tool force foot prints for uncontrolled welds with different offsets from groove center.

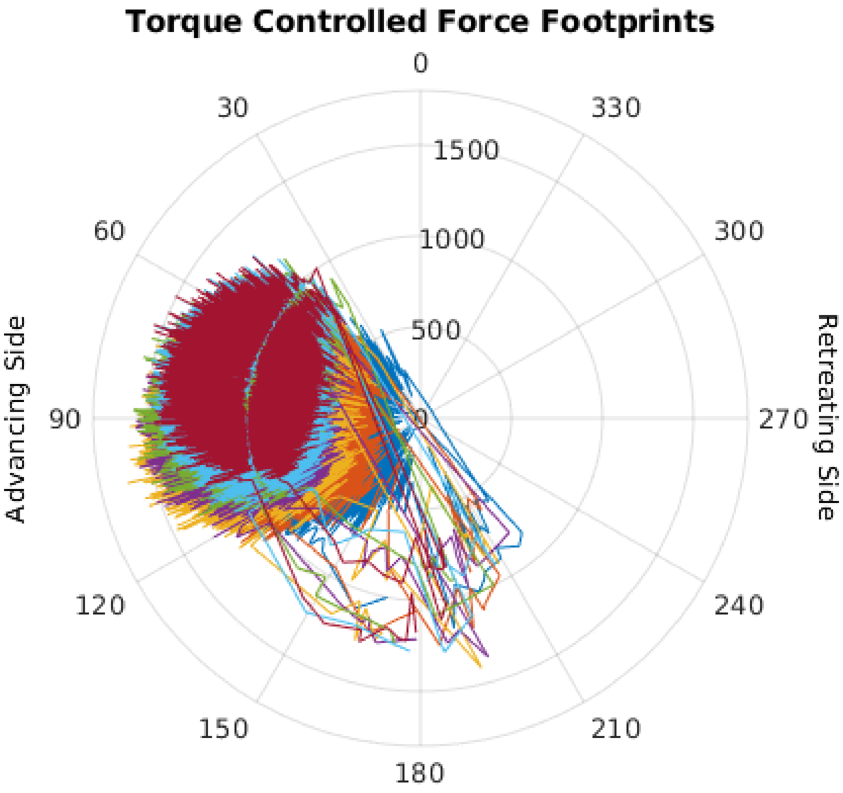

Figure A.27: Tool force foot print for torque controlled welds with expanding groove.

ing of the system and the number of inputs needed. Single-Ended measurements can be both ground-references or non-referenced. Single end measurements work by measuring all input signals against a common reference. During Ground-references signals, DAQ Ground is used at the reference. Non-referenced input mode references all signals to a common AI Sense. Single-ended ground-referenced input modes can be used to measure floating signals but it is not recommended for grounded signals. Using ground-references measurements on a grounded signal create ground loops, and could induce noise in the system. Non-referenced signals can be used to measure both floating and grounded signals. But, Differential measurements are preferred for noise reduction. Differential input modes measure the difference between a transducers negative and positive leads. This method effectively subtracts out the noise from the input signal but halves the number of possible DAQ inputs. Differential measurement techniques can be used to measure both floating and grounded.

Differential inputs from shielded twisted pairs were preferred for data integrity. Most of our sources were grounded sources for safety.

The vertical axis motor was found to be the largest source of EMF due to the rapid switching of the VFD to produce a holding torque when the motor is not spinning. So, shielded XLPE VFD cabling was used to replace the power cable to the vertical axis motor. The drain line and shielding were tied to ground to both the VFD and motor side.

The positional feedback system was hardened to EM interference by adding additional shielding and designing a low impedance source with differential outputs. The potentiometer is a high impedance source by definition, and high impedance sources are more vulnerable to EMI than low impedance sources. The power supply and signal conditioning boards were moved to as close to the potentiometers as possible. The mounting brackets for the potentiometers had to be remade to group them together. The relocation enabled the shortening of the high impedance signal wires between the potentiometers and sensor box. Then, low impedance wires could be ran over to the DAQS.

The potentiometers were powered by a grounded power supply. the low impedance wire to the DAQs was changed to twisted pair with additional woven shielding added. The shielding was tied to the chassis ground of the sensor box system. So, the DAQ was placed in a differential grounded source mode.

The Kistler system cannot be modified to increase its interference rejection. The Kistler system is a grounded source unless the binding screw in the back of the unit is removed. The screw was left in and the system was measured as a grounded source in differential mode for both the NI-6024E and the MCCDaq PCI card.

The cable for the telemetry pick up was much longer than needed. So, excess cabling was placed into a metal container that was tied to system ground to try and minimize the potential for interference.

As stated above, the best strategy for reducing VFD EMF is adequate grounding and shielding. The quality of the ground coming from the 3 phase circuits was unknown. So an Auxilary ground between the frame of the machine and the girder of the building was added. The auxiliary ground could be connected before each weld.

A.1.8 Tool Runout

The data produced by the Dynamometer during welds had high variability across all processing forces beginning from when the tool transverses through the welded materials until the end of the weld. The torque, planar force, and Z-Force measured during a FSE weld is presented in Figure A.28. Large variations in measured processing forces can be seen to occur around 80 seconds into the weld and continue until the tool retracts. It is believed that 80 Seconds corresponds with the start of the transverse motion of the tool. Z-force also seems to have the best signal to noise ratio without additional processing. Some variability in the processing forces are expected during a friction stir weld due to the periodic nature of FSW. However, the magnitude of the variations here were through to be in excess of what could be expected.

Tool runout was thought to be the cause of the variations. If the tool has a runout, it will rotate about a center not concentric with the tool. On the advancing side, the tool adds its tangential velocity to the welding speed, requiring more force to sweep the tool through the material, and on the retreating side, the opposite happens. This effect is illustrated in Figure A.29. Since the z-force is not largely effected by tangential forces on the tool, it sees the smallest variations.

If the tool runout is responsible for the variations observed, then the power spectrum could be expected to show a strong peak corresponding to the RPM of the tool, the driving frequency 1500 rpm or 25 Hz. When the spectrum of the torque is evaluated, the predicted strong peak is visable at 25 Hz, Figure A.30.

One final piece of evidence can be presented. The histogram of the torque during the transverse portion of the weld reveals a wide distribution of values with a two peak design. A peak is viable around 4 Nm and 17 Nm, Figure A.31. The two peaked design is exactly what would expected from a sinusoidal signal from tool runout.

It was determined that a significant portion of the tool runout originated with the interface between the dynamometer and the tool holder. the reference surface on the dynamometer had lost circularity and concentricity with the spindle. Accurate positioning of the tool holder on the dynamometer depended on a cylindrical pin and mating cavity. It was measured the reference pin on the dynamometer was 0.004” offset from the center axis of the tool and 0.003” undersized. The tool and holder had at least 0.002” of play between them as well.

Elimination of the run out would be preferable to other mitigation techniques. However, It was determined that a full rebuilding of the mating surfaces of the spindle would be required for complete elimination. The full rebuild would involve re-griding the reference pin to be concentric with the taper. Then, measuring the new diameter

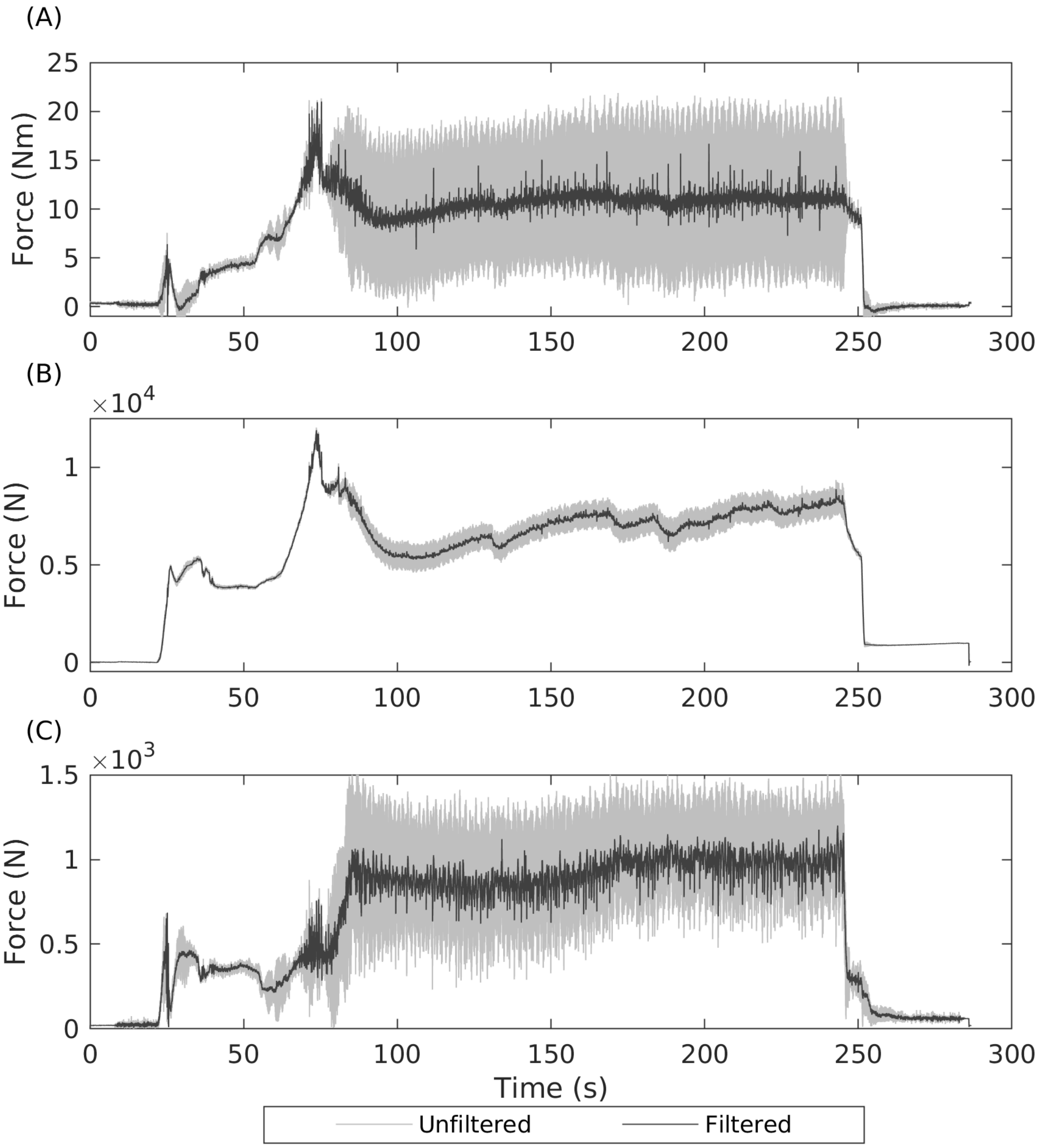

Figure A.28: Unfiltered and filtered force measurements taken from the Kistler dynamometer during a normal Friction Stir Extrusion weld for (A) Torque, (B) Z-Force, and (C) Planar Forces

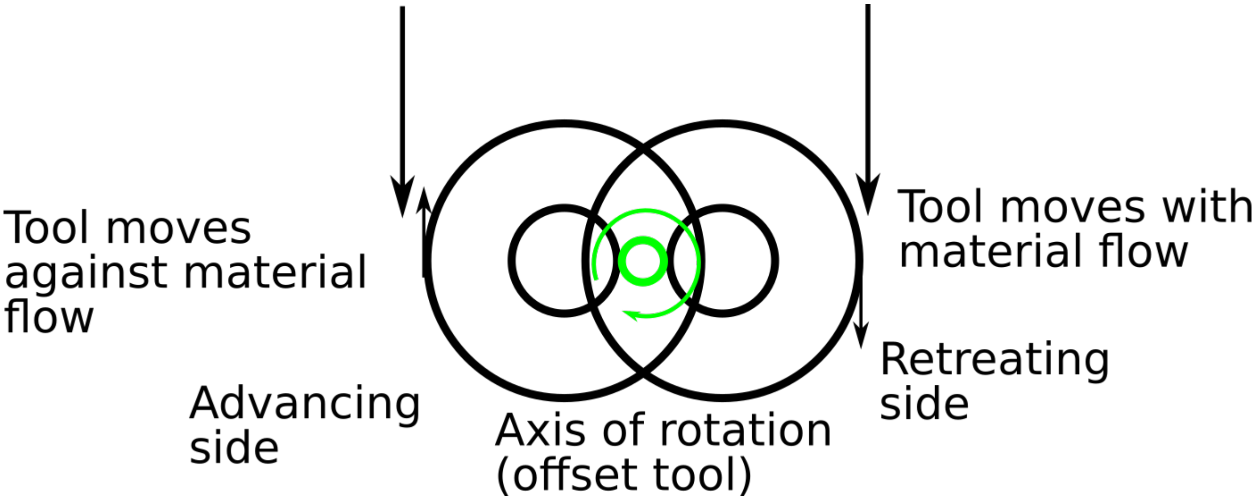

Figure A.29: Top down view of the effects of tool runout while transversing through the material. The magnitude of the runout is greatly exaggerated for visual effect.

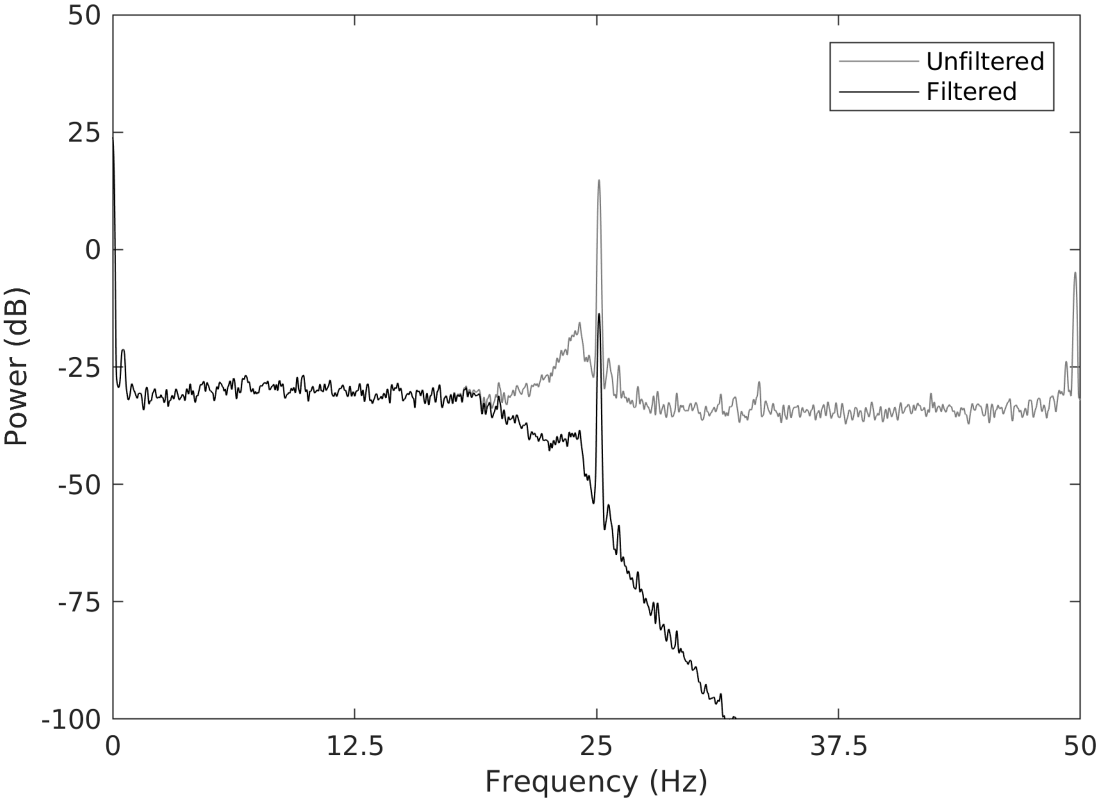

Figure A.30: Unfiltered and Filtered Spectrum for the torque signal during the transverse portion of the weld.

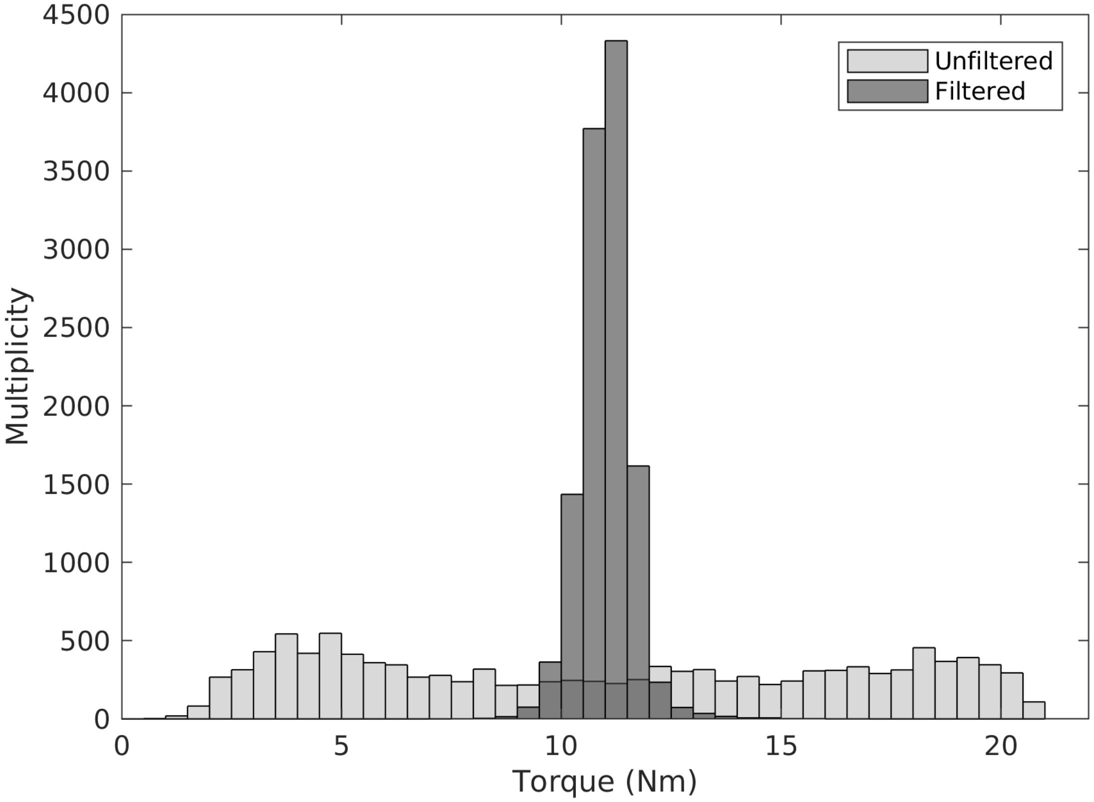

Figure A.31: Unfiltered and filtered histogram of the torque values during the transverse portion of the weld.

of the reference pin and building a new tool holder from tool steel with bore sized to be a locational transitional fit. The tool holder can then be heat treated. Adding Shims to the mating surfaces reduced the tool run out from 0.030" to 0.008".

There is a possibility that the inherent periodic nature of Friction Stir Welding was responsible for the observed effects. However, the measured 0.030" of runout was in excess of normal amounts expected for a precision spindle. To avoid any possibility of data loss, when presented as an average the forces were left unfiltered. It was though that that any variations would average out over the course of one weld. When presented as force vs. time, a filter was developed to reduce the periodicity.

In this case, a low pass filter was developed using Matlab's filter designer utility to reduce the periodicity around 25 Hz. The low pass filter helps to also eliminate sources of noise external to the welding process, such as mains frequency or high speed switching power supplies. When applied to the data series presented previously, there was significant improvements in the signal to noise ratio, Figure A.28. The effect of the filter on the spectra of the torque is shown in Figure A.30, and when the filtered torque is plotted as a histogram the two peak design has become one strong peak in the center, Figure A.31. The filter was applied to the weld software in control applications and used in the post processing of open loop weld data.

Appendix B

Software and Simulation

Many changes were made to the machines software to extend the data acquisition, develop additional weld programs, and standardize the required interface blocks. These changes are detailed here as well as special scripts used to analyze the data generated.

B.1 Changes to the base weld program

Changes were made to the basic input and output block for the simulink welding model. The input block was modified to regroup all signals from their source to two fields: Location or Force. The output block was modified to account for the new VFD programming. The logging block was created as a single location to save all singles plotted and saved during the weld.

B.1.1 Input Block

The input block houses all of the data acquisition from PCI DAQs and from the GUI computer. Both analog and digital signals are taken in from the DAQs. The potentiometers and dynamometer produce an analog signal, and the encoders produce digital signals. The signal sorting into the buses that contain like signals occur in this block. Some math on the signals is preformed. The scaling between voltage from the potentiometer and location of the table is is included. The algorithms to convert the encoder pulses in usable angular rotation, and voltage to linear position are contained within the input block.

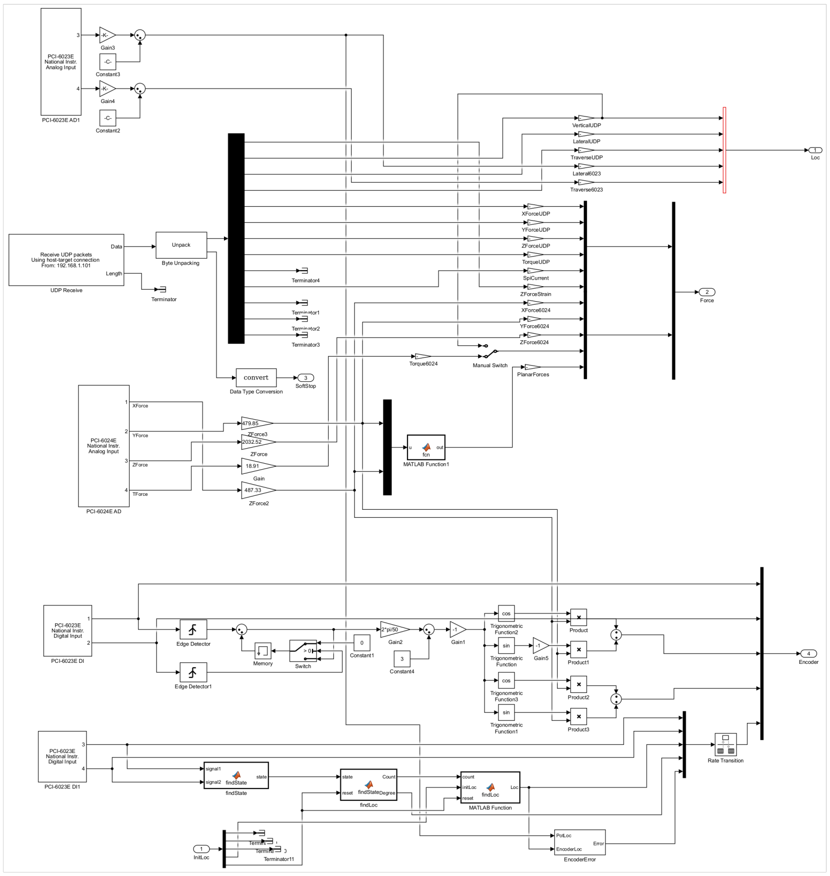

Figure B.1: The input block receives data from multiple different sources: PCI DAQs connected to the computer, and UDP packets from the GUI computer.

B.1.2 Output Block

The output block exports commanded speed data to the VFDs to control the motors. For the lateral and transverse motors, the IPM commanded by the weld program is converted into voltages to be exported to the VFDs. The data for the vertical motor speed and spindle speed is exported back to the GUI computer via UDP.

The IPM for the transverse and lateral motors are converted to voltages by accounting for the gearing ratio and the programming of the VFD. An extra correction factor was added to the lateral output to correct for any unknown reason that prevented accurate reproduction of the commanded speed.

B.1.3 Logging Block

A logging block was written to serve as a consolidated location for saving all signals of interest from the weld control Simulink model, and displaying a selected subset on the output monitor, Figure B.3. This block became necessary to standardize the method of data collection when implementing different controllers.

Three data collection structures are expected to remain constant for each welding model: Location, Force, and Out. Two structures are used in controlled welds: Control and Encoder. Encoder records all relevant signals from the spindle and y-axis encoder. The control structure logs all signals relevant to the control system. If needed, these fields can be modified. If the first three structures are unmodified, then general data analysis scripts will work for any weld, and custom scripts can be written for a specific controller. Thus streamlining the data analysis process

The sampling rate of signals entering into the logging block was standardized to the highest sampling rate and grouped according to use and not collection method. This move streamlined the process for comparing signals from different sources, but

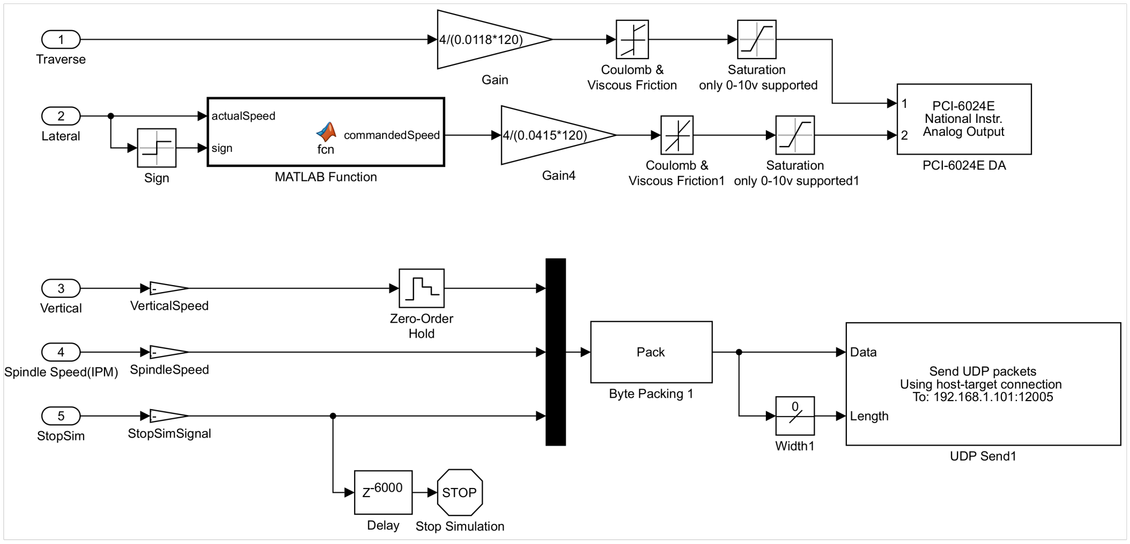

Figure B.2: The output block converts the IPM signals used in the controller to voltages usable to the VFDs, and writes the vertical speed, spindle speed, and stop signal to the GUI computer.

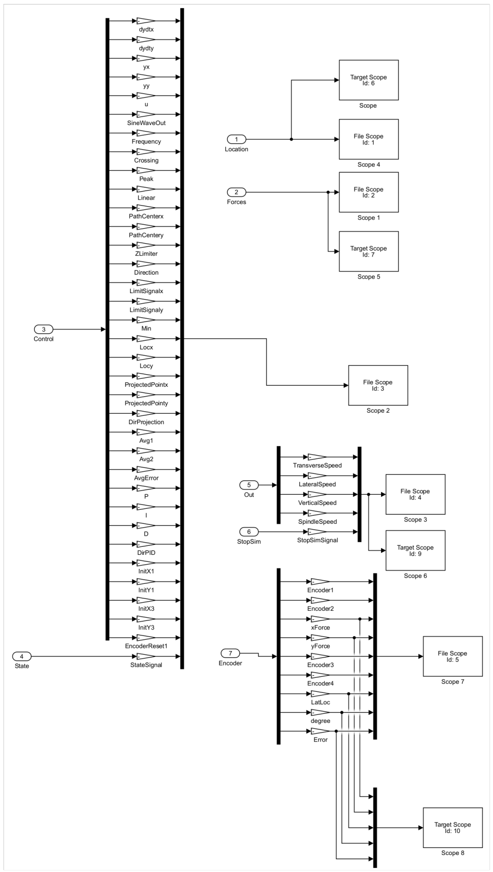

Figure B.3: The logger Simulink subsystem collects all signals and allows users to select some for display on a UI.

did create repeated data points for some signals. It was more common and code heavy to build a relational script to identify indices of the same time step across multiple sampling rates. It was thought that removing duplicates if needed would be a better solution.

The Location variable contains all of the data from the string potentiometers and z-axis encoder. The potentiometers are measured at both the GUI and control computers. Its structure is as follows:

The Force variable contains all data measured by the Kistler dynamometer and other indicators of the force or torque the machine is exerting during the weld. The dynamometer is measured at both the GUI and control computers. The other com-

	Location
1	VerticalUDP
2	LateralUDP
3	TransverseUDP
4	Lateral6023
5	Transverse6023
6	Time

Table B.1: Location Variable

	Force
1	XForceUDP
2	YForceUDP
3	ZForceUDP
4	TorqueUDP
5	SPICurrent
6	ZForceStrain
7	XForce6024
8	YForce6024
9	ZForce6024
10	Torque6024
11	PlanarForces
12	Time

Table B.2: Force Variable

ponents are measured at the GUI computer.

The Encoder variable contains data originating from the digital inputs from the encoders and data regarding their processing.

The Out variable logs the outputs to all motors and the commanded stop for the machine.

The Controller variable logs all data that pertains to any custom controller introduced into the weld software. In the case of the groove controller the variable contains metrics for the path generation, spline generation, and directional controllers.

	Encoder
1	Encoder1
2	Encoder2
3	xForce
4	yForce
5	Encoder3
6	Encoder4
7	LatLoc
8	degree
9	Error
10	Time

Table B.3: Encoder Variable

	Out
1	TransverseSpeed
2	LateralSpeed
3	VerticalSpeed
4	SpindleSpeed
5	StopSimSignal
6	Time

Table B.4: Out Variable

	Path
1	dY/dt_x
2	dY/dt_y
3	Y_x
4	Y_y
5	u
	SineWave
6	Out
7	Frequency
8	Crossing
9	Peak
10	Linear
	PathCenter
11	$Center_x$
12	$Center_y$
13	ZLimiter
14	Direction
	LimitSignal
15	$LimitSignal_x$
16	$LimitSignal_y$
	ControllerMetrics
17	Min
18	Loc_x
19	Loc_y
20	$ProjectedPoint_x$
21	$ProjectedPoint_y$
22	ProjectedDir
23	Avg1
24	Avg2
25	Error
26	P
27	D
28	I
29	PIDDir
30	InitX1
31	InitY1
32	InitX3
33	InitY3
34	EncoderReset
35	StateSignal
36	Time

Table B.5: Control Variable

B.2 Groove Controller

During work on through the tool groove tracking, a new controller was developed to create a path to follow and control the weld speed through the path. The controller was built in Matlab Simulink and interfaced with the already established weld program, Figure B.4.

Additional blocks were added to the state space block to both calibrate the encoder and start the groove controller. A safety zone was set up so that if the tool approached the zone while trying to track the groove, the program would immediately moved to end the weld, Figure B.5.

The groove controller was made of three different sub-models: the directional controller, The motion controller, and the position controller, Figure B.6.

B.2.1 Motion Controller

The motion controller created the tool path to follow as well as controls the speed along the path. The path is dynamically generated by a direction in the form of an angle from the current heading.

The outermost model of the motion controller is the constant speed model, Figure B.7. This model takes input from the path generation block and solves for the motor speeds and tool positions to follow the path with constant speed. The model solves a governing differential equation,

$$\sigma = \left| \frac{d\vec{r}}{du} \right| \frac{du}{dt}, \tag{B.1}$$

,detailed by David Eberly [169]. The algorithm solves for u, a pseudo-time value whose values maintain a constant length of the path for each step in time. Saturation blocks and a custom implementation of derivatives, Figure B.8 have been added to the implementation of the algorithm to prevent division by zero and imaginary values

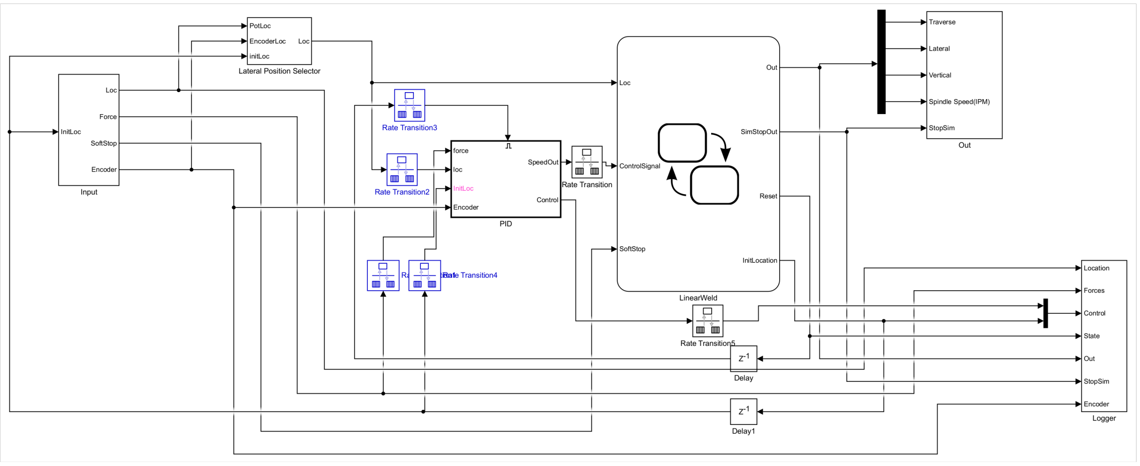

Figure B.4: The groove controller simulink model is made of four major blocks: Input, Controller, State flow, and Output.

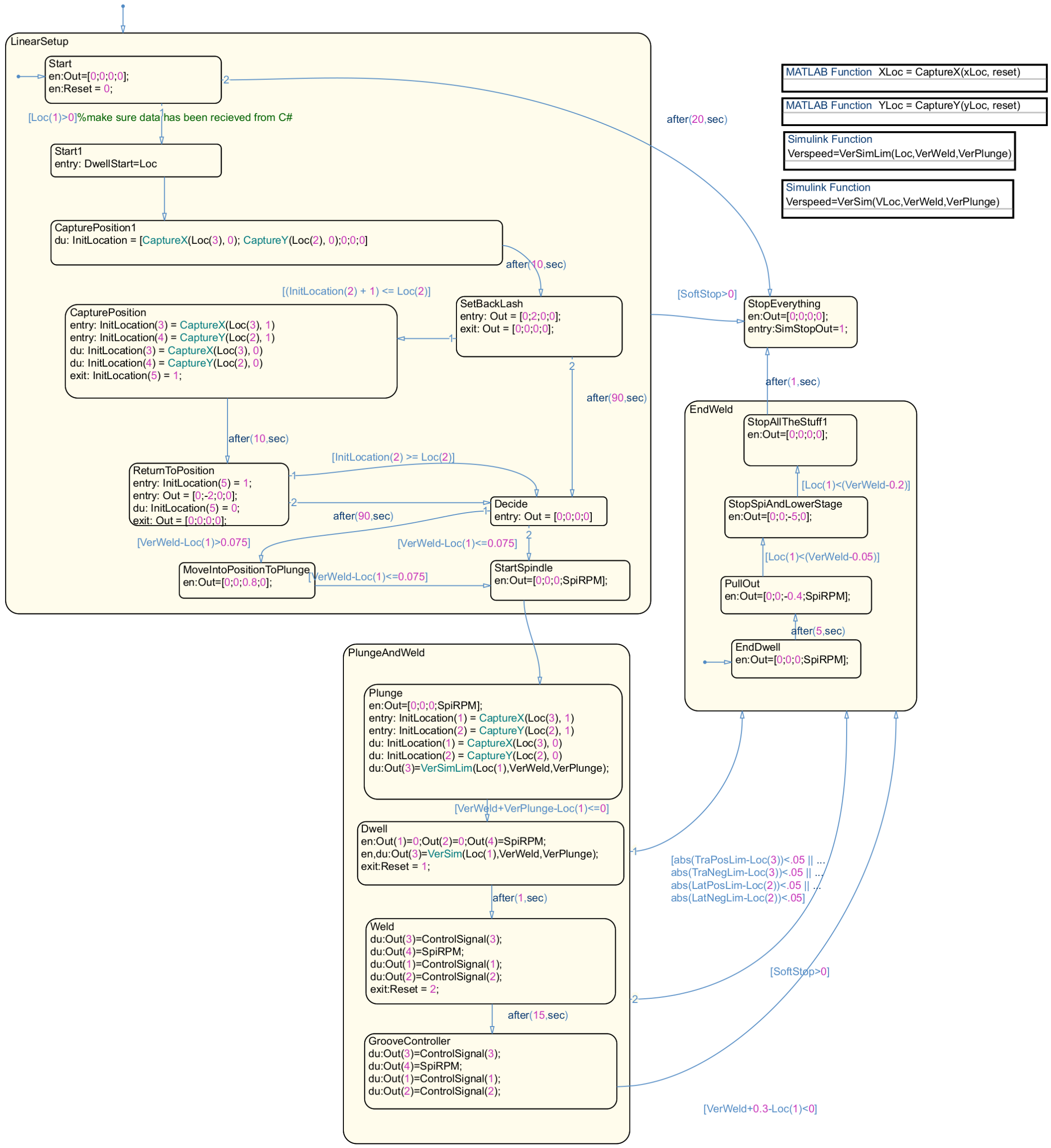

Figure B.5: The state flow model controls what state (start up, plunge, dwell, weld, end) the machine is in based upon its inputs.

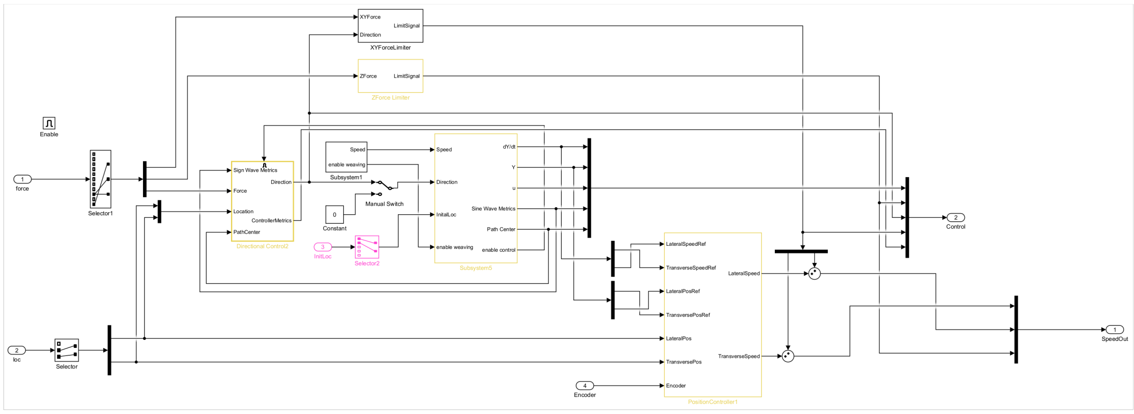

Figure B.6: The weaving controller is a combination of three different control systems. The first is the directional controller, the second is the position controller, and the third is the motion controller.

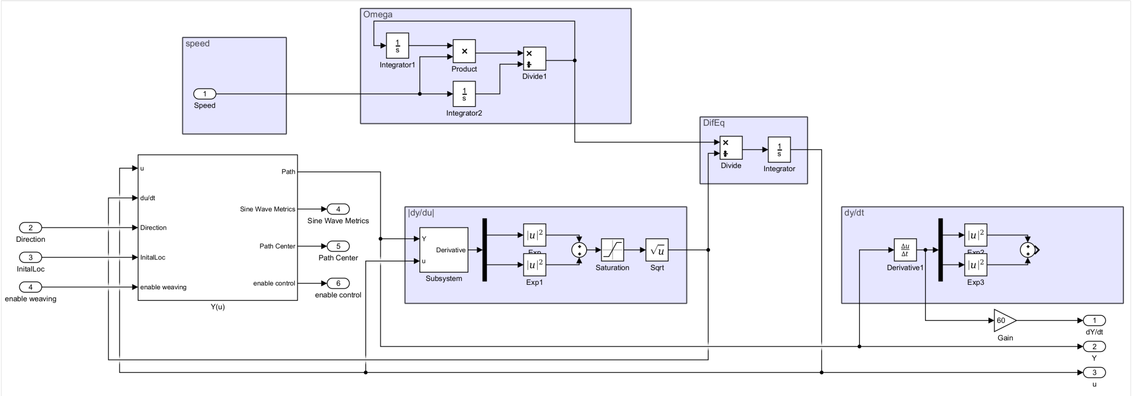

Figure B.7: The position controller solves the constant speed spline problem for the generated path, supplying a speed and position to the motion controller.

that can occur at the start of the weld.

The path generation function procedurally generates a path for the controller to follow, Figure B.9. It does this by splitting the generation into two parts. First a base path is iteratively created by taking a unit step in a defined direction, starting for the initial location of the welding tool. The second part is overlaying a generated sine wave over the base path. The two signals are overlayed through matrix math. In other words, the sine wave is plotted in a corrinate axis system defined by the direction, normal, and translation to the end of the base path.

In the future, the generated path can be overwritten with a predefined function to create a raster pattern for Friction Stir Processing or other needs.

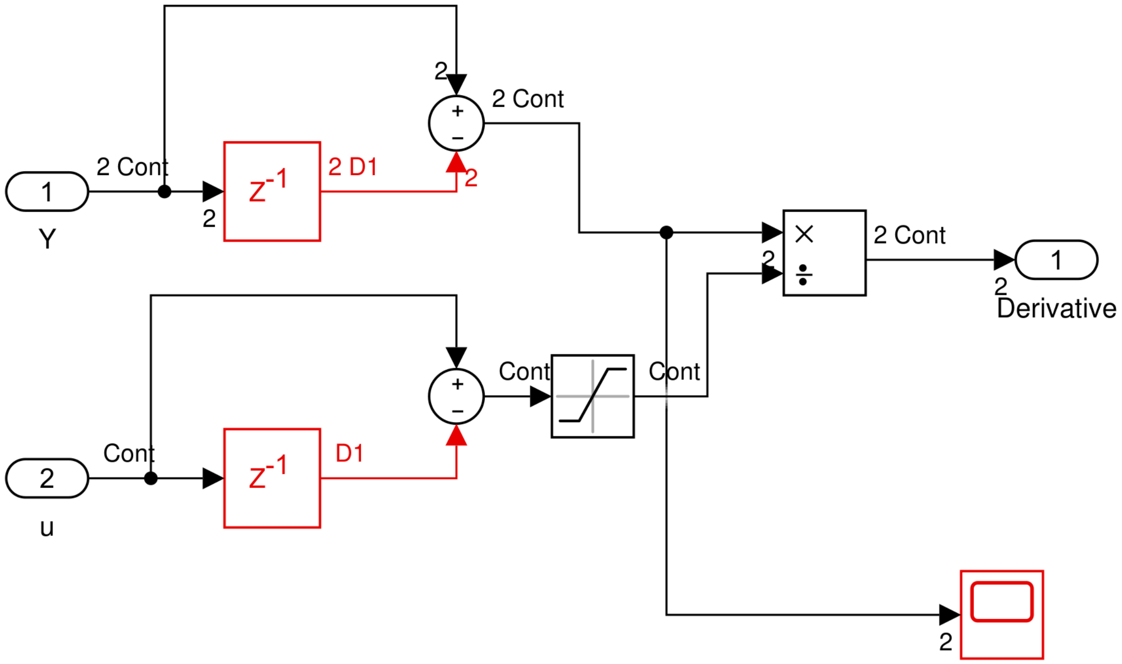

Figure B.8: Custom derivative algorithm written to prevent division by zero during startup.

The sine wave generator tunes the phase and amplitude of the sine wave as well as provides multiple triggering flags used in the direction controller, Figure B.10. The sine wave could be toggled on by the signal input. This input was typically triggered after the initial dwell and welding speed ramp had been completed.

On activation of the sine wave, the amplitude of the sine wave was gradually increased to prevent large or discontinuous motions in the path generation.

It was found through test welds that phase compensation was necessary. Without the compensation, the path generation would generate a path the tool could not follow during start up of the sine wave. The path could jump from the base path through a significant distance of aluminum if the sine wave was near a peak. The phase capture and compensation insures that the sine wave is at a zero crossing.

The phase compensation uses the enable signal as a triggering signal for a simple memory latch, Figure B.11

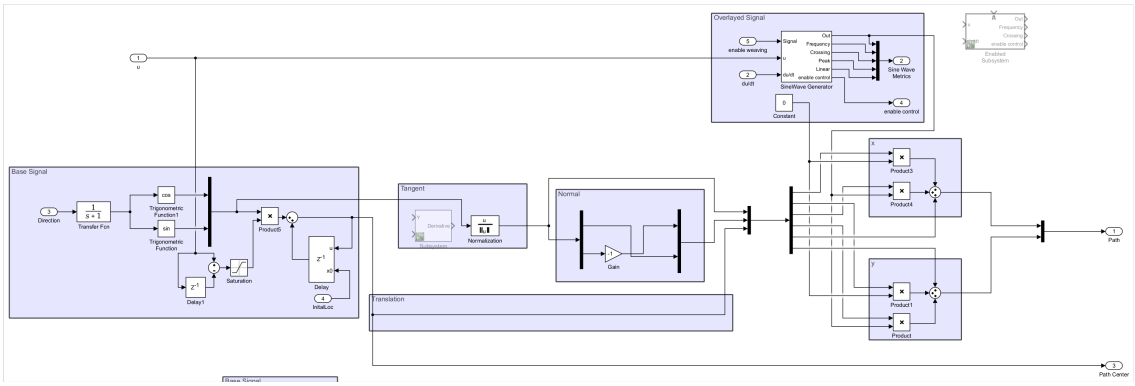

Figure B.9: The path generation begins by generating a path center from the direction. Then, a sine wave is interposed overlayed over the base path via matrix.

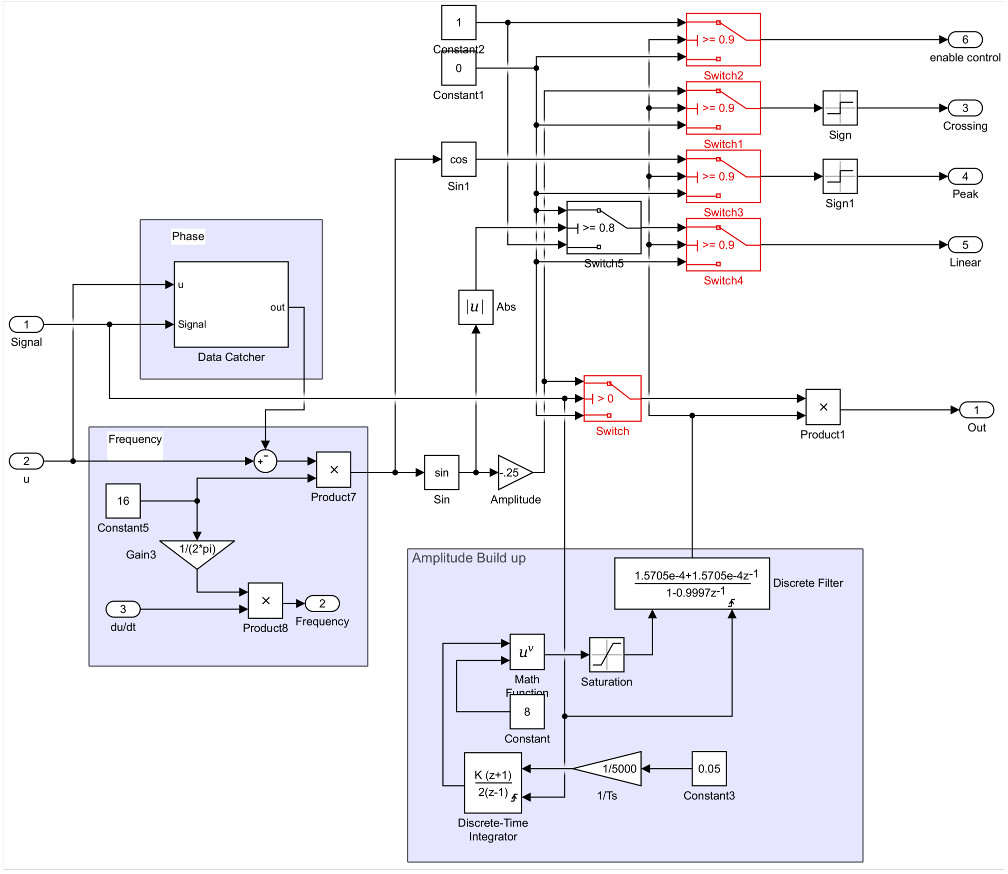

Figure B.10: The sine wave generator sets phase and amplitude. It also provides multiple signals for other control components.

There were many triggering signs generated from the sine wave, They indicated completion of start up, zero crossings, peaks, and the approximately linear portions of the sine wave. All of these signals were used to trigger different data captures in the directional controller.

The transverse speed was also gradually ramped on start up. This insured gradual loading of the tool, Figure B.12. The rapid increase in welding speed that occurred with out the ramp could cause the welder to hit safety limits and stop the weld. The ramp functioned as an accumulator that increased in value each iteration of the control system. The value was saturated at the configured transverse speed. This ramp was then run through a filter to behave as a damper on the system, smoothing

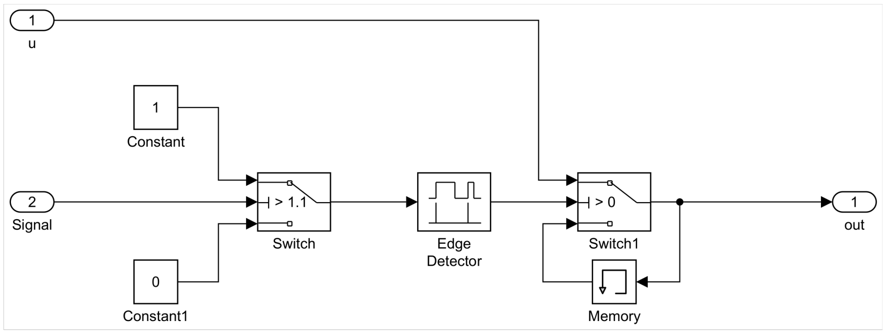

Figure B.11: The phase correction model captures the current position of the weld tool and passes it to the sine wave generator for phase correciton.

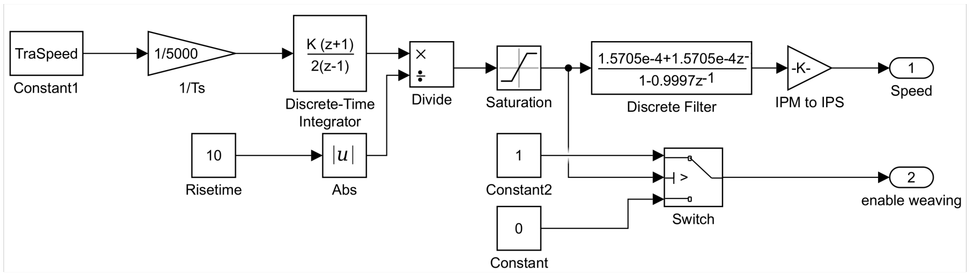

Figure B.12: Custom speed ramp written to functional within the State Space block

out the sharp transitions.

A signaling system was also included to activate the Sine Wave. This system increased the enable signal from a 0 to a 1 when the ramp had reached 90 percent of its final value.

B.2.2 Direction Controller

The directional controller set the direction of the path generation of the motion controller. The controller block contained two different control systems: the averaging controller and the projection controller, Figure B.13.

The averaging controlller functioned by summing the forces above and below the base path, then comparing the result. The zero crossing signal from the sine wave

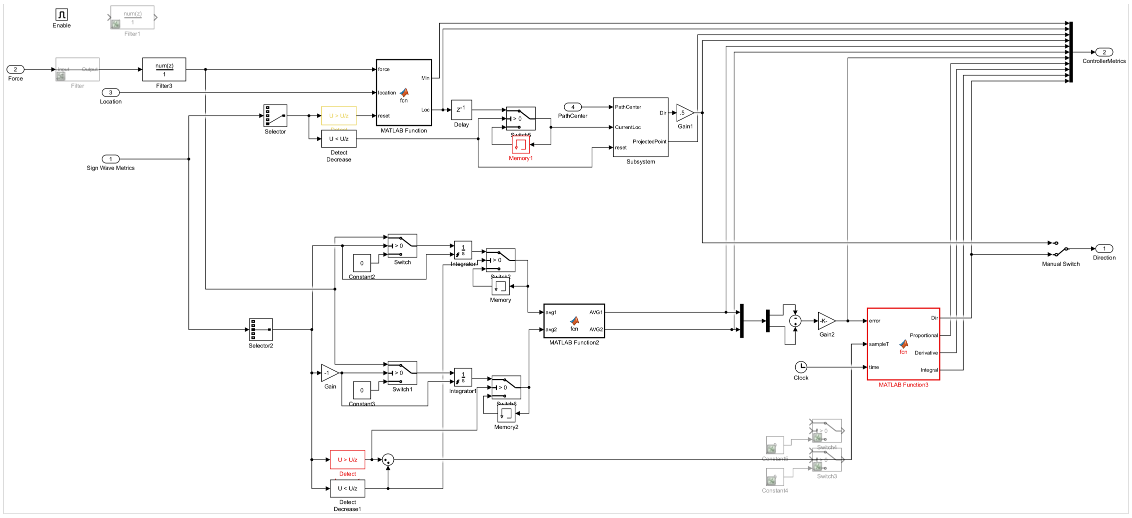

Figure B.13: The directional controller is an enabled subsystem the top algorithm is the averaging controller and the bottom subsystem is the projection controller.

generation was used to differentiate between the two sides and switch between two different accumulation blocks. After the HasData function, the accumulated values are then compared. The resultant error signal is then fed into a PID controller to set the change in direction.

```matlab
% The hasData function prevents the dirctional controller from operating
% before one full weaving period has been completed.
function [AVG1, AVG2] = hasData(avg1, avg2)
if avg1 ~= 0 && avg2 ~= 0
    AVG1 = avg1;
    AVG2 = avg2;
else
    AVG1 = 0;
    AVG2 = 0;
end
```

The hasData function was added to the averaging controller to solve an issue, where The first iteration would drive the direction far to one side. The cause is first iteration of the PID controller occurs after the first half period of the weave tracker but before there is actual data for above and below the weld center. This function insures that both above and below center line averages has data before passing the data to the PID controller. If one of the averages is zero, then both averages are sent as zero.

```matlab
function [Dir,Proportional,Derivative,Integral] = fcn(error, sampleT, time)
persistent dir errorD01 errorD02 errorI priorT01 priorT02 proportional derivative integral divStart rise;
% Initialization of all persistent variables
if isempty(dir)
    dir = 0;
    errorD01 = 0;
    errorD02 = 0;
    errorI = 0;
    priorT01 = 0;
    priorT02 = 0;
    proportional = 0;
    derivative = 0;
    integral = 0;
    divStart = 4;
    rise = 0;
end

```

```
%the if statement insures that the PID lop is only run once per
%zerocrossing.
if sampleT == 1 && rise == 0
    rise = 1;

    % Evaluating the Proportional component
    proportional = 0.002*error;

    %enabling the derivative component only after divStart number of
    %zerocrossings.
    if divStart == 0
        derivative = 0.15*(errorD02-error)/(priorT02-time);
    else
        derivative = 0;
    end

    %Saturated integral component to prevent wind up
    integral = .0005*errorI;
    if integral > .01
        integral = .01;
    elseif integral < -.01
        integral = -.01;
    end

    dir = dir + (proportional + derivative + integral);

    %Variables insure that the derivative is evaluated by comparing
   every
    %other data set. Helps to increase the stability of the controller.
    errorD02 = errorD01;
    priorT02 = priorT01;
    errorD01 = error;
    priorT01 = time;

    errorI = errorI+error;

    %Reducing the derivative countdown variable
    if divStart ~= 0
        divStart = divStart - 1;
    end

elseif sampleT == 0 && rise == 1
    rise = 0;
end

Dir = dir;
Proportional = proportional;
Derivative = derivative;
Integral = integral;
```

A custom PID loop had to be written for the minima tracking controller. The built in PID controller iterated based upon the some multiple of the sample time of the model. The controller PID loop needed to evaluate with each zeros crossing of the sine wave. Therefore, the custom PID loop had an external sampling signal that took in a zero crossing signal from the motion controller.

The derivative compared data from every other zero crossing. Otherwise the derivative component would react to the change in processing forces from either side of the sine wave, and not the change in difference between the processing forces of the system.

One change to be made in future versions is to first divide the accumulated value by the number of samples taken before comparing the two values. Potentially other measures of central tendency of the accumulated dataset could be attempted if the noise from the signal source could be reduced.

The projection controller functions by estimating the location of the groove at a projected point and attempted to set the heading to intersect with the groove at the point. The groove location is estimated by looked at the past two minimum force locations identified during a peak to peak sweep and projecting a straight line out ahead of the tool to select a point.

The selection of the minimum locations was handled by the following function. The function looks for the lowest value from the force input. Saving the result in a persistent variable. A reset toggle allows the persistent variables to be cleared each cycle.

```
function [Min, Loc] = fcn(force, location, reset)
persistent min loc rise;
if isempty(min)
    min = force;
    loc = location;
    rise = 0;
end

if reset == 1 && rise == 0
    rise = 1;
    min = force;
    loc = location;
elseif reset == 0 && rise == 1
```

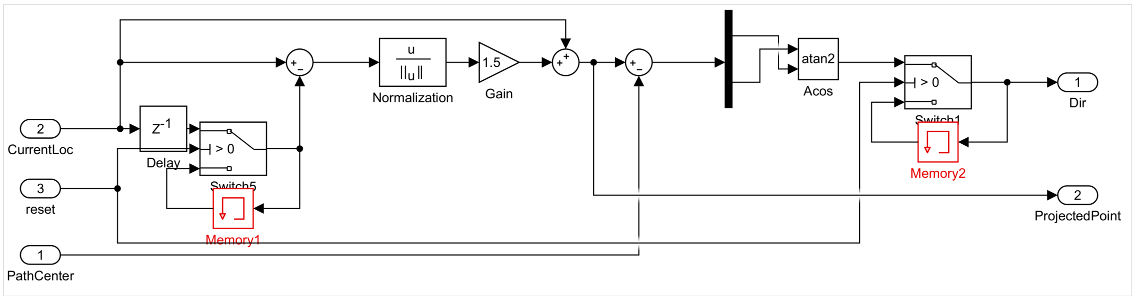

Figure B.14: Simulink Submodel used to calculate a direction from the last two found force minimum locations.

```
    rise = 0;
end

if force < min
    min = force;
    loc = location;
end

Min = min;
Loc = loc;
```

The location is stored in a memory block external to the function.

A Simulink submodel was written to take the difference of the last two detected minimum locations and created a direction for the tool to follow, Figure B.14. This was accomplished by using the difference between the minimums create a directional vector, which could then be scaled and translated to the last minimum. The end of

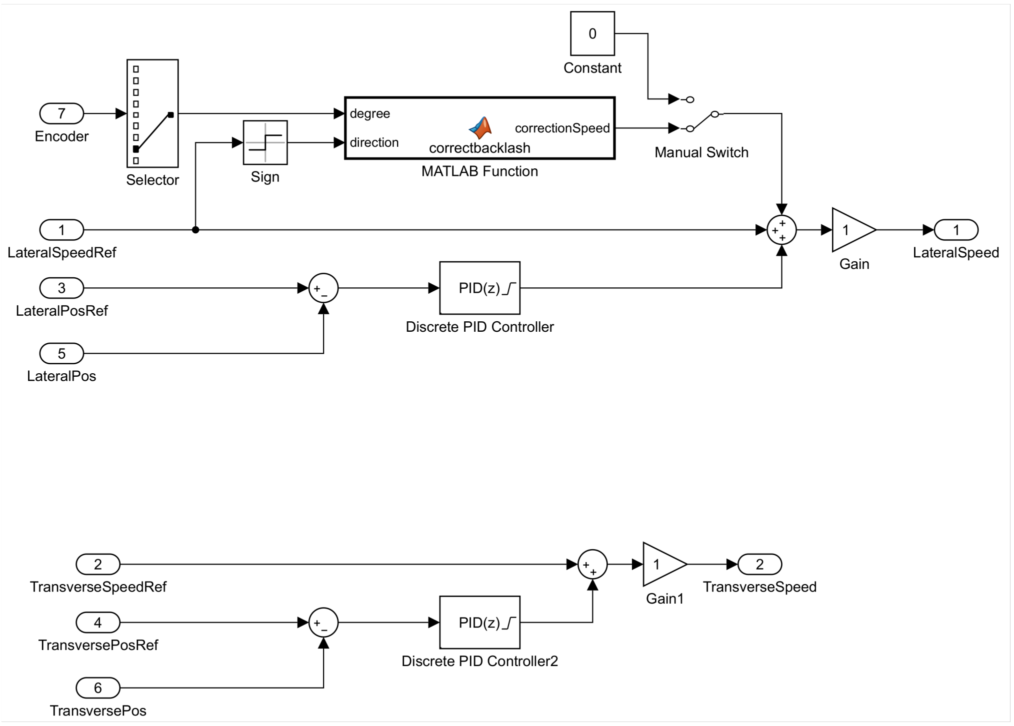

Figure B.15: The motion controller corrects for positional differences as well as backlash correction in the y-direction.

the vector is the estimated groove center ahead of the tool. Then, the angle between the projected point and the current location could be calculated and used to find a direction using the inverse tangent function.

B.2.3 Position Controller

The position controller corrects any deviation from the expected position by adding minor modifications to each motor speed, and accounts for directional changes in the Y-axis, Figure B.15. The differences between measured and expected position are used as the error signal for a PID controller. The PID controller produces a speed correction that is added to the reference speed generated by the motion controller.

Direct measurement of the y-axis lead screw enabled backlash correction. The backlash correction function speeds up the motors rotation to ensure that the backlash dead zone is taken up as quickly as possible without jerking the tool in the material.

The backlash correction is handled by a segment of Matlab code. When a directional change occurs, the function adds a constant value to the y-motor output speed until the encoder has rotated through a set amount of degrees. The amount of degrees of the y-axis lead screw required was found by measurement, and trial and error. The process for calibration is described above. The degree signal comes from the backlash compensation accumulator from findCount encoder function. In this case the degrees is measured in counts of the encoder.

There is a small source of error in the backlash controller when the actual path lags the reference path. The reference speed has flipped sign before the actual path does. The backlash compensation function will be engaged. So, the sign function's input could be changed to the output lateral speed and not the reference. Testing would be needed to insure that the model is solvable and if the change increases the lag in the path following. Additionally, the planar forces present during FSW may cause the table to be pushed to one side of the lead screw prematurely, and requiring less compensation.

```matlab
function correctionSpeed = correctbacklash(degree, direction)
if degree > 28 && direction == 1
    correctionSpeed = 3;
elseif degree < 110 && direction == -1
    correctionSpeed = -3;
else
    correctionSpeed = 0;
end
```

Force limiters were added to the controller to prevent welds from completely failing at the force limit. The force limiters work by finding the difference between a slightly reduced safety limit of the machine and the current processing force, and if the result is close to zero, the transverse speed is massively slowed down or the tool is rapidly pulled out of the material. This system is build off an exponential function which switches from exponentially small when the processing force is smaller than the limit to exponentially large when the processing force is near the limit, Figures B.16, B.17. The value produced by the exponential is subtracted from the current motor speeds.

The XY Limiter respects the current direction of the weld. This ensures that the velocity of the tool is actually reduced, and the direction is not changed.

The z limiter is subtracted from the z axis motor speed. Therefore, the tool is retracted from the material with the z-force is near the limit.

These systems where initially tested in simulation, then as an air weld with a much smaller limit in place to validate them for use in actual weld. For future use of the limiter blocks, the output should be limited such that the transverse speed cannot be driven negative, inverting the direction of travel rapidly.

Multiple real world weaving tracking welds were completed using the groove controller with four different initial positions to the groove: centered, advancing offset, retreating offset, and angled. The set speed, commanded speed, and measured speed for each of the welds are displayed in Figure B.18. The measures speed was found by fitting a smoothing spline to the measured location data and taking the derivative of the spline. Both the commanded and measured welding speed is slightly higher than 3 IPM, but it is consistent through the weld. The peaks to 6 IPM in the commanded speed is the directional change at each peak. The speed is rapidly doubled to compensate for backlash. However, the measured speed is much lower, because the backlash is not completely accounted for by the speed increase.

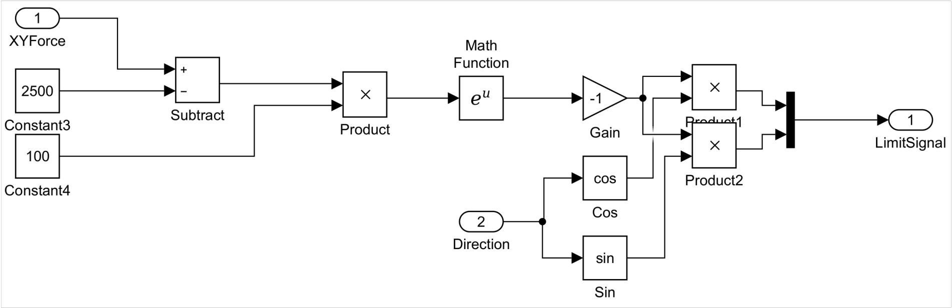

Figure B.16: The XY limiter is a exponential function that will rapidly slow down the tool in when a safety limit is neared.

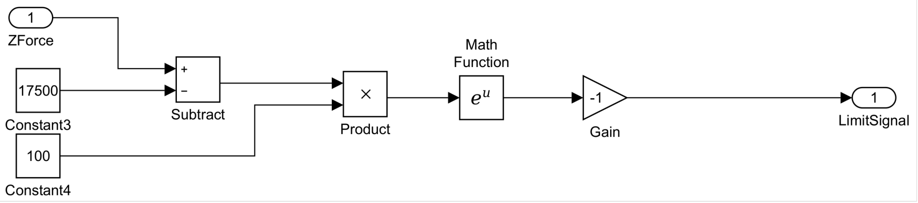

Figure B.17: The Z limiter is a exponential function that will rapidly retract the tool in when a safety limit is neared.

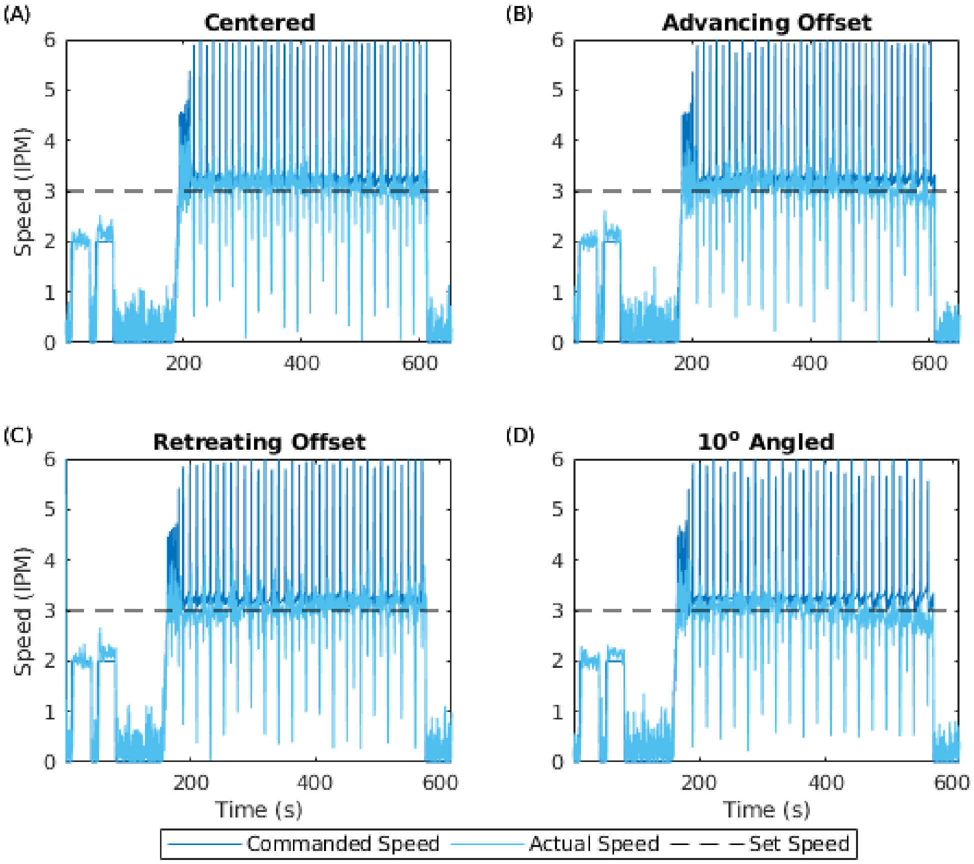

Figure B.18: Speed recorded during three weave tracking welds utilizing the motion controller and speed controller

B.3 Torque controller

The torque controller was built to complete the research project in Chapter 5. The standard set of Input and Output blocks were used, but a customized state flow diagram was used to engage the controller at the correct time, Figure B.19 .

The torque controller is a PID controller with filtered input, Figure B.20. More details on the filtering can be found in Appendix A.1.8. The controller also features a Z-force Limiter block, detailed in Subsection B.2.3. The gains and other performance metrics are gathered into a single bus wire and sent out of the subsystem to be logged.

The state flow diagram was customized to engage the torque controller after 15 seconds of normal weld, Figure B.21. This gave time for the weld speed to ramp to full value ,and the tool leaved the area of material disturbed by the plunge and dwell.

A safety depth limit has been added. The height of the anvil, fixture, or FSE top sheet is set before the weld begins using the auto zero routine. Then, the parameter is manually entered using a GUI field. The state flow diagram ends the weld if the tip of the tool gets within 0.005" of the material height. This prevents the controller from rapidly and unexpectedly retracting from the material.

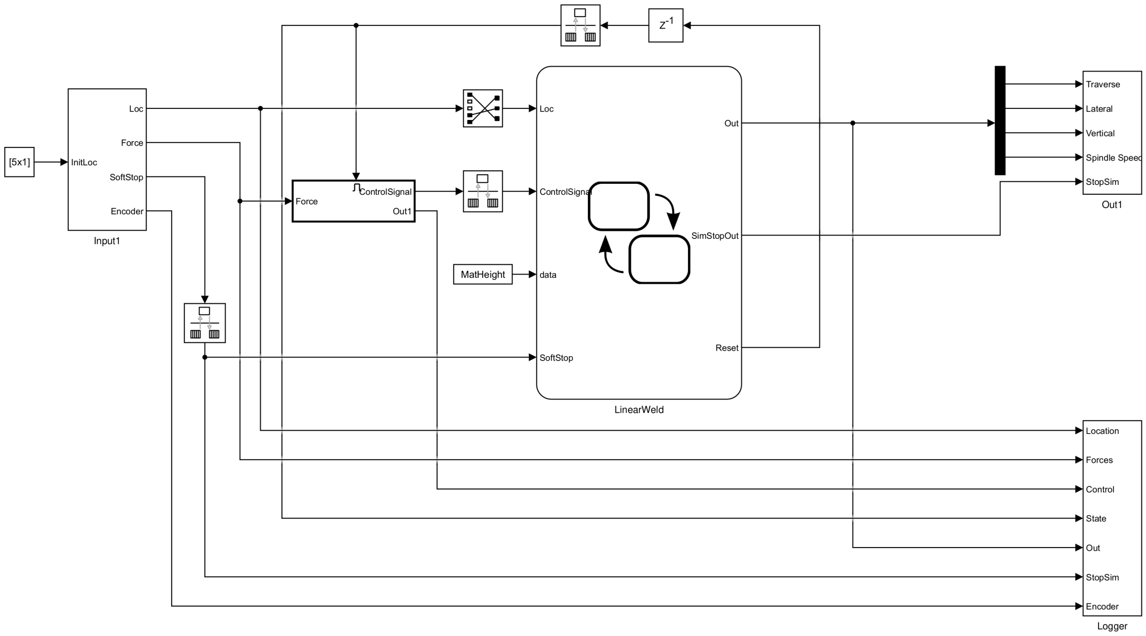

Figure B.19: The Simulink block diagram for the torque control weld program.

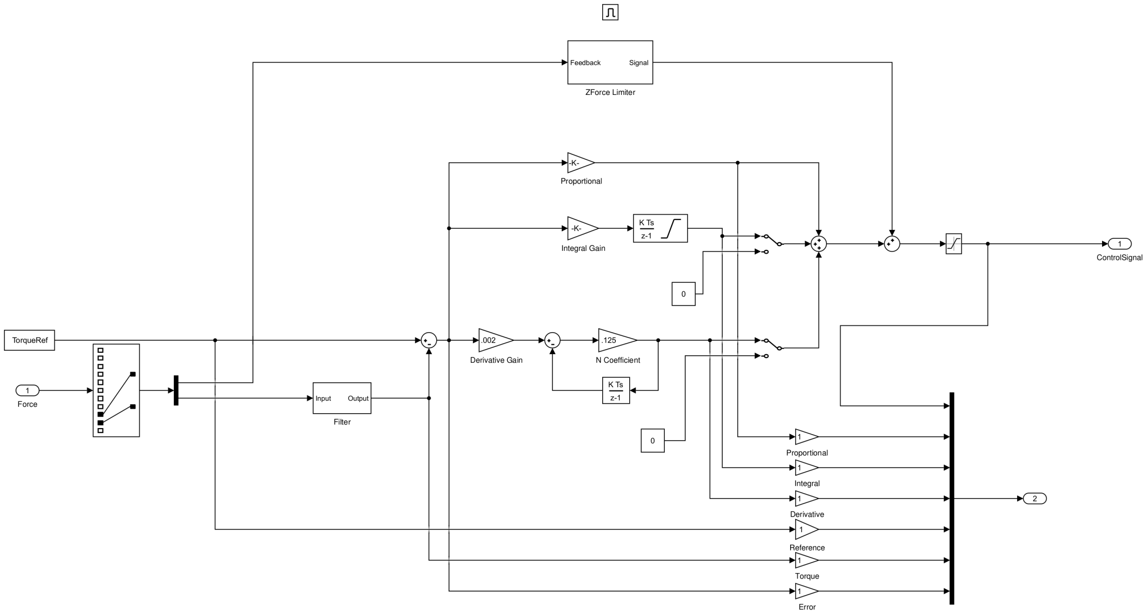

Figure B.20: The torque controller is a PID controller with some filtering and high force protection.

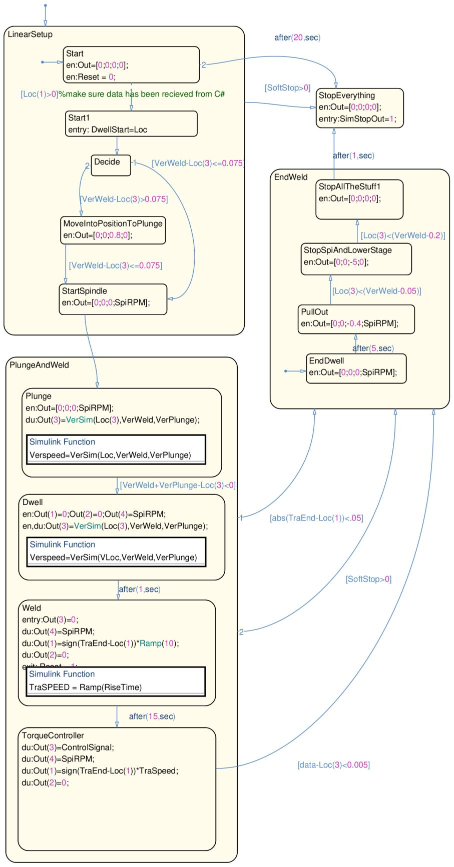

Figure B.21: The torque controller state flow diagram controls the stages of the weld and enables the torque controller.

B.4 Analyzing Processing Forces and Simulating Measurement Noise

The simulation of noise was needed to test the stability of differing control methods in MATLAB Simulink. The frequency domain of a normal weld the was very well understood from the measurements made for both the torque controller and weave controller. So, the signal could be recreated by selectively filtering the random number generator in MATLAB Simulink. The random number generator allows for the selection of the mean and variance of the random number generator. These numbers can be derived from subtracting the filtered signal from the raw data for one weld.

B.5 Data Analysis Techniques

During the course of this research, multiple scripts were written to automate data analysis and focus on specific time periods within the welds. The data anaylsis script uses indicators during the weld to signal different stages of the weld. Then, known transient portions of the weld, dwell and initial motion, can be seperated from the rest of the well so accurate averages of the processing forces can be evaluated. The processing force data can also be filtered and their frequency response evaluated.

The Analysis script calls the TrialHandeling script for multiple data sets, passing the .mat files, subplot number, and text title. The resultant figures are then formated and saved at publicaion ready DPI.

```
% Calling the TrialHandling function for each set of processing
    parameters

TrialHandling(["FinalDataCollection93.mat" "FinalDataCollection94.mat" "
    FinalDataCollection95.mat"], 1, '0.000')

figure(3)
hold on

figure(6)
hold on

TrialHandling(["FinalDataCollection90.mat" "FinalDataCollection91.mat" "
    FinalDataCollection92.mat"], 2, '0.025')
```

```

TrialHandling(["FinalDataCollection87.mat” "FinalDataCollection88.mat” "FinalDataCollection89.mat”], 3, '0.050')

TrialHandling(["FinalDataCollection84.mat” "FinalDataCollection85.mat” "FinalDataCollection86.mat”], 4, '0.075')

TrialHandling(["FinalDataCollection81.mat” "FinalDataCollection82.mat” "FinalDataCollection83.mat”], 5, '0.100')

TrialHandling(["FinalDataCollection77.mat” "FinalDataCollection78.mat” "FinalDataCollection79.mat”], 6, '0.125')

TrialHandling(["FinalDataCollection74.mat” "FinalDataCollection75.mat” "FinalDataCollection76.mat”], 7, '0.150')

TrialHandling(["FinalDataCollection71.mat” "FinalDataCollection72.mat” "FinalDataCollection73.mat”], 8, 'Step')

TrialHandling(["FinalDataCollection96.mat” "FinalDataCollection97.mat” "FinalDataCollection98.mat”], 9, 'Cont.')

%% Configure Figures

% Figure 1

fig = figure(1);
fig.Units = 'inches';
fig.Position(3) = 6.5;
fig.Position(4) = 4.9;

s1 = subplot(3,3,1);
s1.Units = 'inches';
s1.Position = [0.8459 3.5917 1.3834 0.8790];
ylabel('Force (N)');
grid on
set(s1,'GridAlpha',0.3);

s2 = subplot(3,3,2);
s2.Units = 'inches';
s2.Position = [2.6684 3.5917 1.3873 0.8790];
grid on
set(s2,'GridAlpha',0.3);

s3 = subplot(3,3,3);
s3.Units = 'inches';
s3.Position = [4.4932 3.5917 1.3759 0.8790];
grid on
set(s3,'GridAlpha',0.3);

s4 = subplot(3,3,4);
s4.Units = 'inches';
s4.Position = [0.8459 2.2387 1.3834 0.8872];
ylabel('Force (N)');
```

```
grid on
set(s4,'GridAlpha',0.3);

s5 = subplot(3,3,5);
s5.Units = 'inches';
s5.Position = [2.6684 2.2387 1.3873 0.8872];
grid on
set(s5,'GridAlpha',0.3);

s6 = subplot(3,3,6);
s6.Units = 'inches';
s6.Position = [4.4932 2.2387 1.3759 0.8872];
grid on
set(s6,'GridAlpha',0.3);

s7 = subplot(3,3,7);
s7.Units = 'inches';
s7.Position = [0.8459 0.8962 1.3834 0.8812];
xlabel('Time (s)');
ylabel('Force (N)');
grid on
set(s7,'GridAlpha',0.3);

s8 = subplot(3,3,8);
s8.Units = 'inches';
s8.Position = [2.6684 0.8962 1.3873 0.8812];
xlabel('Time (s)');
grid on
set(s8,'GridAlpha',0.3);

s9 = subplot(3,3,9);
s9.Units = 'inches';
s9.Position = [4.4932 0.8962 1.3893 0.8812];
xlabel('Time (s)');
grid on
set(s9,'GridAlpha',0.3);

lgd = legend({'Trial 1', 'Trial 2', 'Trial 3'});
lgd.Orientation = 'horizontal';
lgd.Position(1) = .3;
lgd.Position(2) = .02;
lgd.Position(3) = .425;
lgd.Position(4) = .05;
print('ControlledZForce', '-dpng', '-r300')

% Figure 2

fig = figure(2);
fig.Units = 'inches';
fig.Position(3) = 6.5;
fig.Position(4) = 4.9;

s1 = subplot(3,3,1);
s1.Units = 'inches';
```

```
s1.Position = [0.8459 3.5917 1.3834 0.8790];
ylabel('Power (dB)');
grid on
set(s1,'GridAlpha',0.3);

s2 = subplot(3,3,2);
s2.Units = 'inches';
s2.Position = [2.6684 3.5917 1.3873 0.8790];
grid on
set(s2,'GridAlpha',0.3);

s3 = subplot(3,3,3);
s3.Units = 'inches';
s3.Position = [4.4932 3.5917 1.3759 0.8790];
grid on
set(s3,'GridAlpha',0.3);

s4 = subplot(3,3,4);
s4.Units = 'inches';
s4.Position = [0.8459 2.2387 1.3834 0.8872];
ylabel('Power (dB)');
grid on
set(s4,'GridAlpha',0.3);

s5 = subplot(3,3,5);
s5.Units = 'inches';
s5.Position = [2.6684 2.2387 1.3873 0.8872];
grid on
set(s5,'GridAlpha',0.3);

s6 = subplot(3,3,6);
s6.Units = 'inches';
s6.Position = [4.4932 2.2387 1.3759 0.8872];
grid on
set(s6,'GridAlpha',0.3);

s7 = subplot(3,3,7);
s7.Units = 'inches';
s7.Position = [0.8459 0.8962 1.3834 0.8812];
ylabel('Power (dB)');
xlabel('Frequency (Hz)');
grid on
set(s7,'GridAlpha',0.3);

s8 = subplot(3,3,8);
s8.Units = 'inches';
s8.Position = [2.6684 0.8962 1.3873 0.8812];
xlabel('Frequency (Hz)');
grid on
set(s8,'GridAlpha',0.3);

s9 = subplot(3,3,9);
s9.Units = 'inches';
s9.Position = [4.4932 0.8962 1.3893 0.8812];
```

```
xlabel('Frequency (Hz)');
grid on
set(s9,'GridAlpha',0.3);

lgd = legend({'Trial 1', 'Trial 2', 'Trial 3'});
lgd.Orientation = 'horizontal';
lgd.Position(1) = .3;
lgd.Position(2) = .02;
lgd.Position(3) = .425;
lgd.Position(4) = .05;
print('ControlledZForceSpectrum', '-dpng', '-r300')

% Figure 3

fig = figure(3);
hold off
legend show
xlabel('Frequency (Hz)');
ylabel('Power (dB)');
grid on
set(get(fig,'CurrentAxes'),'GridAlpha',0.3);
xticks([0 12.5 25 37.5 50])
print('ControlledZForceAveragedSpectrum', '-dpng', '-r300')

% Figure 4

fig = figure(4);
fig.Units = 'inches';
fig.Position(3) = 6.5;
fig.Position(4) = 4.9;

s1 = subplot(3,3,1);
s1.Units = 'inches';
s1.Position = [0.8459 3.5917 1.3834 0.8790];
ylabel('Torque (Nm)');
grid on
set(s1,'GridAlpha',0.3);

s2 = subplot(3,3,2);
s2.Units = 'inches';
s2.Position = [2.6684 3.5917 1.3873 0.8790];
grid on
set(s2,'GridAlpha',0.3);

s3 = subplot(3,3,3);
s3.Units = 'inches';
s3.Position = [4.4932 3.5917 1.3759 0.8790];
grid on
set(s3,'GridAlpha',0.3);

s4 = subplot(3,3,4);
s4.Units = 'inches';
s4.Position = [0.8459 2.2387 1.3834 0.8872];
ylabel('Torque (Nm)');
```

```
grid on
set(s4,'GridAlpha',0.3);

s5 = subplot(3,3,5);
s5.Units = 'inches';
s5.Position = [2.6684 2.2387 1.3873 0.8872];
grid on
set(s5,'GridAlpha',0.3);

s6 = subplot(3,3,6);
s6.Units = 'inches';
s6.Position = [4.4932 2.2387 1.3759 0.8872];
grid on
set(s6,'GridAlpha',0.3);

s7 = subplot(3,3,7);
s7.Units = 'inches';
s7.Position = [0.8459 0.8962 1.3834 0.8812];
xlabel('Time (s)');
ylabel('Torque (Nm)');
grid on
set(s7,'GridAlpha',0.3);

s8 = subplot(3,3,8);
s8.Units = 'inches';
s8.Position = [2.6684 0.8962 1.3873 0.8812];
xlabel('Time (s)');
grid on
set(s8,'GridAlpha',0.3);

s9 = subplot(3,3,9);
s9.Units = 'inches';
s9.Position = [4.4932 0.8962 1.3893 0.8812];
xlabel('Time (s)');
grid on
set(s9,'GridAlpha',0.3);

lgd = legend({'Trial 1', 'Trial 2', 'Trial 3'});
lgd.Orientation = 'horizontal';
lgd.Position(1) = .3;
lgd.Position(2) = .02;
lgd.Position(3) = .425;
lgd.Position(4) = .05;
print('ControlledTorque', '-dpng', '-r300')

% Figure 5

fig = figure(5);
fig.Units = 'inches';
fig.Position(3) = 6.5;
fig.Position(4) = 4.9;

s1 = subplot(3,3,1);
s1.Units = 'inches';
```

```
s1.Position = [0.8459 3.5917 1.3834 0.8790];
ylabel('Power (dB)');
grid on
set(s1,'GridAlpha',0.3);

s2 = subplot(3,3,2);
s2.Units = 'inches';
s2.Position = [2.6684 3.5917 1.3873 0.8790];
grid on
set(s2,'GridAlpha',0.3);

s3 = subplot(3,3,3);
s3.Units = 'inches';
s3.Position = [4.4932 3.5917 1.3759 0.8790];
grid on
set(s3,'GridAlpha',0.3);

s4 = subplot(3,3,4);
s4.Units = 'inches';
s4.Position = [0.8459 2.2387 1.3834 0.8872];
ylabel('Power (dB)');
grid on
set(s4,'GridAlpha',0.3);

s5 = subplot(3,3,5);
s5.Units = 'inches';
s5.Position = [2.6684 2.2387 1.3873 0.8872];
grid on
set(s5,'GridAlpha',0.3);

s6 = subplot(3,3,6);
s6.Units = 'inches';
s6.Position = [4.4932 2.2387 1.3759 0.8872];
grid on
set(s6,'GridAlpha',0.3);

s7 = subplot(3,3,7);
s7.Units = 'inches';
s7.Position = [0.8459 0.8962 1.3834 0.8812];
xlabel('Frequency (Hz)');
ylabel('Power (dB)');
grid on
set(s7,'GridAlpha',0.3);

s8 = subplot(3,3,8);
s8.Units = 'inches';
s8.Position = [2.6684 0.8962 1.3873 0.8812];
xlabel('Frequency (Hz)');
grid on
set(s8,'GridAlpha',0.3);

s9 = subplot(3,3,9);
s9.Units = 'inches';
s9.Position = [4.4932 0.8962 1.3893 0.8812];
```

```
xlabel('Frequency (Hz)');
grid on
set(s9,'GridAlpha',0.3);

lgd = legend({'Trial 1', 'Trial 2', 'Trial 3'});
lgd.Orientation = 'horizontal';
lgd.Position(1) = .3;
lgd.Position(2) = .02;
lgd.Position(3) = .425;
lgd.Position(4) = .05;
print('ControlledTorqueSpectrum', '-dpng', '-r300')

% Figure 6

fig = figure(6)
hold off
legend show
xlabel('Frequency (Hz)');
ylabel('Power (dB)');
grid on
set(get(fig,'CurrentAxes'),'GridAlpha',0.3);
xticks([0 12.5 25 37.5 50])
print('ControlledTorqueAveragedSpectrum', '-dpng', '-r300')

% Figure 7

fig = figure(7);
fig.Units = 'inches';
fig.Position(3) = 6.5;
fig.Position(4) = 4.9;

s1 = subplot(3,3,1);
s1.Units = 'inches';
s1.Position = [0.8459 3.5917 1.3834 0.8790];
ylabel('Height (in)');
grid on
set(s1,'GridAlpha',0.3);

s2 = subplot(3,3,2);
s2.Units = 'inches';
s2.Position = [2.6684 3.5917 1.3873 0.8790];
grid on
set(s2,'GridAlpha',0.3);

s3 = subplot(3,3,3);
s3.Units = 'inches';
s3.Position = [4.4932 3.5917 1.3759 0.8790];
grid on
set(s3,'GridAlpha',0.3);

s4 = subplot(3,3,4);
s4.Units = 'inches';
s4.Position = [0.8459 2.2387 1.3834 0.8872];
ylabel('Height (in)');
```

```
grid on
set(s4,'GridAlpha',0.3);

s5 = subplot(3,3,5);
s5.Units = 'inches';
s5.Position = [2.6684 2.2387 1.3873 0.8872];
grid on
set(s5,'GridAlpha',0.3);

s6 = subplot(3,3,6);
s6.Units = 'inches';
s6.Position = [4.4932 2.2387 1.3759 0.8872];
grid on
set(s6,'GridAlpha',0.3);

s7 = subplot(3,3,7);
s7.Units = 'inches';
s7.Position = [0.8459 0.8962 1.3834 0.8812];
xlabel('Time (s)');
ylabel('Height (in)');
grid on
set(s7,'GridAlpha',0.3);

s8 = subplot(3,3,8);
s8.Units = 'inches';
s8.Position = [2.6684 0.8962 1.3873 0.8812];
xlabel('Time (s)');
grid on
set(s8,'GridAlpha',0.3);

s9 = subplot(3,3,9);
s9.Units = 'inches';
s9.Position = [4.4932 0.8962 1.3893 0.8812];
xlabel('Time (s)');
grid on
set(s9,'GridAlpha',0.3);

lgd = legend({'Trial 1', 'Trial 2', 'Trial 3'});
lgd.Orientation = 'horizontal';
lgd.Position(1) = .3;
lgd.Position(2) = .02;
lgd.Position(3) = .425;
lgd.Position(4) = .05;
print('ControlledHeight', '-dpng', '-r300')
```

When plotting each data set from multiple weld trials, it was possible to abstract the analysis process. The TrialHandling function picks the relevant processing force data out of the .mat files for all three welds, post processes the data, and plots them in the designated subplots. The processing forces are filted by a low pass filtering objects and truncated to the actual start of the weld. The start is found by identifying the time when the z-force or torque rises above a threshold of 100 N or 1 Nm. The power spectrum is evaluated for z-force and torque. Then, all collected data are ploted on the designated subplot of preselected figure numbers.

```
% The trial handling function takes an array of weld files and plots out
% processing force data in the designated subplot. This function only
   works
% in concert with the analysis.m script. Function is designed to take an
% array of three weld files. However, it can be designed to take more.
function TrialHandling(Files, subplotIndex, subplotTitle)

% Creating the filter object
Hd = LowPass20Hz();
frequencyLimits = [0 50];

m = gray(10);

% Load the first file and create variables for the filtered processing
% variables
load(Files(1))
ZForceNI01 = Force.data(:,9);
Time01 = Force.data(:,12);
ZForceNI25Hz01 = filter(Hd,ZForceNI01);
TorqueNI01 = Force.data(:,10);
TorqueBP25Hz01 = filter(Hd,TorqueNI01);
ZHeight01 = Location.data(:,1)-VerWeld-VerPlunge;

%Find the start time of the actual weld.
for i = 1:length(ZForceNI25Hz01)
    if ZForceNI25Hz01(i) > 100
        starttimeZ01 = i;
        break;
    end
end

for i = 1:length(TorqueBP25Hz01)
   if TorqueBP25Hz01(i) > 1
       starttimeT01 = i;
       break;
   end
end

% Truncate the processing forces to when the weld starts.
ZForceNI01 = ZForceNI01(starttimeZ01:end);
TimeZ01 = Time01(starttimeZ01:end)-Time01(starttimeZ01);
ZForceNI25Hz01 = ZForceNI25Hz01(starttimeZ01:end);
TorqueNI01 = TorqueNI01(starttimeT01:end);
TimeT01 = Time01(starttimeT01:end)-Time01(starttimeT01);
TorqueBP25Hz01 = TorqueBP25Hz01(starttimeT01:end);
```

```
ZHeight01 = ZHeight01(starttimeT01:end);

% Repeat the process for the other two weld files

load(Files(2))
ZForceNI02 = Force.data(:,9);
Time02 = Force.data(:,12);
ZForceNI25Hz02 = filter(Hd,ZForceNI02);
TorqueNI02 = Force.data(:,10);
TorqueBP25Hz02 = filter(Hd,TorqueNI02);
ZHeight02 = Location.data(:,1)-VerWeld-VerPlunge;

for i = 1:length(ZForceNI25Hz02)
    if ZForceNI25Hz02(i) > 100
        starttimeZ02 = i;
        break;
    end
end

for i = 1:length(TorqueBP25Hz02)
   if TorqueBP25Hz02(i) > 1
       starttimeT02 = i;
       break;
   end
end

ZForceNI02 = ZForceNI02(starttimeZ02:end);
TimeZ02 = Time02(starttimeZ02:end)-Time02(starttimeZ02);
ZForceNI25Hz02 = ZForceNI25Hz02(starttimeZ02:end);
TorqueNI02 = TorqueNI02(starttimeT02:end);
TimeT02 = Time02(starttimeT02:end)-Time02(starttimeT02);
TorqueBP25Hz02 = TorqueBP25Hz02(starttimeT02:end);
ZHeight02 = ZHeight02(starttimeT02:end);

load(Files(3))
ZForceNI03 = Force.data(:,9);
Time03 = Force.data(:,12);
ZForceNI25Hz03 = filter(Hd,ZForceNI03);
TorqueNI03 = Force.data(:,10);
TorqueBP25Hz03 = filter(Hd,TorqueNI03);
ZHeight03 = Location.data(:,1)-VerWeld-VerPlunge;

for i = 1:length(ZForceNI25Hz03)
    if ZForceNI25Hz03(i) > 100
        starttimeZ03 = i;
        break;
    end
end

for i = 1:length(TorqueBP25Hz03)
   if TorqueBP25Hz03(i) > 1
       starttimeT03 = i;
       break;
   end
```

```
end

ZForceNI03 = ZForceNI03(starttimeZ03:end);
TimeZ03 = Time03(starttimeZ03:end)-Time03(starttimeZ03);
ZForceNI25Hz03 = ZForceNI25Hz03(starttimeZ03:end);
TorqueNI03 = TorqueNI03(starttimeT03:end);
TimeT03 = Time03(starttimeT03:end)-Time03(starttimeT03);
TorqueBP25Hz03 = TorqueBP25Hz03(starttimeT03:end);
ZHeight03 = ZHeight03(starttimeT03:end);

% Evaluate the power spectrum for all three welds

ZForceTT01 = timetable(seconds(TimeZ01), ZForceNI01);
ZForceTT02 = timetable(seconds(TimeZ02), ZForceNI02);
ZForceTT03 = timetable(seconds(TimeZ03), ZForceNI03);

TorqueTT01 = timetable(seconds(TimeT01), TorqueNI01);
TorqueTT02 = timetable(seconds(TimeT02), TorqueNI02);
TorqueTT03 = timetable(seconds(TimeT03), TorqueNI03);

[p1,f1] = pspectrum(ZForceTT01,'FrequencyLimits',frequencyLimits);
[p2,f2] = pspectrum(ZForceTT02,'FrequencyLimits',frequencyLimits);
[p3,f3] = pspectrum(ZForceTT03,'FrequencyLimits',frequencyLimits);

% Plotting the weld data and adding subplot specific formating

figure(1);
subplot(3,3,subplotIndex);
plot(TimeZ01, ZForceNI25Hz01, 'color', [0, 0, 0]);
hold on
plot(TimeZ02, ZForceNI25Hz02, 'color', [.66, .66, .66]);
plot(TimeZ03, ZForceNI25Hz03, 'color', [.33, .33, .33]);
hold off
title(subplotTitle)
xlim([0 250])
ylim([0 12500])
ax = gca;
ax.YAxis.Exponent = 3;

figure(2)
subplot(3,3,subplotIndex)
plot(f1,10*log10(p1), 'color', [0, 0, 0]);
hold on
plot(f2,10*log10(p2), 'color', [.66, .66, .66]);
plot(f3,10*log10(p3), 'color', [.33, .33, .33]);
hold off
title(subplotTitle)
xticks([0 12.5 25 37.5 50])
yticks([0 20 40 60])
ylim([0 60]);

figure(3)
plot(f1, 10*log10((p1+p2+p3)/3), 'color', m(subplotIndex,1:3), 'DisplayName', subplotTitle)
```

```

[p1,f1] = pspectrum(TorqueTT01,'FrequencyLimits',frequencyLimits);
[p2,f2] = pspectrum(TorqueTT02,'FrequencyLimits',frequencyLimits);
[p3,f3] = pspectrum(TorqueTT03,'FrequencyLimits',frequencyLimits);

figure(4)
subplot(3,3,subplotIndex)
plot(TimeT01, TorqueBP25Hz01, 'color', [0, 0, 0]);
hold on
plot(TimeT02, TorqueBP25Hz02, 'color', [.66, .66, .66]);
plot(TimeT03, TorqueBP25Hz03, 'color', [.33, .33, .33]);
plot([0 250],[11 11], '--', 'color', [0, 0, 0]);
plot([0 250],[11*.9 11*.9], '--', 'color', [0, 0, 0]);
plot([0 250],[11*1.1 11*1.1], '--', 'color', [0, 0, 0]);
hold off
title(subplotTitle)
xlim([0 250])
ylim([0, 25])

figure(5)
subplot(3,3,subplotIndex)
plot(f1,10*log10(p1), 'color', [0, 0, 0]);
hold on
plot(f2,10*log10(p2), 'color', [.66, .66, .66]);
plot(f3,10*log10(p3), 'color', [.33, .33, .33]);
hold off
title(subplotTitle)
xticks([0 12.5 25 37.5 50])
yticks([-40 -20 0 20])
ylim([-40 20])

figure(6)
plot(f1, 10*log10((p1+p2+p3)/3), 'color', m(subplotIndex,1:3), 'DisplayName', subplotTitle)

figure(7)
subplot(3,3,subplotIndex)
plot(TimeT01, ZHeight01, 'color', [0, 0, 0]);
hold on
plot(TimeT02, ZHeight02, 'color', [.66, .66, .66]);
plot(TimeT03, ZHeight03, 'color', [.33, .33, .33]);
hold off
title(subplotTitle)
ylim([-.015 .025])
xlim([0 250])

end
```

To quantify the effects of a certain set of processing parameter on the processing forces, the average of the processing forces was evaluated. Since the raw data contains regions considered to be transient, plunge and initial movement, the data had to be truncated to only contain the steady state portion before averaging. A script was written to accomplish this for larger data sets. The script uses the internal state signals as well as the outputs to determine the time range when the conditions for steady state have been met. The conditions are 1 inch beyond the start of the weld until the tool stops transverse at the end of the weld. Once the processing forces have been truncated, they can be averaged and post processed, plotting the power spectrum. The script also plots the post processed in a publication ready plot with trend lines.

```matlab
% The truncation scrip generates publicaiton ready figures from all weld
% files in its directory. The loop pulls in one weld file and cuts down all
% weld data to the ”Steady state” region 1 inch after plunge until the tool
% stops moving. The averages are evaluated and plotted against groove width
% or offset.
%% Set up variables
files = dir('*.mat');
len = length(files);
GrooveWidthAry = zeros(len,1);
AvgXForce = zeros(len,1);
AvgYForce = zeros(len,1);
AvgZForce = zeros(len,1);
AvgPlaForce = zeros(len,1);
AvgStrain = zeros(len,1);
AvgTorque = zeros(len,1);
AvgSpiCur = zeros(len,1);

%% Run Loop

for i = 1:length(files)
    load(files(i).name);

    GrooveWidthAry(i) = GrooveWidth;

    % Spectrum Analysis
    frequencyLimits = [0 50];

    %ForceData
    TorqueNI = Force.data(:,10);
    ZForceNI = Force.data(:,9);
    PlanerForce = Force.data(:,11);

    %Location Data
    Transverse = Location.data(:,5);
```

```
    Start = mean(Location.data(1:400,5));
    Transverse = Transverse - Start;

    %XYForce Anlysis
    xForce = timeseries(Force.data(:,7), Force.data(:,12));
    yForce = timeseries(Force.data(:,8), Force.data(:,12));
    Encoder1 = timeseries(Encoder.data(:,1), Encoder.data(:,9));
    Encoder2 = timeseries(Encoder.data(:,2), Encoder.data(:,9));

    %Outputs
    SpeedOut = Out.data(:,1);

    %Times
    Time = Force.data(:,12); %Location and Force
    OutTime = Out.data(:,6);

    %Important times
    StartTime = 0;
    ConstantSpeedTime = 0;
    SteadyStateTime = 0;
    StopTime = 0;

    %% Simulink Model

    sim('SpindleEncoder02.slx', Time(end))

    %% Splines

    SplineTime = linspace(Time(1), Time(end), 10000);
    p = .5;
    TransverseSmooth = csaps(Time,Transverse,p,SplineTime);

    %% Finding Times

    %Iterating through the out signals to find the time where the Out
    %signal changes
    State = 0;
    for j = 1:length(SpeedOut)
        if StartTime == 0 && SpeedOut(j) > 0 && State == 0
            StartTime = OutTime(j);
            State = 1;
        elseif ConstantSpeedTime == 0 && SpeedOut(j) == TraSpeed && State == 1
            ConstantSpeedTime = OutTime(j);
            State = 2;
        elseif StopTime == 0 && SpeedOut(j) == 0 && State == 2
            StopTime = OutTime(j);
            break;
        elseif j == length(SpeedOut) && StopTime == 0 && State == 2
            StopTime = OutTime(j);
        end
    end

    %Finding one inch of movement past the plunge location
```

```
    SteadyStateLoc = 0;
    State = 0;
    for p = 1:length(SplineTime)
        if SplineTime(p) > ConstantSpeedTime && State == 0
            SteadyStateLoc = TransverseSmooth(p) + 1;
            if SteadyStateLoc > TransverseSmooth(end)
                SteadyStateLoc = TransverseSmooth(p);
            end
            State = 1;
        elseif State == 1
            if TransverseSmooth(p) >= SteadyStateLoc
                SteadyStateTime = SplineTime(p);
                break;
            end
        end
    end



    %% Find time Indecies

    %relating the out time to the data times (the original signals not
    %simplified/filtered) for the devices attached to the Computer
    State = 0;
    for n = 1:length(Time)-1
        if Time(n) <= SteadyStateTime && Time(n+1) >= SteadyStateTime &&
     State == 0
            StartIndex = n;
            State = 1;
        elseif State == 1
            if Time(n) <= StopTime && Time(n+1) >= StopTime
                EndIndex = n;
                break;
            else
                EndIndex = n;
            end
        end
    end

    %% Truncating Data (Averages)

    AvgXForce(i) = mean(xForceTable.data(StartIndex:EndIndex));
    AvgYForce(i) = mean(yForceTable.data(StartIndex:EndIndex));
    AvgZForce(i) = mean(Force.data(StartIndex:EndIndex,9));
    AvgPlaForce(i) = mean(Force.data(StartIndex:EndIndex,11));
    AvgTorque(i) = mean(Force.data(StartIndex:EndIndex,10));
    AvgStrain(i) = mean(Force.data(StartIndex:EndIndex,6));
    AvgSpiCur(i) = mean(Force.data(StartIndex:EndIndex,5));


    %% Filtering (Plotting)

    Hd = LowPass20Hz();

```

```
    TorqueBandPass25Hz = filter(Hd,TorqueNI);
    PlanerForcePass25Hz = filter(Hd, PlanerForce);
    ZForcePass25Hz = filter(Hd, ZForceNI);
    xForceTable25Hz = filter(Hd,xForceTable.data(StartIndex:EndIndex));
    yForceTable25Hz = filter(Hd,yForceTable.data(StartIndex:EndIndex));

    %% Spectrum

    xForceTableTT = timetable(seconds(xForceTable.Time), xForceTable.data);
    yForceTableTT = timetable(seconds(yForceTable.Time), yForceTable.data);

    TorqueTT = timetable(seconds(Time), TorqueNI);

end

%% Plotting

%Plotting and Formating Images

x = (0:.01:.15);

p1 = polyfit(GrooveWidthAry, AvgTorque, 1);
y1 = polyval(p1, x);
p2 = polyfit(GrooveWidthAry, AvgSpiCur, 1);
y2 = polyval(p2, x);

fig = figure(1);

s1 = subplot(3,1,1);

yyaxis left
plot(GrooveWidthAry, AvgTorque, 'o', 'Color', [0, 0, 0]);
hold on
plot(x,y1, 'Color', [0, 0, 0],'HandleVisibility','off');
ylabel(”Torque (Nm)”);
grid on
set(s1,'GridAlpha',0.3);
xticks([0 .025 .05 .075 .1 .125 .15])
hold off

yyaxis right
plot(GrooveWidthAry, AvgSpiCur, 'x', 'Color', [.5, .5, .5]);
hold on
plot(x,y2, 'Color', [.5, .5, .5],'HandleVisibility','off');
hold off

ax = gca;
ax.YAxis(1).Color = [0 0 0];
ax.YAxis(2).Color = [.5 .5 .5];

ylabel(”Spindle Current (A)”);
lgd1 = legend('Torque', 'Spindle Current');
```

```

p = polyfit(GrooveWidthAry, AvgZForce, 1);
y1 = polyval(p, x);
p = polyfit(GrooveWidthAry, AvgStrain, 1);
y2 = polyval(p, x);

s2 = subplot(3,1,2);
plot(GrooveWidthAry, AvgZForce, 'o', 'Color', [0, 0, 0]);
hold on
plot(GrooveWidthAry, AvgStrain, 'x', 'Color', [.5, .5, .5]);
plot(x,y1, 'Color', [0, 0, 0]);
plot(x,y2, 'Color', [.5, .5, .5]);
ylabel("Z-Force (N)");
lgd2 = legend('Z-Force (Dyno)', 'Z-Force (Strain Gauge)');
grid on
set(s2,'GridAlpha',0.3);
xticks([0 .025 .05 .075 .1 .125 .15])
hold off

p1 = polyfit(GrooveWidthAry, AvgXForce, 1);
y1 = polyval(p1, x);
p2 = polyfit(GrooveWidthAry, AvgYForce, 1);
y2 = polyval(p2, x);
p3 = polyfit(GrooveWidthAry, AvgPlaForce, 1);
y3 = polyval(p3, x);

s3 = subplot(3,1,3);
plot(GrooveWidthAry, AvgPlaForce, 'o', 'Color', [.0, .0, .0]);
hold on
plot(GrooveWidthAry, AvgYForce, 'x', 'Color', [.33 .33 .33])
plot(GrooveWidthAry, AvgXForce, '+', 'Color', [.66 .66 .66])
plot(x, y1, 'Color', [.66, .66, .66])
plot(x, y2, 'Color', [.33, .33, .33]);
plot(x,y3, 'Color', [0, 0, 0]);
grid on
set(s3,'GridAlpha',0.3);
xticks([0 .025 .05 .075 .1 .125 .15])
hold off
ylabel("Forces (N)");
lbl = xlabel("Groove Width (in)");
ylabel("Force (N)");
lgd3 = legend('X-Force', 'Y-Force', 'Planar Force');

fig.Units = 'inches';
fig.Position(3) = 6.5;
fig.Position(4) = 6.5;

s1.Units = 'inches';
s2.Units = 'inches';
s3.Units = 'inches';

s1.Position = [0.8457 4.6141 5.0418 1.4035];
s2.Position = [0.8457 2.6649 5.0418 1.4035];
s3.Position = [0.8457 0.7156 5.0418 1.4035];
```

```

lgd1.Units='inches';
lgd2.Units='inches';
lgd3.Units='inches';

lgd1.Orientation='horizontal';
lgd2.Orientation='horizontal';
lgd3.Orientation='horizontal';

lgd1.Position = [2.0937 4.1633 2.4707 0.2033];
lgd2.Position = [1.6432 2.1963 3.4267 0.2033];
lgd3.Position = [1.7979 0.2842 3.2830 0.2033];

lbl.Units = 'inches';
lbl.Position = [2.522 -0.476 0];

annotation('textbox', [.065 .98 0 0], 'string', '(A)')
annotation('textbox', [.065 .68 0 0], 'string', '(B)')
annotation('textbox', [.065 .38 0 0], 'string', '(C)')

print('ControlledForcesOverview', '-dpng', '-r300')
```

The LowPassFilter is the filter object used to filter the raw processing forces for presentation. It is a 20 Hz cut off lowpass butterworth filter. The filter was primarily used in the TrialHandling function.

```
function Hd = LowPass20Hz
%LOWPASS20HZ Returns a discrete-time filter object.

% MATLAB Code
% Generated by MATLAB(R) 9.3 and Signal Processing Toolbox 7.5.
% Generated on: 23-Nov-2020 23:18:53

% Butterworth Lowpass filter designed using FDESIGN.LOWPASS.

% All frequency values are in Hz.
Fs = 100;  % Sampling Frequency

N  = 10;  % Order
Fc = 20;  % Cutoff Frequency

% Construct an FDESIGN object and call its BUTTER method.
h  = fdesign.lowpass('N,F3dB', N, Fc, Fs);
Hd = design(h, 'butter');

% [EOF]
```

B.5.1 Image Processing

Micrographs taken via election microscopy allows for the rough differentiation of elemental composition by utilizing Z-contrast. Z-contrast is a mechanism by which elements lower on the periodic table generate larger signal due to a higher chance of back-scattering or secondary electron emission. The Z-contrast was used to differentiate between iron (White) containing inclusions from Magnesium/Silicon (Black) participates in the aluminum bulk (Gray). Further, the process could be automated via an image processing technique called thresholding, and automatically tallied to provide compositional data.

A binary image was generated for both the light and dark inclusions by defining a grayscale threshold, figure B.22. Every thing above the threshold was converted to white and vise versa. Then, the images could be filtered for artifacts and noise. The remaining particles could be identified and scaled according to there pixel area. Potential particles under a 10 pixels in area was discounted due to the inability to manually verify the identification. The particles could not be ruled out as noise.

This technique was used to determine the quality of post heat treatment FSWed samples in Chapter 4.

Two grayscale threasholds, both black and white, were manually set for each micrograph by examining the performance on known particles and rejection of everything else. The micrograph specific values helped to eliminate variations due to white balance. Then, a script was written to automatically binarize and count particles.

The Analyze Image script loaded in all four micrographs and applied both a white and black threshold to them through the AnalyzeImage function. Various statistical values were also calculated for each image and type of particle.

```
scale = (1/9)^2;
cutOff = 10;

%%%%%%%%%%%%%%%%%%%%%%%%%%%%%% Base Material
```

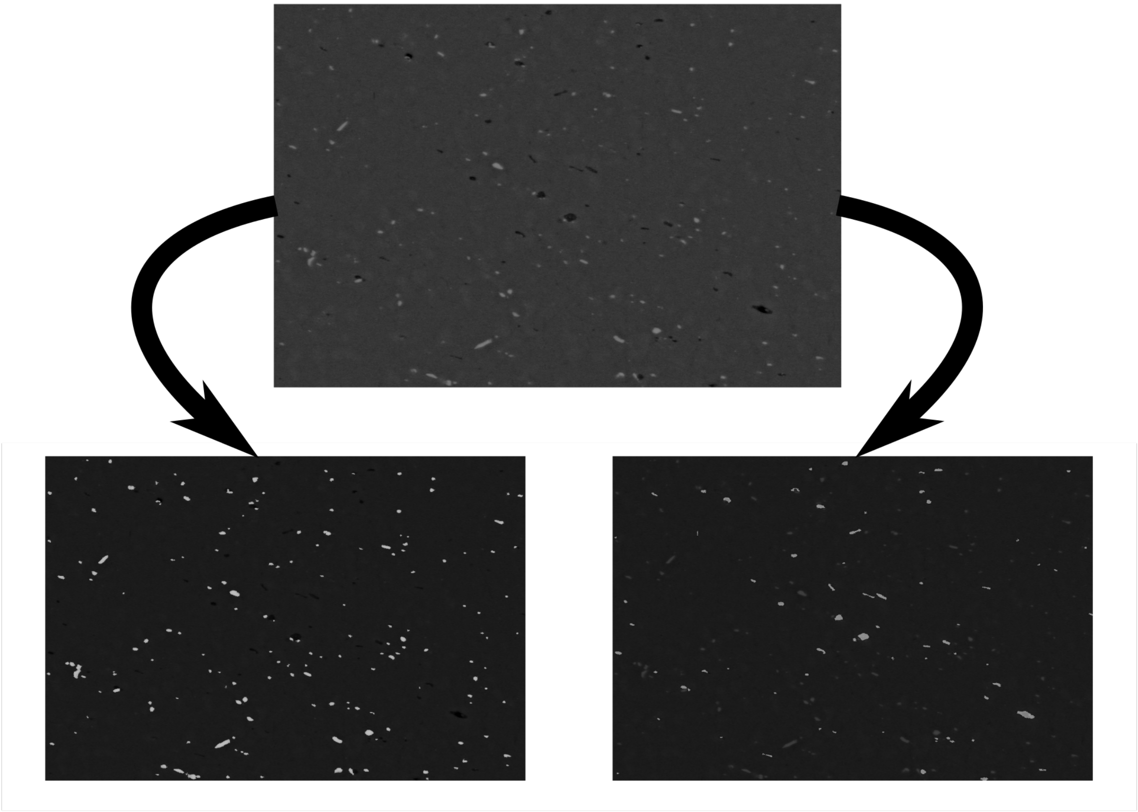

Figure B.22: SEM micrographs had two thresholds applied to them. One to identify the white inclusions, and one to identify the black precipitate. The threshold black precipitates are color inverted for visibility.

```
%%%%%%%%%%%%%%%%%%%%%%%%%%%%%%

[I1, W_ovrly_1, B_ovrly_1, W_prt_1, B_prt_1] = AnalyzeImage('2019-09-30_FSE_base_Al_00(edited).tif', 0.27, 0.18, cutOff, scale);


%%%%%%%%%%%%%%%%%%%%%%%%%% As Welded %%%%%%%%%%%%%%%%%%%%%%%%%%%%%%%%%%%%%%

[I2, W_ovrly_2, B_ovrly_2, W_prt_2, B_prt_2] = AnalyzeImage('2019-09-30_FSE_heat treated_S2T0_00(edited).tif', 0.29, 0.18, cutOff, scale);


%%%%%%%%%%%%%%%%%%%% 10Min Heat Treated %%%%%%%%%%%%%%%%%%%%%%%%%%%%%%%%%%%

[I3, W_ovrly_3, B_ovrly_3, W_prt_3, B_prt_3] = AnalyzeImage('2019-09-17_FSE_heat treated_S2T1_10(edited).tif', 0.27, 0.18, cutOff, scale);


%%%%%%%%%%%%%%%%%%%%%%%%%%% 10 Hour Heat Treated %%%%%%%%%%%%%%%%%%%%%%%%%%

[I4, W_ovrly_4, B_ovrly_4, W_prt_4, B_prt_4] = AnalyzeImage('2019-09-17_FSE_heat treated_S2T9_11(edited).tif', 0.27, 0.15, cutOff, scale);


%%%%%%%%%%%%%%%%%%%%%%%%%%% Statistics %%%%%%%%%%%%%%%%%%%%%%%%%%%%%%%%%%%


white_means = [mean(W_prt_1), mean(W_prt_2), mean(W_prt_3), mean(W_prt_4)];
black_means = [mean(B_prt_1), mean(B_prt_2), mean(B_prt_3), mean(B_prt_4)];

white_med = [median(W_prt_1), median(W_prt_2), median(W_prt_3), median(W_prt_4)];
black_med = [median(B_prt_1), median(B_prt_2), median(B_prt_3), median(B_prt_4)];

white_SD = [std(W_prt_1), std(W_prt_2), std(W_prt_3), std(W_prt_4)];
black_SD = [std(B_prt_1), std(B_prt_2), std(B_prt_3), std(B_prt_4)];

white_per_25 = [prctile(W_prt_1, 25), prctile(W_prt_2, 25), prctile(W_prt_3, 25), prctile(W_prt_4, 25)];
black_per_25 = [prctile(B_prt_1, 25), prctile(B_prt_2, 25), prctile(B_prt_3, 25), prctile(B_prt_4, 25)];

white_per_75 = [prctile(W_prt_1, 75), prctile(W_prt_2, 75), prctile(W_prt_3, 75), prctile(W_prt_4, 75)];
black_per_75 = [prctile(B_prt_1, 75), prctile(B_prt_2, 75), prctile(B_prt_3, 75), prctile(B_prt_4, 75)];

```

```

function [image, white_overlay, black_overlay, white_part, black_part] = AnalyzeImage(img, white_thr, black_thr, cutOff, scale)
    image = imread(img);

    white_overlay = imbinarize(image, white_thr);
    white_overlay = imfill(white_overlay, 'holes');
    white_overlay = bwareaopen(white_overlay,cutOff);

    black_overlay = imbinarize(image, black_thr);
    black_overlay = imcomplement(black_overlay);
    black_overlay = imfill(black_overlay, 'holes');
    black_overlay = bwareaopen(black_overlay,cutOff);

    [L,Ne] = bwlabel(white_overlay);
    white_part = regionprops(L,'Area');
    white_part = transpose(struct2cell(white_part));
    white_part = cell2mat(white_part)*scale;

    [L,Ne] = bwlabel(black_overlay);
    black_part = regionprops(L,'Area');
    black_part = transpose(struct2cell(black_part));
    black_part = cell2mat(black_part)*scale;
end
```

The CreateHistorgram script first called the Analyze Image script to get the statistical data. Then, the histograms were defined and plotted using the previously generated data.

```
run('AnalyzeImages.m');
bins = 0:.1:4;
edges = 0:.025:4;
a = 3.35;
y = .45;
z = 3.35 - y;
x = .35*z;
% w = .5*x;
b = 4*y + 4*x+.2;
str = ”median: ”;

hc1 = histcounts(B_prt_1, [bins, Inf]);
hc2 = histcounts(B_prt_2, [bins, Inf]);
hc3 = histcounts(B_prt_3, [bins, Inf]);
hc4 = histcounts(B_prt_4, [bins, Inf]);

%%%%%%%%%%%%%%%%%%%%%%%%%Create and Format Image %%%%%%%%%%%%%%%%%%%%%%%%%%%

fig = figure(1);
figC1 = subplot(4,1,1);
    hb1 = bar(bins+.05, hc1,1);
    hold on
    plot([black_med(1) black_med(1)], [0 60], 'Color', [0/255, 0/255, 0/255])
```

```
    hold off
    ylim([0,50]);
    xlabel('Particle Area \mum^2', 'fontsize', 8);
    ylabel('Number of Particles', 'fontsize', 8);
    ax = ancestor(figC1, 'axes');
  xrule = ax.XAxis;
    yrule = ax.YAxis;
    xrule.FontSize = 8;
    yrule.FontSize = 8;
    text(0,-.25,'(a)',...
             'FontSize',10,'HorizontalAlignment','center', 'Units', 'normalized');
    text(.37,.7,str + num2str(black_med(1)),...
             'FontSize',8,'HorizontalAlignment','center', 'Units', 'normalized');
figC2 = subplot(4,1,2);
    hb2 = bar(bins+.05, hc2, 1);
    hold on
    plot([black_med(2) black_med(2)], [0 60], 'Color', [0/255, 0/255, 0/255])
    hold off
    ylim([0,50]);
    xlabel('Particle Area \mum^2', 'fontsize', 8);
    ylabel('Number of Particles', 'fontsize', 8);
    ax = ancestor(figC2, 'axes');
  xrule = ax.XAxis;
    yrule = ax.YAxis;
    xrule.FontSize = 8;
    yrule.FontSize = 8;
    text(0,-.25,'(b)',...
             'FontSize',10,'HorizontalAlignment','center', 'Units', 'normalized');
    text(.25,.7,str + num2str(black_med(2)),...
             'FontSize',8,'HorizontalAlignment','center', 'Units', 'normalized');
figC3 = subplot(4,1,3);
    hb3 = bar(bins+.05, hc3, 1);
    hold on
    plot([black_med(3) black_med(3)], [0 60], 'Color', [0/255, 0/255, 0/255])
    hold off
    ylim([0,50]);
    xlabel('Particle Area \mum^2', 'fontsize', 8);
    ylabel('Number of Particles', 'fontsize', 8);
    ax = ancestor(figC3, 'axes');
  xrule = ax.XAxis;
    yrule = ax.YAxis;
    xrule.FontSize = 8;
    yrule.FontSize = 8;
    text(0,-.25,'(c)',...
             'FontSize',10,'HorizontalAlignment','center', 'Units', 'normalized');
    text(.33,.7,str + num2str(black_med(3)),...
             'FontSize',8,'HorizontalAlignment','center', 'Units', '
```

```
normalized');
figC4 = subplot(4,1,4);
    hb4 = bar(bins+.05, hc4, 1);
    hold on
    plot([black_med(4) black_med(4)], [0 60], 'Color', [0/255, 0/255, 0/255])
    hold off
    ylim([0,50]);
    xlabel('Particle Area \mum^2', 'fontsize', 8);
    ylabel('Number of Particles', 'fontsize', 8);
    ax = ancestor(figC4, 'axes');
  xrule = ax.XAxis;
    yrule = ax.YAxis;
    xrule.FontSize = 8;
    yrule.FontSize = 8;
    text(0,-.25,'(d)',...
             'FontSize',10,'HorizontalAlignment','center', 'Units', 'normalized');
    text(.33,.7,str + num2str(black_med(4)),...
             'FontSize',8,'HorizontalAlignment','center', 'Units', 'normalized');

hb1.EdgeColor = [0, 0, 0];
hb2.EdgeColor = [0, 0, 0];
hb3.EdgeColor = [0, 0, 0];
hb4.EdgeColor = [0, 0, 0];
hb1.FaceColor = [0/255, 0/255, 0/255];
hb2.FaceColor = [96/255, 96/255, 96/255];
hb3.FaceColor = [192/255, 192/255, 192/255];
hb4.FaceColor = [255/255, 255/255, 255/255];
fig.Units = 'inches';
figC1.Units = 'inches';
figC2.Units = 'inches';
figC3.Units = 'inches';
figC4.Units = 'inches';

fig.Position(3) = a;
fig.Position(4) = b;
figC1.Position = [y 4*y+3*x z-.05 x];
figC2.Position = [y 3*y+2*x z-.05 x];
figC3.Position = [y 2*y+x z-.05 x];
figC4.Position = [y y z-.05 x];

print('SiMgHistogram', '-dpng', '-r600')
print('Fig6', '-dpng', '-r600')
print('Fig6', '-dtiff', '-r600')

hc1 = histcounts(W_prt_1, [bins, Inf]);
hc2 = histcounts(W_prt_2, [bins, Inf]);
hc3 = histcounts(W_prt_3, [bins, Inf]);
hc4 = histcounts(W_prt_4, [bins, Inf]);


fig = figure(2);
```

```
figC1 = subplot(4,1,1);
    hb1 = bar(bins+.05, hc1,1);
    hold on
    plot([white_med(1) white_med(1)], [0 60], 'Color', [0/255, 0/255, 0/255])
    hold off
    ylim([0,60]);
    xlabel('Particle Area \mum^2', 'fontsize', 8);
    ylabel('Number of Particles', 'fontsize', 8);
    ax = ancestor(figC1, 'axes');
  xrule = ax.XAxis;
    yrule = ax.YAxis;
    xrule.FontSize = 8;
    yrule.FontSize = 8;
    text(0,-.25,'(a)',...
             'FontSize',10,'HorizontalAlignment','center', 'Units', 'normalized');
    text(.33,.7,str + num2str(white_med(1)),...
             'FontSize',8,'HorizontalAlignment','center', 'Units', 'normalized');
figC2 = subplot(4,1,2);
    hb2 = bar(bins+.05, hc2, 1);
    hold on
    plot([white_med(2) white_med(2)], [0 60], 'Color', [0/255, 0/255, 0/255])
    hold off
    ylim([0,60]);
    xlabel('Particle Area \mum^2', 'fontsize', 8);
    ylabel('Number of Particles', 'fontsize', 8);
    ax = ancestor(figC2, 'axes');
  xrule = ax.XAxis;
    yrule = ax.YAxis;
    xrule.FontSize = 8;
    yrule.FontSize = 8;
    text(0,-.25,'(b)',...
             'FontSize',10,'HorizontalAlignment','center', 'Units', 'normalized');
    text(.33,.7,str + num2str(white_med(2)),...
             'FontSize',8,'HorizontalAlignment','center', 'Units', 'normalized');
figC3 = subplot(4,1,3);
    hb3 = bar(bins+.05, hc3, 1);
    hold on
    plot([white_med(3) white_med(3)], [0 60], 'Color', [0/255, 0/255, 0/255])
    hold off
    ylim([0,60]);
    xlabel('Particle Area \mum^2', 'fontsize', 8);
    ylabel('Number of Particles', 'fontsize', 8);
    ax = ancestor(figC3, 'axes');
  xrule = ax.XAxis;
    yrule = ax.YAxis;
    xrule.FontSize = 8;
    yrule.FontSize = 8;
```

```
    text(0,-.25,'(c)',...
             'FontSize',10,'HorizontalAlignment','center', 'Units', 'normalized');
    text(.33,.7,str + num2str(white_med(3)),...
             'FontSize',8,'HorizontalAlignment','center', 'Units', 'normalized');
figC4 = subplot(4,1,4);
    hb4 = bar(bins+.05, hc4, 1);
    hold on
    plot([white_med(4) white_med(4)], [0 60], 'Color', [0/255, 0/255, 0/255])
    hold off
    ylim([0,60]);
    xlabel('Particle Area \mum^2', 'fontsize', 8);
    ylabel('Number of Particles', 'fontsize', 8);
    ax = ancestor(figC4, 'axes');
  xrule = ax.XAxis;
    yrule = ax.YAxis;
    xrule.FontSize = 8;
    yrule.FontSize = 8;
    text(0,-.25,'(d)',...
             'FontSize',10,'HorizontalAlignment','center', 'Units', 'normalized');
    text(.33,.7,str + num2str(white_med(4)),...
             'FontSize',8,'HorizontalAlignment','center', 'Units', 'normalized');

hb1.EdgeColor = [0, 0, 0];
hb2.EdgeColor = [0, 0, 0];
hb3.EdgeColor = [0, 0, 0];
hb4.EdgeColor = [0, 0, 0];
hb1.FaceColor = [0/255, 0/255, 0/255];
hb2.FaceColor = [96/255, 96/255, 96/255];
hb3.FaceColor = [192/255, 192/255, 192/255];
hb4.FaceColor = [255/255, 255/255, 255/255];
fig.Units = 'inches';
figC1.Units = 'inches';
figC2.Units = 'inches';
figC3.Units = 'inches';
figC4.Units = 'inches';

fig.Position(3) = a;
fig.Position(4) = b;
figC1.Position = [y 4*y+3*x z-.05 x];
figC2.Position = [y 3*y+2*x z-.05 x];
figC3.Position = [y 2*y+x z-.05 x];
figC4.Position = [y y z-.05 x];

print('FeMgHistogram', '-dpng', '-r600')
print('Fig7', '-dpng', '-r600')
print('Fig7', '-dtiff', '-r600')

%%%%%%%%%%%%%%%%%%%%%%%%%%%%%%%%%%%%%%%%%%%%%%%%%%%%%%%%%%%%%%%%%%%%%%%%%%%%
```

Appendix C

Data Set

Data for both controls chapters was pulled from a large data set of welds preformed in tight succession. A configuration of the Friction Stir Welding machine remained constant through the weld set and is described in the prior chapters. The consistent configuration was thought to be the best method to reduce variability between welds. It is likely that more trends can be pulled from the data set. So, A key to the complete set of processing parameters and weld software is provided in Figure C.1. The temperature of the anvil and weld tool was logged before and after each weld. It was thought that rising temperatures of the anvil and tool could be a potential source of variability. High temperatures can lead to inaccurate measurements by the dynamometer or heat the aluminum before the weld begins. The before and after temperatures are recorded in Figure C.2. The raw transducer output was saved for the welds according to Section B.1.3, and the raw data and weld images can be digitally distributed.

Weld	Rotation Rate	Weld Speed	Initial Plunge Depth	Offset	Groove Width	Weld Program	Torque Seting
1	1500	3	0.220	0.1	0	LinearWeldV3	N/A
2	1500	3	0.220	0.1	0	LinearWeldV3	N/A
3	1500	3	0.220	0.1	0	LinearWeldV3	N/A
4	1500	3	0.220	0.1	0	LinearWeldV3	N/A
5	1500	3	0.220	0.1	0.025	LinearWeldV3	N/A
6	1500	3	0.220	0.1	0.025	LinearWeldV3	N/A
7	1500	3	0.220	0.1	0.025	LinearWeldV3	N/A
8	1500	3	0.220	0.1	0.05	LinearWeldV3	N/A
9	1500	3	0.220	0.1	0.05	LinearWeldV3	N/A
10	1500	3	0.220	0.1	0.05	LinearWeldV3	N/A
11	1500	3	0.220	0.1	0.05	LinearWeldV3	N/A
12	1500	3	0.220	0.1	0.075	LinearWeldV3	N/A
13	1500	3	0.220	0.1	0.075	LinearWeldV3	N/A
14	1500	3	0.220	0.1	0.075	LinearWeldV3	N/A
15	1500	3	0.220	0.1	0.1	LinearWeldV3	N/A
16	1500	3	0.220	0.1	0.1	LinearWeldV3	N/A
17	1500	3	0.220	0.1	0.1	LinearWeldV3	N/A
18	1500	3	0.220	0.1	0.125	LinearWeldV3	N/A
19	1500	3	0.220	0.1	0.125	LinearWeldV3	N/A
20	1500	3	0.220	0.1	0.125	LinearWeldV3	N/A
21	1500	3	0.220	0.1	0.15	LinearWeldV3	N/A
22	1500	3	0.220	0.1	0.15	LinearWeldV3	N/A
23	1500	3	0.220	0.1	0.15	LinearWeldV3	N/A
24	1500	3	0.220	0	0.1	LinearWeldV3	N/A
25	1500	3	0.220	0	0.1	LinearWeldV3	N/A
26	1500	3	0.220	0	0.1	LinearWeldV3	N/A
27	1500	3	0.220	0	0.1	LinearWeldV3	N/A
28	1500	3	0.220	0	0.1	LinearWeldV3	N/A
29	1500	3	0.220	0.025	0.1	LinearWeldV3	N/A
30	1500	3	0.220	0.025	0.1	LinearWeldV3	N/A
31	1500	3	0.220	0.025	0.1	LinearWeldV3	N/A
32	1500	3	0.220	0.05	0.1	LinearWeldV3	N/A
33	1500	3	0.220	0.05	0.1	LinearWeldV3	N/A
34	1500	3	0.220	0.05	0.1	LinearWeldV3	N/A
35	1500	3	0.220	0.125	0.1	LinearWeldV3	N/A
36	1500	3	0.220	0.125	0.1	LinearWeldV3	N/A
37	1500	3	0.220	0.125	0.1	LinearWeldV3	N/A
38	1500	3	0.220	0.25	0.1	LinearWeldV3	N/A
39	1500	3	0.220	0.25	0.1	LinearWeldV3	N/A
40	1500	3	0.220	0.25	0.1	LinearWeldV3	N/A
41	1500	3	0.220	-0.025	0.1	LinearWeldV3	N/A
42	1500	3	0.220	-0.025	0.1	LinearWeldV3	N/A
43	1500	3	0.220	-0.025	0.1	LinearWeldV3	N/A
44	1500	3	0.220	-0.025	0.1	LinearWeldV3	N/A
45	1500	3	0.220	-0.05	0.1	LinearWeldV3	N/A
46	1500	3	0.220	-0.05	0.1	LinearWeldV3	N/A
47	1500	3	0.220	-0.05	0.1	LinearWeldV3	N/A
48	1500	3	0.220	-0.125	0.1	LinearWeldV3	N/A
49	1500	3	0.220	-0.125	0.1	LinearWeldV3	N/A
50	1500	3	0.220	-0.125	0.1	LinearWeldV3	N/A
51	1500	3	0.220	-0.125	0.1	LinearWeldV3	N/A
52	1500	3	0.220	-0.125	0.1	LinearWeldV3	N/A
53	1500	3	0.220	-0.25	0.1	LinearWeldV3	N/A
54	1500	3	0.220	-0.25	0.1	LinearWeldV3	N/A
55	1500	3	0.220	-0.25	0.1	LinearWeldV3	N/A
56	1500	3	0.220	N/A	0-0.125	LinearWeldV3	N/A
57	1500	3	0.220	N/A	0-0.125	LinearWeldV3	N/A
58	1500	3	0.220	N/A	0-0.125	LinearWeldV3	N/A
59	1500	3	0.220	N/A	.065-0.095	LinearWeldV3	N/A
60	1500	3	0.220	N/A	.065-0.095	LinearWeldV3	N/A
61	1500	3	0.220	N/A	.065-0.095	LinearWeldV3	N/A
62	1500	3	0.220	N/A	.065-0.095	LinearWeldV3	N/A
63	1500	3	0.220	N/A	.065-0.095	TorqueWeldV6	N/A
64	1500	3	0.220	N/A	.065-0.095	TorqueWeldV6	N/A
65	1500	3	0.220	N/A	.065-0.095	TorqueWeldV6	N/A
66	1500	3	0.220	N/A	.065-0.095	TorqueWeldV6	N/A
67	1500	3	0.220	N/A	.065-0.095	TorqueWeldV6	10
68	1500	3	0.220	N/A	.065-0.095	TorqueWeldV6	13
69	1500	3	0.220	N/A	.065-0.095	TorqueWeldV6	13
70	1500	3	0.220	N/A	.065-0.095	TorqueWeldV6	11
71	1500	3	0.220	N/A	.065-0.095	TorqueWeldV6	11
72	1500	3	0.220	N/A	.065-0.095	TorqueWeldV6	11
73	1500	3	0.220	N/A	.065-0.095	TorqueWeldV6	11
74	1500	3	0.220	0.1	0.15	TorqueWeldV6	11
75	1500	3	0.220	0.1	0.15	TorqueWeldV6	11
76	1500	3	0.220	0.1	0.15	TorqueWeldV6	11
77	1500	3	0.220	0.1	0.125	TorqueWeldV6	11

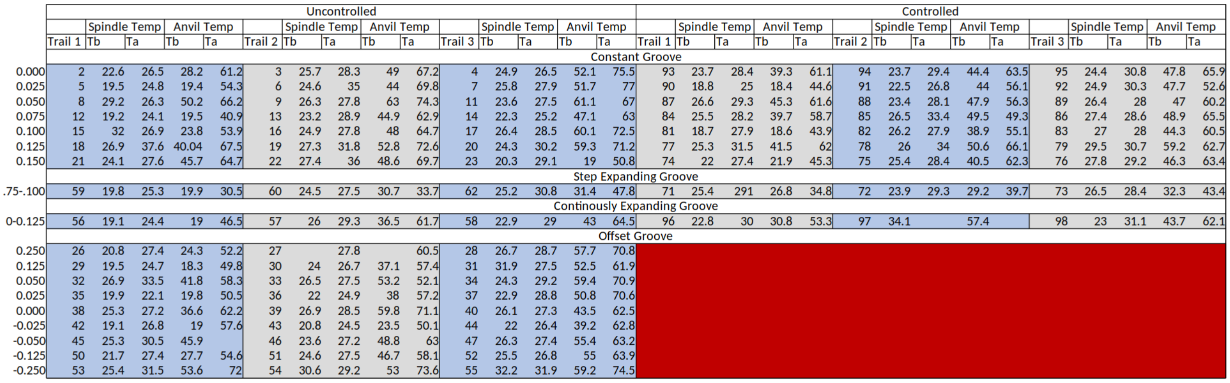

	Uncontrolled															Controlled														
		Spindle Temp		Anvil Temp			Spindle Temp		Anvil Temp			Spindle Temp		Anvil Temp			Spindle Temp		Anvil Temp			Spindle Temp		Anvil Temp			Spindle Temp		Anvil Temp	
	Trail 1	Tb	Ta	Tb	Ta	Trail 2	Tb	Ta	Tb	Ta	Trail 3	Tb	Ta	Tb	Ta	Trail 1	Tb	Ta	Tb	Ta	Trail 2	Tb	Ta	Tb	Ta	Trail 3	Tb	Ta	Tb	Ta
Constant Groove																														
0.000	2	22.6	26.5	28.2	61.2	3	25.7	28.3	49	67.2	4	24.9	26.5	52.1	75.5	93	23.7	28.4	39.3	61.1	94	23.7	29.4	44.4	63.5	95	24.4	30.8	47.8	65.9
0.025	5	19.5	24.8	19.4	54.3	6	24.6	35	44	69.8	7	25.8	27.9	51.7	77	90	18.8	25	18.4	44.6	91	22.5	26.8	44	56.1	92	24.9	30.3	47.7	52.6
0.050	8	29.2	26.3	50.2	66.2	9	26.3	27.8	63	74.3	11	23.6	27.5	61.1	67	87	26.6	29.3	45.3	61.6	88	23.4	28.1	47.9	56.3	89	26.4	28	47	60.2
0.075	12	19.2	24.1	19.5	40.9	13	23.2	28.9	44.9	62.9	14	22.3	25.2	47.1	63	84	25.5	28.2	39.7	58.7	85	26.5	33.4	49.5	49.3	86	27.4	28.6	48.9	65.5
0.100	15	32	26.9	23.8	53.9	16	24.9	27.8	48	64.7	17	26.4	28.5	60.1	72.5	81	18.7	27.9	18.6	43.9	82	26.2	27.9	38.9	55.1	83	27	28	44.3	60.5
0.125	18	26.9	37.6	40.04	67.5	19	27.3	31.8	52.8	72.6	20	24.3	30.2	59.3	71.2	77	25.3	31.5	41.5	62	78	26	34	50.6	66.1	79	29.5	30.7	59.2	62.7
0.150	21	24.1	27.6	45.7	64.7	22	27.4	36	48.6	69.7	23	20.3	29.1	19	50.8	74	22	27.4	21.9	45.3	75	25.4	28.4	40.5	62.3	76	27.8	29.2	46.3	63.4
Step Expanding Groove																														
.75-.100	59	19.8	25.3	19.9	30.5	60	24.5	27.5	30.7	33.7	62	25.2	30.8	31.4	47.8	71	25.4	291	26.8	34.8	72	23.9	29.3	29.2	39.7	73	26.5	28.4	32.3	43.4
Continously Expanding Groove																														
0-0.125	56	19.1	24.4	19	46.5	57	26	29.3	36.5	61.7	58	22.9	29	43	64.5	96	22.8	30	30.8	53.3	97	34.1		57.4		98	23	31.1	43.7	62.1
Offset Groove																														
0.250	26	20.8	27.4	24.3	52.2	27		27.8		60.5	28	26.7	28.7	57.7	70.8															
0.125	29	19.5	24.7	18.3	49.8	30	24	26.7	37.1	57.4	31	31.9	27.5	52.5	61.9															
0.050	32	26.9	33.5	41.8	58.3	33	26.5	27.5	53.2	52.1	34	24.3	29.2	59.4	70.9															
0.025	35	19.9	22.1	19.8	50.5	36	22	24.9	38	57.2	37	22.9	28.8	50.8	70.6															
0.000	38	25.3	27.2	36.6	62.2	39	26.9	28.5	59.8	71.1	40	26.1	27.3	43.5	62.5															
-0.025	42	19.1	26.8	19	57.6	43	20.8	24.5	23.5	50.1	44	22	26.4	39.2	62.8															
-0.050	45	25.3	30.5	45.9		46	23.6	27.2	48.8	63	47	26.3	27.4	55.4	63.2															
-0.125	50	21.7	27.4	27.7	54.6	51	24.6	27.5	46.7	58.1	52	25.5	26.8	55	63.9															
-0.250	53	25.4	31.5	53.6	72	54	30.6	29.2	53	73.6	55	32.2	31.9	59.2	74.5															

Figure C.2: The measured temperature in Celsius of the tool and anvil before and after each weld. Only the welds used in the study were recorded. Failures and tuning samples where deleted.